Diamond Based Electronic Devices

Alexander Freeman

Supervisors: Prof. J. Goss
Prof. N. Wright

School of Engineering
Newcastle University

This dissertation is submitted for the degree of
Doctor of Philosophy

April 2024

Abstract

Recent advances in high-power electronic devices using wide bandgap materials such as SiC and GaN highlight a growing need for enhanced efficiency, longevity, and capacity in energy applications. As silicon-based IGBTs, crucial in global power conversion, face challenges in achieving high efficiencies, the urgency to reduce energy loss becomes more pronounced amidst rising climate concerns and increasing global energy demand. Diamond, renowned for its exceptional material properties and figures of merit, stands on the cusp of revolutionising power electronics, potentially marking the beginning of a new era in high-performance devices. Despite diamond's potential, significant foundational work in doping, metal contact formation, and crystal growth is essential for its practical deployment. While p-type boron-doped diamond has matured, n-type doping with phosphorous continues to be an active research area. Conceptual devices using both n-type and p-type diamond show promise, yet practical limitations of diamond such as that of the strong Fermi-level pinning experienced necessitate innovative manufacturing approaches. This work focuses on the intricacies of fabricating ohmic contacts on nominally phosphorous-doped diamond, supported by thorough material characterisation, to advance the development of feasible diamond-based electronic devices.

A notable development reported here is the enhancement of ohmic contacts through laser graphitisation, a method that significantly improves the electrical performance of contacts to phosphorous-doped diamond. This paves the way for more efficient diamond-based devices, wherever ohmic contacts are required. The mechanisms behind enhanced ohmic contacts are also investigated, with potential device applications examined via finite element modelling. These findings paint an encouraging picture for diamond-based technologies in sectors where energy efficiency is paramount, aligning with the global pursuit of sustainability. As the production of large-scale diamond substrates progresses, diamond-based devices employing innovative techniques like laser graphitisation are well-positioned to penetrate high-power system markets, especially in extreme environments where silicon fails, and even other wide bandgap materials like SiC may falter. Particularly promising are devices like solid-state cold cathodes that leverage diamond's negative electron affinity surface terminations, finding applications in Hall effect thrusters and X-ray sources. Devices reliant on p-n or p-i-n junctions, such as in LED applications, will also benefit from the advancements in reliable ohmic contacts. Similarly, the development of improved Schottky diodes opens avenues for higher performance and broader application.

Declaration

I hereby declare that except where specific reference is made to the work of others, the contents of this dissertation are original and have not been submitted in whole or in part for consideration for any other degree or qualification in this, or any other university. This dissertation is my own work and contains nothing which is the outcome of work done in collaboration with others, except as specified in the text and Acknowledgements. This dissertation contains fewer than 65,000 words including appendices, bibliography, footnotes, tables and equations.

Alexander Freeman
April 2024

Acknowledgements

I am very grateful to the Centre for Doctoral Training (CDT) in Diamond Science and Technology (DST) at Warwick University, and the EPSRC for funding this project opportunity. Additional COVID-19 support from the DST CDT allowed me to continue experimental characterisation of emitter structures, substantially improving the quantity of primary data collected and mitigating the unprecedented delay that COVID-19 had on my experimental work. The coincidental timing of the lockdown starting just as I was preparing for experimental training posed a significant challenge.

I would like to thank my supervisors, Prof. Jon Goss and Prof. Nick Wright. While it is quite natural (hopefully) for PhD students to laud their supervisors impact on their work, I can say with confidence that I would never have been able to complete the work required for a PhD without the insight, support, and all-round expertise that both Jon and Nick have provided for me.

Further thanks go to Dr. Patrick Salter and Dr. Ravi Shivaraman, who were able to provide a one of a kind laser processed sample based on my conceptual designs, that proved to be an excellent case study. The future of laser processed diamond devices appears to hold a lot of promise.

This work would not have been possible without the material support of phosphorous doped diamond, and general wisdom offered by Evince Technology Ltd. Dr. Gareth Taylor, Dr. Paul Farrar and Dr. Hassan Ganjitabar all had a significant impact on my development as a researcher, laying the foundations I needed to progress with this endeavour.

I would also like to thank my peers within the Newcastle University power electronic group, who helped me with clean room and characterisation training. Dr. Johannes Gausden in particular was deeply helpful during this process.

Finally I would like to acknowledge those who perhaps don't need mentioning. Emma, John and David, thanks for helping with some proof reading and everything else along the way. My mum and dad, all of those who have been supportive at Climb Newcastle and Matthew for the trips out and mutual support as we both made our ways through a PhD.

Table of Contents

List of Figures

List of Tables

Introduction

1. Background

Electronic devices based on transistors have transformed the world, with common everyday devices such as smartphones and computers dependent upon a vast infrastructure of modern engineering. One particular focus in the modern world is on the usage of energy, and how best to reduce the amount of energy that we consume. This is an essential step as we progress towards a world in which renewable energy sources can sustain all of the normal devices that we have come to rely on. Power electronics is a unique bottleneck for electrical power consumption, as power electronic devices such as diodes, thyristors, and transistors in general are crucial for all applications. Just as micro-electronics pushes ever onwards with the miniaturisation of small transistors for the purpose of manufacturing processors with increasing densities, power electronics endeavours to provide the electrical energy necessary for these devices.

Unlike micro-electronics, which has found ingenious ways to maintain progress in miniaturisation through continual refinement of the manufacturing processes, power electronics is fundamentally limited by the materials at the heart of such devices. Alternative semiconductors to that of silicon are fast developing, with examples such as that of silicon carbide and gallium nitride clearly demonstrating the practical applications of devices based on wide bandgap semiconductors. However progress at the top-end of power electronics is relatively static, with devices over the last decade or more rarely showing any substantial improvements, and still being generally reliant upon silicon. One competitor which may end the reign of silicon in power electronics is that of diamond.

In the last 20–30 years, massive technological progress has been achieved in the growth, doping and surface treatment of diamond. Many varieties of diamond-based devices have been tested and proven in a prototypical fashion, such as Schottky diodes, field effect transistors, bipolar transistors, metal oxide based devices and even light emitting diode applications. In particular, laser treatment of diamond has come to the forefront of diamond device manufacturing processes, with significant implications for the fabrication of devices that may be able to make use of the offered ability to laser write devices made up of graphitic, diaphitic [2], and diamond forms of carbon. One may speculate on a future in which power electronic devices are based entirely upon carbon, with diamond offering both a substrate for the fabrication of devices, as well as the best ability to act as a heatspreader of any material. However, to achieve this, further development in the field of diamond electronics is required. With new methods of diamond growth at room pressure

and utilising liquid metal catalysts still being discovered [1], the future of diamond specific techniques remains bright.

2. Aims and Objectives

In this project, initial aims primarily focused upon the development and refinement of devices based upon cold field effect emitters within diamond. However, the challenges of fabricating diamond electronics with phosphorous doped diamond led to work being pursued in the methodologies of diamond device fabrication in a more general context. Of particular interest was the plausibility of laser writing devices into diamond, which offers both simplification of the fabrication processes and potentially an improvement when compared to the novel, diamond unique techniques actively being developed. One specific hypothesis that was tested was the comparability of these laser graphitisation techniques

3. Thesis Outline

This thesis contributes to the ongoing worldwide research into diamond electronics by investigating the electrical performance of phosphorous doped diamond and the formation of electrical contacts to said diamond. Additionally, the concept of forming devices which take advantage of diamond to form field effect emitters is examined, with laser written test structures demonstrating that these devices may well have some merit for further investigation. The thesis is arranged as follows:

Chapter 1 - Introductory Content and Historical Footing This chapter attempts to explain the significance of diamond in electronic applications through the lens of historical development at large in the field of electrical devices.

Chapter 2 - Theory and Background In this chapter, the specific diamond properties which make it such an attractive prospect for power electronics are introduced. Further to this, fundamental theoretical work that is essential for later work within the thesis is outlined to provide a general reference before experimental work is presented in the following chapters.

Chapter 3 - Metal Contacts to Phosphorous Doped Diamond With this chapter, the first sets of experimental work concerning the usage of metal contacts to phosphorous doped diamond are presented. While the initial goal of such experiments was to characterise the phosphorous doped diamond itself, significant challenges due to low electrical conduction through these samples led to investigations into how these simple devices may be improved. With phosphorous doped diamond still a relatively rare substrate due to the challenges involved with growth of high quality doped diamond, effort was taken to maximise the work that can be done on only a handful of samples.

Chapter 4 - Characterisation of Laser Processed Phosphorous Doped Diamond Following the work performed with metal contacts formed on phosphorous doped diamond, laser processing is investigated as a potential avenue for improvement of electrical contacts and also for specific device structure formation. This chapter contains the characterisation work that was performed on a laser processed sample, in an effort to better understand the resulting electrical behaviours.

Chapter 5 - Laser Processing for Ohmic Contacts In this chapter, the laser processing is experimentally tested to compare and contrast with the earlier metal contact based devices. Within the backdrop of novel approaches to forming ohmic contacts to phosphorous doped diamond, the data presented herein represent a new method of reducing contact resistance. As part of this, more specific characterisation is performed of the laser written structures themselves, to provide a suitable backing for the more complex device structures that make use of phosphorous doped diamond channels.

Chapter 6 - Testing of Laser Written Emitters and Simulations With this chapter, electrical characterisation of novel laser written emitter structures is outlined. To elucidate on the physical meaning behind the observed results of experimentation, computational modelling is used to further investigate these devices.

Chapter 7 - Conclusions and Future Work Finally, this chapter summarises the key findings of the work reported in this thesis, and sets out the next steps that may be taken to further develop diamond electronic devices that make use of laser processing and phosphorous doped diamond. These two components may be critical to the future commercial success of diamond power electronics.

References

[1] Yan Gong et al. “Growth of diamond in liquid metal at 1 atm pressure”. In: *Nature* (Apr. 2024). ISSN: 1476-4687. DOI: 10.1038/s41586-024-07339-7. URL: http://dx.doi.org/10.1038/s41586-024-07339-7.

[2] Péter Németh et al. “Diaphite-structured nanodiamonds with six- and twelve-fold symmetries”. In: *Diamond and Related Materials* 119 (Nov. 2021), p. 108573. ISSN: 0925-9635. DOI: 10.1016/j.diamond.2021.108573. URL: http://dx.doi.org/10.1016/j.diamond.2021.108573.

Chapter 1. Introductory Content and Historical Footing

1.1. Evolution of Electrical Devices

1.1.1. A Brief History of Electricity

Electricity has been recognised for millennia, with ancient Egyptian texts referring to a fish capable of generating electric shocks ("thunderer of the Nile") as early as 2750 BCE [21]. The phenomenon of static electricity was noted by Thales of Miletus in 585 BCE through the interaction of amber and fur. Centuries later, William Gilbert's seminal work "De Magnete," published in the seventeenth century, argued that the Earth itself was a giant magnet and controversially suggested that it rotated on its axis. His work, which used the term "electricus" derived from the Greek "elektron," meaning amber, was both influential and contentious, sparking debates that resonated during Galileo's trial in 1633 [37, 17].

In 1730, Stephen Gray coined the terms 'conductor' and 'insulator' [3]. This terminology was extended by Benjamin Franklin in 1751 when he introduced 'negative' and 'positive' to describe electrical charges and demonstrated that lightning was a form of static electricity [24, 35].

Luigi Galvani's 1780 discovery that frogs' legs twitched when struck by an electrical spark suggested a link between biology and electricity [38]. Alessandro Volta built upon Galvani's findings, observing that different metals affected the reaction and creating the voltaic pile, an early battery [12].

Hans Ørsted revealed the relationship between electricity and magnetism in 1820, leading to Michael Faraday's 1821 breakthrough that a magnetic field could generate an electric field, laying the groundwork for the electric motor. André-Marie Ampére quantified the force between electric currents in 1826, and George Ohm articulated a comprehensive theory of electricity the following year, after whom the unit of electrical resistance is named.

Joseph Henry's work on electromagnetic induction in 1830 and Charles Wheatstone's measurement of electricity's velocity via a rotating mirror and four miles of wire in 1834 further advanced the field [14]. Samuel Morse's invention of the telegraph and Morse Code in 1838 revolutionised long-distance communication, perhaps representing one of the most significant applications of electronics to the world up to this point in time.

One of the most influential authors from the 19th century was that of James Clerk Maxwell. His first contribution was to generalise the work of Ampére to fully define the

forces due to a moving electronic charge in 1855 [32]. Then, with a four-part paper in 1861, he established the four laws of electromagnetism [19]. The significance of these laws (commonly known as Maxwell's equations) places Maxwell among some of the most lauded of physicists or indeed scientists as a whole, such as Isaac Newton and Albert Einstein.

During the 19th century, vacuum tubes illuminated the existence of electrons as charge carriers. Initially developed as Geissler tubes by Heinrich Geissler in 1857, these precursors to neon lights consisted of shaped glass tubes with air removed to around 100 Pa or approximately 0.1% of atmospheric pressure, filled with gases like neon or argon. Figure 1.1 from a 1914 advertisement displays various designs. In 1859, Plücker first noticed a glow near the cathode, suggesting electron emission [25, 26].

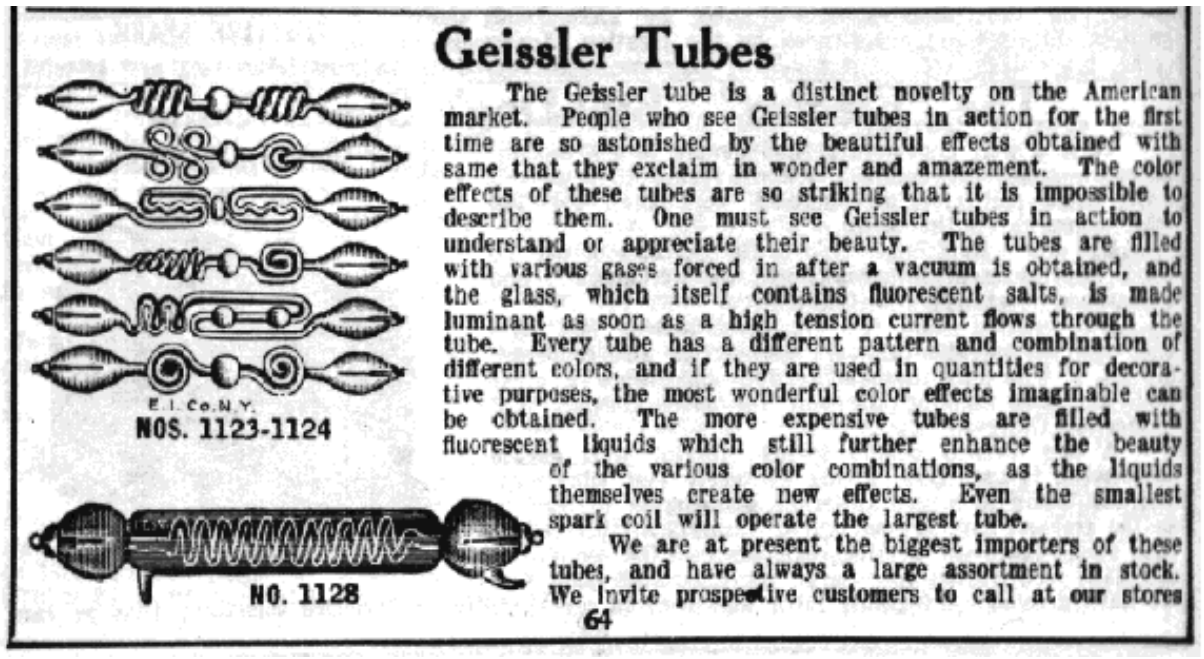

Figure 1.1 A 1914 advertisement showcasing Geissler tube designs [4].

Hittorf's 1869 experiments showed that the glow was obstructed by materials between the cathode and the tube's wall, pinpointing the cathode as the source [15]. Goldstein's 1876 findings demonstrated that with a large negative bias, sharp shadows formed, differing from light's behaviour and leading to the term "Kathodenstrahlen", or cathode rays.

In the 1870s, advancements in vacuum pumping systems allowed vacuum tubes to reach pressures as low as 0.1 Pa to 0.005 Pa, a drastic reduction to just 0.000005% of atmospheric pressure. This enabled a critical observation: only the glass near the anode glowed due to fluorescence, unlike earlier Geissler tubes where the entire glass structure glowed. These enhanced vacuum tubes, later termed "Crookes tubes" after William Crookes's 1879 studies, demonstrated that cathode rays might consist of negatively charged particles hurled at high velocities towards the positively biased anodes [36]. Unlike Crookes, who thought these were "radiant matter," others like Hertz and Goldstein suggested they were "aether vibrations", a type of electromagnetic wave [34]. The debate concluded in 1897 when J.J. Thomson quantified the particles mass through experiments using magnetic fields

to deflect their path, proving they were particles approximately 1800 times lighter than hydrogen atoms. They are now known as electrons [33].

1.1.2. The Rectifying Diode

In 1904, the electronic vacuum tube was developed, capable of achieving pressures as low as 10^{-4}Pa—over 50 times lower than those in Crookes tubes. At such low pressures, ionisation due to residual gases was negligible, and electron conduction only occurred via the emission of electrons from a heated cathode, known historically as the "Edison effect" from Thomas Edison's experiments in 1883. This is now more generally known as "thermionic" emission, due to the historical description of "thermions" prior to the discovery of electrons [34]. To address the problem of soot accumulation darkening the bulbs in his filament lamps, Edison inserted a metal electrode into the bulbs, experimenting with both positive and negative biases [23]. He observed current flow with a positive bias, but not with a negative, contingent on the filament's temperature. At the time, the electron had not yet been discovered, leaving Edison without a theoretical explanation for this phenomenon. Nonetheless, he secured a patent for devices utilising this effect in 1884 [8].

Figure 1.2 An early Fleming Diode [7].

The advent of the vacuum diode is subject to debate, with various iterations appearing globally. The first practical vacuum tube device is widely credited to J. A. Fleming in 1904, who designed the simple vacuum "diode" comprising a hot electron-emitting cathode and an anode to permit unidirectional current flow in circuits [9]. Known also as the "Fleming valve," this device initially served as a detector in early radio receivers, converting weak alternating signals into direct current suitable for enhancing audio clarity in telephone receivers.

1.1.3. Triodes

The triode vacuum tube, invented in 1906 by Lee De Forest, consists of a cathode (electron emitter), a control grid, and an anode, representing a significant advancement in electronics [10].

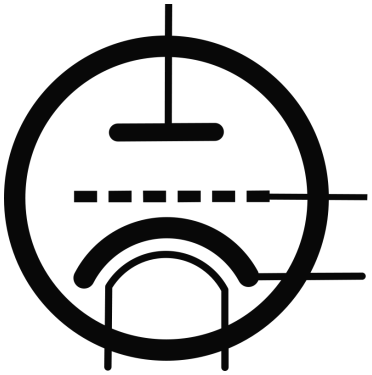

Figure 1.3 A circuit-style diagram of a triode, with a curved cathode indicating the flow of electrons from the bottom to the top, passing through the "gate" grid.

Prior to the triode, rectifying diodes, comprising only a cathode and an anode, were the main application of vacuum tubes. De Forest introduced a third component, the control grid, into the diode to develop the triode, as shown in Figure 1.3. This addition allowed the electron flow from the cathode to the anode to be modulated by a small voltage applied to the grid, enabling the triode to function as an amplifier, as the comparatively weak gate voltage (perhaps the end of a long telegraph wire) produces a large effect in the current across the diode which may be biased at a very high voltage. This breakthrough allowed weak electrical signals, such as those from radios or telegraphs, to be amplified to audible levels.

Initially used only as a wireless signal detector due to performance issues related to the vacuum, the triode's potential for signal amplification was recognised by various researchers in 1912, leading to its adoption in a broad spectrum of applications [10]. For example, devices that were developed due to the triode include radio receivers, loudspeakers, oscilloscopes, early television sets and the first generation of digital computers including the Colossus of Bletchley park [5] and electronic numerical integrator and computer (ENIAC) at the Univeristy of Pennsylvania [11].

However, vacuum tubes have significant operational issues, with cathodes relying upon heated filaments for the source of electrons naturally leading to burning issues, especially if the vacuum formed within the tube is anything less than perfect. Thermal shock induced by turning these devices on or off drastically reduced lifetime, a particular issue for applications where switching was essential (most applications). For an interesting example of how large the factor of thermal shock is, see the Centennial Light, a filament light bulb installed at the Livermore-Pleasanton Fire Department since 1901 which has only been turned off a handful of times, and has a live-stream available at all times for those who enjoy a century old light bulb [18].

1.2. Solid State Transistors: Surpassing Vacuum Tube Technology

Transistors revolutionised the field of electronics by offering an alternative to the bulky and less efficient vacuum tubes. Their development marked the beginning of miniaturisation and enhanced performance of electronic devices, paving the way into the information age which we currently live in.

1.2.1. Creation and Evolution of the Transistor

The invention of the transistor in 1947 by John Bardeen, Walter Brattain, and William Shockley at Bell Laboratories was a major breakthrough that set the stage for the semiconductor era of electronics. This initial transistor was a point-contact transistor using germanium, a small, efficient, and more reliable alternative to the vacuum tube based diode. It won the trio a Nobel Prize in Physics in 1956 and was the start of solid-state electronics, so named due to its ability to incorporate multiple electrical elements within a single solid piece of material. Point contact transistors did replace the vacuum triode in many applications, but the device's operation depended on semiconductor surface structures, making it extremely fragile and susceptible to surrounding humidity.

The bipolar junction transistor (BJT), with a similar physical operation but designed to use the semiconductor bulk rather than the surface, became the dominant triode replacement until the 1970's. This was famously developed by William Shockley in response to being excluded from the original patent application of the point contact transistor [40].

Shockley continued within the field of solid state electronics, providing one of the first truly comprehensive textbooks on the topic in 1976 [30]. Further device structures such as the metal oxide semiconductor field effect transistor (MOSFET), junction field effect transistor (JFET), insulated gate bipolar transistor (IGBT), the family of metal oxide semiconductor (MOS) devices, all depend upon the foundational physics discovered with the creation of simple point contact transistors. Today, transistors have evolved into sophisticated 3D structures, with the class of multi gate field effect transistors (MuGFETs) including the likes of fin field effect transistors (FinFETs), gate all around field effect transistors (GAAFETs) and more recently, multi bridge channel field effect transistors (MBCFETs).

1.2.2. Silicon

While the earliest transistors were made using germanium, silicon quickly became the material of choice due to its superior thermal stability and relative abundance (found in practically all types of rocks, the earths crust is around 59% silicon dioxide [13]). Methods of production such as the Czochralski method developed in 1915 also helped to cement silicon as the semiconductor of choice, in which highly pure and large silicon ingots are crystallised through the careful drawing of material from a molten state [28]. The ability

of silicon to form a stable oxide layer (SiO_2 = silicon dioxide) was also instrumental in the development of metal oxide field effect transistors, aiding in the miniaturisation of transistor devices.

1.2.3. Doping

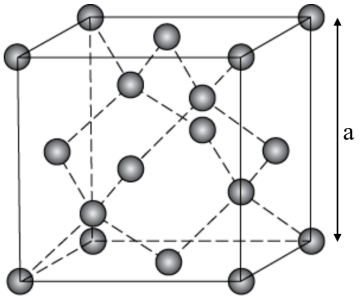

Figure 1.4 A representation of the diamond crystal unit cell.

Of particular importance for all transistor devices is that of "doping". Practically, this is the substitution of crystal atoms with other atoms that have more or less electrons. This replacement of atoms changes the balance of electrons within the crystal structure. In the case of elemental semiconductors such as silicon or carbon, their crystals can be thought of as charge neutral, due to the four valence electrons of silicon and carbon being shared with the four nearest neighbours. A depiction of the unit cell of diamond is shown in figure 1.4. This unit cell represents the smallest possible section of diamond that can be stacked infinitely, hence forming the foundation of the entire crystal structure. Note that within this cube, dashed lines represent the bonds between adjacent atoms. In a complete crystal structure, every atom will have 4 bonds, forming a tetrahedral shape as shown in figure 1.5 by a central red atom with 4 bonds to neighbouring blue atoms.

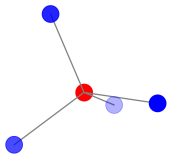

Figure 1.5 A representation of diamond tetrahedral bonding.

Introduction of elements with different numbers of valence electrons, such as boron (one less electron) and phosphorous (one more electron) can hence increase or decrease the total number of electrons in the crystal. The movement of electrons is the fundamental mechanism of charge transfer within the crystal structure, and hence the conduction of electricity. When there is a missing electron, as with boron, this introduces a "hole" where ordinarily an electron would be shared between neighbouring atoms. In the case of an extra electron, as with phosphorous, all of the neighbours the atom is bonded to have

filled valence shells, and the spare electron is hence relatively free to move within the crystal structure. The hole induced by a missing electron can similarly move from the original boron to adjacent atoms. When this happens, the boron "accepts" an electron from a neighbouring atom. Hence the naming convention is that dopants which have less electrons are acceptors and dopants with spare electrons are donors.

1.2.4. Bandgap

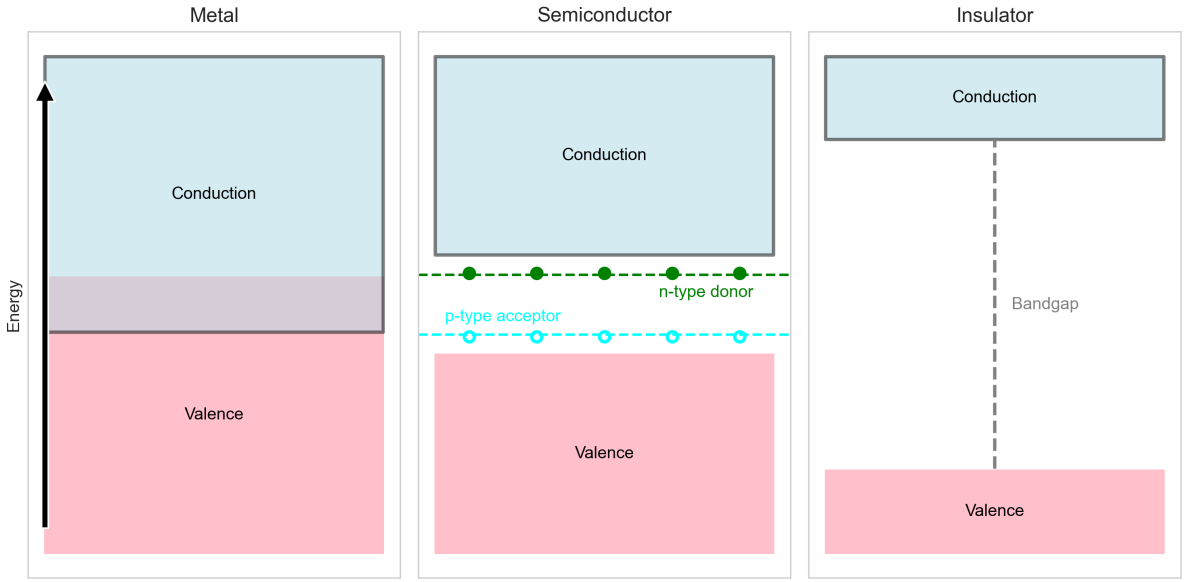

Figure 1.6 A representation of the electronic band theory of solids.

A final necessary detail is the band theory of solids. As represented by figure 1.6, metals and insulators can be very simply described by two "bands" which are named the conduction and valence bands. The valence band represents tightly bound electrons, which do not participate in the flow of current. On its own, the conduction band merely represents the band of empty energy states, corresponding to higher excitation energies of electrons. In the case of a metal, these conduction states overlap with that of the valence states, such that there is a mix of states which are able to move, and hence conduct electricity freely. In the case of an insulator, there is a large "bandgap" between the conduction and valence bands, making it almost impossible for the valence electrons to reach the conductive states (at room temperature). Semiconductors are the middle ground in which there is a bandgap, but a narrow one. It is possible for some electrons from the valence band to jump into the conduction band thanks to thermal energy at typical room temperatures. This is related to one of the distinguishing features of semiconductors - they have a lower resistance as the temperature increases, due to the rise in conduction state electrons (carrier density). This is in contrast to metals, in which at higher temperatures there is a higher resistance, due to the increase of electron scattering mechanisms. While semiconductors also experience such scattering mechanisms at elevated temperatures, the rising carrier densities are the dominant process.

Finally, for completeness, states representing donors and acceptors are included in figure 1.6. The electrons of donor states only require a very small amount of thermal energy to jump into the conduction band. Similarly, the holes of the acceptor states allow for electrons from the valence band to jump up and conduct along the acceptor states. This is usually interpreted as holes being excited into the valence states, and then moving in the opposite direction to electrons, with a positive charge, but is simply another way of interpreting the same physical process of moving electrons.

1.2.5. Challenges and Competition with Silicon Transistors

Despite the remarkable success of silicon transistors, the relentless miniaturisation raises challenges such as increased leakage currents and heat generation. Innovations in transistor design such as FinFETs and Multi-Gate transistors have been developed to address these challenges, pushing the boundaries of silicon technology further. However these novel approaches are still fundamentally limited by the silicon at the heart of such devices, and these approaches are not suitable for different applications, such as power electronics. Alternative materials have been the subject of intense study over the last few decades, with superior material properties offering improvements in efficiency and miniaturisation of high power devices, to name two key areas of study. The climate crisis is ever looming, putting pressure on research to find new solutions for a world which is increasingly tied to the power demands of transistor based technology. In particular, study is focused on using less power to achieve the same results, with natural benefits from a cost and performance perspective also arising as the cost of manufacturing these materials is reduced. Much as the old vacuum tubes are now considered to be dated, inefficient, and unreliable devices, perhaps silicon based technology will be viewed in a similar light in the decades ahead.

1.3. Beyond Silicon

1.3.1. Light Emitting Diodes (LED's)

Light emitting diodes (LEDs) are based on semiconductor junctions that emit light when a forward voltage is applied. LEDs are widely used for illumination, displays, and optical communications, among other applications. While it would be ideal to simply use silicon for this application, the electronic properties of silicon make it quite unsuitable for this purpose (due to an indirect band gap). Instead, LEDs are mostly based on compound semiconductors (with direct bandgaps). These are crystal structures made up of more than one element, such as indium gallium nitride (InGaN), aluminium gallium indium phosphide (AlGaInP) and alumininium gallium arsenide (AlGaAs). Gallium Nitride (GaN) in particular is vital to the production of white light, since the wider electronic bandgap of GaN allows for the creation of blue LED's. The fabrication of GaN-based LEDs involves the growth of a thin GaN layer on a sapphire or silicon carbide substrate, followed by the p-type doping of GaN, to form the required junctions, before metal contacts are formed

[22]. These processes can be performed using techniques such as metalorganic chemical vapor deposition (MOCVD) and plasma-assisted molecular beam epitaxy (PAMBE).

1.3.2. Extreme Conditions

1.3.2.1. Temperature

When silicon reaches its temperature limit of around 125–150°C, the mobility of charge carriers decreases, causing increased electrical resistance and reduced device performance [29]. The diffusion of dopants can also occur, leading to changes in the doping profile and altering the electrical properties of the device. Additionally, high temperatures can cause thermal stress, leading to mechanical failure. The temperature limit for semiconductor devices is determined by several factors, including the thermal expansion coefficient of the materials used, the electrical bandgap, the thermal conductivity of the device, and the melting point of the metal contacts used to make electrical connections [39].

1.3.2.2. High Power

Another limiting condition is electrical breakdown, which occurs when the electric field in the device reaches a critical value and causes a flow of current through the material. One possible reason for this is that high electric fields can cause electrons to gain enough energy to generate electron-hole pairs through impact ionisation [31]. Electron-hole pairs are then free to move within the crystal, and due to the strong electric field, separate, leading to an avalanche effect and the formation of a conductive path [20]. Ionising radiation can also have a detrimental effect on the performance and reliability of semiconductor devices due to the generation of electron-hole pairs, effectively altering the doping profile and causing increased leakage currents [16]. Finally, at high frequencies, there is a limited time available for charge carriers to move across the device. This results in lost power, and reduced device performance at high frequencies. Parasitic capacitance due to device geometry and packaging can also cause significant delay and attenuation of high frequency signals [2].

1.3.2.3. Wide Bandgap Materials

Wide bandgap materials such as silicon carbide (SiC) and gallium nitride (GaN) have gained interest due to their ability to operate at high temperatures and voltages, offering an improved performance compared to silicon [6]. The bandgap values of these materials are significantly larger than silicon, with SiC having an estimated bandgap range of 2.2–3.3 eV and GaN having an estimated bandgap range of 3.2–3.4 eV in contrast to silicon with a bandgap of 1.1 eV [31]. The first implication of a larger bandgap is the significant rise in required temperature for valence electrons at the top of the valence band to jump to the conduction band. It also means that a higher energy of electron collisions is required to generate electron-hole pairs, leading to a significantly higher breakdown voltage. These

advantages make wide bandgap semiconductors promising candidates for next-generation power electronics [1].

1.3.3. Diamond

Diamond is mostly well known for being an incredibly valuable gemstone. However, what makes it truly well known are its material properties [27]. Diamond is used as the definition of hardness, with no other gemstone or material able to scratch it. It is also the definition of a thermal conductor, able to transfer heat at 5 times the rate of silver, which is the most thermally conductive metal. It is possible to compare almost any material characteristic to that of diamond, to observe that diamond comes out on top. This is entirely due to the carbon crystal lattice, which is composed of a dense, three-dimensional network of covalently bonded carbon atoms. As carbon is the lightest element with four valence electrons, it is uniquely positioned in the periodic table of elements to have the strongest crystal structure in every respect. Due in large part to the resilience of diamond, this makes it a difficult material to work with, yet in every comparison, diamond has the highest potential [27]. For comparison with the previously mentioned wide bandgap materials, diamond has a bandgap of around 5.5 eV. In the past, diamond was only regarded as an insulator due to this, as it most closely resembles the insulator of figure 1.6. But with further study, it has become clear that diamond can instead be used as a semiconductor.

1.3.4. This Work

Diamond transistors offer a great many advantages if produced correctly, including higher current densities, higher breakdown voltages, and faster switching speeds. Diamond diodes are in active development for use in high-power rectifiers and detectors, particularly in environments where all other semiconductors would fail. Additionally, diamond is being investigated for use in radiation-hard electronics and quantum information processing. The potential applications of diamond are far and wide, but the production of practical devices that live up to the exceptional material properties is a slow process. While it is now possible to manufacture silicon-like devices with diamond, as well as uniquely diamond devices, the resulting performances are simply not good enough to replace the best silicon devices. In the work presented in this thesis, investigations into the production and possible improvement of diamond based electronics are presented. In particular, the possibility of using laser processing to create devices has been studied, both experimentally and via computational modelling techniques. In a twist of fate, the vacuum devices of 1904 find a resurgence with diamond, as diamond can both be used to replace the vacuum of these devices, and also to remove the need for a vacuum. Hence, it is possible to create devices which finally address the niche concerns of high power, high frequency applications. A final specific example is that of x-ray generation, which requires a vacuum-tube era heated cathode for electron generation. Diamond may be the key to cold-field effect emitters to replace these.

References

[1] B. Jayant Baliga. *Fundamentals of Power Semiconductor Devices*. Springer International Publishing, 2019. ISBN: 9783319939889. DOI: 10.1007/978-3-319-93988-9. URL: http://dx.doi.org/10.1007/978-3-319-93988-9.

[2] B.J. Baliga. "Power semiconductor device figure of merit for high-frequency applications". In: *IEEE Electron Device Letters* 10.10 (Oct. 1989), pp. 455–457. ISSN: 1558-0563. DOI: 10.1109/55.43098. URL: http://dx.doi.org/10.1109/55.43098.

[3] C. Carnle. *Popular Mechanics*. Popular Mechanics Co, 1931, pp. 772–776.

[4] The Electro Importing Co. *Electro Importing Catalog 14*. Vol. 2. Lindsay Publications Inc, 1914.

[5] B.J. Copeland. "Colossus: its origins and originators". In: *IEEE Annals of the History of Computing* 26.4 (Oct. 2004), pp. 38–45. ISSN: 1058-6180. DOI: 10.1109/mahc.2004.26. URL: http://dx.doi.org/10.1109/MAHC.2004.26.

[6] Maurizio Di Paolo Emilio. *GaN and SiC Power Devices: From Fundamentals to Applied Design and Market Analysis*. Springer Nature Switzerland, 2024. ISBN: 9783031506543. DOI: 10.1007/978-3-031-50654-3. URL: http://dx.doi.org/10.1007/978-3-031-50654-3.

[7] *Early Fleming Diode*. https://ethw.org/File:Fleming_Diode_0351.jpg. Accessed: 2023-02-09.

[8] T. A. Edison. "Electrical Indicator." US307031A. 1884.

[9] J. A. Fleming. "Instrument for Converting Alternating Electric Currents into Continueous Currents." US803684A. 1905.

[10] Lee de Forest. "Dawn of the Electronic Age". In: *Popular Mechanics* (Dec. 1940), pp. 154–159, 358, 360, 362, 364.

[11] H.H. Goldstine and A. Goldstine. "The Electronic Numerical Integrator and Computer (ENIAC)". In: *IEEE Annals of the History of Computing* 18.1 (1996), pp. 10–16. ISSN: 1058-6180. DOI: 10.1109/85.476557. URL: http://dx.doi.org/10.1109/85.476557.

[12] M. Guarnieri. "The Big Jump from the Legs of a Frog". In: 8 (4 2014). DOI: 10.1109/MIE.2014.2361237.

[13] Gordon B. Haxel, James B. Hedrick, and Greta J. Orris. *Rare Earth Elements—Critical Resources for High Technology*. Tech. rep. Fact Sheet 087-02. Accessed: 2024-04-12. U.S. Geological Survey, Nov. 2002. URL: https://pubs.usgs.gov/fs/2002/fs087-02/.

[14] Alexander Hellemans. *The timetables of science*. Simon & Schuster, Nov. 1988.

[15] Hittorf. In: *Pogg. Ann.* 136 (1869), p. 8.

[16] Arijit Karmakar et al. “A Review of Semiconductor Based Ionising Radiation Sensors Used in Harsh Radiation Environments and Their Applications”. In: *Radiation* 1.3 (Aug. 2021), pp. 194–217. ISSN: 2673-592X. DOI: 10.3390/radiation1030018. URL: http://dx.doi.org/10.3390/radiation1030018.

[17] Douglas Linder. “The Trial of Galileo”. In: *SSRN Electronic Journal* (2002). DOI: 10.2139/ssrn.1021251. URL: https://doi.org/10.2139/ssrn.1021251.

[18] Livermore-Pleasanton Fire Department. *Centennial Light Bulb Live Stream*. Webcam live stream. Accessed on 2024-04-10. Located at Livermore-Pleasanton Fire Department Station #6, 4550 East Ave., Livermore, CA. Visiting hours are daily when on-duty personnel are available, from 10:00 a.m. to 11:30 a.m. and 3:00 p.m. to 5:00 p.m. 2024. URL: http://bulbcam.cityofpleasantonca.gov/.

[19] J.C. Maxwell. “On physical lines of force”. In: *Philosophical Magazine* 90.sup1 (Feb. 2010), pp. 11–23. DOI: 10.1080/14786431003659180. URL: https://doi.org/10.1080/14786431003659180.

[20] K. G. McKay. “Avalanche Breakdown in Silicon”. In: *Physical Review* 94.4 (May 1954), pp. 877–884. ISSN: 0031-899X. DOI: 10.1103/physrev.94.877. URL: http://dx.doi.org/10.1103/PhysRev.94.877.

[21] Peter Moller. “Electric Fish Electrocommunication in Teleost Fishes: Behavior and Experiments Bernd Kramer”. In: *BioScience* 41.11 (Dec. 1991), pp. 794–796. DOI: 10.2307/1311732. URL: https://doi.org/10.2307/1311732.

[22] Shuji Nakamura, Takashi Mukai, and Masayuki Senoh. “Candela-class high-brightness InGaN/AlGaN double-heterostructure blue-light-emitting diodes”. In: *Applied Physics Letters* 64.13 (Mar. 1994), pp. 1687–1689. DOI: 10.1063/1.111832. URL: https://doi.org/10.1063/1.111832.

[23] Frederik Nebeker. *Dawn of the Electronic Age: Electrical Technologies in the Shaping of the Modern World, 1914 to 1945*. John Wiley and Sons, 2009. ISBN: 9780470409756.

[24] B. Park. *A history of electricity: The intellectual rise in electricity from antiquity to the days of Benjamin Franklin*. New York: John Wiley % Sons., 1898.

[25] Plücker. In: *Pogg. Ann* 107 (1859).

[26] Plücker. In: *Pogg. Ann* 116 (1862).

[27] H. Umezawa S. Koizumi and M. Suzuki. *Power Electronics Device Applications of Diamond Semiconductors*. Elsevier, 2018. ISBN: 9780081021835. DOI: 10.1016/c2016-0-03999-2. URL: http://dx.doi.org/10.1016/C2016-0-03999-2.

[28] K. Sangwal. “Czochralski Method of Crystal Growth in the Scientific Literature: An Informetric Study”. In: *Acta Physica Polonica A* 124.2 (Aug. 2013), pp. 173–180. ISSN: 1898-794X. DOI: 10.12693/aphyspola.124.173. URL: http://dx.doi.org/10.12693/APhysPolA.124.173.

[29] W. Shockley. “The theory of p-n junctions in semiconductors and p-n junction transistors”. In: *The Bell System Technical Journal* 28.3 (1949), pp. 435–489. DOI: 10.1002/j.1538-7305.1949.tb03645.x.

[30] William Shockley. *Electrons and holes in semiconductors, with applications to transistor electronics*. en. 1976.

[31] S.M. Sze and Kwok K. Ng. *Physics of Semiconductor Devices*. Wiley, Apr. 2006. DOI: 10.1002/0470068329. URL: https://doi.org/10.1002/0470068329.

[32] *The scientific papers of James Clerk Maxwell*. Vol. 1. New York, Dover Publications, 1890.

[33] J. J. Thomson. “On Bodies Smaller Than Atoms.” In: *The Popular Science Monthly* (1901), pp. 323–335.

[34] J. J. Thomson. *The Dsicahrge of Electricity Through Gases.* New York Charles Scribner’s Sons, 1903.

[35] M. A. Uman. *All About Lightning.* New York: Dover Productions, 1986.

[36] “V. The Bakerian Lecture.—On the illumination of lines of molecular pressure, and the trajectory of molecules”. In: *Philosophical Transactions of the Royal Society of London* 170 (Dec. 1879), pp. 135–164. DOI: 10.1098/rstl.1879.0065. URL: https://doi.org/10.1098/rstl.1879.0065.

[37] (Translation - P. F. Mottelay) W. Gilbert. *De Magnete, (Translation - On the Loadstone and Magnetic Bodies)*. London B. Quaritch, 1600, (Translation - 1893).

[38] E. T. Whittaker. *Theories of Aether and Electricity.* Thomas Nelson, 1953.

[39] W. Wondrak. “Physical limits and lifetime limitations of semiconductor devices at high temperatures”. In: *Microelectronics Reliability* 39.6–7 (June 1999), pp. 1113–1120. ISSN: 0026-2714. DOI: 10.1016/s0026-2714(99)00158-4. URL: http://dx.doi.org/10.1016/S0026-2714(99)00158-4.

[40] Glenn Zorpette. *How the First Transistor Worked*. IEEE Spectrum. This article appears in the December 2022 print issue as "The First Transistor and How it Worked.". Nov. 2022. URL: https://spectrum.ieee.org/transistor-history.

Chapter 2. Theory and Background

In this chapter, the necessary methodologies and theoretical footing necessary for later chapters is established. Additionally, background into the application of diamond within the context of power electronics engineering is given to assist in the progression from electronics to diamond electronics.

2.1. Electronics Background

2.1.1. Introduction

Electronic devices based on semiconductors are the backbone of modern technology, long since replacing vacuum-tube based devices in power electronics and consumer electronic applications. As implied by the name, power electronic devices in particular deal with applications where the conversion and control of electrical power is concerned. Over the past half a century, the global electrical consumption has slowly, and continuously grown. Between 1980 and 2022, electrical consumption rose from 7300 to 25,000 terawatt-hours [20]. This is likely to increase ever further, with the electricity consumption due to data centres, artificial intelligence (AI) and cryptocurrency sectors predicted to double by 2026 [36]. This is supported in large by the significant growth in renewable energy sources, which are set to provide more than a third of total electricity generation globally by early 2025, overtaking the market share of coal [36].

When it comes to the power electronics themselves, a mix of silicon-based devices with more recent wide bandgap substrates such as GaN and SiC are the most advanced solutions for power applications that range from high voltage direct current (HVDC) converter stations to flexible ac transmission system (FACTS) devices. These devices are used for variable-speed drivers in motors, the regulation of ac power grids and more recently throughout the electric vehicle (EV) market in the form of EV battery chargers in particular [100, 2]. Depending on the application, various blocking voltages and maximum operating frequencies can be readily acquired [97].

ID	Type	x (mm)	V_B (kV)	F (kHz)	I (kA)	R_t ($\mathrm{K\,kW^{-1}}$)	T_{max} (°C)
T1503	Thyristor	150	8	0.06	55	6.3	120
DZ950	Diode	70	4.4	0.06	29	42	150
TT240	Thyristor	60	3.8	0.05	6.1	39	125
D2601	Diode	121	9	0.06	52	8.9	160
AIKQ120	IGBT	16	750	4.1	0.36	170	175

Table 2.1 A sample of readily available silicon power electronic devices, as sourced from Infineon Technologies AG [69, 81, 68, 80, 18].

Table 2.1 summarises a small sample of current power electronic devices based on silicon. In this table, x is is the approximate diameter (thyristors are in a circular package, diodes and IGBT's are in a rectangular package), V_B is the maximum reverse bias or blocking voltage, F is the estimated maximum operating frequency, I is the maximum forward surge current, R_t is the maximum thermal resistance from junction to case and T_{max} is the maximum operating junction temperature. The exact type of device used will always be a trade-off, while thyristors of up to 10 kV are available, these devices inevitably require a significantly larger junction size, which increases the challenge of thermal management solutions, the cost of such devices overall, and also raises the complexity of such devices. While variations of thyristors such as the integrated gate-commutated thyristor (IGCT) or gate turn off (GTO) thyristors both allow for higher operating frequencies of between 0.1–1 kHz, this comes at the expense of a lower blocking voltage and peak surge current rating. IGCT or GTOs are widely used within motor control, renewable energy management, and anywhere with large power draws such as rail travel [100]. In the case of power inverters, where fast switching frequency is necessary, insulated gate bipolar transistors (IGBT) due to the ideal balance between breakdown voltage and operating frequency offered. For smaller systems such as conventional power supplies, amplifiers and consumer electronics in general, less specific transistors such as metal oxide semiconductor field effect transistors (MOSFETs), junction field effect transistors (JFETs) and bipolar junction transistors (BJTs) are in wide usage [97].

Silicon based devices are limited by a few key factors. First, the low thermal conductivity of silicon and narrow bandgap limit operating temperatures to around 150°C. Second is the critical electric field of silicon, which is around 0.3 $\mathrm{MV\,cm^{-1}}$ [55]. Due to the low critical electric field of silicon, there is a need for series stacking of silicon based devices with complex triggering systems to ensure that the potential bias across any single junction does not exceed the critical electric field [51, 100]. Finally, as a result of both the requirement for stacked silicon devices and also advanced thermal management solutions, the electrical power losses can rise significantly [65].

2.1.2. Wide Bandgap Semiconductors

A key solution to the issues faced by silicon power electronics is to utilise a wide-bandgap semiconductor. In particular, Si can be compared to silicon carbide (SiC), gallium nitride (GaN), gallium oxide (Ga_2O_3) and diamond. All of these materials have larger critical electric fields and higher thermal conductivities, significantly improving the viability of devices based on single structures in contrast to the series stacking of Si [97]. Diamond stands apart from these comparators, with a critical field 30 times higher than Si and 3 times higher than SiC [110]. The maximum carrier mobility of diamond is another best in class comparison, with intrinsic carrier mobilities of 4500 and 3800 $\mathrm{cm^2\,V^{-1}\,s^{-1}}$ for electrons and holes respectively [37]. It should be noted that practical carrier mobilities in phosphorous or boron doped diamond are significantly lower than these maximum values, with lightly doped material in the range of 600–700 $\mathrm{cm^2\,V^{-1}\,s^{-1}}$ as measured via Hall effect measurements [41]. The theoretical maximum of such material has previously been predicted to be 1000 $\mathrm{cm^2\,V^{-1}\,s^{-1}}$ [67], however it is limited by the compensation ratio of donors, which is dependent upon crystal orientation and growth conditions [94]. Diamond also has a best in class thermal conductivity, at 2200 $\mathrm{W\,m^{-1}\,K}$, with a relative dielectric constant of 5.7 [110]. To compare differing materials figures of merit (FOM) are typically used [107]. In the case of diamond, two important FOMs were introduced by Baliga [3]. First is the Baliga FOM (BFOM), given by:

$$BFOM = \epsilon_r \mu E_{max}^3 \tag{2.1}$$

where ϵ_r is the relative dielectric constant, μ is the carrier mobility and E_{max}^3 is the breakdown field, typically given in units of $\mathrm{MV\,cm^{-1}}$. The second is Baliga's high-frequency FOM (BHFOM), using the same notation:

$$BHFOM = \mu E_{max}^2 \tag{2.2}$$

While the BFOM is used to estimate the trade off between conductive losses and breakdown voltage for a unipolar device, the BHFOM is used to include switching losses associated with a gate capacitance, as in FET's [88]. There are further FOM's, but for the comparison of materials presented here, the BFOM and BHFOM are used.

Table 2.2 provides the relevant material properties and the two FOM's for all materials. In this table, γ is used to represent the thermal conductivity, and the second column is used to denote electrons (e-) or holes (h+) for the material properties that require this distinction, namely the saturation drift velocity v_s and carrier mobility μ. As the electrical properties of diamond are quite dependent upon the crystal structure, with defect centres strongly impacting the carrier mobility due to the rise in coulombic scattering events [30, 38, 101], it is typical give a range of FOMs for diamond, which helps to represent the range of crystal dependent properties. At the low end, highly defective, disordered diamond with low carrier velocities and critical electric fields is considered. While at the high end,

		Si	4H-SiC	GaN	Ga_2O_3	Diamond
E_g (eV)		1.12	3.20	3.45	4.9	5.47
v_s (10^7 $cm^2 V^{-1} s^{-1}$)	e-	1.1	1.9	2.5	2	2.5, 1.9 [72, 73]
	h+	0.8	1.2	-	-	1.0, 1.4 [72]
μ ($cm^2 V^{-1} s^{-1}$)	e-	1500	1000	1500	300	4500 [37]
	h+	450	120	200	-	3800[37]
E_{max} ($MV\,cm^{-1}$)		0.3	2.8	5	8	10–22[104]
ϵ_r		11.9	9.66	8.9	9.93	5.7 [110]
γ ($W\,m^{-1} K^{-1}$)		150	490	130	23	2200 [110]
BFOM		1.0	440	2950	3516	3380–473078
BHFOM		1.0	58	237	158	1486–12510

Table 2.2 Material properties and figures of merit (FOM) for various semiconductors [83, 109, 97, 85].

electronic grade diamond with less than 5 parts per billion nitrogen defect centres and highly oriented single crystal growth is used to represent the peak upper limit. These properties are also orientation specific [57], due in part to differing rates of compensation within doped diamond films [71, 93], so care must be taken in the selection of crystal substrate if a high FOM is required.

2.1.3. Characterisation Techniques

In the following sections, an overview of the general principles behind characterisation techniques used throughout the experimental work in this thesis are given.

2.1.3.1. TLM

The Transmission Line Method (TLM) is widely used for evaluating the contact resistivity between metal and semiconductor regions, especially when the semiconductor region is isolated from the substrate by a junction [85]. This technique, however, faces challenges when the junction isolation is leaky, potentially resulting in incorrect parameter extraction due to parasitic leakage currents [13].

Basic Assumptions and Limitations TLM assumes a uniform sheet resistance, an isotropic interface between conducting regions and current flow restriction to the channel of interest [97].

These assumptions may not hold in certain cases, such as in GaN/AlGaN two-dimensional electron gas systems where the sheet resistance under the contact area varies, leading to discrepancies in applying standard TLM equations for contact resistivity determination [11].

Assumptions The core assumption in TLM is that the metal's resistivity in the contact is negligible compared to the contact resistivity, thus simplifying the resistance of a single contact to primarily R_c [97]. Under this assumption, total resistance can be expressed and

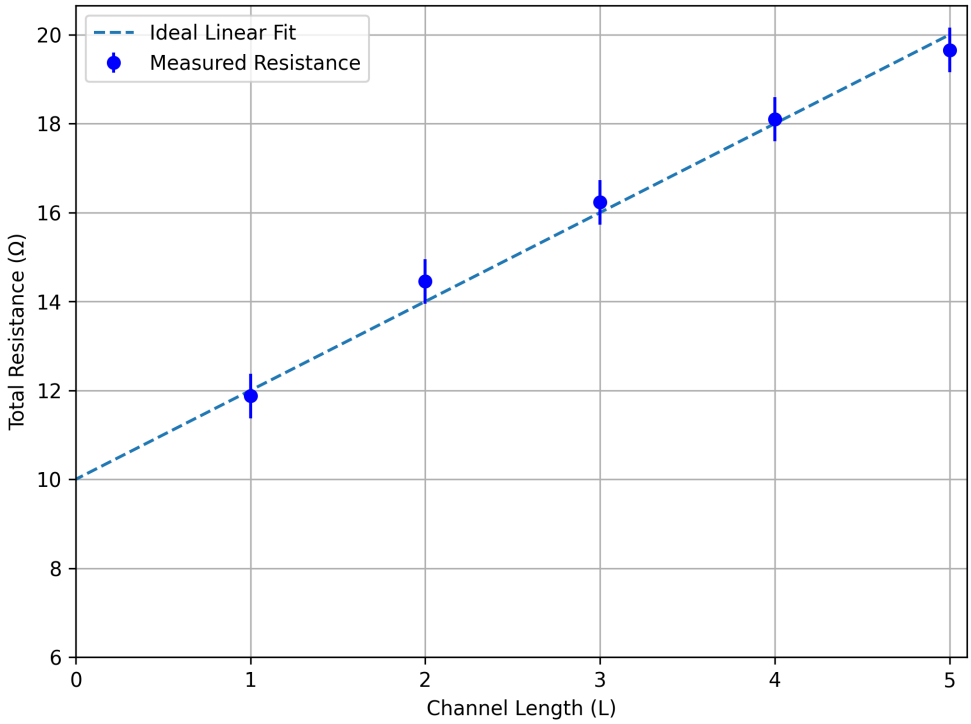

Figure 2.1 A typical linear TLM plot, with a linear best fit extrapolated to zero channel length and minimal deviation from the linear fit across multiple arbitrary channel lengths L.

analysed by constructing test structures of varying lengths and measuring the resultant resistance. By plotting these resistances against the length and extrapolating to zero length, the intercept gives twice the contact resistance, and the slope provides the sheet resistance of the semiconductor. This is demonstrated by figure 2.1, in which arbitrary channel lengths L are used to show the extrapolation of a linear best fit to the case of zero channel length. Similarly, the slope of the graph is used to determine the sheet resistivity, with a known channel width.

Contact Resistivity and Current Crowding Specific contact resistivity (ρ_c) is defined as $\rho_c = A \cdot R_c$, where A is the contact area. It is critical to differentiate between physical and effective contact areas due to the non-uniformity of current flow into the semiconductor, a phenomenon known as current crowding. While the current flow through the semiconductor itself is still uniform, we can no longer use the physical length and width of the contacts to determine the contact area. Current crowding, particularly pronounced near the edges of the contact, leads to a variation in the effective current distribution [79, 97].

Transfer Length and Effective Contact Area An important parameter in the standard Transmission Line Method is the transfer length, L_T, which represents the characteristic distance over which current transfers from the metal contact into the

semiconductor. When this is considered, the methodology may then be referred to as the Transfer Length Method (also using the acronym TLM). It is defined as [85]:

$$L_T = \sqrt{\rho_c / R_{sh}} \tag{2.3}$$

where ρ_c is the specific contact resistivity and R_{sh} is the sheet resistance of the semiconductor. The transfer length determines the effective current injection area, meaning that for contacts longer than L_T, most of the current flows into the semiconductor before reaching the contact edge. However, if the contact length is comparable to or shorter than L_T, current crowding becomes severe, leading to an overestimation of contact resistivity due to increased lateral resistance effects [59]. Conversely, excessively long contacts may give an artificially low resistivity measurement by overemphasising current spreading effects [4]. This makes L_T a crucial design parameter for optimizing test structures, as it ensures accurate extraction of ρ_c while minimising distortions caused by non-ideal current distributions. Understanding L_T is particularly important when dealing with non-uniform or non-ideal contacts, where variations in surface properties, doping concentrations, or contact geometry can further influence current spreading under the contact [79].

LTLM Theory

$$R_T = 2R_m + 2R_c + R_{semi} \tag{2.4}$$

The core derivation of linear TLM theory derives from the observation that total resistance R_T is made up of two contact resistances R_c, two resistances due to wires in the circuits/probes R_m, and one resistance of the semiconductor in question R_{semi} [97]. By measuring the total resistance across differing channel lengths, with known areas of metal contacts to the semiconductor, it is possible to derive the following [85]:

$$R_T = \frac{R_{sh}}{W} d + 2R_c \tag{2.5}$$

where $R_{sh} = \frac{R_{semi} W}{d}$ is the sheet resistance, W is the width of the contacts and d is the spacing between contacts. While more sophisticated transfer length methodologies are applicable, initial testing began with this simple LTLM approach.

2.1.3.2. AFM

Atomic Force Microscopy (AFM) is a type of scanning probe microscopy that offers nanoscale resolution. It utilises a cantilever with a sharp tip to physically scan the surface of a sample. As the tip moves across the surface, forces between the tip and the sample cause the cantilever to deflect. These deflections are monitored via a laser beam reflected off the top of the cantilever into a photodiode, translating physical interactions into topographical maps of the surface [12].

AFM operates in several modes, including contact, non-contact, and tapping (dynamic) modes. Contact mode maintains the tip in constant contact with the surface, suitable

for hard and smooth surfaces but may damage soft or rough samples. Non-contact mode involves oscillating the cantilever near the surface to measure van der Waals forces without actual contact, ideal for delicate samples. Tapping mode, a hybrid approach, allows the tip to intermittently "touch" the surface, reducing sample damage while providing high-resolution images. This method is particularly useful in studying the surface properties of materials, such as the roughness and corrosion characteristics, without extensive preparation.

2.1.3.3. Raman

Raman spectroscopy is an analytical technique based on the raman effect, where monochromatic light (usually from a laser) interacts with molecular vibrations, leading to scattering of light at energy levels different from the incident light. This scattering results in a raman spectrum, unique to the molecular structure of the sample, allowing for both qualitative and quantitative analysis. The technique is especially valued for its non-destructive nature and minimal preparation requirements.

In raman spectroscopy, when light interacts with a sample, most of the light scatters elastically (Rayleigh scattering) without a change in energy. However, a small fraction scatters inelastically (raman scattering), with a change in energy corresponding to vibrational energy levels of the molecules in the sample. This shift provides a fingerprint by which the molecule can be identified. The intensity of a raman signal varies with the polarisability of the molecular bonds, making it highly sensitive to the chemical structure and state of the substance [8].

2.1.3.4. SIMS

Secondary Ion Mass Spectrometry (SIMS) is a technique used to analyse the composition of solid surfaces and thin films by sputtering the surface with a focused primary ion beam and then collecting and analysing ejected secondary ions. The process involves the use of a primary ion source such as O_2^+, O^-, Cs^+, Ar^+, or Ga^+, which bombards the sample surface under ultra-high vacuum conditions, causing the ejection of secondary ions.

SIMS is highly sensitive, capable of detecting elements from hydrogen (H) to uranium (U) and can achieve detection limits down to parts per billion. This makes it particularly useful for trace level analysis. The method also allows for the measurement of isotopic ratios with high precision, and the spatial distribution of elements can be mapped with high resolution due to the localised nature of the sputtering process.

Despite its advantages, SIMS analysis can be complex due to the formation of molecular ions and clusters during sputtering, which can complicate the mass spectrum. Quantitative analysis requires the use of standards similar in composition to the sample because the ionisation probability of sputtered atoms is influenced by the matrix. Additionally, since SIMS requires the sample to be stable under high vacuum, it limits the type of samples that can be analysed [22].

2.1.3.5. XPS

X-ray Photoelectron Spectroscopy (XPS) leverages the photoelectric effect to analyse surface chemical states by measuring the kinetic energy of electrons ejected from a material when irradiated with X-rays. The core principle involves directing X-rays of sufficient energy (typically >1200 eV) onto a sample to eject core-level electrons. The binding energy of these electrons is then precisely determined, providing a detailed electronic and chemical state analysis of the material's surface up to a depth of about 20 nm.

The process is sensitive to all elements with an atomic number greater than hydrogen and can distinguish between different chemical states of the elements. For instance, variations in electron binding energy can indicate different oxidation states or the presence of chemical bonds. XPS spectra not only display peaks corresponding to the core levels of the elements present but may also show satellite peaks due to additional electron transitions such as shake-up and shake-down events, where electrons are excited to higher or lower energy states during the photoionisation process [58].

2.1.3.6. HIM

Helium Ion Microscopy (HIM) employs a gas field ionisation source to generate a focused beam of helium ions from a three-sided pyramidal tip, where ionisation occurs at the very apex consisting of only three atoms (a trimer). This setup allows for extremely high-resolution imaging, significantly surpassing that of conventional scanning electron microscopes (SEM). The helium ions penetrate deeper into the sample compared to electrons due to their additional mass, depositing energy primarily through forward scattering which enhances secondary electron emission and provides high contrast images with minimal surface damage. This makes HIM particularly effective for detailed surface studies of samples at resolutions five times greater than those achievable with modern SEMs. The deep penetration of helium ions also reduces surface charging, a common issue with non-conductive materials in SEM, which can be further mitigated by using a low-voltage electron flood gun [40].

2.2. Diamond

2.2.1. Crystal Structure of Diamond

Diamond is a carbon allotrope characterised by each carbon atom being covalently bonded to four others in a tetrahedral configuration, forming a three-dimensional lattice. This structure arises from the sp^3 hybridisation of one 2s and three 2p orbitals, resulting in a face-centred cubic (FCC) crystal structure with two distinct sub-lattices [64]. The unit cell of diamond contains eight carbon atoms and features bond lengths of 0.154 nm and bond angles of 109.5 degrees, embodying a tetrahedral symmetry. This closely packed arrangement yields diamond's exceptional atomic density of 3.52 $\mathrm{g\,cm^{-3}}$, equivalent to 1.76×10^{23} $\mathrm{at\,cm^{-3}}$, making it the solid with the highest atomic density known [62].

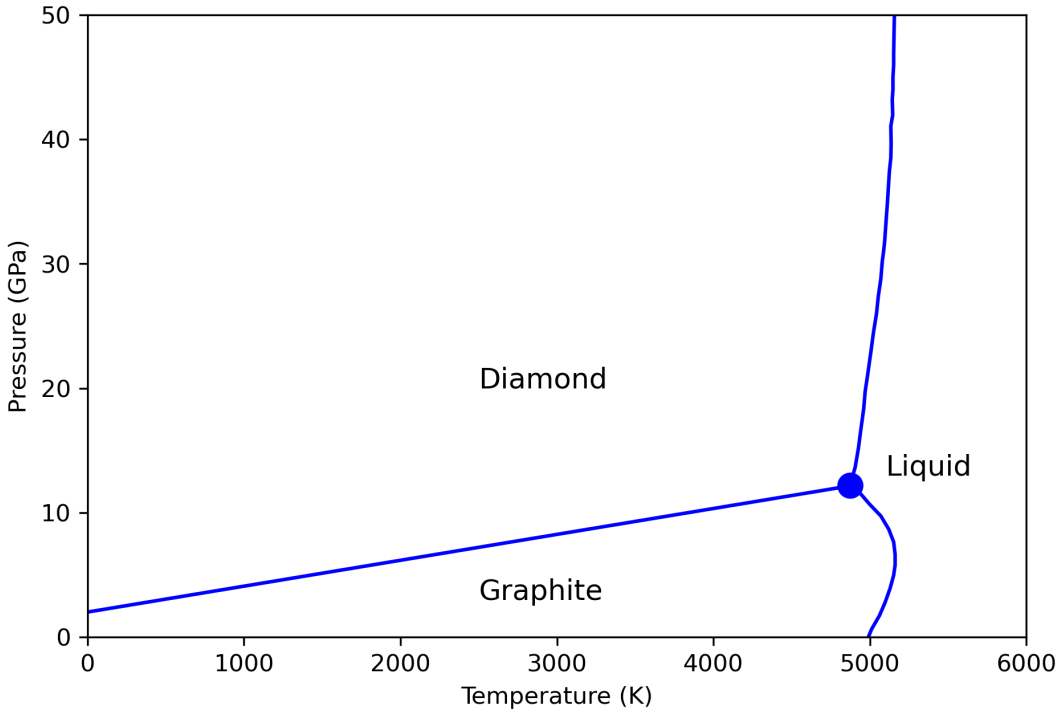

Figure 2.2 The simple phase diagram of carbon to 50 GPa, which corresponds to approximately a 1500 km depth within the Earth. Original data sourced from [6].

2.2.2. Diamond Synthesis

The synthesis of diamond has been a focal point in materials science due to the ability to control the supply, quality, size, and dopant levels in synthetic diamonds as compared to their natural counterparts. High-pressure high-temperature (HPHT) and chemical vapour deposition (CVD) methods are the predominant methods employed for the manufacture of both polycrystalline and single-crystal diamonds. Figure 2.2 represents the key phase diagram of interest in the synthesis of diamond. HPHT and CVD synthetic diamonds are cultivated under distinctly different pressure and temperature conditions. The Berman-Simon line [10], which represents the graphite-diamond equilibrium, demarcates the thermodynamically stable region for diamond under HPHT conditions from the graphite-stable region where CVD diamonds are grown [7].

2.2.3. HPHT

High Pressure High Temperature (HPHT) synthesis replicates the natural conditions under which diamonds form, but allows for enhanced control over the diamonds qualities such as colour and clarity. Early attempts to synthesise diamonds using HPHT began in the 19th century, culminating in the first successful synthesis by General Electric in 1954 [9]. Although high-clarity diamonds are challenging to obtain through HPHT, making this process less desirable for applications requiring optical clarity, advancements have enabled the production of larger, high-quality colourless diamonds for jewellery. One key factor in

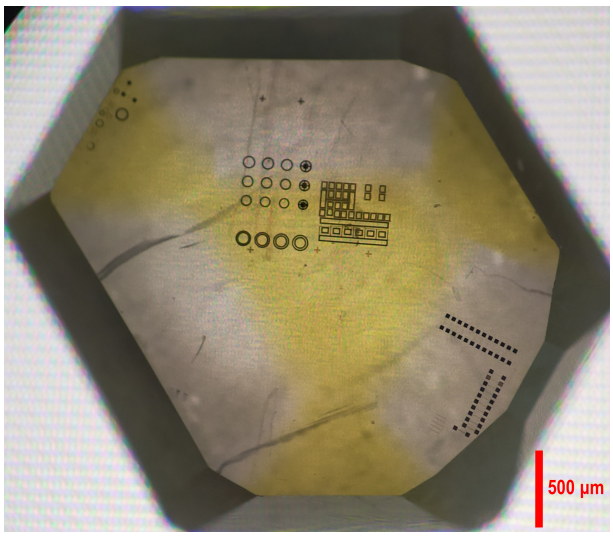

Figure 2.3 A HPHT substrate used for electrical devices in later chapters.

usage with modern HPHT presses is that of the usage of catalysts, and the careful control of catalyst mixtures [95]. While it is common for HPHT growth to result in high nitrogen defect concentrations, leading to the characteristic yellow colour as might be seen in figure 2.3, it is also possible to use nitrogen getters in the catalytic mix, such as Al, Ti, Zr and Mg which will combine with nitrogen atoms to form insoluble nitrates or nitrides, reducing the available nitrogen for incorporation within the growing diamond [91].

2.2.4. LMD

Liquid Metal Diamond (LMD) synthesis represents a novel and promising approach to diamond manufacturing, which operates at significantly lower pressures (1 atm) and moderate temperatures (1025°C). Unlike traditional methods, LMD uses a liquid metal catalyst at atmospheric conditions composed of elements like gallium, iron, nickel, and silicon to facilitate the growth of diamonds. This method involves catalytic activation of methane and the diffusion of carbon atoms within the liquid metal. Additional hydrogen is also essential, though the exact mechanisms are unclear at this stage. The key physical mechanism of LMD is its ability to supersaturate carbon in the metal, leading to the nucleation and growth of diamond at conditions that are less extreme than those required for either HPHT or CVD [28]. This method of diamond growth may grow substantially in the near future.

2.2.5. CVD

Chemical Vapour Deposition (CVD) is a highly controlled process used to produce synthetic diamonds by decomposing carbon-rich gases, such as methane, at elevated temperatures (typically 600–1200°C) in a vacuum chamber. This decomposition is often facilitated by a microwave plasma, although other methods like hot filaments [47] and acetylene flames [25] are also utilised. The resulting carbon atoms are deposited onto a substrate, forming

diamond layers that are particularly useful for applications in electronics and optics due to the versatility in doping and the growth over large areas.

The growth process, significantly influenced by the ratio of hydrogen to methane, is critical in determining the purity, morphology, and overall quality of the diamond films. A plasma generated by microwave power is common in modern CVD setups, but alternative techniques such as hot filaments or blowtorches are also employed. These methods facilitate the dissociation of gas precursors into radicals or ions necessary for diamond growth.

Control over various parameters such as temperature, pressure, gas flow rates, and substrate misorientation is crucial in CVD [52]. Diamond growth via CVD can be categorised into homoepitaxy and heteroepitaxy. Homoepitaxy describes the growth of diamond on a diamond substrate, typically derived from HPHT processes, while heteroepitaxy refers to diamond growth on non-diamond substrates. The latter poses significant challenges due to differences in thermal expansion coefficients and lattice constants, which can lead to defects and dislocations in the diamond film.

CVD technology has evolved since the 1970s, following the pioneering work by Derjaguin et al., who in 1975 demonstrated the feasibility of diamond growth under metastable conditions with cyclic growth and etching processes [16]. This method was further refined by Spitsyn in 1981 [92] and Nakazawa in 1987 [61], contributing to a deeper understanding of homoepitaxial growth. Concurrently, heteroepitaxial growth has also been explored, with early attempts by Spitsyn in 1981 to grow diamond layers on various substrates such as copper, silicon, and tungsten, among others. These efforts underscored the critical role of atomic hydrogen in suppressing unwanted graphite deposition and enhancing diamond nucleation [43].

Despite advancements, the heteroepitaxial growth of high-quality, single-crystal CVD diamond remains challenging due to lattice mismatches causing significant strain in the grown layers [106].

2.2.6. Doped Diamond

2.2.6.1. Incorporation Efficiency

In studies examining the growth of n or p-type diamond, it is possible to consider the incorporation efficiency of the dopants involved. First, the density and molar mass of diamond are utilised to calculate the number of carbon atoms present in a cubic centimetre of diamond. With an approximate density of 3.51 $\mathrm{g\,cm^{-3}}$ and a molar mass of 12.01 $\mathrm{g\,mol^{-1}}$, the number of carbon atoms present can be calculated:

$$\text{Number of carbon atoms per cm}^3 = \left(\frac{\text{Density}}{\text{Molar mass}}\right) \times N_A \tag{2.6}$$

Which results in $\approx 1.76 \times 10^{23}\,\mathrm{at\,cm^{-3}}$. For simple reference, it is convenient to consider the magnitudes of phosphorous incorporation and their resulting atomic concentrations. Hence, incorporation efficiencies of 100%, 10%, 1% and 0.1% are used in the following sections in

consideration of the doping concentrations. These efficiencies can then be considered for the various dopant:carbon sources for CVD growth. Naturally, it is unrealistic to consider the extreme cases in which there is no carbon source, but ratios of up to 50% have been used to grow highly doped diamond films [42, 32].

Therefore, as in [44], diamond growth where there is a dopant:carbon ratio of 0.1%, an incorporation ratio of 10% results in approximately 0.01% of the dopant being grown into the diamond lattice, corresponding to $0.01 \times 1.76 \times 10^{23} = 1.76 \times 10^{19}$ at cm^{-3}. The actual measured concentration of dopant in this example had an incorporation efficiency of around 15%, with the authors observing 2.5×10^{19} at cm^{-3} of dopant as measured via SIMS analysis.

2.2.7. Phosphorous Doped Diamond

2.2.7.1. Effective Electron Masses

Within semiconductors, the effective electron mass is generally determined via the energy-momentum (E-k) relationship for carriers. This describes the interactions of electrons, holes, photons and phonons, and is the basis of semiconductor physics in general. As defined in many semiconductor textbooks, the E-k relationship can be approximated at the band edges (bottom of conduction band E_c and top of valence band E_v) by a quadratic equation [97, 85, 109, 90]:

$$E(k) = \frac{\hbar^2 k^2}{2m^*} \tag{2.7}$$

where $\hbar$ is the reduced Plank constant, k is the momentum, given as wave vectors and m^* is the effective mass. Along a given direction, it is possible to approximate these quadratic curves and estimate the effective mass from the second differential term:

$$\frac{1}{m^*_{ij}} = \frac{1}{\hbar^2} \frac{\partial^2 E(k)}{\partial k_i \partial k_j} \tag{2.8}$$

where the indices i, j are used to indicate the tensorial components of effective mass in differing momentum space directions. The conduction band is made up of a number of sub-bands [84], with the bottom of the conduction band appearing either at the centre (given by the standard Wigner-Seitz cell symmetry notation of Γ) or at another position in k-space. Similarly, the valence band is made up of a number of sub-bands, which may or may not line up with the bottom of the conduction band. Semiconductors in which the bandgap is aligned are known as direct-bandgap semiconductors, such as InAs, GaN and GaAs [97]. These semiconductors are of particular interest for applications involving radiative emission, as the emission of light in direct bandgap semiconductors has a significantly greater quantum efficiency due to the lack of change in momentum required (requiring phonon interactions) [35]. Indirect bandgaps in which a change in momentum space is necessary for electronic transitions across the bandgap are seen in Si, Ge and also C - that of the sp^3 bonded diamond crystal lattice of carbon. While it is common practice

to refer to semiconductors by their shorthand elemental composition, this does not work very well with that of carbon due to the quantity, diversity and colossal range of carbon allotropes.

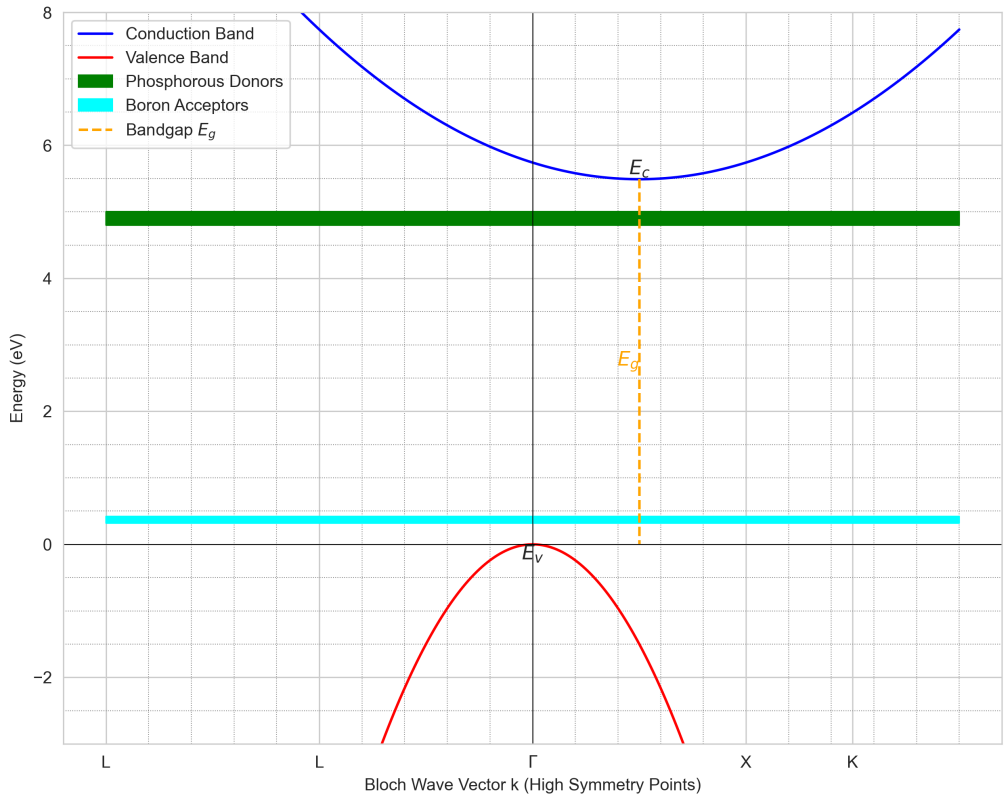

Figure 2.4 An approximate depiction of the parabolas responsible for diamond's electronic band structure. Loosely based on the full electronic structure as depicted in [108], including highly simplified defect states of phosphorous and boron.

Figure 2.4 shows a simplified parabola representation of of diamond. Shown is an indirect bandgap, which is measured at low temperatures approaching 0 K to be 5.49 eV via transmission/absorption spectra [1, 56] and density of states calculations [87]. For a full review of diamond dopant species and surface terminations on the electronic properties, such as the bandgap, see the work by Prof. K. Larsson [48].

The determination of effective carrier masses has been obtained in several ways throughout the literature. For the work described in following chapters, the effective mass of electrons within highly phosphorous doped diamond is of particular interest, but for ultra-pure intrinsic diamond, it has been experimentally observed via time-resolved cyclotron resonance that the transverse and longitudinal electron masses are $0.280m_0$ and $1.56m_0$ respectively [60]. These values represent what is currently believed to be the top-end limit of high velocity carriers within intrinsic diamond. A more relevant example of experimental measurements is that of Gheeraert et al. [26] who used infrared absorption to observe

the electronic transitions for phosphorous donors and hence determine the effective mass within electronically active, doped diamond films. In this work, the effective masses are determined to be $m_{\perp} = 0.306m_0$ and $m_{\parallel} = 1.81m_0$. These are the values that are widely used as reference values for phosphorous doped diamond [67, 66], and will hence be used in this work as a reference point also. These values can be contrasted to theoretically based work using a linear muffin-tin-orbital local density approximation for intrinsic diamond by Willatzen et al. who gave values of $m_{\perp} = 0.341m_0$ and $m_{\parallel} = 1.5m_0$. A final comparison is measured via a Monte Carlo analysis of electron drift velocity [63] by Nava et al. This is one of the earliest works in studying this property via Hall effect measurements, giving values of $m_{\perp} = 0.36m_0$ and $m_{\parallel} = 1.4m_0$ for intrinsic diamond.

2.3. Graphitisation of Diamond

The roots of laser graphitisation in diamond can be traced back to 1996, with a seminal paper by Davies et al. demonstrating that the usage of tightly focused femtosecond laser pulses could be used to permanently modify the optical properties of a small volume within the transparent substrate [15]. With careful tuning of the irradiation conditions, it is possible to induce a localised refractive index increase within the focal volume, allowing for the writing of optical waveguides with only a translation of the substrate.

The advantages of this technique can also be seen through the lens of diamond device processing and graphitisation rather than the tuning of optical properties, though a significant portion of the current industrial applications for laser graphitisation within diamond are in writing serial numbers and other optical markers for jewellers to identify lab-grown diamond:

- Laser fabrication is a direct, mask-less technique. Without the need for complex clean room facilities it is possible to create surface tracks or buried wires within the diamond. This allows for the rapid prototyping and refinement of a small number of devices, without the added need of dedicated photolithographic masks.

- This technique is highly flexible, as different irradiation parameters such as wavelength, pulse energy, translation speed, focusing conditions and repetition rate can be used to calibrate the laser for different materials like silicon carbide, diamond and other crystal structures. This also allows for more specific control over the graphitic content which is formed within the diamond substrate, with differing conductivities for various sp^2 and sp^3 content in the formed wires.

- With the usage of adaptive optics it is possible to create fully three-dimensional graphitic wires within the diamond substrate, of various thicknesses and conductivities at arbitrary depths. The degrees of freedom offered by this technique allow for geometries that are impossible or highly difficult with standard fabrication techniques, which may be an important factor in the design and manufacturing of certain device structures.

The fundamental process of writing graphitic regions within diamond is governed by the crystal structure meta-stability. At room temperature and under atmospheric pressure the stable phase of carbon is that of graphite, as shown previously in figure 2.2, hence when the diamond lattice damage density exceeds a critical value, it will form graphite. This can also be viewed as a sufficient number of diamond sp^3 bonds being broken, then reforming into the stable graphitic phase with sp^2 bonds. One simple way to cause this damage to a diamond lattice is to essentially burn it, or otherwise raise the temperature of the sample. A diamond lattice will tend to rearrange globally when heated to $T_G \approx 2000$ K, which is called the process of thermal graphitisation [14]. However, it has been observed that in cases where a laser pulse does not generate this critical temperature, graphitisation may still occur.

2.3.1. Ion Implantation

Another way to break the diamond sp^3 bonds is to bombard the diamond lattice with ions of a sufficiently high kinetic energy to also break the sp^3 bonds. Ion implantation was first investigated in the 70s by Vavilov et al [102], and resulted in a series of studies examining the electrical properties of the resultant amorphous carbon. Hauser et al. demonstrated the similarities of sputtered graphite to that of the ion implanted diamond, with a high conductivity of $\approx 10^{-2}\ \Omega^{-1}\,\mathrm{cm}^{-1}$ and also concluded that the resulting hardness of the implanted regions was an intermediate between that of silicon and diamond [34, 33]. With the proper combinations of implanting ions, ion energies, dosages and post implantation annealing, diamond based heterostructure can be formed which have layers of insulating, semi-conducting, luminescent and fully conductive regions [27, 77, 78].

One more specific case occurs in the case of implanting boron ions in polycrystalline diamond, where a "percolative threshold" fluence exists at which a conductive path of sp^3 bonded defects is formed in the diamond structure and a variable range hopping conduction mechanism is introduced. At a higher "amorphisation threshold", sp^2 bonded defects are formed, leading to permanent graphitisation in the implanted areas after annealing [21].

2.3.2. Laser Graphitisation

In the case of laser graphitisation, the mechanism of localised heating through the non-linear absorption of laser pulses requires some clarification, especially since diamond is generally regarded as a "thermal short" with its thermal conductivity of up to 2200-2500 $\mathrm{W\,m^{-1}\,K^{-1}}$ [29]. As presented in an article by Sundaram and Mazur in 2002, while intense laser pulses from a nanosecond pulsed laser within silicon is a thermally driven process, experimentally observed ultrashort femtosecond laser pulse effects cannot be explained with merely a thermal process [96]. Instead, the femtosecond pulses drive a large fraction of the valence electrons ($> 10\%$) into the conduction band, modifying the inter-atomic forces and destabilising the crystal lattice. A model presented by Kononenko et al. in 2015 relies primarily upon the expansion of graphitic inclusions through so called photographitisation,

and argues that the laser induced direct creation of graphitic nucleation sites within diamond is unlikely [45]. Instead, graphite inclusion defects within the diamond structure are the source, with inclusions forming the seeds of growing and overlapping graphitic regions. This growth of inclusions is then a two step process, with a distinct mechanism for each stage. Similar work presented by Bennington et al. in 2009 on single crystal (111) oriented HPHT diamonds concurs with this model, observing that the generated graphite was likely seeded by defects within the crystal lattice [5].

2.3.2.1. Photographitisation

Under femtosecond irradiation, it has been observed that the transition from diamond to graphite is not one driven by a thermal process, but instead it is one driven by an electron-hole plasma that is generated by the laser. Pulsed X-ray diffraction experiments in germanium, silicon, GaAs and InSb observed this same process in 1999 and 2001 with the laser-induced promotion of a large fraction of valence electrons (more than 10%) and with a low "melting time" on the order of femtoseconds [89, 82]. Once excited, these electrons strongly interact with one another and reach thermal equilibrium in under 10 fs [19]. Through the process of photoionisation, light is absorbed by the substrate and photon energy promotes electrons from bonding orbitals in the valence band to the conduction band, in unbound or even antibonding states. This absorption within diamond is a multiphoton process, depending upon the lasing wavelength. For 800 nm, there is a four or five photon transition, while 400 and 266 nm wavelengths have an indirect and two photon transition respectively [76]. The direct band gap in intrinsic diamond for these transitions is 7.3 eV. However, the presence of substitutional nitrogen or phosphorous will introduce donor like centres with a thermal ionisation energy of 1.7 eV and 0.6 eV respectively, complicating the band structure. The electron-hole density within diamond when illuminated by Kononenko et al. with a $TiAl_2O_3$ laser of wavelength 800 nm at fluencies of under 10 $J\,cm^{-2}$ reached up to 10^{21} cm^{-3}. The experimental data from this work is plotted in figure 2.5.

In the case of a perfect diamond lattice, these generated electron hole pairs would eventually relax and reform the C−C bonds of sp^3 orbitals. The diamond lattice is highly rigid, which prevents the deformation of bonds via electron hole pairs in contrast to other wide band gap semiconductors [53]. However, when these electron hole pairs are generated close to the edge of a graphite inclusion or other such graphitic region, then the chemical bonds making up the diamond lattice experience a significant distortion due to local Coulomb forces. Hence when there is a significant density of electron hole pairs, the C−C bonds at the interface of diamond and graphite have a chance to change in hybridisation from sp^3 to sp^2 orbitals, permanently breaking the diamond lattice and expanding the graphitic region. The exact ratio of sp^2/sp^3 within an amorphous carbon structure such as that formed under photographitisation may vary in regions, but areas of less graphitic content may have a ratio approaching 3 based on previous XPS/XAES measurements of

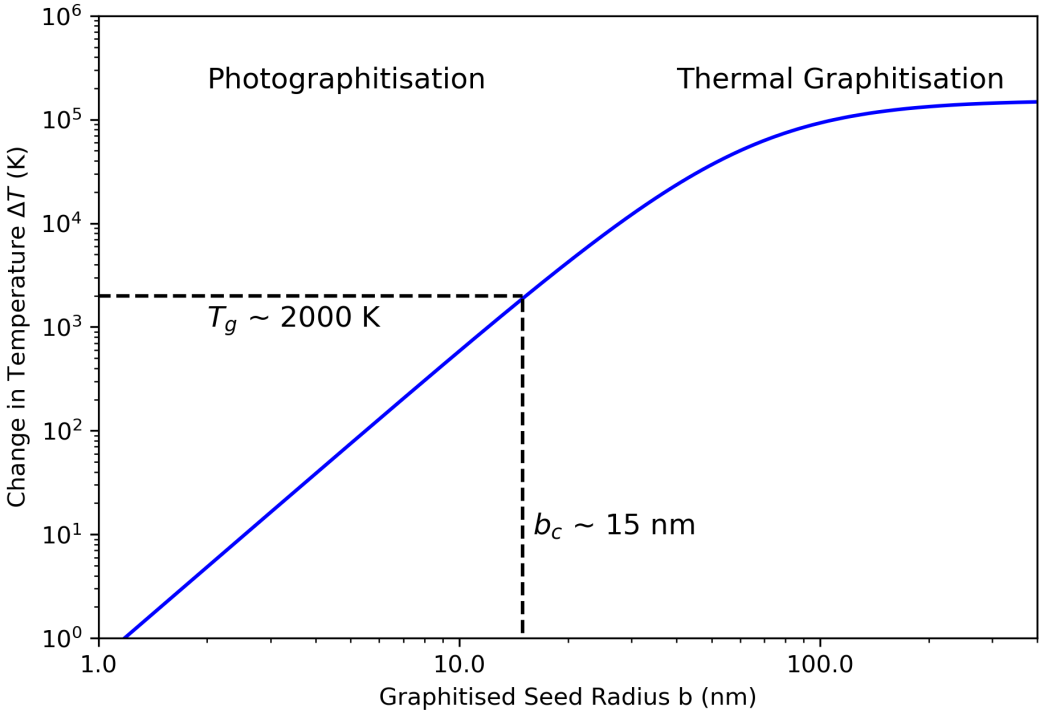

Figure 2.5 The concentration of electron hole pairs in single crystal diamond just below the crystal surface, as measured by Kononenko et al [46].

amorphous carbon as formed with ion bombardment [49]. Under subsequent pulses of laser irradiation, this process will slowly expand the graphitic inclusion, layer by layer.

2.3.2.2. Density Functional Theory

Through the usage of DFT, atomistic calculations examining the transition from diamond to graphite have estimated that the graphitisation due to photoionisation will complete within 100 fs [39] to 200 fs [105]. In particular, the work by Wang et al in 2000 examined the particular case of laser induced graphitisation on the (111) surface. This is particularly relevant for devices written on phosphorous doped, n-type diamond, as the (111) surface provides the highest dopant concentration and also most active carrier concentration when compared to other growth facets. Their conclusions can be summarised as:

- When the overall diamond temperature reaches 2700 K the surface will rapidly graphitise.
- Graphitisation occurs vertically for the simulations of longer pulse (nanosecond) durations, with graphite-like regions penetrating down through the surface layers into the bulk.
- Graphite sheets are formed in the case of femtosecond pulse durations, with a reduced time for complete graphitisation at higher effective electron temperatures.

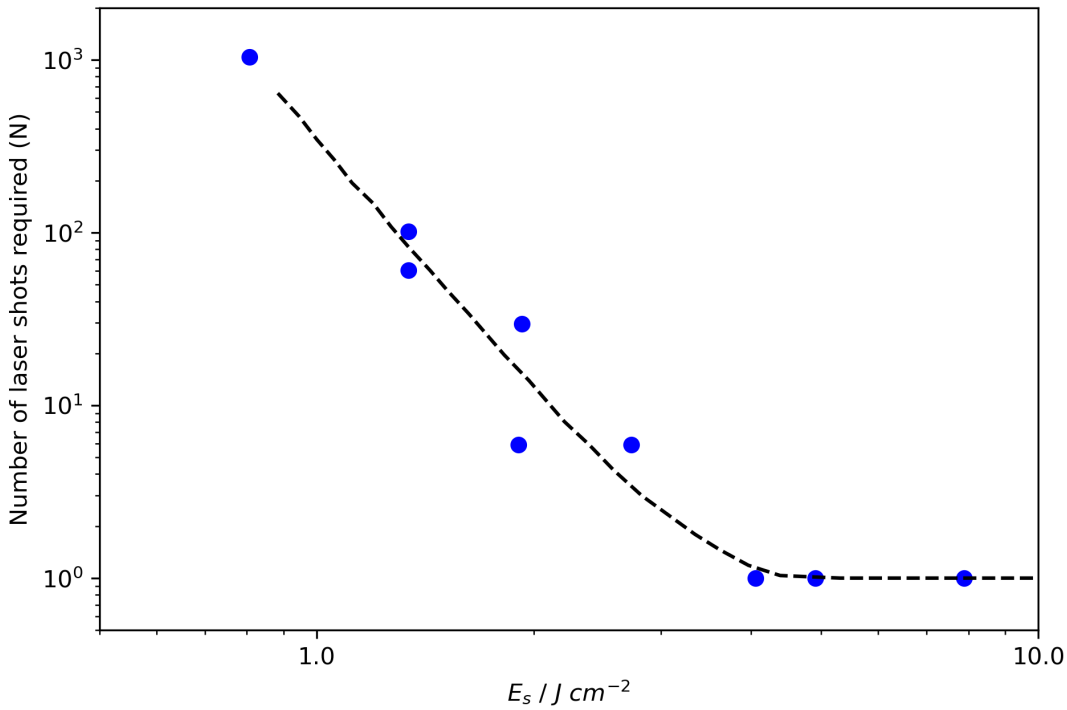

Figure 2.6 The number of laser shots required for visible damage of the diamond surface as a function of laser fluence, as measured by Kononenko et al [98].

- The energy barrier to graphitisation is lower in the case of higher electron temperatures, also corresponding to a reduced time required for complete graphitisation.

More recent studies examining the stability of diamond and graphite bonds with larger supercells provide further confirmation of the energy barrier between the two carbon hybridisations [74, 31]. A first-principle study by F. Mauri in 1995 explored the electron lattice interactions, concluding that valence excitons are highly likely to bind together when in a high density electron-hole plasma [54]. Self-trapping does not occur in the case of isolated valence excitons, but it is predicted that self trapping should occur with valence biexcitons. This biexciton trapping will cause a distortion, involving the breaking of a bond perpendicular to the (111) direction. As graphite is semi-metallic in nature, electron-hole pairs migrating from the excited diamond regions to that of a graphite seed will rapidly multiply through impact ionisation. Impact will also reduce their energy below the diamond band gap, trapping such pairs and collecting them within the graphitic region. Graphite's π orbitals are able to hold a large number of electron-hole pairs without changing the covalent bond network, lending a greater stability to the graphite region than the diamond in conditions of high electron-hole pairs in addition to the refractory nature of graphite [5].

2.3.2.3. Thermal Graphitisation

As these graphite seeds grow due to the photostimulated lattice rearrangement of carbon atoms adjacent to the graphite, the amount of light that is absorbed due to the change in the optical properties will increase. Also, when stimulated by light, the electron subsystem of graphite will take longer to relax than its sp^3 counterpart from the excited π-band electron population. This effect slows the heating of graphitic regions on a scale of $\tau_{e-ph} \approx 1$ ps, where τ_{e-ph} is the electron-phonon thermalisation [86]. Diamond has a remarkably high thermal diffusivity of $\chi_d \approx 10\ \mathrm{cm^2\,s^{-1}}$ [99]. This is high enough that the process of thermalisation can overlap in time with the heat spreading from graphite seeds into the diamond lattice. Hence, the temperature of these diamond seeds as induced by laser stimulation will strongly depend upon the seed size, which can be expressed in the following way:

$$\Delta T \approx \sigma_a F / l_D^3 / c_d \tag{2.9}$$

$$\sigma_a \approx \frac{2\pi}{\lambda} Im\left(4\pi b^3 \frac{\epsilon_g - \epsilon_d}{\epsilon_g + 2\epsilon_d}\right) \tag{2.10}$$

$$l_D = \left(4\chi_d \tau_{e-ph} + b^2\right)^{1/2} \tag{2.11}$$

Where σ_a is the absorption cross section, $\epsilon_g = 6.0825 + 10.673i$ [17] is the permittivity of graphite and $\epsilon_d = 5.76$ [70] is the permittivity of diamond, F is the laser fluence, b is the graphite seed radius and $c_d = 1.75\ \mathrm{J\,cm^{-3}\,K^{-1}}$ is the specific heat capacity of diamond [75]. The energy absorbed by the graphite seed will dissipate in a volume l_D^3, defined by the current radius of the seed and the heat diffusion length within diamond. Heat diffusion length is defined by the thermalisation time of electron-phonons $\tau_{e-ph} \approx 1$ ps. $\Delta T(b)$ as calculated with equations 2.9, 2.10, 2.11 at a fluence of 0.75, 1.5 and 3 $\mathrm{J\,cm^{-2}}$ and $\tau_{e-ph} = 1$ ps is depicted in figure 2.7.

The critical seed radius at which thermal graphitisation becomes possible is marked as $b_{c1,2,3}$ for the three different fluencies respectively. It can be noted that at a lower laser fluence, a larger critical radius is calculated as the fluencies 0.75, 1.5 and 3 $\mathrm{J\,cm^{-2}}$ resulted in a calculated critical radius of 19, 15 and 12 nm respectively. This can be compared to figure 2.6, in which the number of laser pulse "shots" required for experimentally observed graphitisation is plotted against the laser fluence. This comparison is represented in figure 2.8. It is possible to infer a few points from this comparison, as the natural conclusion of lower fluence laser pulses requiring a larger critical radius also demands a larger number of laser shots to observe experimental graphite growth. This fits the model well, as the photographitisation step of adding layers to the graphitic defects will take far longer than the thermal graphitisation step. Indeed, this manifests as the requirement for an order of magnitude more laser pulses at merely half the laser fluence. It is hoped that under a certain fluence, the critical radius will be reduced to the scale of sub-microns and such

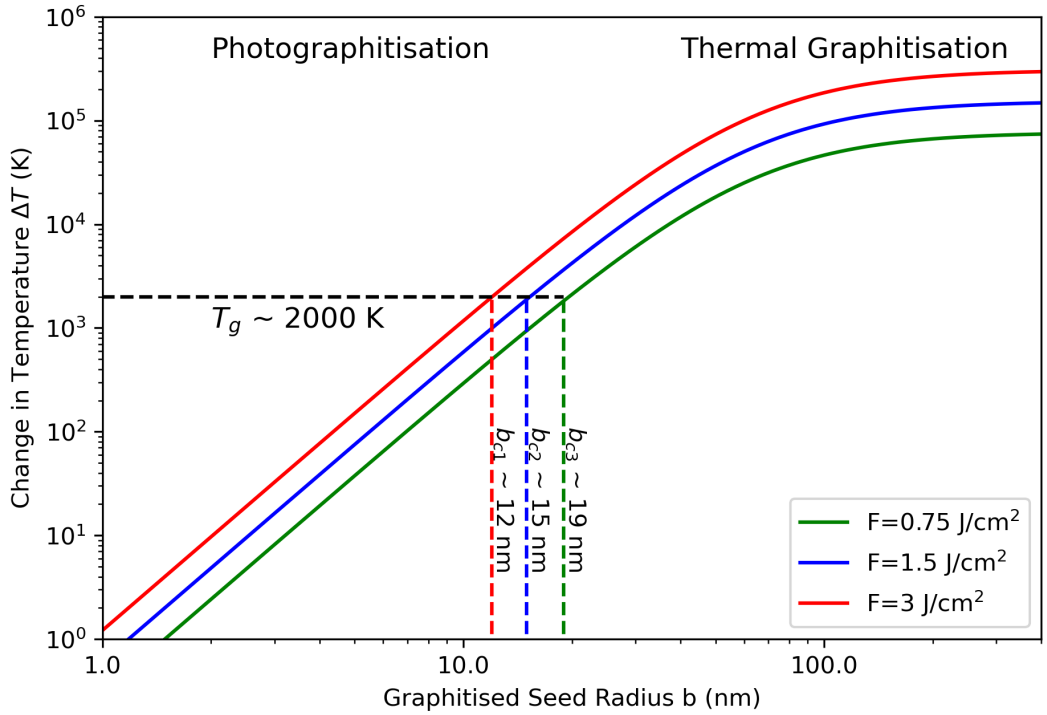

Figure 2.7 The estimated laser-induced heating according to the model presented by Kononenko et al, represented by equations 2.9, 2.10, 2.11 at fluencies from 0.75 $\mathrm{J\,cm^{-2}}$ to 3 $\mathrm{J\,cm^{-2}}$.

will never be able to reach the thermal graphitisation stage of growth. Hence, the only graphitisation mechanism will be that of photographitisation at very low laser fluencies.

2.3.3. Graphite

Graphite is typically manufactured by pressing or extruding a mixture of carbon containing materials such as pitch, coal, petrochemicals or other high molecular weight hydrocarbon, followed by a super-heating bake at anywhere from 2000 °C to more than 4000 °C to crystallise the amorphous carbon precursors.

This heating is typically a multi-stage process, with the first step requiring a long, complex heating in vacuum of the carbon containing material to convert it into coke. This process is known as destructive distillation, with a "good coke" containing a very high carbon content and few if any impurities. The coke is then calcinated, crushed and sieved to obtain a certain distribution of particle sizes. These particles are then bound with a binding substance such as coal tar pitch, petroleum pitch or a synthetic resin and extruded or moulded to form the graphite products. Next, a carbonisation bake at around 1000–1200°C will thermally decompose the binder into elementary carbon and other volatile components, binding the powdered graphite together. The resulting volume of the formed carbon is lower than that of the binder, due to the formation of pores, with a relative volume or porosity depending upon the binder quantity.

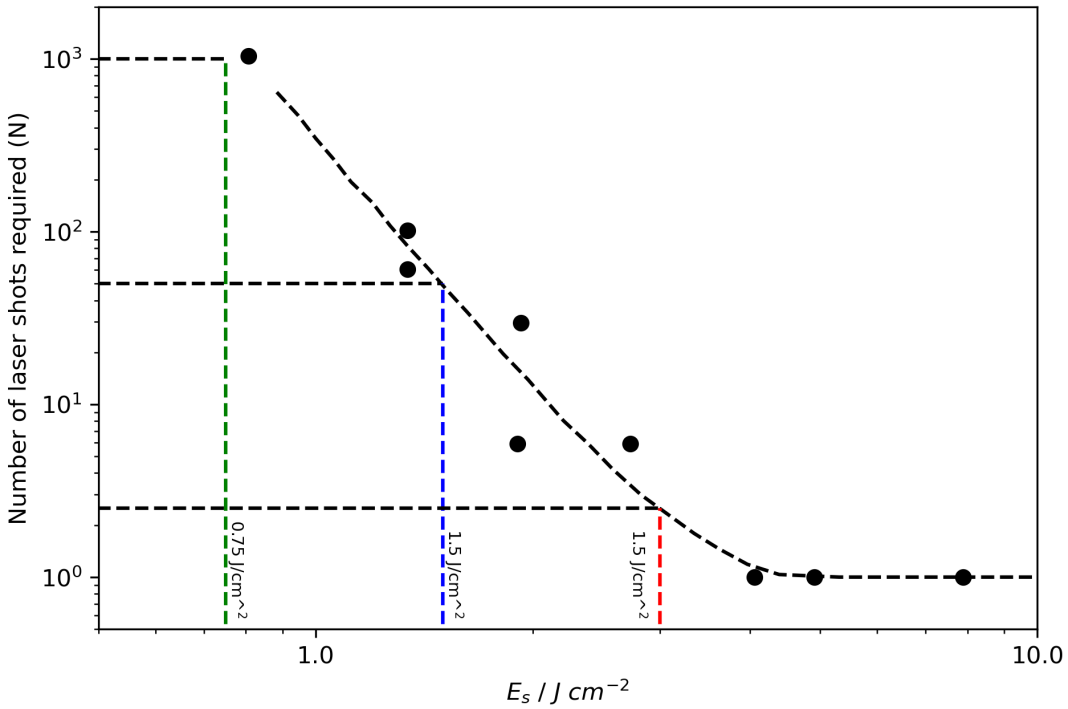

Figure 2.8 A comparison of the laser fluencies used in the calculation of critical seed radii and the observed number of laser shots required for the process of graphitisation. The lower fluence requires a larger seed radius for thermal graphitisation and hence requires many more laser pulses for the photographitisation growth.

Finally, the shaped and carbonised parts can be baked in the absence of oxygen, or in vacuum, at very high temperatures to induce crystallisation of the amorphous precursor carbon. Typical operating temperatures are in the 2500–3000°C range, which will also purify the graphite parts due to the vaporisation of impurities such as any remaining binder residue, oxides or gases. This is usually achieved with either induction based heating, or passing electric currents directly through the parts to utilise Joule heating.

A variety of precursors can be used, with gilsocarbon being a common choice for usage in nuclear power plants [50].

It is also possible to form graphite via chemical vapour deposition (CVD) techniques, which is known as pyrolitic graphite. This form of graphite will have a very low porosity, approaching the theoretical density of graphite, with correspondingly improved material properties in most other aspects too.

2.4. Metal-Semiconductor Contacts

2.4.1. Image Force/Schottky Effect

Given a point charge q at a distance x from a conducting plate, an "image" surface charge of opposite polarity is induced in the plate, with an induced electric field that is equivalent in magnitude and opposite to the point charge [23]. The force exerted on the "real" point charge is the "image force", with a corresponding force of:

$$F = -\frac{q^2}{16\pi\epsilon_0 x^2} \tag{2.12}$$

where q is the charge (typically the charge of an electron, though generally for the point charge it is the charge of the point charge), ϵ_0 is the permittivity of free space and x is the distance of the point charge from the conductive plate. When the point charge is an electron, with an external electric field $\vec{E}$ applied to the system, the total potential energy PE as a function of the distance is given by [85]:

$$PE(x) = -\frac{q^2}{16\pi\epsilon_0 x} - q\vec{E}x \tag{2.13}$$

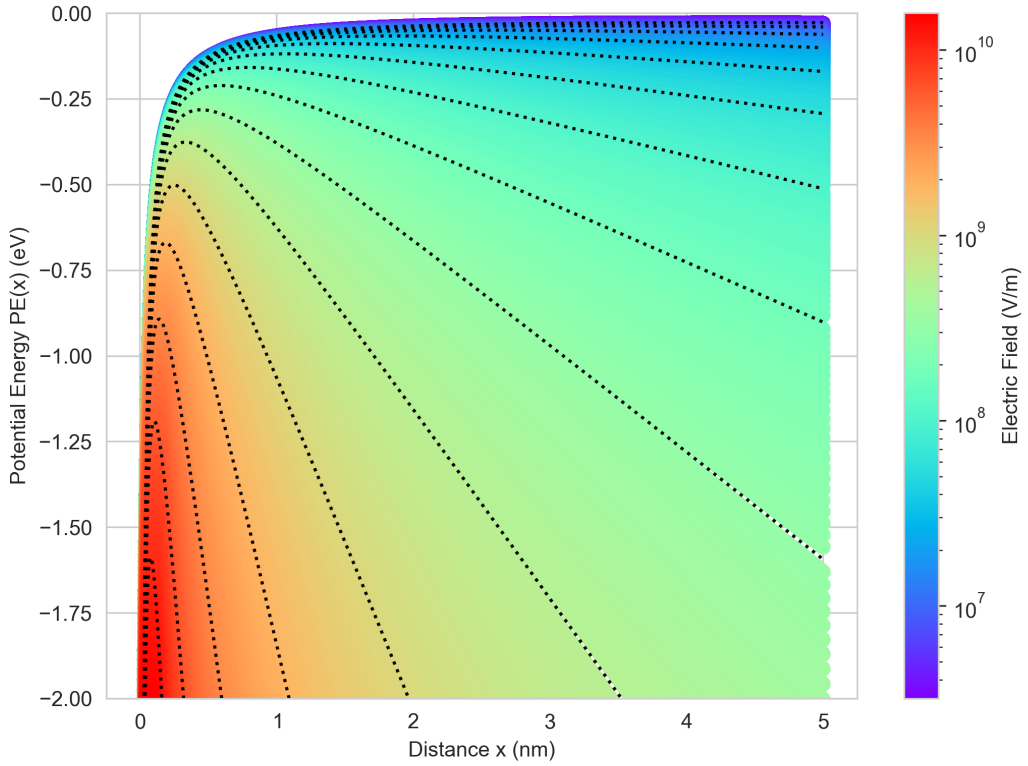

Figure 2.9 The potential energy of an electron due to the image charge effect at a metal-diamond boundary.

Figure 2.9 shows the application of equation 2.13 to a range of high electric fields (10^6–10^{10} $\mathrm{V\,m^{-1}}$. This visualisation uses a colour map to show the full spread of data, with black dotted lines for every quarter in the log scale. Very high electric fields form very sharp barriers, with heights substantially below the lower electric field Schottky curves. It should be noted that for lower electric fields below 10^7 $\mathrm{V\,m^{-1}}$, the barrier lowering effect is much more slight, and is not possible to see on the scales used for this figure. Extension of this model in vacuum leads to the derivations of field effect emission, due to the possibility of quantum-mechanical tunnelling through these very thin high field barriers. The peaks of the barriers, or the point at which the rate of change of the potential energy barrier $\frac{d}{dx}(PE)$ is zero, are defined to be the position of x_m, which is where the barrier is shifted by an amount $\Delta\phi$ [103, 97]:

$$\Delta\phi = \sqrt{\frac{q\left|\vec{E}\right|}{4\pi\epsilon_0}} = 2\left|\vec{E}\right|x_m \tag{2.14}$$

$$x_m = \sqrt{\frac{q}{16\pi\epsilon_0\left|\vec{E}\right|}} \tag{2.15}$$

where $\vec{E}$ is a uniform electric field applied in the negative x direction of the conductor, determining the sign of $\Delta\phi$.

When the metal-semiconductor interface is considered, the Debye length is crucial. If the semiconductor Debye length is much less than the range of the image force, of the order of Å, then the semiconductor acts as a metal and equation 2.14 is used. The Debye length for semiconductors is given as [97]:

$$L_D = \sqrt{\frac{\epsilon_s k_B T}{q^2 N}} \tag{2.16}$$

where N is either N_A or N_D, depending upon whether the material is p or n-type respectively. When the Debye length is larger than the range of the image force, the semiconductor is considered to be a dielectric, and the modified form of image force barrier lowering is used for semiconductors:

$$\Delta\phi = \sqrt{\frac{q\vec{E}_m}{4\pi\epsilon_s}} \tag{2.17}$$

Where ϵ_s is the permittivity of the semiconductor, and the electric field within the semiconductor is not zero due to built-in potential bias. $\vec{E}_m$ is the maximum value of the electric field at the semiconductor at the surface based on a depletion approximation [97]:

$$\vec{E}_m = \sqrt{\frac{2qN|\Psi_s|}{\epsilon_s}} \tag{2.18}$$

with surface potential Ψ_s defined for ideal barrier heights ϕ_{Bn0} on n-type semiconductors:

$$|\Psi_s| = \phi_{Bn0} - \phi_n + V_R \tag{2.19}$$

Finally, the Schottky effect for metal contacts to n-type semiconductors under differing biasing conditions is given as:

$$\Delta\phi = \sqrt{\frac{q\vec{E}_m}{4\pi\epsilon_s}} = \left[\frac{q^3 N_D |\Psi_s|}{8\pi^2\epsilon_s^3}\right]^{1/4} \tag{2.20}$$

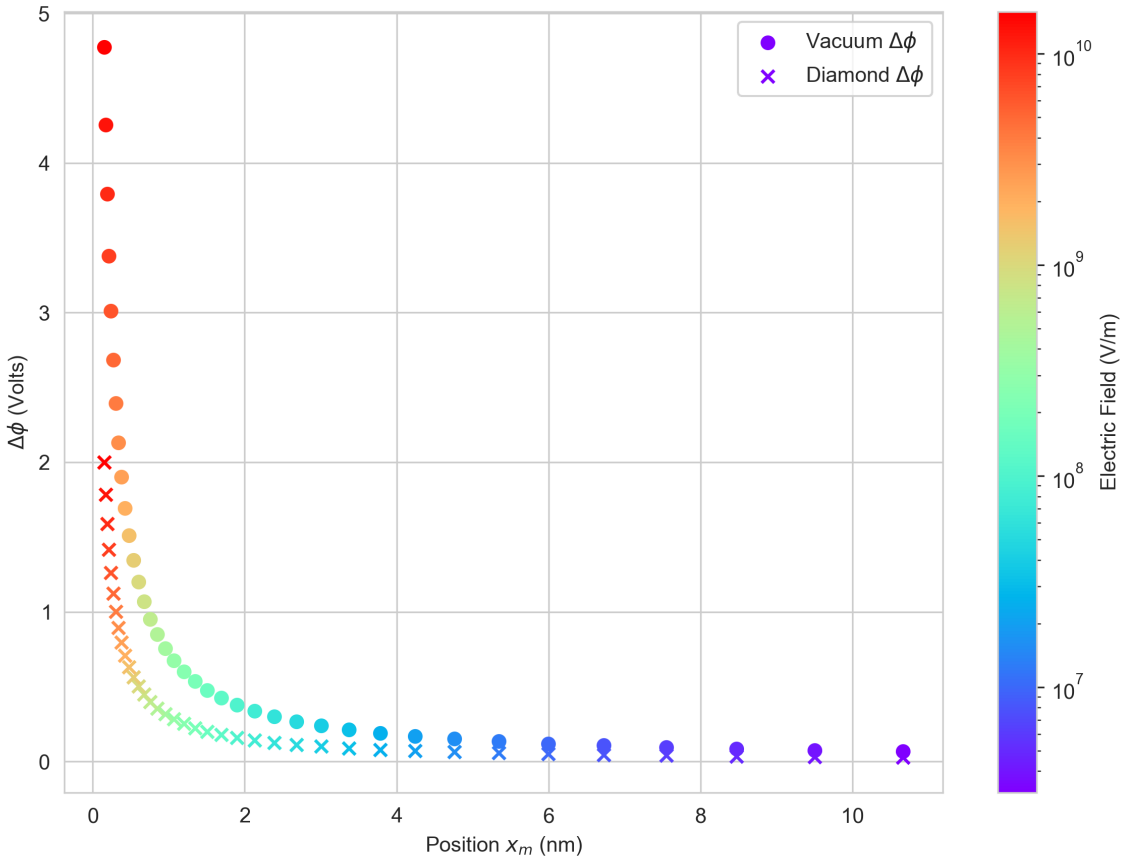

Figure 2.10 The position and magnitude of the image force reduction of Schottky barrier height for metal-vacuum (circles) and metal-diamond (crosses). $\Delta\phi$ is calculated following equation 2.20, over a range of positions within the vacuum or diamond medium. A colour scale is used to indicate the magnitude of the electric field at each position.

Figure 2.10 presents a visual application of equation 2.14 and 2.20. The resulting magnitude and location of the image force or Schottky effect can be seen to differ between the cases of a metal in a vacuum, and that of an ideal metal and n-type diamond boundary with relative dielectric constant of 5.7 within the diamond [24, 110]. Overall, the diamond dielectric constant facilitates a much lower Schottky barrier than that of the vacuum case, with a maximum value of approximately 2 V when compared to that of the vacuum's near 5 V barrier.

References

[1] In: *Proceedings of the Royal Society of London. Series A. Mathematical and Physical Sciences* 277.1370 (Feb. 1964), pp. 312–329. ISSN: 2053-9169. DOI: 10.1098/rspa.1964.0025. URL: http://dx.doi.org/10.1098/rspa.1964.0025.

[2] Joao L. Afonso et al. "A Review on Power Electronics Technologies for Electric Mobility". In: *Energies* 13.23 (Dec. 2020), p. 6343. ISSN: 1996-1073. DOI: 10.3390/en13236343. URL: http://dx.doi.org/10.3390/en13236343.

[3] B.J. Baliga. "Power semiconductor device figure of merit for high-frequency applications". In: *IEEE Electron Device Letters* 10.10 (Oct. 1989), pp. 455–457. ISSN: 1558-0563. DOI: 10.1109/55.43098. URL: http://dx.doi.org/10.1109/55.43098.

[4] Léo Basset et al. "In depth analysis of transfer length method application on passivated contacts under illumination". In: *Solar Energy Materials and Solar Cells* 230 (Sept. 2021), p. 111255. ISSN: 0927-0248. DOI: 10.1016/j.solmat.2021.111255. URL: http://dx.doi.org/10.1016/j.solmat.2021.111255.

[5] S. M. Bennington et al. "Turning diamond to graphite". In: *Central Laser Facility Annual Report* (2009). URL: https://www.clf.stfc.ac.uk/Pages/ar08-09_s6_turning-diamond-into-graphite.pdf.

[6] Vladimir D Blank et al. "Phase diagram of carbon and the factors limiting the quantity and size of natural diamonds". In: *Nanotechnology* 29.11 (2018), p. 115603. DOI: 10.1088/1361-6528/aaa857. URL: https://doi.org/10.1088/1361-6528/aaa857.

[7] H. P. Bovenkerk et al. "Errors in diamond synthesis". In: *Nature* 365.6441 (Sept. 1993), pp. 19–19. ISSN: 1476-4687. DOI: 10.1038/365019a0. URL: http://dx.doi.org/10.1038/365019a0.

[8] Gurvinder Singh Bumbrah and Rakesh Mohan Sharma. "Raman spectroscopy – Basic principle, instrumentation and selected applications for the characterization of drugs of abuse". In: *Egyptian Journal of Forensic Sciences* 6.3 (Sept. 2016), pp. 209–215. ISSN: 2090-536X. DOI: 10.1016/j.ejfs.2015.06.001. URL: http://dx.doi.org/10.1016/j.ejfs.2015.06.001.

[9] F. P. BUNDY et al. "Man-Made Diamonds". In: *Nature* 176.4471 (July 1955), pp. 51–55. ISSN: 1476-4687. DOI: 10.1038/176051a0. URL: http://dx.doi.org/10.1038/176051a0.

[10] F. P. Bundy et al. "Diamond-Graphite Equilibrium Line from Growth and Graphitization of Diamond". In: *The Journal of Chemical Physics* 35.2 (Aug. 1961), pp. 383–391. ISSN: 1089-7690. DOI: 10.1063/1.1731938. URL: http://dx.doi.org/10.1063/1.1731938.

[11] Svetlana N. Bystrova et al. "Dealing with leakage current in TLM and CTLM structures with vertical junction isolation". In: *2017 International Conference of Microelectronic Test Structures (ICMTS)*. IEEE, Mar. 2017. DOI: 10.1109/icmts.2017.7954257. URL: http://dx.doi.org/10.1109/ICMTS.2017.7954257.

[12] Ling-Zhi Cheong et al. "Lab on a tip: Applications of functional atomic force microscopy for the study of electrical properties in biology". In: *Acta Biomaterialia* 99 (Nov. 2019), pp. 33–52. ISSN: 1742-7061. DOI: 10.1016/j.actbio.2019.08.023. URL: http://dx.doi.org/10.1016/j.actbio.2019.08.023.

[13] S. S. Cohen and G. Sh. Gildenblatt. "Test Structures for Ohmic Contact Characterization". In: *VLSI Electronics Microstructure Science*. Vol. 13. Elsevier, 1986. Chap. 4. ISBN: 9780122341137.

[14] G. Davies, Trevor Evans, and Robert William Ditchburn. "Graphitization of diamond at zero pressure and at a high pressure". In: *Proceedings of the Royal Society of London. A. Mathematical and Physical Sciences* 328.1574 (1972), pp. 413–427. DOI: 10.1098/rspa.1972.0086. eprint: https://royalsocietypublishing.org/doi/pdf/10.1098/rspa.1972.0086. URL: https://royalsocietypublishing.org/doi/abs/10.1098/rspa.1972.0086.

[15] K. M. Davis et al. "Writing waveguides in glass with a femtosecond laser". In: *Opt. Lett.* 21.21 (1996), pp. 1729–1731. DOI: 10.1364/OL.21.001729. URL: http://opg.optica.org/ol/abstract.cfm?URI=ol-21-21-1729.

[16] B. V. Derjaguin and D. B. Fedoseev. "The Synthesis of Diamond at Low Pressure". In: *Scientific American* 233.5 (1975), pp. 102–109. ISSN: 00368733, 19467087. URL: http://www.jstor.org/stable/24949942 (visited on 03/09/2023).

[17] A. B Djurišić and E. H Li. "Optical properties of graphite". In: *Journal of applied physics.* 85.10 (1999), pp. 7404–7410. ISSN: 0021-8979.

[18] *EDT2 IGBT AIKQ120N75CP2.* AIKQ120N75CP2. Rev. 1.10. Infineon Technologies AG. Mar. 2022.

[19] Thomas Elsaesser et al. "Initial thermalization of photoexcited carriers in GaAs studied by femtosecond luminescence spectroscopy". In: *Phys. Rev. Lett.* 66 (13 1991), pp. 1757–1760. DOI: 10.1103/PhysRevLett.66.1757. URL: https://link.aps.org/doi/10.1103/PhysRevLett.66.1757.

[20] Enerdata. *Net electricity consumption worldwide in select years from 1980 to 2022 (in terawatt-hours) [Graph].* https://www.statista.com/statistics/280704/world-power-consumption/. In Statista. 2023. (Visited on 04/28/2024).

[21] A. Deneuville F. Fontaine E. Gheeraert. In: *Diamond Relat. Mater.* 5 (1995), p. 572.

[22] Sarah Fearn. "Introduction". In: *An Introduction to Time-of-Flight Secondary Ion Mass Spectrometry (ToF-SIMS) and its Application to Materials Science*. Morgan and Claypool Publishers, Oct. 2015, 1–1–1–6. ISBN: 9781681740249. DOI: 10.1088/978-1-6817-4088-1ch1. URL: http://dx.doi.org/10.1088/978-1-6817-4088-1ch1.

[23] Richard P. Feynman et al. "The Feynman Lectures on Physics; Vol. I". In: *American Journal of Physics* 33.9 (Sept. 1965), pp. 750–752. ISSN: 1943-2909. DOI: 10.1119/1.1972241. URL: http://dx.doi.org/10.1119/1.1972241.

[24] John Fontanella et al. "Temperature and pressure variation of the refractive index of diamond". In: *Applied Optics* 16.11 (Nov. 1977), p. 2949. ISSN: 1539-4522. DOI: 10.1364/ao.16.002949. URL: http://dx.doi.org/10.1364/AO.16.002949.

[25] I García and A.J Vázquez. "Oxy-acetylene flame chemical vapour deposition of diamond films. Part I: the influence of deposition parameters on diamond morphology". In: *Thin Solid Films* 325.1–2 (July 1998), pp. 99–106. ISSN: 0040-6090. DOI: 10.1016/s0040-6090(98)00504-5. URL: http://dx.doi.org/10.1016/S0040-6090(98)00504-5.

[26] E. Gheeraert et al. "Low temperature excitation spectrum of phosphorus in diamond". In: *Diamond and Related Materials* 10.3–7 (Mar. 2001), pp. 444–448. ISSN: 0925-9635. DOI: 10.1016/s0925-9635(00)00408-8. URL: http://dx.doi.org/10.1016/S0925-9635(00)00408-8.

[27] A.A. Gippius et al. "Formation and characterization of graphitized layers in ion-implanted diamond". In: *Diamond and Related Materials* 8.8 (1999), pp. 1631–1634. ISSN: 0925-9635. DOI: https://doi.org/10.1016/S0925-9635(99)00047-3. URL: https://www.sciencedirect.com/science/article/pii/S0925963599000473.

[28] Yan Gong et al. "Growth of diamond in liquid metal at 1 atm pressure". In: *Nature* (Apr. 2024). ISSN: 1476-4687. DOI: 10.1038/s41586-024-07339-7. URL: http://dx.doi.org/10.1038/s41586-024-07339-7.

[29] John E. Graebner. "Thermal Conductivity of Diamond". In: *Diamond: Electronic Properties and Applications*. Ed. by Lawrence S. Pan and Don R. Kania. Boston, MA: Springer US, 1995, pp. 285–318. ISBN: 978-1-4615-2257-7. DOI: 10.1007/978-1-4615-2257-7_7. URL: https://doi.org/10.1007/978-1-4615-2257-7_7.

[30] Ben L. Green, Alan T. Collins, and Christopher M. Breeding. "Diamond Spectroscopy, Defect Centers, Color, and Treatments". In: *Reviews in Mineralogy and Geochemistry* 88.1 (July 2022), pp. 637–688. ISSN: 1529-6466. DOI: 10.2138/rmg.2022.88.12. URL: http://dx.doi.org/10.2138/rmg.2022.88.12.

[31] Wojciech Grochala. "Diamond: Electronic Ground State of Carbon at Temperatures Approaching 0 K". In: *Angewandte Chemie International Edition* 53.14 (2014), pp. 3680–3683. DOI: https://doi.org/10.1002/anie.201400131. eprint: https://onlinelibrary.wiley.com/doi/pdf/10.1002/anie.201400131. URL: https://onlinelibrary.wiley.com/doi/abs/10.1002/anie.201400131.

[32] T.A. Grotjohn et al. "Heavy phosphorus doping by epitaxial growth on the (111) diamond surface". In: *Diamond and Related Materials* 44 (Apr. 2014), pp. 129–133. DOI: 10.1016/j.diamond.2014.02.009. URL: https://doi.org/10.1016/j.diamond.2014.02.009.

[33] J. J. Hauser, J. R. Patel, and J. W. Rodgers. "Hard conducting implanted diamond layers". In: *Applied Physics Letters* 30.3 (1977), pp. 129–130. DOI: 10.1063/1.89323. eprint: https://doi.org/10.1063/1.89323. URL: https://doi.org/10.1063/1.89323.

[34] J.J. Hauser and J.R. Patel. “Hopping conductivity in C-implanted amorphous diamond, or how to ruin a perfectly good diamond”. In: *Solid State Communications* 18.7 (1976), pp. 789–790. ISSN: 0038-1098. DOI: https://doi.org/10.1016/0038-1098(76)90205-2. URL: https://www.sciencedirect.com/science/article/pii/0038109876902052.

[35] Henning Helmers, Christian Karcher, and Andreas W. Bett. “Bandgap determination based on electrical quantum efficiency”. In: *Applied Physics Letters* 103.3 (July 2013). ISSN: 1077-3118. DOI: 10.1063/1.4816079. URL: http://dx.doi.org/10.1063/1.4816079.

[36] International Energy Agency (IEA). *Electricity 2024*. https://www.iea.org/reports/electricity-2024. Licence: CC BY 4.0. Paris: IEA, 2024.

[37] Jan Isberg et al. “High Carrier Mobility in Single-Crystal Plasma-Deposited Diamond”. In: *Science* 297.5587 (Sept. 2002), pp. 1670–1672. ISSN: 1095-9203. DOI: 10.1126/science.1074374. URL: http://dx.doi.org/10.1126/science.1074374.

[38] Kay D Jahnke et al. “Electron–phonon processes of the silicon-vacancy centre in diamond”. In: *New Journal of Physics* 17.4 (Apr. 2015), p. 043011. ISSN: 1367-2630. DOI: 10.1088/1367-2630/17/4/043011. URL: http://dx.doi.org/10.1088/1367-2630/17/4/043011.

[39] H. Jeschke, M. Garcia, and K. Bennemann. “Theory for laser-induced ultrafast phase transitions in carbon”. In: *Appl Phys A* 69 (), S49–S53. DOI: 10.1007/s003399900340.

[40] Matthew S. Joens et al. “Helium Ion Microscopy (HIM) for the imaging of biological samples at sub-nanometer resolution”. In: *Scientific Reports* 3.1 (Dec. 2013). ISSN: 2045-2322. DOI: 10.1038/srep03514. URL: http://dx.doi.org/10.1038/srep03514.

[41] Masayuki Katagiri et al. “Lightly phosphorus-doped homoepitaxial diamond films grown by chemical vapor deposition”. In: *Applied Physics Letters* 85.26 (Dec. 2004), pp. 6365–6367. ISSN: 1077-3118. DOI: 10.1063/1.1840119. URL: http://dx.doi.org/10.1063/1.1840119.

[42] Hiromitsu Kato et al. “Characterization of specific contact resistance on heavily phosphorus-doped diamond films”. In: *Diamond and Related Materials* 18.5 (2009). Proceedings of Diamond 2008, the 19th European Conference on Diamond, Diamond-Like Materials, Carbon Nanotubes, Nitrides and Silicon Carbide, pp. 782–785. ISSN: 0925-9635. DOI: https://doi.org/10.1016/j.diamond.2009.01.033. URL: https://www.sciencedirect.com/science/article/pii/S0925963509000363.

[43] Koji Kobashi et al. “Synthesis of diamonds by use of microwave plasma chemical-vapor deposition: Morphology and growth of diamond films”. In: *Physical Review B* 38.6 (Aug. 1988), pp. 4067–4084. DOI: 10.1103/physrevb.38.4067. URL: https://doi.org/10.1103/physrevb.38.4067.

[44] S. Koizumi et al. “Growth and characterization of phosphorous doped {111} homoepitaxial diamond thin films”. In: *Applied Physics Letters* 71.8 (Aug. 1997), pp. 1065–1067. DOI: 10.1063/1.119729. URL: https://doi.org/10.1063/1.119729.

[45] V V Kononenko et al. “Photoinduced graphitization of diamond”. In: *Laser Physics Letters* 12.1 (2015), p. 016101. DOI: 10.1088/1612-2011/12/1/016101. URL: https://doi.org/10.1088/1612-2011/12/1/016101.

[46] V V Kononenko et al. “Propagation and absorption of high-intensity femtosecond laser radiation in diamond”. In: *Quantum Electronics* 44.12 (2014), pp. 1099–1103. DOI: 10.1070/qe2014v044n12abeh015459. URL: https://doi.org/10.1070/qe2014v044n12abeh015459.

[47] A. Kromka et al. “Diamond nucleation and seeding techniques for tissue regeneration”. In: *Diamond-Based Materials for Biomedical Applications*. Elsevier, 2013, pp. 206–255. DOI: 10.1533/9780857093516.2.206. URL: http://dx.doi.org/10.1533/9780857093516.2.206.

[48] Karin Larsson. “The Combined Influence of Dopant Species and Surface Termination on the Electronic Properties of Diamond Surfaces”. In: *C — Journal of Carbon Research* 6.2 (Apr. 2020), p. 22. ISSN: 2311-5629. DOI: 10.3390/c6020022. URL: http://dx.doi.org/10.3390/c6020022.

[49] J.C. Lascovich, R. Giorgi, and S. Scaglione. “Evaluation of the sp2/sp3 ratio in amorphous carbon structure by XPS and XAES”. In: *Applied Surface Science* 47.1 (1991), pp. 17–21. ISSN: 0169-4332. DOI: https://doi.org/10.1016/0169-4332(91)90098-5. URL: https://www.sciencedirect.com/science/article/pii/0169433291900985.

[50] Dong Liu et al. “Damage tolerance of nuclear graphite at elevated temperatures”. In: *Nature Communications* 8.1 (June 2017). DOI: 10.1038/ncomms15942. URL: https://doi.org/10.1038/ncomms15942.

[51] Zhiwei Liu et al. “Silicon-Controlled Rectifier Stacking Structure for High-Voltage ESD Protection Applications”. In: *IEEE Electron Device Letters* 31.8 (Aug. 2010), pp. 845–847. ISSN: 1558-0563. DOI: 10.1109/led.2010.2050575. URL: http://dx.doi.org/10.1109/LED.2010.2050575.

[52] Mikhail A. Lobaev et al. “Misorientation Angle Dependence of Boron Incorporation Into CVD Diamond Delta Layers”. In: *physica status solidi (b)* 256.7 (Jan. 2019). ISSN: 1521-3951. DOI: 10.1002/pssb.201800606. URL: http://dx.doi.org/10.1002/pssb.201800606.

[53] P. Martin et al. “Subpicosecond study of carrier trapping dynamics in wide-band-gap crystals”. In: *Phys. Rev. B* 55 (9 1997), pp. 5799–5810. DOI: 10.1103/PhysRevB.55.5799. URL: https://link.aps.org/doi/10.1103/PhysRevB.55.5799.

[54] Francesco Mauri and Roberto Car. "First-Principles Study of Excitonic Self-Trapping in Diamond". In: *Phys. Rev. Lett.* 75 (17 Oct. 1995), pp. 3166–3169. DOI: 10.1103/PhysRevLett.75.3166. URL: https://link.aps.org/doi/10.1103/PhysRevLett.75.3166.

[55] F Patrick McCluskey, Thomas Podlesak, and Richard Grzybowski. *High temperature electronics*. Boca Raton, FL: CRC Press, Dec. 1996.

[56] Rich P. Mildren. *Intrinsic Optical Properties of Diamond*. Mar. 2013. DOI: 10.1002/9783527648603.ch1. URL: http://dx.doi.org/10.1002/9783527648603.ch1.

[57] José Millán, Philippe Godignon, and Amador Pérez-Tomás. "Wide Band Gap Semiconductor Devices for Power Electronics". In: *Automatika* 53.2 (Jan. 2012), pp. 107–116. ISSN: 1848-3380. DOI: 10.7305/automatika.53-2.177. URL: http://dx.doi.org/10.7305/automatika.53-2.177.

[58] David J. Morgan. "X-Ray Photoelectron Spectroscopy (XPS) : An Introduction". In: 2012. URL: https://api.semanticscholar.org/CorpusID:108289028.

[59] H. Murrmann and D. Widmann. "Current crowding on metal contacts to planar devices". In: *IEEE Transactions on Electron Devices* 16.12 (Dec. 1969), pp. 1022–1024. ISSN: 0018-9383. DOI: 10.1109/t-ed.1969.16904. URL: http://dx.doi.org/10.1109/T-ED.1969.16904.

[60] Nobuko Naka et al. "Direct measurement via cyclotron resonance of the carrier effective masses in pristine diamond". In: *Physical Review B* 88.3 (July 2013). ISSN: 1550-235X. DOI: 10.1103/physrevb.88.035205. URL: http://dx.doi.org/10.1103/PhysRevB.88.035205.

[61] Hiromoto Nakazawa et al. "X-ray section topographs of a vapour-grown diamond film on a diamond substrate". In: *Thin Solid Films* 151.2 (Aug. 1987), pp. 199–206. DOI: 10.1016/0040-6090(87)90233-1. URL: https://doi.org/10.1016/0040-6090(87)90233-1.

[62] Roger J Narayan, Ryan D. Boehm, and Anirudha V. Sumant. "Medical applications of diamond particles and surfaces". In: *Materials Today* 14.4 (Apr. 2011), pp. 154–163. ISSN: 1369-7021. DOI: 10.1016/s1369-7021(11)70087-6. URL: http://dx.doi.org/10.1016/S1369-7021(11)70087-6.

[63] F. Nava et al. "Electron effective masses and lattice scattering in natural diamond". In: *Solid State Communications* 33.4 (Jan. 1980), pp. 475–477. ISSN: 0038-1098. DOI: 10.1016/0038-1098(80)90447-0. URL: http://dx.doi.org/10.1016/0038-1098(80)90447-0.

[64] Roslan Md Nor et al. "Diamond: Synthesis, Characterisation and Applications". In: *Carbon and Oxide Nanostructures*. Springer Berlin Heidelberg, 2010, pp. 195–217. ISBN: 9783642146732. DOI: 10.1007/8611_2010_17. URL: http://dx.doi.org/10.1007/8611_2010_17.

[65] Filippo Pellitteri et al. "Power losses comparison between Silicon Carbide and Silicon devices for an isolated DC-DC converter". In: *2021 IEEE 15th International Conference on Compatibility, Power Electronics and Power Engineering (CPE-POWERENG)*. IEEE, July 2021, pp. 1–6. DOI: 10.1109/cpe-powereng50821.2021.9501191. URL: http://dx.doi.org/10.1109/CPE-POWERENG50821.2021.9501191.

[66] J. Pernot and S. Koizumi. "Electron mobility in phosphorous doped 111 homoepitaxial diamond". In: *Applied Physics Letters* 93.5 (Aug. 2008). ISSN: 1077-3118. DOI: 10.1063/1.2969066. URL: http://dx.doi.org/10.1063/1.2969066.

[67] J. Pernot et al. "Hall electron mobility in diamond". In: *Applied Physics Letters* 89.12 (Sept. 2006). ISSN: 1077-3118. DOI: 10.1063/1.2355454. URL: http://dx.doi.org/10.1063/1.2355454.

[68] *Phase Control Thyristor Module TT240N*. TT240N. Rev. 1. Infineon Technologies AG. Oct. 2002.

[69] *Phase Control Thyristor T1503N*. T1503N. Rev. 8.0. Infineon Technologies AG. May 2011.

[70] H. R. Phillip and E. A. Taft. "Kramers-Kronig Analysis of Reflectance Data for Diamond". In: *Phys. Rev.* 136 (5A 1964), A1445–A1448. DOI: 10.1103/PhysRev.136.A1445. URL: https://link.aps.org/doi/10.1103/PhysRev.136.A1445.

[71] Marie-Amandine Pinault-Thaury et al. "Attractive electron mobility in (113) n-type phosphorus-doped homoepitaxial diamond". In: *Carbon* 175 (Apr. 2021), pp. 254–258. DOI: 10.1016/j.carbon.2021.01.011. URL: https://doi.org/10.1016/j.carbon.2021.01.011.

[72] M. Pomorski et al. "Charge transport properties of single crystal CVD-diamond particle detectors". In: *Diamond and Related Materials* 16.4–7 (Apr. 2007), pp. 1066–1069. ISSN: 0925-9635. DOI: 10.1016/j.diamond.2006.11.016. URL: http://dx.doi.org/10.1016/j.diamond.2006.11.016.

[73] Michal Pomorski. "Electronic Properties of Single Crystal CVD Diamond and Its Suitability for Particle Detection in Hadron Physics Experiments". Available from INIS: http://inis.iaea.org/search/search.aspx?orig_q=RN:40093695. PhD thesis. GSI (Gesellschaft für Schwerionenforschung), Aug. 2008. URL: http://inis.iaea.org/search/search.aspx?orig_q=RN:40093695.

[74] Ilya V. Popov et al. "Relative stability of diamond and graphite as seen through bonds and hybridizations". In: *Physical chemistry chemical physics.* 21.21 (2019), pp. 10961–10969. ISSN: 1463-9076.

[75] M. A. Prelas, G. Popovici, and L. K. Bigelow. *Handbook of Industrial Diamonds and Diamond Films*. New York: Marcel Dekker, 1998. ISBN: 0-8247-9994-1.

[76] S. Preuss and M. Stuke. “Subpicosecond ultraviolet laser ablation of diamond: Nonlinear properties at 248 nm and time-resolved characterization of ablation dynamics”. In: *Applied Physics Letters* 67.3 (1995), pp. 338–340. DOI: 10.1063/1.115437. eprint: https://doi.org/10.1063/1.115437. URL: https://doi.org/10.1063/1.115437.

[77] J. F. Prins. “Electrical resistance of diamond implanted at liquid nitrogen temperature with carbon ions”. In: *Radiation Effects* 76.3 (1983), pp. 79–82. DOI: 10.1080/01422448308209641. eprint: https://doi.org/10.1080/01422448308209641. URL: https://doi.org/10.1080/01422448308209641.

[78] Johan F. Prins. “Onset of hopping conduction in carbon-ion-implanted diamond”. In: *Phys. Rev. B* 31 (4 1985), pp. 2472–2478. DOI: 10.1103/PhysRevB.31.2472. URL: https://link.aps.org/doi/10.1103/PhysRevB.31.2472.

[79] Jeyakumar Ramanujam et al. “Inorganic photovoltaics – Planar and nanostructured devices”. In: *Progress in Materials Science* 82 (Sept. 2016), pp. 294–404. ISSN: 0079-6425. DOI: 10.1016/j.pmatsci.2016.03.005. URL: http://dx.doi.org/10.1016/j.pmatsci.2016.03.005.

[80] *Rectifier Diode D2601N*. D2601N. Rev. 9.1. Infineon Technologies AG. June 2014.

[81] *Rectifier Diode DZ950N*. DZ950N. Rev. 1. Infineon Technologies AG. May 2003.

[82] A. Rousse, C. Fourmaux, and et al. “Non-thermal melting in semiconductors measured at femtosecond resolution”. In: *Nature* 410 (2001), pp. 65–68.

[83] W. Saslow, T. K. Bergstresser, and Marvin L. Cohen. “Band Structure and Optical Properties of Diamond”. In: *Physical Review Letters* 16.9 (Feb. 1966), pp. 354–356. ISSN: 0031-9007. DOI: 10.1103/physrevlett.16.354. URL: http://dx.doi.org/10.1103/PhysRevLett.16.354.

[84] W. Saslow, T. K. Bergstresser, and Marvin L. Cohen. “Band Structure and Optical Properties of Diamond.” In: *Physical Review Letters* 21.10 (Sept. 1968), pp. 715–715. ISSN: 0031-9007. DOI: 10.1103/physrevlett.21.715. URL: http://dx.doi.org/10.1103/PhysRevLett.21.715.

[85] Dieter K Schroder. *Semiconductor material and device characterization*. en. 3rd ed. Wiley - IEEE. Chichester, England: Wiley-Blackwell, Jan. 2006.

[86] K. Seibert et al. “Femtosecond carrier dynamics in graphite”. In: *Phys. Rev. B* 42 (5 1990), pp. 2842–2851. DOI: 10.1103/PhysRevB.42.2842. URL: https://link.aps.org/doi/10.1103/PhysRevB.42.2842.

[87] Abdellah Sellam et al. “Ab Initio Study of the Electronic and Energy Properties of Diamond Carbon”. In: *Applications and Use of Diamond*. Ed. by Guodong (David). Rijeka: IntechOpen, 2023. Chap. 6. DOI: 10.5772/intechopen.111435. URL: https://doi.org/10.5772/intechopen.111435.

[88] Krishna Shenai. "The Figure of Merit of a Semiconductor Power Electronics Switch". In: *IEEE Transactions on Electron Devices* 65.10 (Oct. 2018), pp. 4216–4224. ISSN: 1557-9646. DOI: 10.1109/ted.2018.2866360. URL: http://dx.doi.org/10.1109/TED.2018.2866360.

[89] C. W. Siders et al. "Detection of Nonthermal Melting by Ultrafast X-ray Diffraction". In: *Science* 286.5443 (1999), pp. 1340–1342. DOI: 10.1126/science.286.5443.1340. eprint: https://www.science.org/doi/pdf/10.1126/science.286.5443.1340. URL: https://www.science.org/doi/abs/10.1126/science.286.5443.1340.

[90] John Singleton. *Band theory and electronic properties of solids*. en. Oxford Master Series in Condensed Matter Physics. London, England: Oxford University Press, Aug. 2001.

[91] L.T.S. Soffner et al. "HPHT diamond crystallization in the Ni-Mn-C system: Effect of Mg additions". In: *Journal of Crystal Growth* 550 (Nov. 2020), p. 125888. ISSN: 0022-0248. DOI: 10.1016/j.jcrysgro.2020.125888. URL: http://dx.doi.org/10.1016/j.jcrysgro.2020.125888.

[92] B.V. Spitsyn, L.L. Bouilov, and B.V. Derjaguin. "Vapor growth of diamond on diamond and other surfaces". In: *Journal of Crystal Growth* 52 (Apr. 1981), pp. 219–226. DOI: 10.1016/0022-0248(81)90197-4. URL: https://doi.org/10.1016/0022-0248(81)90197-4.

[93] I. Stenger et al. "Electron mobility in (100) homoepitaxial layers of phosphorus-doped diamond". In: *Journal of Applied Physics* 129.10 (Mar. 2021). DOI: 10.1063/5.0044326. URL: https://doi.org/10.1063/5.0044326.

[94] I. Stenger et al. "Impurity-to-band activation energy in phosphorus doped diamond". In: *Journal of Applied Physics* 114.7 (Aug. 2013), p. 073711. ISSN: 0021-8979. DOI: 10.1063/1.4818946. eprint: https://pubs.aip.org/aip/jap/article-pdf/doi/10.1063/1.4818946/15118921/073711_1_online.pdf. URL: https://doi.org/10.1063/1.4818946.

[95] H. M. Strong. "Catalytic Effects in the Transformation of Graphite to Diamond". In: *The Journal of Chemical Physics* 39.8 (Oct. 1963), pp. 2057–2062. ISSN: 1089-7690. DOI: 10.1063/1.1734582. URL: http://dx.doi.org/10.1063/1.1734582.

[96] S. Sundaram and E. Mazur. "Inducing and probing non-thermal transitions in semiconductors using femtosecond laser pulses". In: *Nature Mater* 1 (2002), pp. 217–224. DOI: 10.1038/nmat767.

[97] S.M. Sze and Kwok K. Ng. *Physics of Semiconductor Devices*. Wiley, Apr. 2006. DOI: 10.1002/0470068329. URL: https://doi.org/10.1002/0470068329.

[98] M. S. Komlenok et al. T. V. Kononenko M. Meier. "Microstructuring of diamond bulk by IR femtosecond laser pulses". In: *Appl. Phys. A.* 90 (2008), pp. 645–651. DOI: 10.1007/s00339-007-4350-9. URL: https://link.springer.com/article/10.1007/s00339-007-4350-9.

[99] A Tokmakoff, W F Banholzer, and M D Fayer. "Thermal diffusivity measurements of natural and isotopically enriched diamond by picosecond infrared transient grating experiments". In: *Applied physics.* 56.1 (1993), pp. 87–90. ISSN: 0947-8396.

[100] L.M. Tolbert. *Power Electronics for Distributed Energy Systems and Transmission and Distribution Applications: Assessing the Technical Needs for Utility Applications.* Dec. 2005. DOI: 10.2172/885985. URL: http://dx.doi.org/10.2172/885985.

[101] K. Tsukioka. "Energy distributions and scattering mechanisms of carriers in diamond". In: *Diamond and Related Materials* 18.5–8 (May 2009), pp. 792–795. ISSN: 0925-9635. DOI: 10.1016/j.diamond.2008.11.012. URL: http://dx.doi.org/10.1016/j.diamond.2008.11.012.

[102] V. S. Vavilov et al. "On structural transitions in ion-implanted diamond". In: *Radiation Effects* 22.2 (1974), pp. 141–143. DOI: 10.1080/00337577408232161. eprint: https://doi.org/10.1080/00337577408232161. URL: https://doi.org/10.1080/00337577408232161.

[103] P. de Visschere. "Image forces and MIS Schottky barriers". In: *Solid-State Electronics* 29.9 (Sept. 1986), pp. 873–875. ISSN: 0038-1101. DOI: 10.1016/0038-1101(86)90006-7. URL: http://dx.doi.org/10.1016/0038-1101(86)90006-7.

[104] Pierre-Nicolas Volpe et al. "High breakdown voltage Schottky diodes synthesized on p-type CVD diamond layer". In: *physica status solidi (a)* 207.9 (Aug. 2010), pp. 2088–2092. ISSN: 1862-6319. DOI: 10.1002/pssa.201000055. URL: http://dx.doi.org/10.1002/pssa.201000055.

[105] C. Z. Wang et al. "Laser-Induced Graphitization on a Diamond (111) Surface". In: *Phys. Rev. Lett.* 85 (19 2000), pp. 4092–4095. DOI: 10.1103/PhysRevLett.85.4092. URL: https://link.aps.org/doi/10.1103/PhysRevLett.85.4092.

[106] Juan Wang et al. "Vertical Diamond Trench MOS Barrier Schottky Diodes With High Breakdown Voltage". In: *IEEE Transactions on Electron Devices* 69.11 (Nov. 2022), pp. 6231–6235. ISSN: 1557-9646. DOI: 10.1109/ted.2022.3206178. URL: http://dx.doi.org/10.1109/TED.2022.3206178.

[107] Zeheng Wang et al. "On the Baliga's Figure-Of-Merits (BFOM) Enhancement of a Novel GaN Nano-Pillar Vertical Field Effect Transistor (FET) with 2DEG Channel and Patterned Substrate". In: *Nanoscale Research Letters* 14.1 (Apr. 2019). ISSN: 1556-276X. DOI: 10.1186/s11671-019-2960-8. URL: http://dx.doi.org/10.1186/s11671-019-2960-8.

[108] M. Willatzen, M. Cardona, and N. E. Christensen. "Linear muffin-tin-orbital and kp calculations of effective masses and band structure of semiconducting diamond". In: *Physical Review B* 50.24 (Dec. 1994), pp. 18054–18059. ISSN: 1095-3795. DOI: 10.1103/physrevb.50.18054. URL: http://dx.doi.org/10.1103/PhysRevB.50.18054.

[109] Peter Y. Yu and Manuel Cardona. *Fundamentals of Semiconductors: Physics and Materials Properties*. Springer Berlin Heidelberg, 2010. ISBN: 9783642007101. DOI: 10.1007/978-3-642-00710-1. URL: http://dx.doi.org/10.1007/978-3-642-00710-1.

[110] Alexander M Zaitsev. *Optical properties of Diamond*. en. Berlin, Germany: Springer, Dec. 2010.

Chapter 3. Metal Contacts to Phosphorous Doped Diamond

3.0.1. Disclosure of Collaborative Content

In this chapter, the growth of phosphorous doped diamond, as well as the procurement of diamond substrates was performed by the industrial partner Evince technology. Deposition of metallic LTLM contacts was also performed by the industrial partner, following consultations with the candidate. Further testing of CTLM contacts was performed wholly by the candidate, including the design, deposition, electrical testing, and further characterisation.

3.1. Introduction

3.1.1. Background

Diamond offers exceptional material properties for electrical devices that are unparalleled by other wide bandgap semiconductors. In the creation of devices that rely upon n and p-type doping however, many challenges arise from the limitations that diamond imposes upon device fabrication. Due to its extraordinary hardness and densely packed crystal lattice, doping via implantation has had marginal success [11] and CVD growth is the preferred choice for doped material [78]. The selection of donor candidates is limited, with nitrogen forming a deep donor level of around 1.6–1.7 eV [42] due to a chemical re-bonding of the donor electron on a neighbouring carbon atom simultaneous with a lone-pair on the nitrogen atom itself [19]. Phosphorous, despite having a lower solubility than nitrogen within the diamond lattice, is able to provide a shallower donor level at around 0.57–0.60 eV [40]. Various strategies of co-doping phosphorous with other elements have been examined theoretically such as in [2], but experimentally, substitutional phosphorous remains the only bulk n-type donor within diamond. The maximum dopant concentration depends primarily on the crystal orientation, with the $\{1\,1\,1\}$ orientation providing the highest observed concentrations of around 1×10^{20} at cm^{-3} [20]. Boron doped p-type material is most readily deposited onto the $\{1\,0\,0\}$ orientation, in large part due to the ready incorporation of crystalline defects on the $\{1\,1\,1\}$ orientation. Typical Hall mobility measurements for boron doped diamond at room temperature on $\{1\,1\,1\}$ oriented samples are around 500 cm^2 V^{-1} s^{-1} with hole concentrations of $\approx 10^{14}$ cm^{-3} [56] while on $\{1\,0\,0\}$ oriented samples the Hall carrier mobility reaches 2000 cm^2 V^{-1} s^{-1} with concentrations of $\approx 5 \times 10^{13}$ cm^{-3} [50]. These defects in $\{1\,1\,1\}$ oriented diamond growth have led to significant efforts in the improvement of $\{1\,0\,0\}$ oriented phosphorous doped CVD growth, with concentrations in the range of $10^{16} - 10^{18}$ [32]. However, high compensation ratios

become a significant limiting factor in phosphorous doped films grown on {1 0 0} oriented substrates as investigated more recently by [60].

3.1.2. Ohmic Contact Formation to Diamond Devices

3.1.2.1. Surface Termination

One common theme throughout the development of diamond based electronic devices is the challenge of ohmic contact formation, as well as reliable Schottky contacts [23]. This is in large part due to the presence of significant surface states and charge screening [10, 8], resulting in strong Fermi level pinning at the diamond surface in both boron [4] and phosphorous [65] doped samples. The extent of pinning is strongly dependent on the surface chemistry, particularly whether the diamond is oxygen-terminated or hydrogen-terminated [57, 68, 65, 77]. For both boron- and phosphorus-doped diamond, oxygen-terminated surfaces typically result in stronger pinning, locking the Fermi level near midgap, whereas hydrogen-terminated surfaces show reduced pinning but can introduce instability due to surface conductivity effects [81]. This pinning behaviour is also highly localised and dependent on ozonation and crystal orientation, due to varying oxidation rates across different crystal facets [64, 83]. Following the surface treatments presented in section 3.2, the surfaces used in the experiments in this chapter are strongly oxygen-terminated. Recent work indicates that this may inhibit the formation of TiC interface states, commonly used for the reduction of Fermi level pinning and subsequent formation of ohmic contacts [25]. Hence, this may be a potential consideration when examining the ohmic nature of these contacts.

3.1.2.2. Doping

Fermi level pinning is a significant issue for devices that require phosphorous doped diamond, due to the significant activation energy required for carrier promotion. While boron doped diamond can reach a metallic level at around 10^{20} at cm^{-3}, allowing for high quality ohmic contact formation via annealed titanium with standard capping layers of gold or platinum/gold, this is not the case for phosphorous doping without novel approaches [73]. This can be expressed with the ideal theory of metal to n-type semiconductor contacts, in which the contact resistivity ρ_c varies exponentially by the factor $\frac{\phi_b}{\sqrt{N_D}}$ where ϕ_b is the Schottky barrier height and N_D is the active donor concentration. Since it is difficult to deviate from the Fermi level pinning of ~ 4.3 eV below the conduction band, one approach to reduce contact resistivity is to increase the doping concentration N_D. This has previously been used to great effect in boron doped diamond, where the Fermi level pinning of oxygen terminated diamond relative to the valence band is around 1.3 eV [77] and has the same issues with regards to the independence of Schottky barrier height from metal contact work functions. With boron doping of 2–6 $\times 10^{17}$ at cm^{-3}, specific contact resistivities of 1.3×10^{-5} Ωcm^2 have been demonstrated using annealed Ti contacts [7].

3.1.3. Overview of Methodology and Novel Techniques

In this chapter, various experimental characterisation methods have been employed to investigate the properties of heavily phosphorous doped diamond as used in ohmic contact fabrication. Recent efforts such as that of [1] in laser-induced ohmic contact formation for diamond detector charge collectors and [73] in corrosion-resistive coaxial arc plasma deposited nanocarbon electrodes clearly demonstrate the ongoing development of phosphorous based devices, with a heavy focus on new methods for forming ohmic contacts in various device structures.

Through standard photolithography and metal deposition, simple Ti/Au and Ti/Pt/Au contacts were investigated and studied across a wide range of temperatures. Differences in the annealing conditions as well as the quality of the photolithography resulted in quite different experimental observations for this material. To understand the possible causes of some of these differences, other material characterisation methods are performed to help elucidate on the nature of heavily phosphorous doped diamond such as secondary ion mass spectroscopy (SIMS), X-ray photoelectron spectroscopy (XPS), atomic force microscopy (AFM) and optical microscopy.

In following chapters, another avenue to improve the characteristics of ohmic contacts to heavily phosphorous doped diamond is explored, that of ohmic contacts formed via laser graphitisation of the surface. Further material characterisation techniques such as PL combined with the previous data provides an intriguing picture of laser graphitised phosphorous doped diamond. In particular, the transition from standard Schottky thermionic emission to Fowler-Nordheim type field effect emission via geometric field enhancement is examined, with a consideration of potential cold cathode style devices that could be fabricated via this material and related fabrication techniques. This is in contrast to contact roughening techniques such as that demonstrated in [69], where Ni-catalysed micro-pyramidal {1 1 1} structures are etched into {1 0 0} diamond samples and then overgrown with highly phosphorous doped diamond.

Sample	Batch	Thickness (µm)	Contacts	Characterisation
A	1	0.3	None	SIMS
B	1	0.3	None	SIMS
C	2	0.3	Ti/Pt/Au - 850°C 30 mins	TLM, AFM
D	2	0.3	Ti/Pt/Au - 600°C 300 mins	TLM, AFM
E	3	1.2	None	XPS
F	3	1.2	Ti/Au - 500°C 10 mins	TLM, AFM, HIM
G	3	1.2	Laser Graphitised	TLM, AFM, FL

Table 3.1 A summary of all {1 1 1} samples, which had differing thicknesses of heavily phosphorous doped surface layers grown via MPCVD at Evince technology. Indicated in the table, various characterisation techniques are used to examine the phosphorous doped diamond and the resulting electrical contacts used in each case. SIMS was performed by an external service (LSA), XPS and HIM was performed by Nexus within Newcastle University with the candidate assisting in parametrisation and analysis, TLM electrical testing, FL and AFM was performed wholly by the candidate.

The samples examined in this chapter are summarised in table 7.1. One significant consideration in comparing results from different samples is that the growth of defect-laden phosphorous doped diamond on differing HPHT substrates may incur some loss of similarity between different samples, even when grown in the same batches. This is partially due to the process of microwave plasma CVD growth itself, multiple samples within the growth chamber at Evince technology will necessarily be situated in differing locations within the plasma. Hence, it is impossible to assume complete consistency between differing samples, despite best efforts to ensure these comparisons are comparable.

3.2. Sample Preparation

Examples of (111) HPHT samples are shown in figure 3.1. All samples ranged from 1.5–2.5 mm^2, with differing (111) polished faces based on the exact cut of the samples. The literature for diamond surface preparation displays a rich evolution of methods tailored to the unique demands of semiconductor surface treatments. Foundational studies, such as that by [5], explored a plethora of cleaning procedures, including the use of sulphuric acid-ammonium persulphate and hydrogen plasma. Yet, these procedures have since lost prominence in the literature, suggesting the rapid development and optimisation in the field.

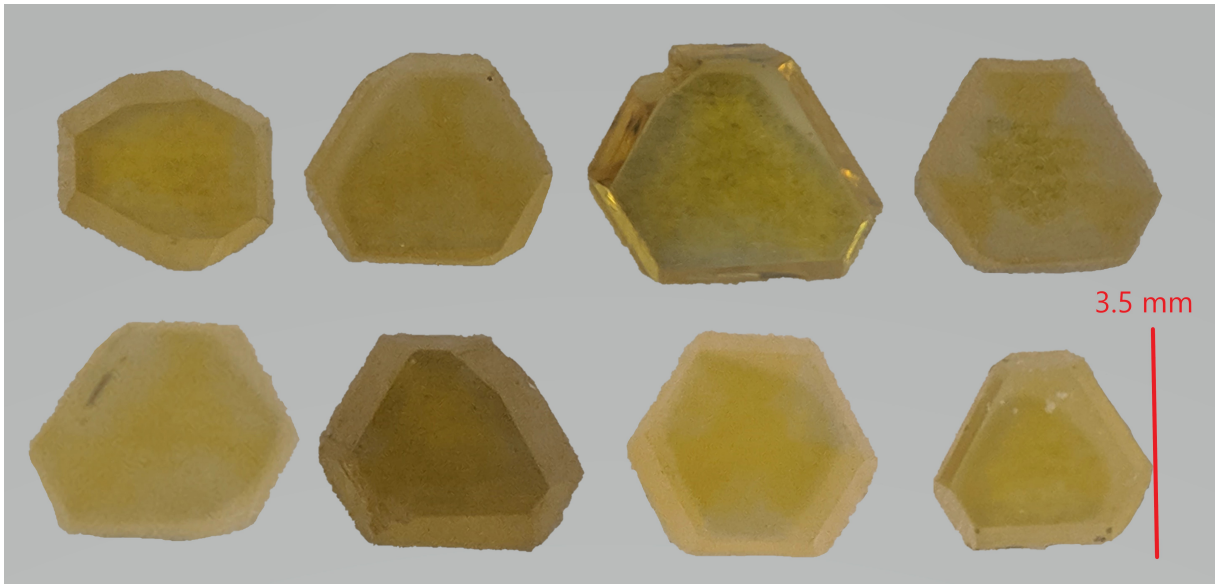

Figure 3.1 HPHT (111) samples as provided by Element Six, prior to cleaning and deposition. A scale bar is included for reference.

Modern techniques have predominantly converged around variations of dual or tri-acid treatments. [40, 70, 71], and [37, 36], for instance, have favoured a triacid mix of H_2SO_4:HNO_3:$HClO_4$, albeit at different ratios and durations. Some researchers such as [29, 30] and [66], however, have leaned towards dual acid organic cleans, utilising H_2SO_4 and H_2O_2 or H_2SO_4 and HNO_3.

The various methods of surface preparation underscores the importance of optimising cleaning conditions to the specifics of the application in question. Evince technology

employed the following standard surface preparation, with a strong focus on ensuring the removal of graphitic carbon and the formation of a consistent oxygen surface termination prior to phosphorous doped CVD growth, and as such this was used for the work in this project:

Decon90/ Deionised (DI) Water - 5 minutes. This acts as an initial cleaning step to remove gross contamination, including organic and inorganic residues. It provides a good general cleaning step that removes common contaminants from the sample surface, especially with a sonication bath providing agitation of the submersed samples.

DI Rinse and Sonication - 5 minutes. Rinsing the samples with deionised water and sonicating them to ensure complete removal of the initial Decon90 solution, along with any remaining contaminants. Thorough rinsing is crucial to prevent any residues from the first cleaning step, which might interfere with subsequent processes, especially the chemical reactions in the following cleaning stages.

1:1 H_2SO_4 and H_2O_2 Mix - 25 minutes at 175°C. This step employs a"piranha solution, a mixture of H_2SO_4 and H_2O_2, to further remove organic residues and contaminants. The strong oxidising nature of this mix at the specified temperature ensures the decomposition of most organic matter, preparing the surface for subsequent treatments. The 1:1 ratio was chosen by Evince technology and was in use as their standard operational cleaning step.

DI Rinse and Sonication - 5 minutes. A rinsing and sonication step with deionised water is essential to remove any remaining traces of the piranha solution, ensuring that no residues are left that could interfere with the following stages of surface preparation. The use of sonication aids in dislodging any stubborn contaminants that might remain adhered to the surface after the strong acid treatment.

Plasma Asher - 0.6 mbar, 5% O2 in He mix for 120 seconds. This stage utilises a plasma asher to further clean the surface by removing any remaining organic contaminants and surface residues. The plasma, formed from a 5% O in He mix at a pressure of 0.67 mbar, generates reactive species that etch away impurities from the surface. This prepares the surface for subsequent treatments, ensuring a consistent and clean base for metal deposition or phosphorous growth. The use of helium in the mix helps in controlling the etching rate by reducing the concentration of oxygen that reacts with the surface, ensuring a gentle but effective cleaning process.

Triacid Mix (1:3:4 $HClO_4$:H_2SO_4:HNO_3) - 7 minutes at 230°C. A triacid mixture serves multiple roles in the cleaning process. It primarily oxidises the diamond surface, preparing it for subsequent metal deposition, and ensures the elimination of any graphitic

material. Notably, the 3:4:1 ratio was chosen to optimise both oxidation and impurity removal, standing in slight contrast to other literature findings.

DI Rinse and Sonication (Repeated 3 Times) After the particularly strong triacid treatment, it is essential to ensure no residual acids remain on the diamond surface. As such, a thorough DI sonication rinsing step is performed to conclude the surface cleaning process.

3.3. Conventional Ohmic Contacts

Initial work focused on characterising the properties of ohmic contacts to heavily phosphorous doped diamond as grown by Evince technology. Active carriers within phosphorous doped diamond have been studied in the literature intensively via Hall effect measurements, with the dependence of carrier mobility due to different scattering mechanisms being examined experimentally and theoretically for a wide range of dopant concentrations in the {111} [61], {100} [60] and {113} [53] orientations.

3.3.1. Growth of Heavily Phosphorous-Doped Diamond

The concentration of phosphorus in diamond films can be modulated by adjusting the ratio of phosphorus to the carbon source (typically methane) in the gas phase during deposition. Numerous studies have observed that an increase in this ratio often leads to a corresponding increase in the as grown diamond films phosphorus concentration [52, 20, 32, 29, 37, 69, 26, 38, 30]. The studies included in this analysis for comparison to films grown by Evince technology predominantly employed samples with a (111) orientation, with the exception of [32], which focused on (001) oriented samples. The choice of crystal orientation has implications for the growth rate, dopant concentration and effective carrier compensation, which all complicate the analysis [72, 51, 53, 60].

3.3.1.1. SIMS Analysis

Secondary ion mass spectroscopy (SIMS) was performed on two samples to verify that the chosen growth conditions resulted in a highly doped phosphorous doped diamond film. This analysis was performed by Loughborough Surface Analysis Limited (LSA Ltd), with the results for samples A and B depicted in Figures 3.2 and 3.3. During SIMS analysis, LSA began monitoring with the minor carbon isotope, ^{13}C, and phosphorus. This choice allowed for a high instrument transmission, enabling the detection of low levels of phosphorus while maintaining the ^{13}C signal on the detector. Upon reaching the substrate, the ^{13}C signal noticeably decreased. This decrease prompted a shift to a lower instrument transmission and the additional monitoring of ^{12}C.

Throughout the profile, the ^{12}C signal remained consistent in both the layer and the substrate. By comparing the ratios of ^{12}C and ^{13}C to each other, it was observed that,

while the ratio in the substrate aligned with the expected ratio for carbon, the ^{13}C signal was proportionally stronger in the epilayer. This discrepancy suggests a significant presence of hydrogen in the epilayer, which appears to combine with ^{12}C, resulting in an overall higher ^{13}C signal.

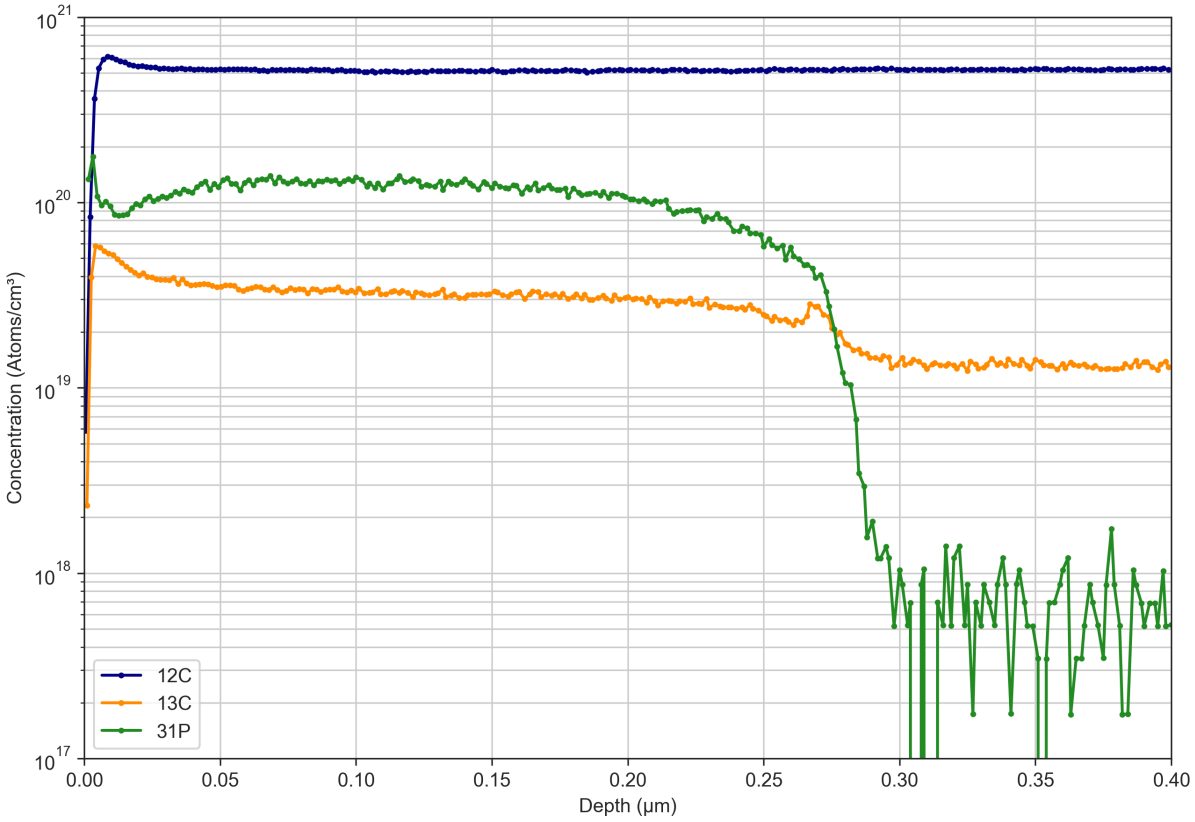

Figure 3.2 The measured concentration of phosphorous in the grown film as measured via SIMS for sample A.

Figure 3.2 represents the first example of SIMS performed to measure the concentration of phosphorous within the grown phosphorous doped surface layers. This growth layer presents a reasonably consistent profile throughout the first 0.2 µm, tailing off towards the maximum thickness of 0.3 µm. This demonstrates a high concentration for the majority of the surface layer, as needed for generation of bulk-like n-type material.

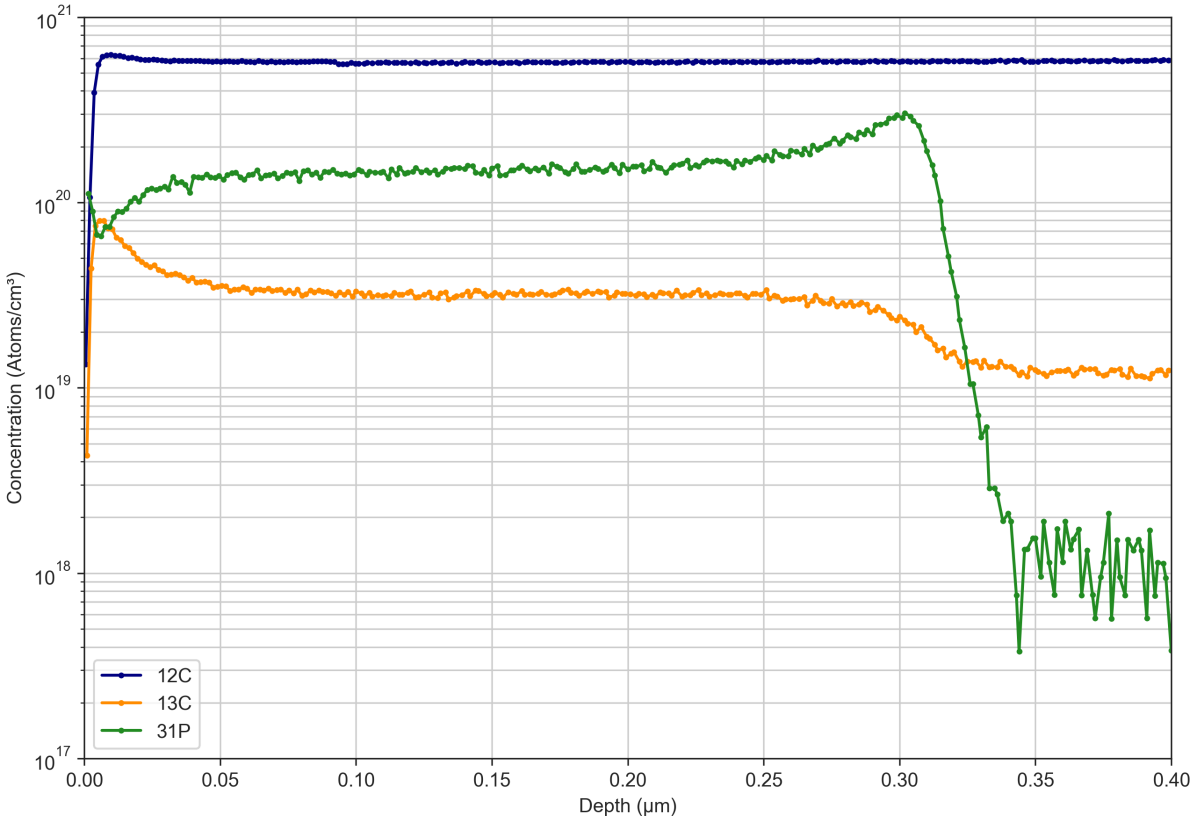

Figure 3.3 The measured concentration of phosphorous in the grown film as measured via SIMS for sample B.

In figure 3.3, the second example of SIMS, for another sample, is presented. In contrast to the first sample in figure 3.2, this growth layer appears to be very slightly thicker, with a high phosphorous concentration until past 0.3 µm. There is also a conspicuous peak at the end of the highly phosphorous doped surface layer, which may represent a higher uptake of phosphorous doping incorporation at the interface between substrate and the highly doped growth layer. It may also be a result of accumulating phosphorous during the depth profiling process itself [6], and hence could be considered as a physical error, intrinsic to the SIMS depth profiling. A final point regarding the depth profiling process itself is that these depths represent a one hour growth duration, and were used as growth rate estimators. The exact depth may differ slightly from that indicated in these figures, as the precise calibration of this experimental process is unknown, and depth resolution can vary from sample to sample [17]. Preferential sputtering, beam uniformity, sample charging and beam or residual gas contamination can all strongly affect the secondary ion signal [82, 22], so it is important to consider the possible variance that may be present in these presented depths.

3.3.2. Phosphorous Incorporation

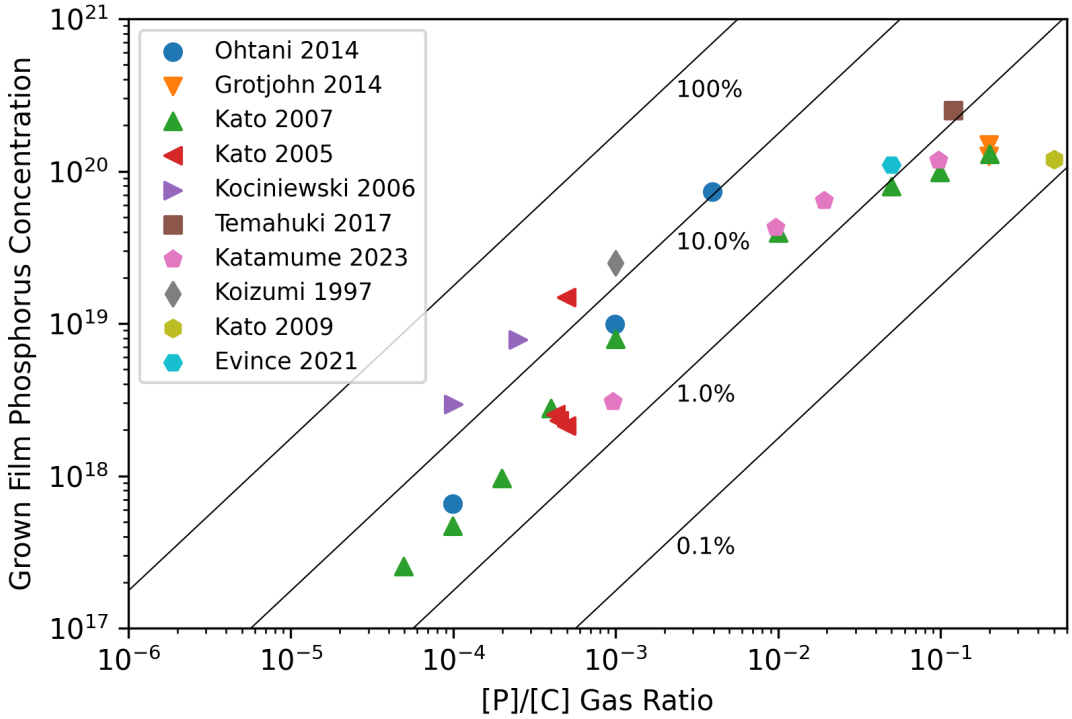

Figure 3.4 Phosphorus concentration ($\mathrm{at\,cm^{-3}}$) of films as a function of measured [P]/[C] ratio. Each marker represents a different study, with scatter points indicating separate samples. The solid lines represent theoretical phosphorus concentrations for given efficiencies of phosphorus incorporation into the lattice. [52, 20, 32, 29, 37, 69, 26, 38, 30]

Figure 3.4 shows the efficiency of phosphorous incorporation from the gas phase into the resulting doped diamond lattice across various ratios. Theoretical efficiencies of incorporation, ranging from 100% to 0.1%, are represented as solid lines. The theoretical efficiency of incorporation for phosphorus from the gas phase into the resulting diamond lattice can be considered as:

$$\text{Incorporation efficiency} = \frac{\text{Resulting dopant concentration}}{\text{Dopant:carbon in CVD feed-gas} \times \text{Atomic density of diamond}} \tag{3.1}$$

For further review of the different incorporation efficiencies as observed in the literature and how CVD growth has been optimised to improve this, please see section 2.2.6.1. In figure 3.4 the phosphorous doped films as grown by Evince technology in 2021 and 2022 can be seen in the upper portion of P/C ratio growth, with both a relatively high ratio of 5% phosphine in the methane feed-gas and a similarly high resultant diamond dopant concentration. This dopant concentration has been measured with SIMS in figures 3.2, 3.3 and appears to match that of the literature comparisons.

While figure 3.4 does show a clear correlation of higher film concentrations with a higher ratio of phosphorous in the carbon containing gas phase, there is a limit at which this

trend plateaus. The phosphorous concentration appears to reach saturation at around 10^{20} atoms/cm^3, which can be attributed to the limited solubility of phosphorous within the diamond lattice [39]. The phosphorous grown films from Evince appear to be at this saturation limit, with around 1×10^{20} at cm^{-3} of phosphorous detected via SIMS to the $\sim 1.76 \times 10^{23}$ at cm^{-3} of carbon within the diamond lattice.

The wide range of scatter points visible at specific P/C ratios suggests that factors beyond the P/C ratio, such as temperature, pressure, and plasma conditions (particularly in microwave plasma CVD growth), significantly influence the phosphorus concentration within grown films [44].

Furthermore, it suggests that the efficiency of phosphorus incorporation can vary between different growth techniques and experimental setups. The natural tendency for incorporation efficiency to diminish when higher concentrations of phosphorous are present in the gas phase could also be influenced by more than just solubility limitations. Factors such as changes in the plasma conditions, or the formation of phosphorous clusters which are not possible to incorporate into the diamond lattice, may also play a role [24].

In comparison to conventional semiconductor dopants, diamond has remarkably high activation energies. Hence, the ionisation of such deep dopants must be considered fully in any diamond device that utilises phosphorous donors.

3.3.3. Incomplete Ionisation

At thermal equilibrium, the electron and hole contributions to current flow across a junction are equivalent, resulting in a constant Fermi level across such a junction. With this condition, the Poisson equation for anisotropic materials, determining the electrostatic potential ψ can be simplified [41]:

(3.2)

$$n + N_a^- = p + N_d^+ \tag{3.3}$$

where n and p are the electron and hole concentrations respectively, N_a^- gives the concentration of ionised acceptors and N_d^+ is the concentration of ionised donors. This is then solved with the mass action law:

$$n \cdot p = n_i^2 \tag{3.4}$$

where n_i is the intrinsic carrier concentration. Then, the equilibrium electron or hole concentration in an n or p-type material respectively is given by [41]:

$$n = \frac{1}{2} \cdot \left(N_d^+ - N_a^- + \sqrt{\left(N_d^+ - N_a^- \right)^2 - 4n_i^2} \right) \tag{3.5}$$

$$p = \frac{1}{2} \cdot \left(N_a^- - N_d^+ + \sqrt{\left(N_d^+ - N_a^- \right)^2 - 4n_i^2} \right) \tag{3.6}$$

The concentration of ionised impurity atoms is given by a steady-state Gibbs distribution as in [15]:

$$N_d^+ = \frac{N_d}{1 + g_d \cdot \frac{n}{n_1}} \tag{3.7}$$

with:

$$n_1 = N_c \cdot \exp\left\{-\frac{E_c - E_d}{k \cdot T}\right\} \tag{3.8}$$

or:

$$N_a^+ = \frac{N_a}{1 + g_a \cdot \frac{p}{p_1}} \tag{3.9}$$

with:

$$p_1 = N_v \cdot \exp\left\{-\frac{E_a - E_v}{k \cdot T}\right\} \tag{3.10}$$

where $N_{d,a}$ are the substitutional and hence active dopant concentrations of donors and acceptors respectively. The ground state degeneracy factor for the donor impurity level in diamond $g_d = 2$, since a donor level can accept one electron with either spin, or have no electron at all [14]. The ground state degeneracy factor for acceptor levels is $g_a = 4$ as each acceptor impurity level can accept a hole of either spin, with a doubly degenerate impurity level as a result of the two degenerate valence bands at $\vec{k} = 0$.

It can also be more convenient to express the ionisation fraction in terms of the carrier concentrations, instead of the relevant quasi-Fermi levels. Taking the Fermi-Dirac statistics form of the carrier concentrations, rather than the Maxwell-Boltzmann form, simply adds the $\gamma_{n,p}$ parameter:

$$n_2 = N_c \gamma_n \cdot \exp\left\{-\frac{E_c - E_f}{k \cdot T}\right\} \tag{3.11}$$

$$p_2 = N_c \gamma_p \cdot \exp\left\{-\frac{E_{fp} - E_v}{k \cdot T}\right\} \tag{3.12}$$

In the non-degenerate limit, the Fermi-Dirac distribution gives the Maxwell-Boltzmann distribution and $\gamma_{n,p} = 1$ [67]. This can be used to define the relevant quasi-Fermi levels as:

$$E_{fn} = kT \ln \frac{n}{\gamma_n N_c} + E_c \tag{3.13}$$

$$E_{fp} = -kT \ln \frac{n}{\gamma_p N_v} + E_v \tag{3.14}$$

with the resulting fraction of ionised carriers given in the form:

$$\frac{N_d^+}{N_d} = \frac{1}{1 + \frac{g_d n}{\gamma_n N_c} \exp\left\{\frac{\Delta E_d}{kT}\right\}} \tag{3.15}$$

$$\frac{N_a^+}{N_a} = \frac{1}{1 + \frac{g_a p}{\gamma_p N_v} \exp\left\{\frac{\Delta E_a}{kT}\right\}} \tag{3.16}$$

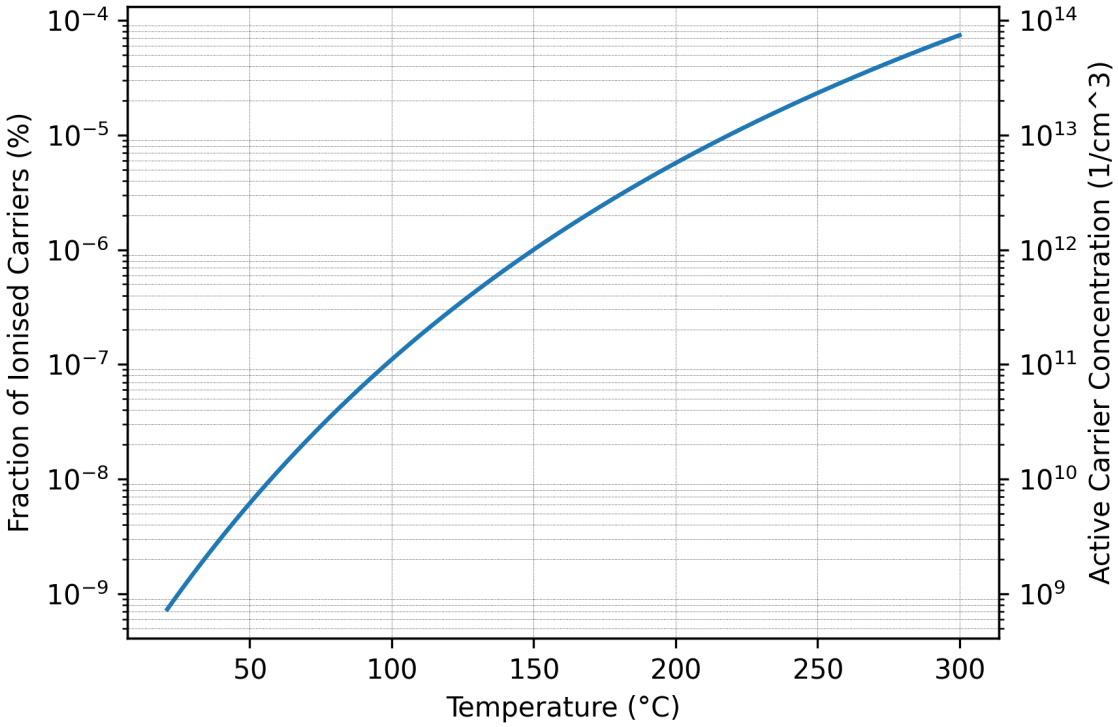

Figure 3.5 The number of active carriers according to the thermal ionisation equation with a donor energy level of 0.6 eV

F where $\Delta E_d = E_c - E_d$ and $\Delta E_a = E_a - E_v$. The results of this equation for phosphorous are shown in figure 3.5. At room temperature with a phosphorous concentration of 1×10^{20} cm^{-3}, the active carrier concentration can be as low as 5.25×10^{9} cm^{-3}, or $5.25 \times 10^{-9}\%$ which is also demonstrated in other works with hall effect measurements [54, 59, 28]. At 300°C this is raised to an active carrier concentration of 5.30×10^{14} cm^{-3}, or $5.30 \times 10^{-4}\%$ of the doping concentration. Hence, this will be a significant factor in the sheet resistance of phosphorous doped diamond.

3.3.3.1. Partly Compensated Donors

Along with the thermal ionisation of donors, it is also important to consider the compensation of donors within diamond. The effective carrier concentration, taking into account the presence of compensating acceptor states, can be given with the following equation:

$$\frac{n(N_A + n)}{N_D - N_A - n} = \frac{N_C}{g_d} \exp\left\{-\frac{E_d}{kT}\right\} \tag{3.17}$$

where $N_{D,A}$ are the carrier concentrations, k is the Boltzmann constant, T is the temperature and N_C is the effective density of state, expressed in this case as:

$$N_C = 12\left(\frac{2\pi m_e^* kT}{h^2}\right)^{3/2} \tag{3.18}$$

where the effective mass of donor electrons $m^* = 0.55m_e$ (m_e) is the mass of a free electron) and h is the Planck constant.

3.3.4. Ti/Pt/Au Contacts

Sample	Batch	Thickness (µm)	Contacts	Characterisation
A	1	0.3	None	SIMS
B	1	0.3	None	SIMS
C	2	0.3	Ti/Pt/Au - 850°C 30 mins	TLM, AFM
D	2	0.3	Ti/Pt/Au - 600°C 300 mins	TLM, AFM

Table 3.2 A summary of relevant samples for this subsection.

Two samples (C and D) were used for initial TLM characterisation. With the same growth conditions as for samples A and B, a heavily phosphorous doped surface layer was grown via MPCVD following the standard cleaning process. In figure 3.6 the final Ti/Pt/Au structure used for both is shown. The linear TLM structure can be seen on the lower portion of the sample's surface. When compared, the sample dimensions were comparable, with sizes of 3.7×3.8 mm for sample C and 3.9×4.1 mm for sample D. The Ti/Pt/Au contacts used were fabricated via electron-beam lithography by Evince technology in collaboration with the candidate, with nominal thicknesses of 20/20/100 µm respectively. Sample C was annealed at 850°C for 30 minutes, while sample D was annealed at 600°C for 300 minutes, as summarised in table 3.2. Annealing conditions were chosen such that a shorter, high temperature anneal could be compared to a longer, low temperature anneal. Crucial to the success of such annealing is the formation of TiC at the diamond interface [70, 71], which is examined further in section 3.5.4.4, but generally is observed from temperatures as low as 400 °C. This is explored further in section 3.5.3.1, for further device fabrication.

The surface thicknesses for samples C and D are estimated at 0.3 µm, as while grown in different batches, the duration of phosphorous growth was consistent between batch 1 and 2, hence the SIMS data for samples A and B may be considered representative for these subsequent samples.

3.4. Linear Transfer Length Method (TLM) and Richardson Analysis

In this section, the analysis of I-V curves for samples C and D ranging from room temperature to 300°C are presented. Due to the phosphorous donor ionisation energy of around 0.6 eV, there is a very significant temperature dependence. At room temperature, the smallest channel width on sample C of approximately 3.5 µm drew a current density of approximately 1.57×10^{-6} A cm^{-2} when normalised by contact surface area with an applied potential bias of 10 V. When this data is instead examined via contact width normalisation, it is in the region of 2.5 pA µm^{-1} as demonstrated in figure 3.9. While at 300°C, this increased to 1.08×10^{-4}A cm^{-2} or 168 pA µm^{-1}, showing both the strong

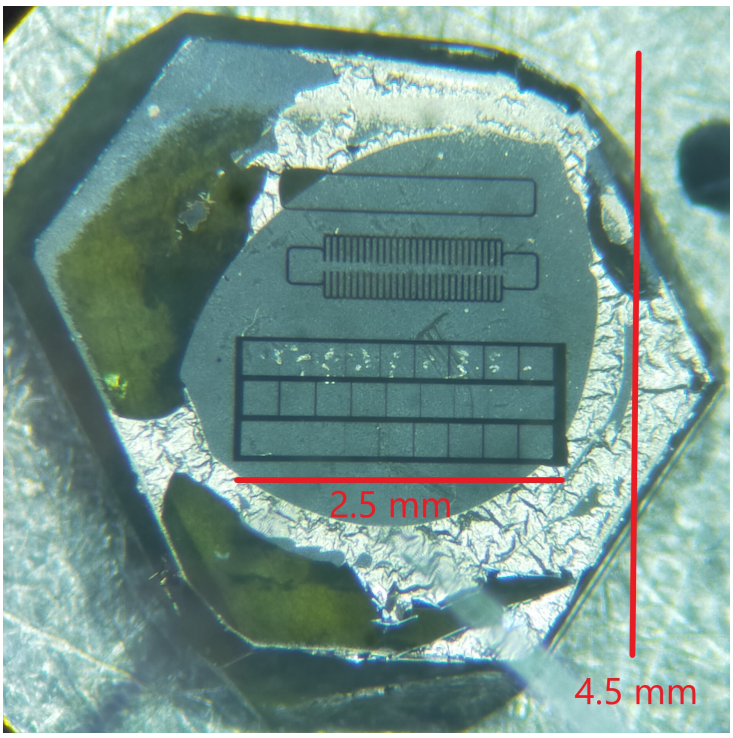

Figure 3.6 Sample B with linear TLM contacts, as seen with an optical microscope. Scale bars are used for feature size reference.

temperature dependence of phosphorous doped diamond and the low number of active carriers involved, with contact width normalised current measurements in the region of $\mathrm{pA\,\mu m^{-1}}$.

3.4.1. Ti/Pt/Au I-V Results

The measured current vs. applied voltage characteristics for samples C and D at 21, 150, and 300 °C are presented in this section. The data is plotted over a bias range of ±10 V.

3.4.1.1. Experimental Error Analysis

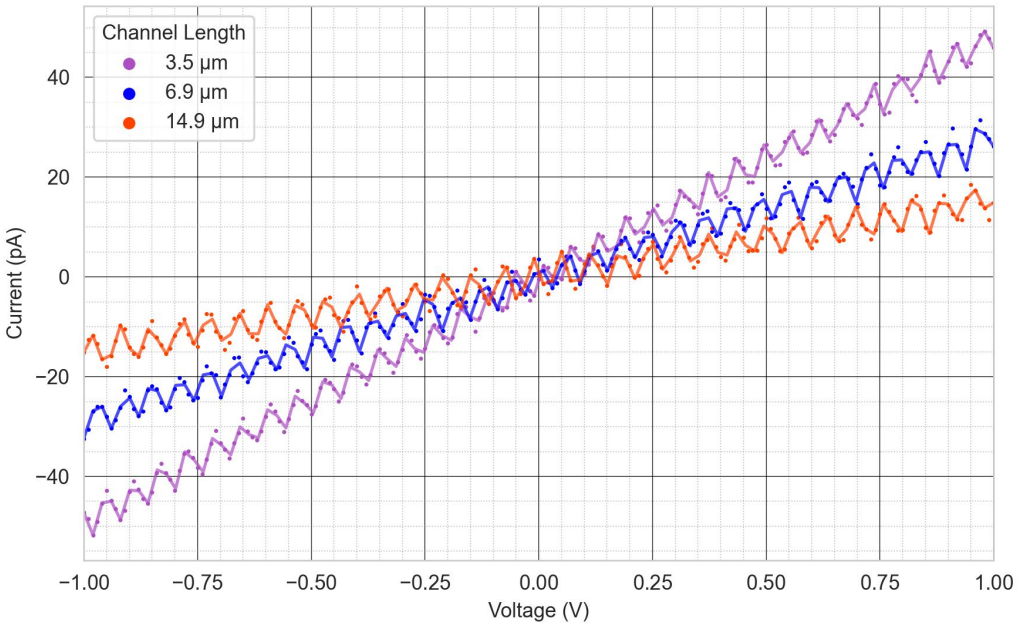

Figure 3.7 Linear plot of measured current vs. applied voltage for three channel lengths over a ±1 V bias range at 21 °C (Sample C). A cubic spline interpolation, applied to groups of three data points, is used to provide a smoothed representation of the data.

To examine potential error magnitudes, Figure 3.7 presents a limited bias range of ±1 V without error bars. The typical calibrated error of the B1500A measurement system is no greater than 2 pA, with the data predominantly exhibiting noise near 0 V. However, due to an observed sinusoidal noise pattern with an approximate amplitude of 5 pA, a conservative worst-case error of 5 pA is applied to all IV plots. The interpolated cubic spline line is included to visually represent this observed noise behaviour.

3.4.1.2. Normalisation Comparison

The measured current across the linear TLM contacts is examined here, with both the raw IV characteristics and the IV plots where the current is normalised by the contact width (50 µm for both sets of contacts on samples C and D). The normalised current density, based on the surface area of the linear contacts, is further analysed in Section 3.4.2 for additional comparison.

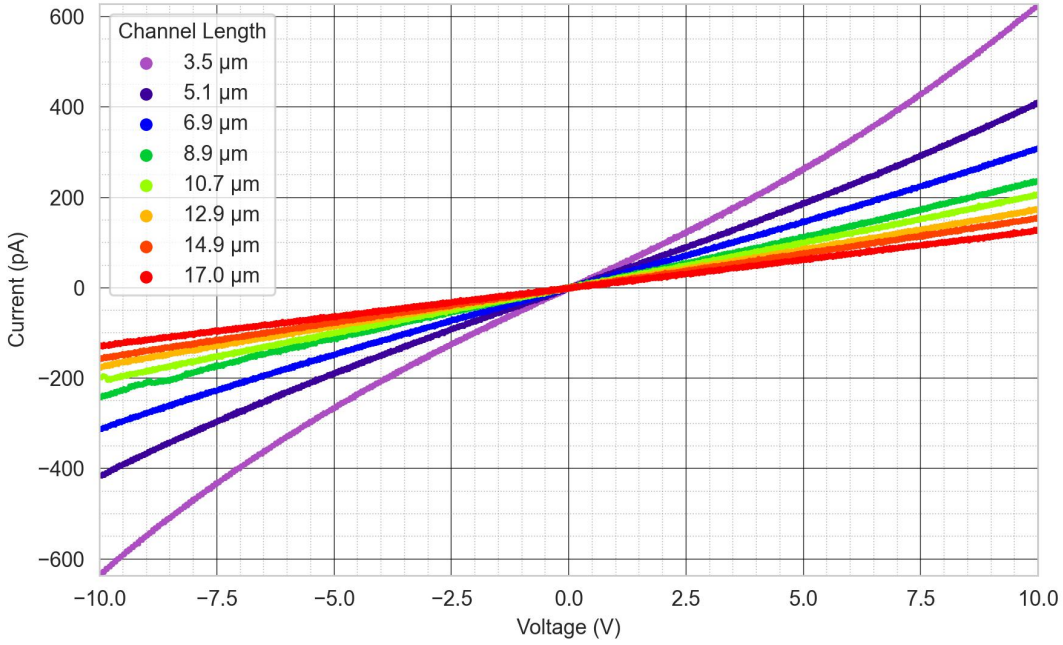

Figure 3.8 Linear plot of measured current vs. applied voltage for all channel lengths at 21 °C (Sample C).

Figure 3.8 presents the room-temperature IV characteristics of Sample C across all LTLM channels. The observed current reflects the influence of both the sheet resistance and the contact resistance to the highly phosphorus-doped diamond.

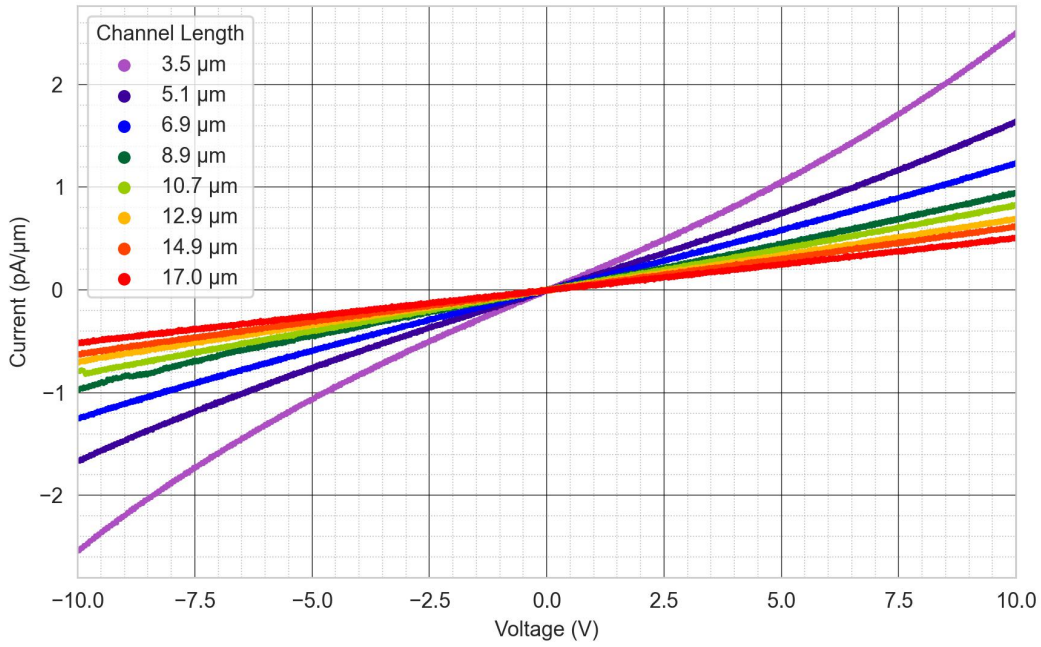

Figure 3.9 Linear plot of normalised current vs. applied voltage for all channel lengths at 21 °C (Sample C).

Figure 3.9 presents the normalised room-temperature IV characteristics of Sample C across all LTLM channels. Since the contact width (250 µm) is constant for all contacts, the trends closely follow those in Figure 3.8. The normalised current reaches a peak of approximately 2.6 pA µm^{-1}.

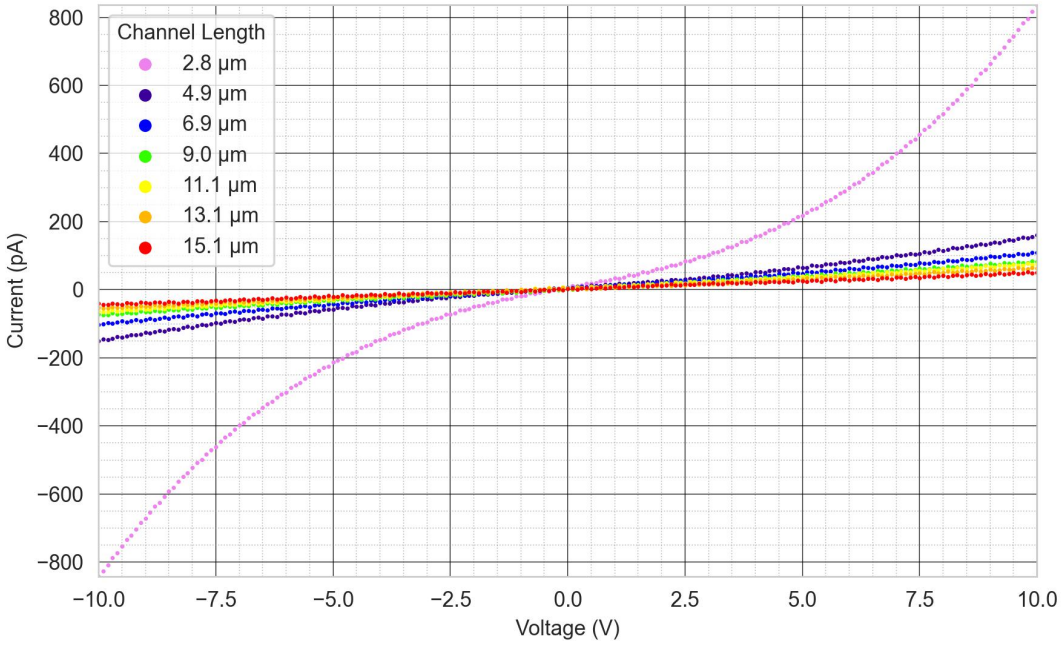

Figure 3.10 Linear plot of measured current vs. applied voltage for all channel lengths at 21 °C (Sample D).

Figure 3.10 presents the room-temperature IV characteristics of Sample D across all LTLM channels. As with Sample C, the high sheet resistance results in currents in the pA range. However, this sample features a slightly narrower channel length of 2.8 µm and exhibits a highly non-linear trend over this voltage range for the smallest channel. Note that the channel lengths are different to that of sample C, due to variation in the photolithographic process despite the same photomask and process being used by the industrial partner Evince technology in their fabrication. The channel lengths as measured via AFM are used in place of the designed channel length, to better reflect the fabricated contacts.

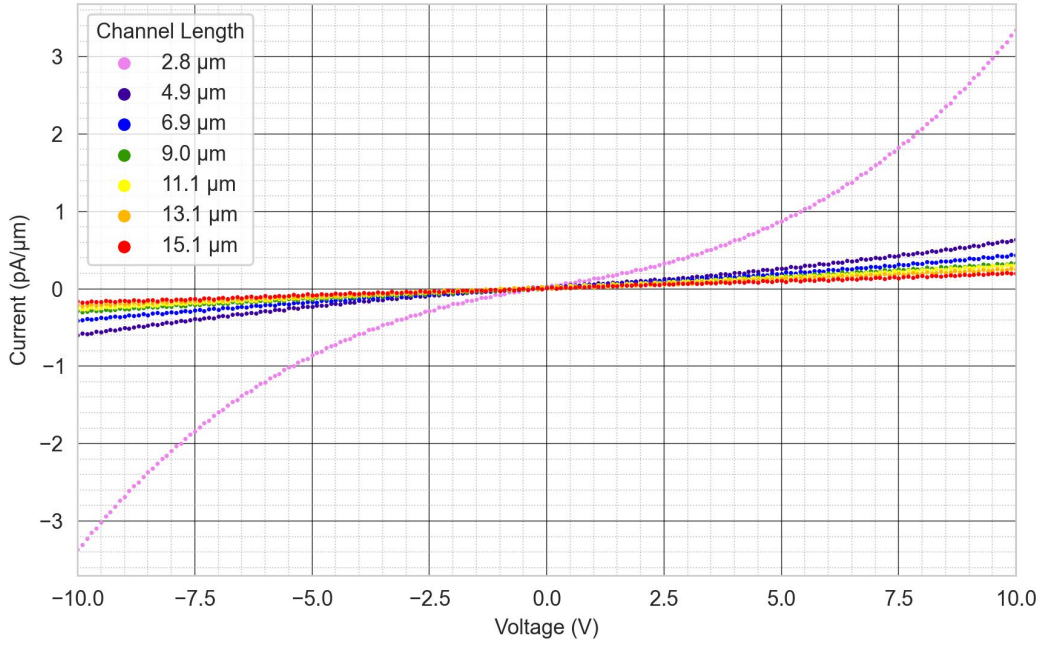

Figure 3.11 Linear plot of normalised current vs. applied voltage for all channel lengths at 21 °C (Sample D).

Figure 3.11 presents the normalised room-temperature IV characteristics of Sample D across all LTLM channels. Given the constant contact width (250 µm) across different channel lengths, this figure further reinforces the consistency between the raw and normalised IV data in this second linear TLM experiment. The peak normalised current for sample D is approximately 3.4 $\mathrm{pA\,\mu m^{-1}}$.

These normalised IV results confirm the very high total resistances measured in the linear TLM experiments, consistent with the raw IV data. The fact that the contact width is constant across all measurements ensures that the linearity observed in the raw IV data is preserved in the normalised plots. Consequently, the inclusion of contact width does not affect the assessment of linearity in IV data and can be considered secondary for comparison purposes. Instead, a key consideration for TLM analysis is the extent of non-linearity in the IV characteristics at higher voltages, as significant deviations from linear behaviour compromise the reliability of extracted resistance values. This aspect will be examined further in Section **??**.

3.4.1.3. Higher Temperature IV Results

This section presents additional raw IV data from linear TLM samples C and D, illustrating the fundamental transport properties of these devices. These measurements provide the basis for further TLM analysis and interpretation.

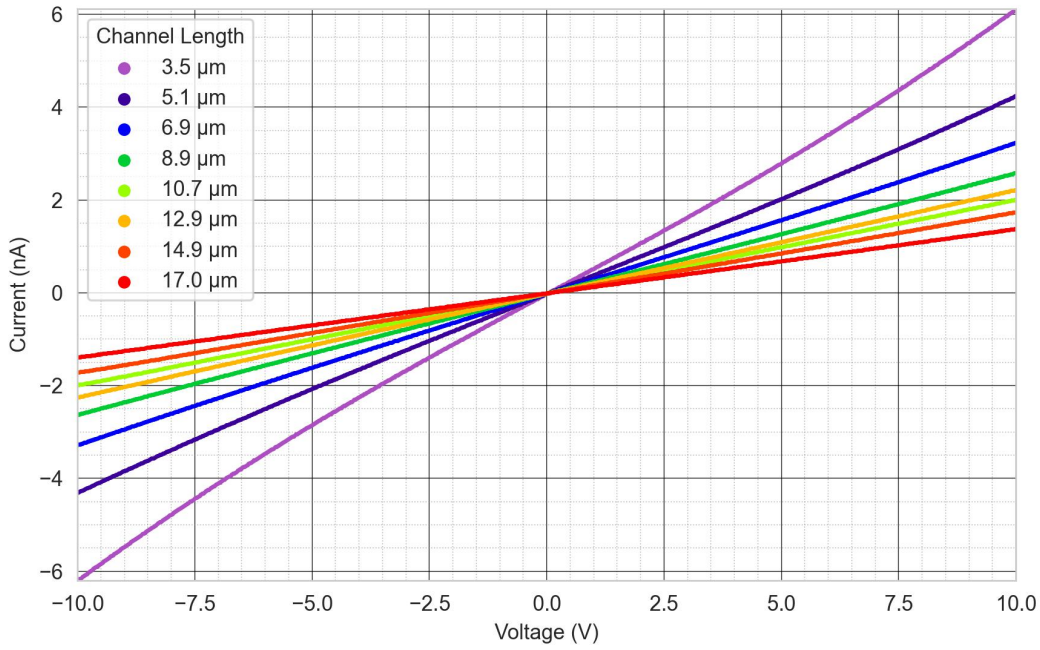

Figure 3.12 Linear plot of measured current vs. applied voltage for all channel lengths at 150 °C (Sample C).

Figure 3.12 presents the IV characteristics of Sample C at 150 °C, showing a reduction in resistance compared to the room-temperature case. While the overall current remains low, this trend is indicative of a semiconducting channel with thermally activated carriers.

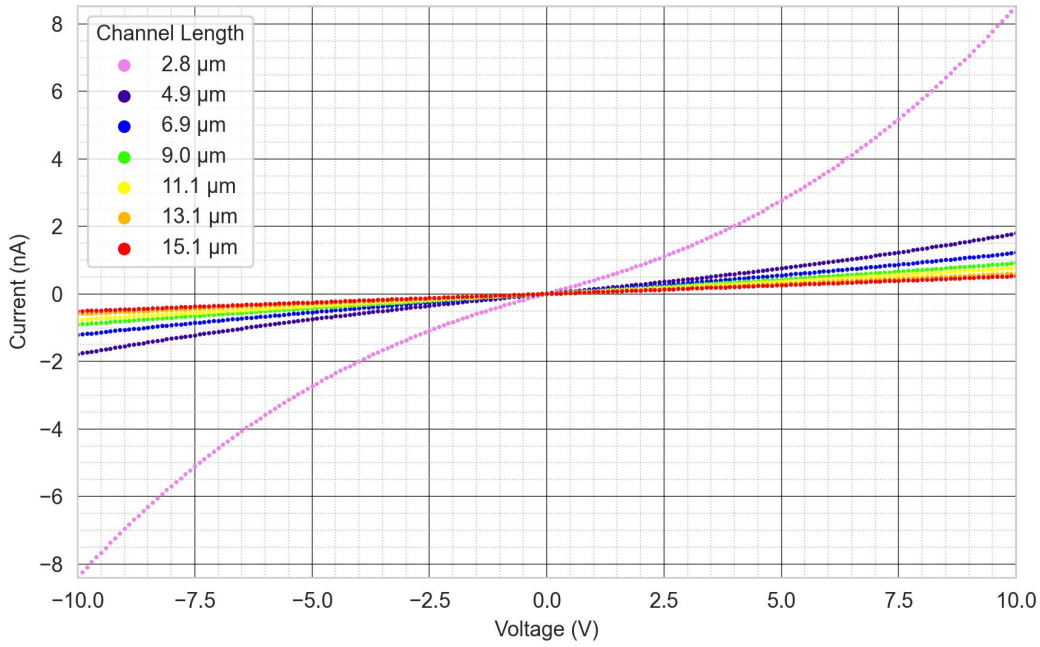

Figure 3.13 Linear plot of measured current vs. applied voltage for all channel lengths at 150 °C (Sample D).

Similarly, Figure 3.13 shows that Sample D follows the same general trend at higher temperatures, with reduced resistance as expected for a thermally activated transport mechanism.

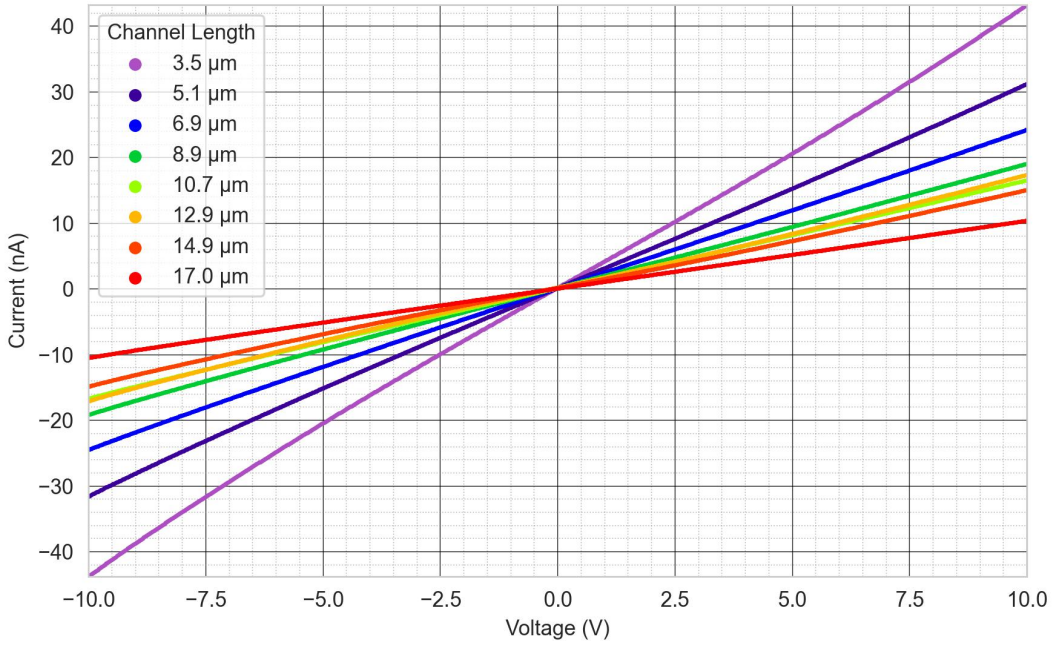

Figure 3.14 Linear plot of measured current vs. applied voltage for all channel lengths at 300 °C (Sample C).

Figure 3.14 presents the highest temperature measurement for Sample C at 300 °C. Although the data appears linear, the current remains very low, and this apparent linearity may be deceptive.

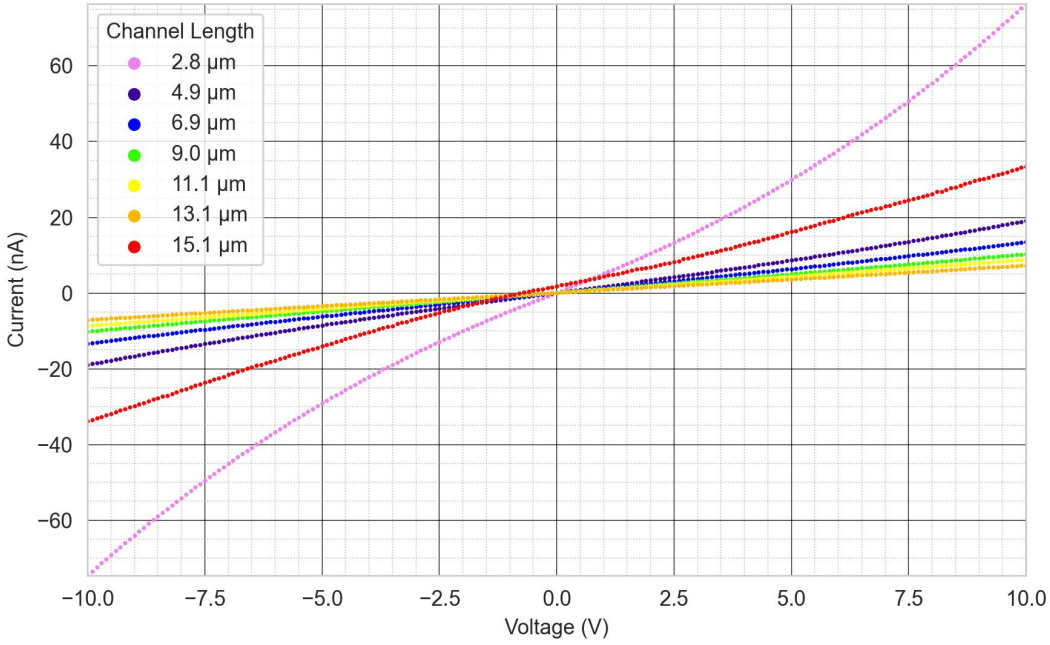

Figure 3.15 Linear plot of measured current vs. applied voltage for all channel lengths at 300 °C (Sample D).

Figure 3.15 presents the 300 °C IV characteristics of Sample D. While similar to Sample C, the narrower channel spacing in Sample D consistently exhibits more pronounced non-linearity, suggesting Schottky-like behaviour at higher potential biases. To investigate this further, additional high-bias measurements were performed for Sample D, though similar measurements were not conducted for Sample C.

In conclusion, the increase in temperature from room temperature to 300 °C demonstrates the expected semiconducting "freeze-out" behaviour of highly phosphorus-doped diamond [62], with a greater number of thermally activated donor states in accordance with theoretical expectations (see Section 3.3.3). A key feature of the raw and normalised IV data is the observed non-linearity, particularly in the smallest channel of Sample D. Since linearity is a fundamental requirement for the valid application of the linear TLM method, this aspect is examined in detail in the following section.

3.4.1.4. Linearity of Raw IV data

This section presents the ±50 V IV data for Sample D at room temperature and 300 °C.

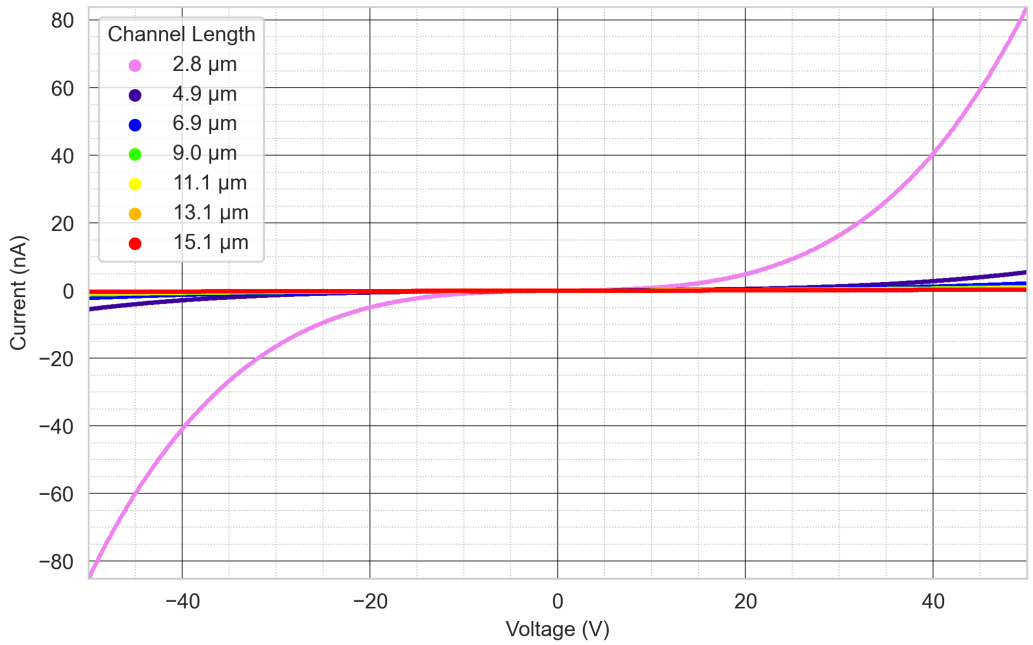

Figure 3.16 Linear plot of measured current vs. applied voltage for all channel lengths at 21 °C (Sample D).

Figure 3.16 presents the room-temperature IV characteristics of Sample D over a bias range of ±50 V. A clear transition is observed: while the lower-bias region appears linear, at higher biases the IV trend becomes strongly non-linear, resembling a Schottky-like response across all channel lengths. This behaviour may be directly related to the different annealing conditions used for Sample D (600 °C for 300 minutes) compared to Sample C (850 °C for 30 minutes).

This is despite the contacts being composed of conventionally "Ohmic" forming metals (Ti/Pt/Au), with annealing at 600 °C having been shown to induce TiC formation in similar studies of heavily phosphorus-doped diamond [26, 27, 30, 70]. However, more recent investigations into TiC formation suggest that the standard surface cleaning procedure employed by the industrial partner in this experiment may have been inappropriate. Specifically, the use of an oxygen plasma processing step could have prevented effective TiC formation, even at temperatures as high as 900 °C [25].

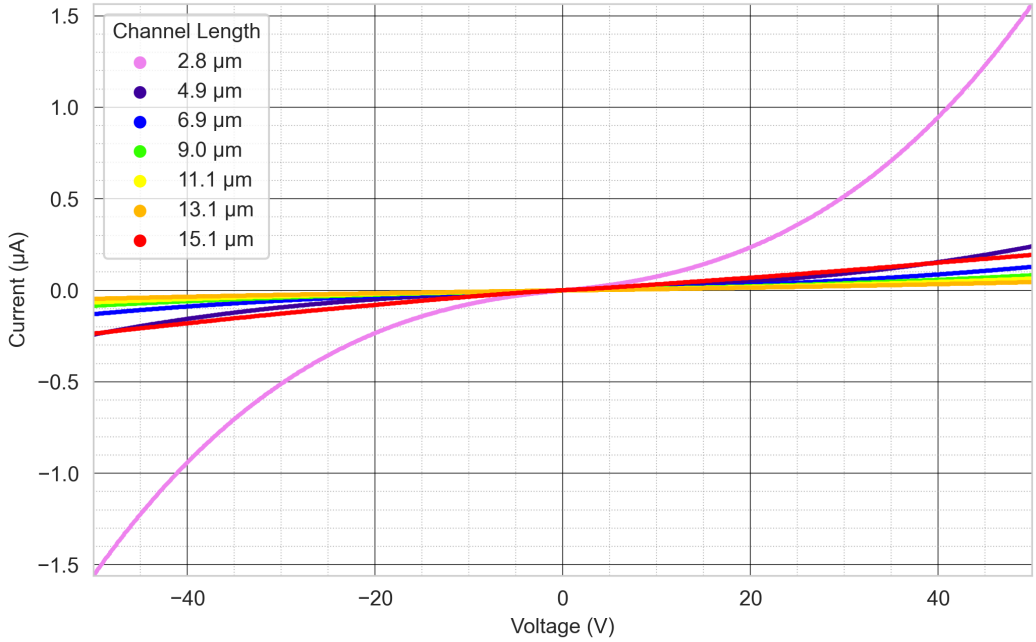

Figure 3.17 Linear plot of measured current vs. applied voltage for all channel lengths at 300 °C (Sample D).

Figure 3.17 presents the highest-temperature IV data for Sample D over the ±50 V bias range. The trend of decreasing resistance at higher temperatures continues, while the increased bias range reveals clear Schottky-like behaviour in the Ti/Pt/Au contacts after annealing.

While this result suggests that a higher annealing temperature may improve Ohmic contact formation, as observed in Sample C, the limited bias range for that sample prevents a direct comparison. This restriction in potential bias during the experimental procedure was due to time constraints, as the industrial partner required the sample for further testing. It is possible that Sample C would also exhibit Schottky-like behaviour at 50 V, highlighting the importance of carefully selecting bias ranges in LTLM analysis. The conventional approach to this issue is to focus on the lower-voltage region of the IV curve, where linearity is most apparent. However, this introduces a practical limitation: at very low currents (in the pA range), measurement errors become significant, as discussed in Section 3.4.1.1. Thus, for these highly resistive samples, it is desirable to select IV data that demonstrates high linearity while also maintaining a substantial potential bias.

3.4.2. Ti/Pt/Au J-V Results

This section presents the current density vs applied voltage plots for samples C and D at temperatures of 21, 150, and 300°C. The bias range used is ±10 V. Error bars representing a current error of 1 pA, are included in all plots. Data points have been processed using a running average over three consecutive points.

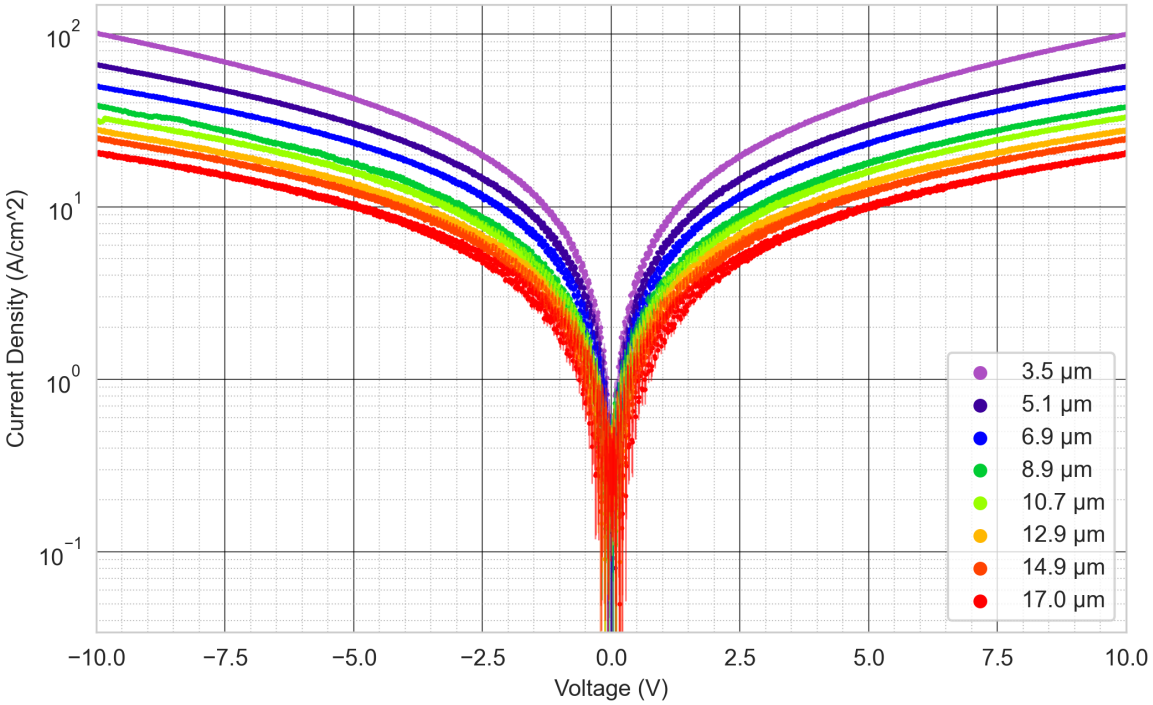

Figure 3.18 A log-linear plot of the measured current density against applied voltage for all channel lengths at 21°C (sample C).

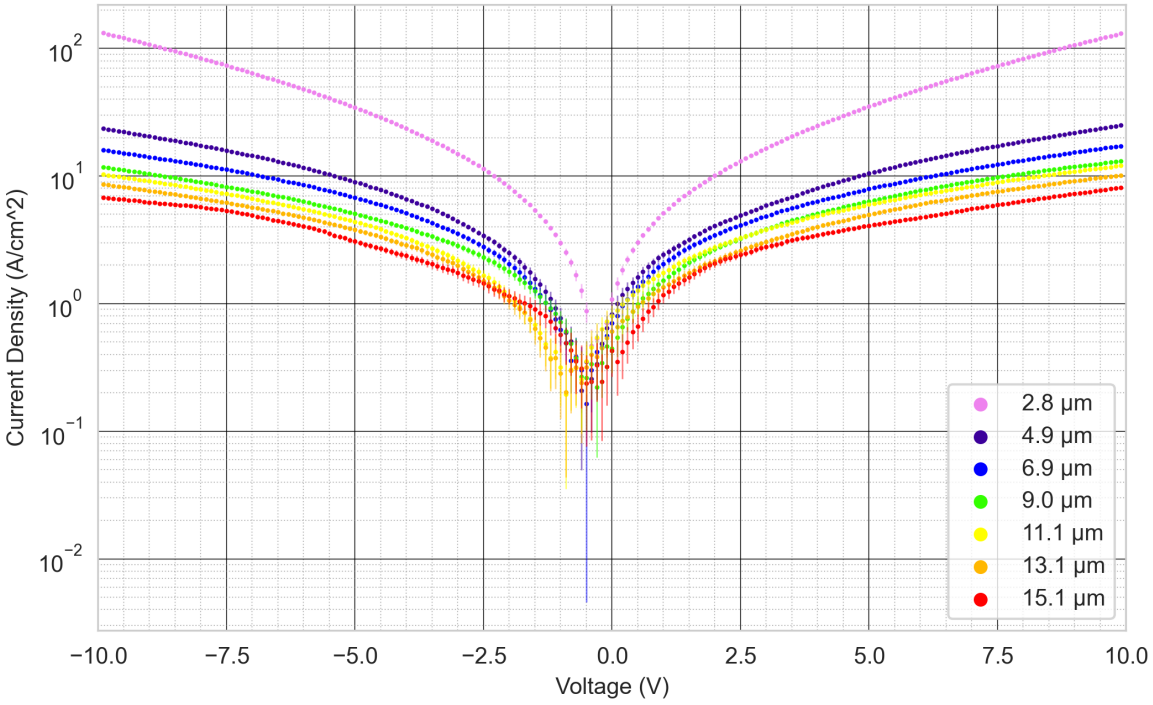

Figure 3.19 A log-linear plot of the measured current density against applied voltage for all channel lengths at 21°C (sample D).

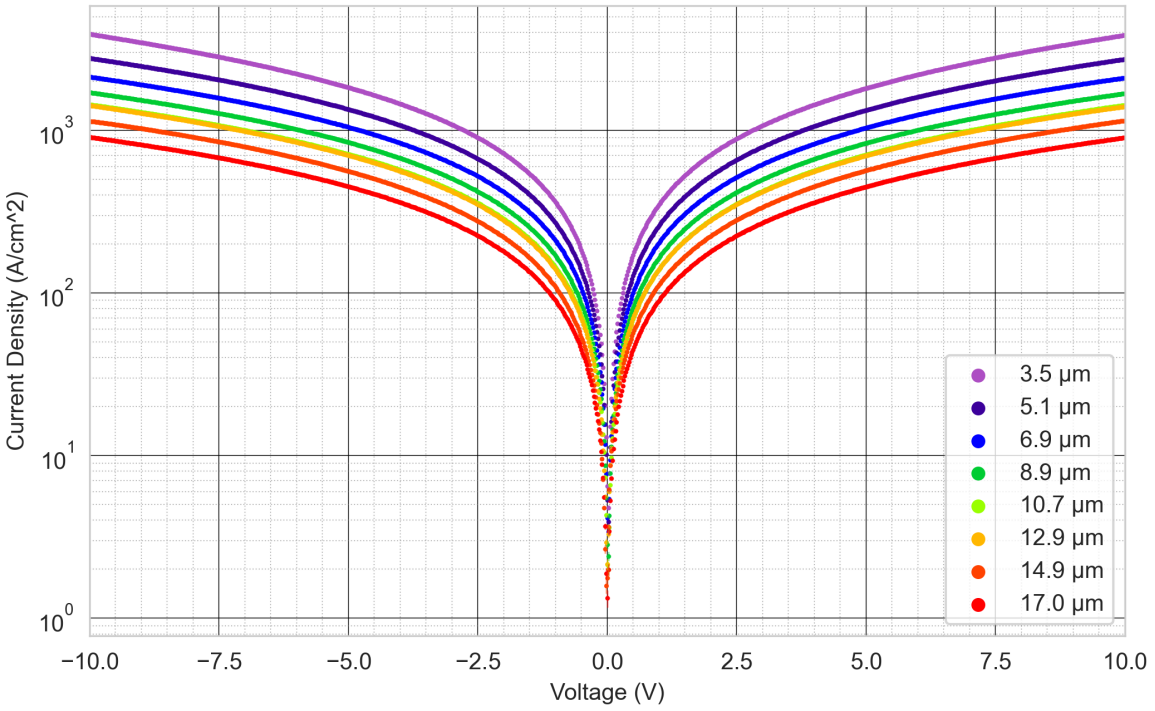

Figure 3.20 A log-linear plot of the measured current density against applied voltage for all channel lengths at 150°C (sample C).

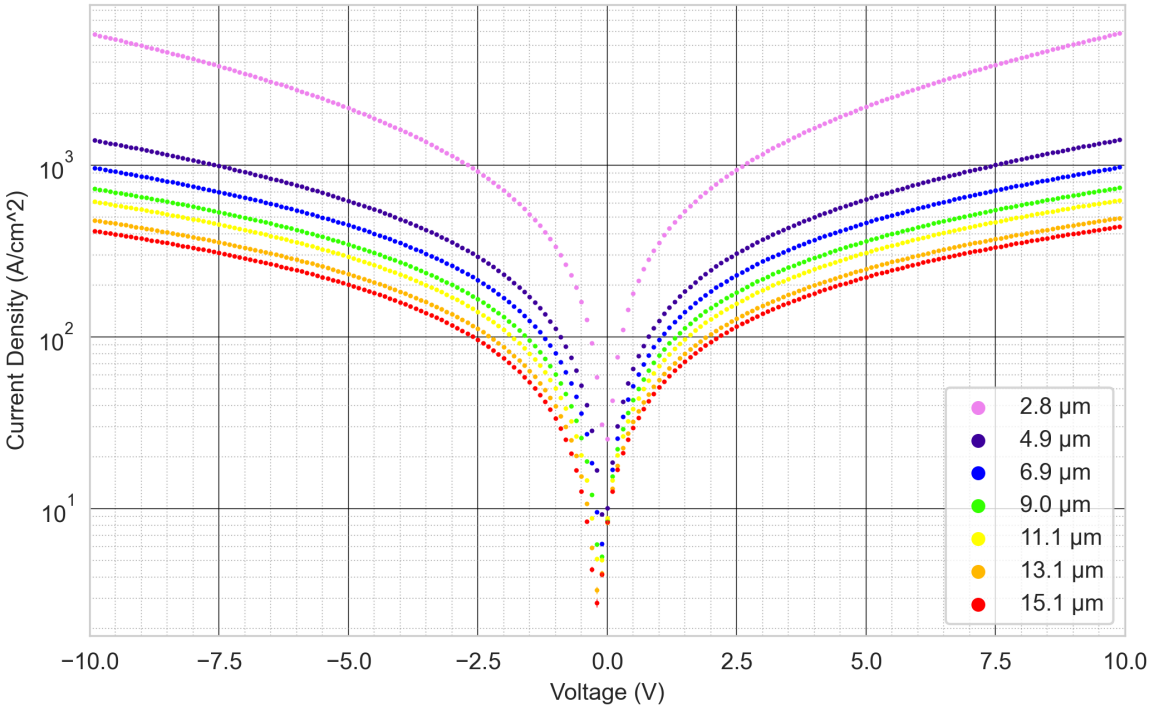

Figure 3.21 A log-linear plot of the measured current density against applied voltage for all channel lengths at 150°C (sample D).

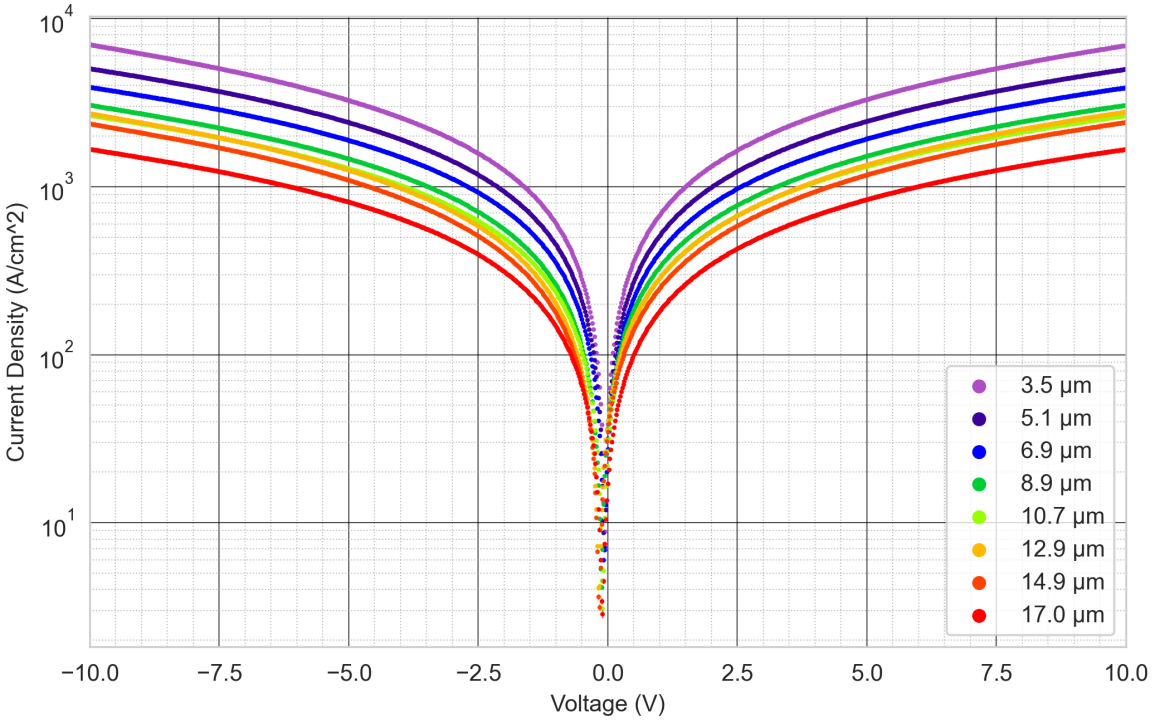

Figure 3.22 A log-linear plot of the measured current density against applied voltage for all channel lengths at 300°C (sample C).

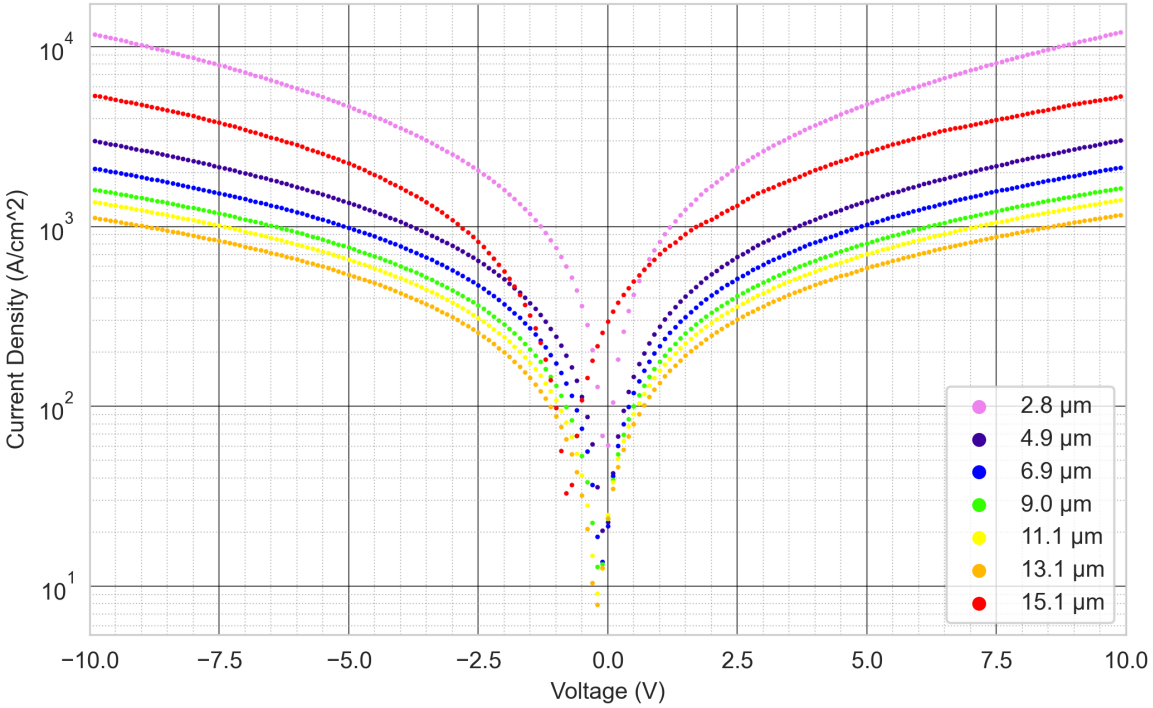

Figure 3.23 A log-linear plot of the measured current density against applied voltage for all channel lengths at 300°C (sample D).

3.4.2.1. Analysis of J-V Data

In figures 3.18–3.23, the measured current characteristics as converted into current density measurements are plotted. While most of these plots are quite natural given the prior IV figures, figure 3.23 in particular is noteworthy due to the off centre dataset for the largest channel size. During high-temperature testing of sample D, the electrical characteristics indicated a significant short in the system. Upon investigation, it was discovered that a large flake of the deposited metal had detached from the diamond surface and come into contact with one of the electrical probes during the test procedure. Consultations with Evince Technology indicated that poor adhesion may be a common problem when annealing times significantly exceed 30 minutes. Therefore, the electrical data presented here is that which was measured prior to the flake delamination. The off centre data of figure 3.23 indicates a large error in the system, which is highly likely to be the onset of issues due to delamination.

Otherwise, these current density plots show a few clear trends, such as sample D consistently showing higher current densities than sample C across the ±10 V range. Both samples generally show a clear dependence of the measured current density on the channel widths, indicating higher resistances for increased channel lengths, and the samples show a clear increase of measured current as a function of the temperature, indicating the reduction of resistance via ionisation of deep donors as predicted for phosphorous doped diamond. The same trends can be seen in the linear I-V plots from the previous section. The highest temperature ±50 V JV plot of sample D is included for a final comparison with the higher voltage region. Note that in all current density plots, error bars are plotted as calculated from the error on current measurements, previously described in section 3.4.1. They are most visible in the low voltage, low current density regions, and highlight the difficulty in interpreting very low voltages for these devices.

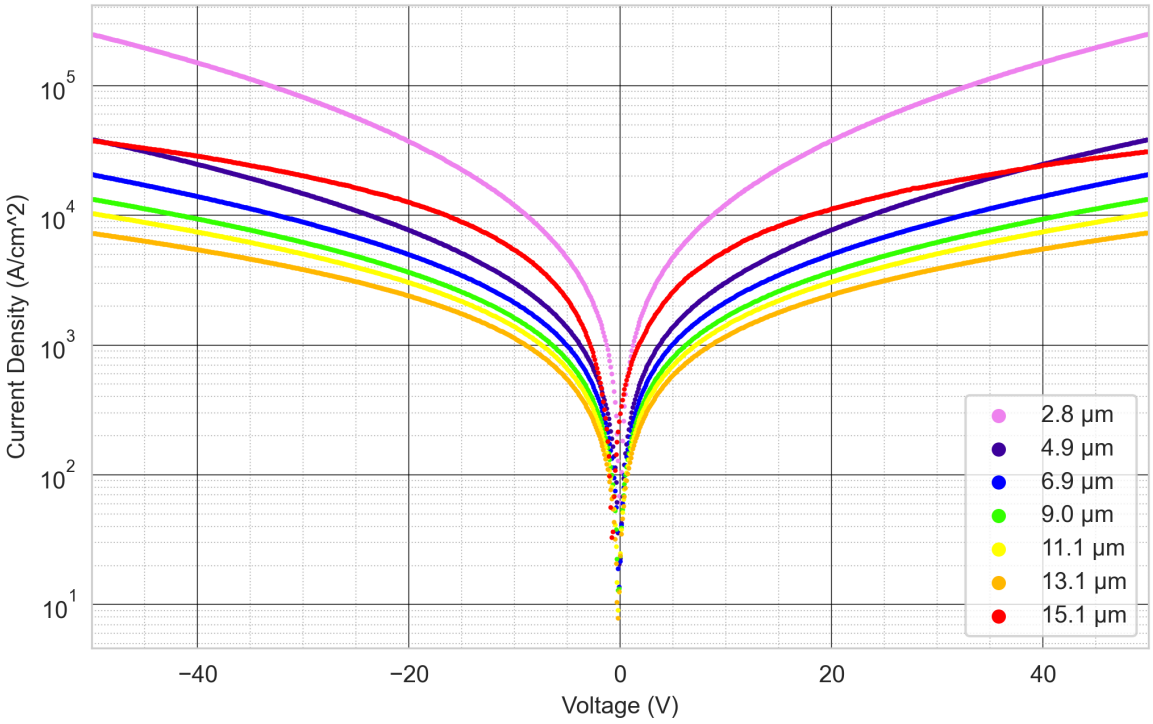

Figure 3.24 A log-linear plot of the measured current density against applied voltage for all channel lengths at 300°C (sample D).

Figure 3.24 shows this final comparison of J-V data for a ±50 V range. The slight offset in the highest channel length indicating a delamination error is difficult to pick out at this scale, with no other significant trends visible at the higher voltage range. Generally, this represents a double Schottky behaviour well.

3.4.3. Richardson Plots

The operating current for an ideal Schottky diode under a forward bias where $qV > 3kT$, based on the thermionic emission of electrons, is given by [67] as:

$$I = I_s \exp\{qV/nkT\}\,[1 - \exp\{-qV/kT\}] \tag{3.19}$$

Where I_s is the saturation current, q is the elementary charge, V is the applied voltage, n is the diode ideality factor, k is the Boltzmann constant and T is the temperature. In this ideal case, the carrier conduction in a forward bias is dominated by the thermal emission of carriers from the semiconductor over a spatially homogenous barrier into the metal. This equation can be rearranged into a format that allows for linear analysis:

$$\ln \frac{I}{1 - \exp\{(-\beta V)\}} = \frac{\beta V}{n} + \ln I_s \tag{3.20}$$

Here, $\beta = \frac{q}{kT}$. The saturation current I_s is given by:

$$\ln \frac{I_s}{AT^2} = -q\frac{\phi_{Beff}}{kT} + \ln A^*_{eff} \tag{3.21}$$

Where A^*_{eff} is the effective Richardson constant, A is the area of the Schottky contact and ϕ_{Beff} is the effective barrier height. The Richardson constant, A^*, which characterises the thermionic emission process, arises from the Richardson-Dushman equation for thermionic emission [67].

In practice, A can vary for different materials. For instance, in polycrystalline metals, A can range from about $32\,\mathrm{A\,cm^{-2}\,K^{-2}}$ to $160\,\mathrm{A\,cm^{-2}\,K^{-2}}$ and can vary even more widely for oxide and composite surfaces. The theoretical value of the Richardson constant is given by:

$$A^* = \frac{4\pi q k^2 m^*}{h^3} \tag{3.22}$$

where m^* is the effective electron mass and h is Planck's constant. The effective electron masses within phosphorous doped diamond are taken to be $m_\perp = 0.306 m_0$ and $m_\parallel = 1.81 m_0$, from Gheeraert et al. [18] who determined the masses via infrared absorption spectroscopy of phosphorous doped films. For further discussion on the background of the effective electron masses in phosphorous doped diamond, see section 2.2.7.1.

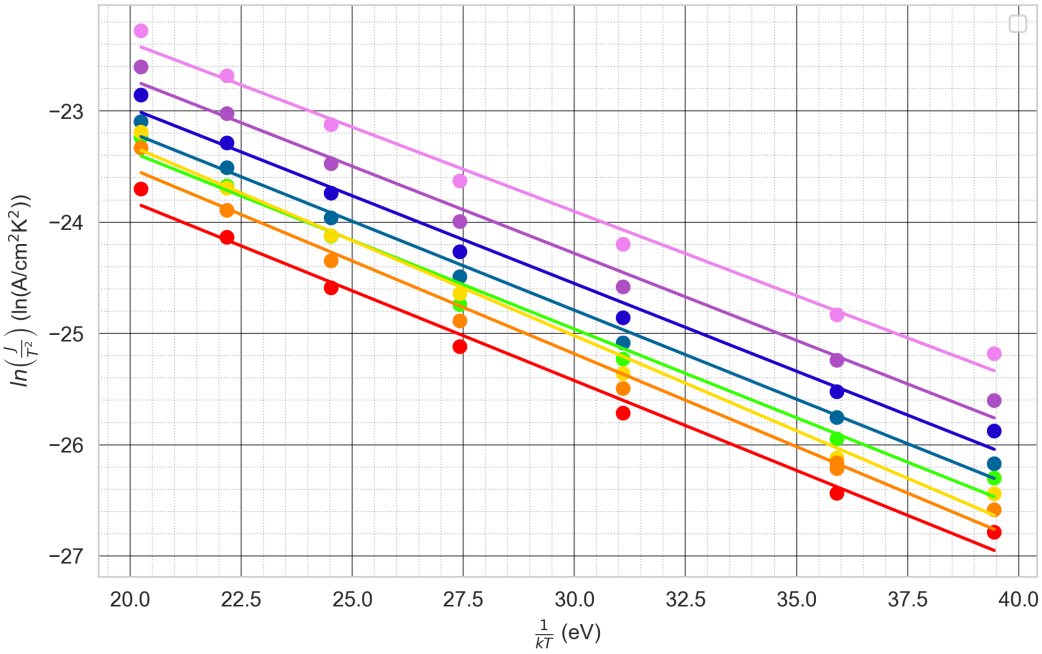

Figure 3.25 A conventional Richardson plot for the various channel widths tested (Sample C, 10V range).

To examine the method of electron emission from the contacts, a conventional Richardson plot is shown in figures 3.25 and 3.26 for a constant bias range of ±10 V. By fitting a linear relationship to these data, as according to equation 3.20, the average Schottky barrier height for samples C and D is extracted to be 0.161 eV and 0.150 eV, with a standard deviation of 5.56 meV and 38.6 meV, respectively. The exact results determined from the best-fit linear lines are shown in tables 3.3 and 3.4.

Channel (µm)	Barrier (eV)	$A*_{eff}$ ($\mathrm{A\,cm^{-2}\,K^{-2}}$)	R^2
3.529	0.1515	3.92e-09	0.9888
5.064	0.1565	3.12e-09	0.9892
6.949	0.1576	2.46e-09	0.9884
8.947	0.1599	2.07e-09	0.9918
10.720	0.1595	1.73e-09	0.9865
12.890	0.1709	2.29e-09	0.9889
14.930	0.1669	1.73e-09	0.9876
16.970	0.1615	1.15e-09	0.9900

Table 3.3 Extracted parameters from the Richardson plot for sample C at 10 V.

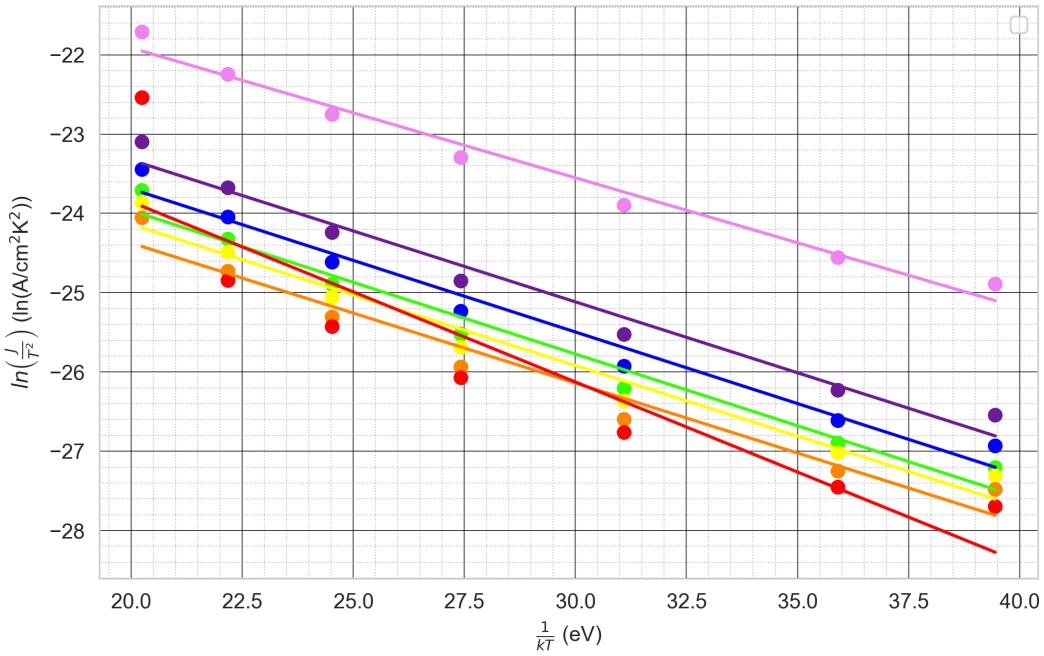

Figure 3.26 A conventional Richardson plot for the various channel widths tested (Sample D, 10 V range).

One observation from these data is that sample C displays a relatively constant barrier height, regardless of the channel length, while sample D shows a proportionality between the channel length and the effective barrier height. This could be due to the difference in the smallest channel sizes. While both sets of metal contacts were formed with the same shadow mask in the process of metal deposition via photolithography, the as formed contacts had a measurably different channel length at the smallest scales. The smallest channel measured by AFM in sample C was ~ 3.5 µm, while sample D had a channel length of ~ 2.8 µm. A visual comparison of the barrier heights extracted for both samples, over the full range of channel lengths and for differing potential biases in the case of sample D is provided in figure 3.28a. The channel length may have influenced the extracted barrier height due to factors such as metal edge roughness, which could locally modify the electric field, particularly in the smallest channels. This may introduce field-enhanced

Channel (µm)	Barrier (eV)	$A*_{eff}$ ($\mathrm{A\,cm^{-2}K^{-2}}$)	R^2
2.803	0.1639	8.08e-09	0.9799
4.862	0.1789	2.65e-09	0.9757
6.945	0.1806	1.90e-09	0.9739
9.029	0.1809	1.46e-09	0.9725
11.110	0.1780	1.16e-09	0.9679
13.150	0.1765	8.86e-10	0.9603
15.130	0.2272	4.11e-09	0.8324

Table 3.4 Extracted parameters from the Richardson plot for sample D at 10 V.

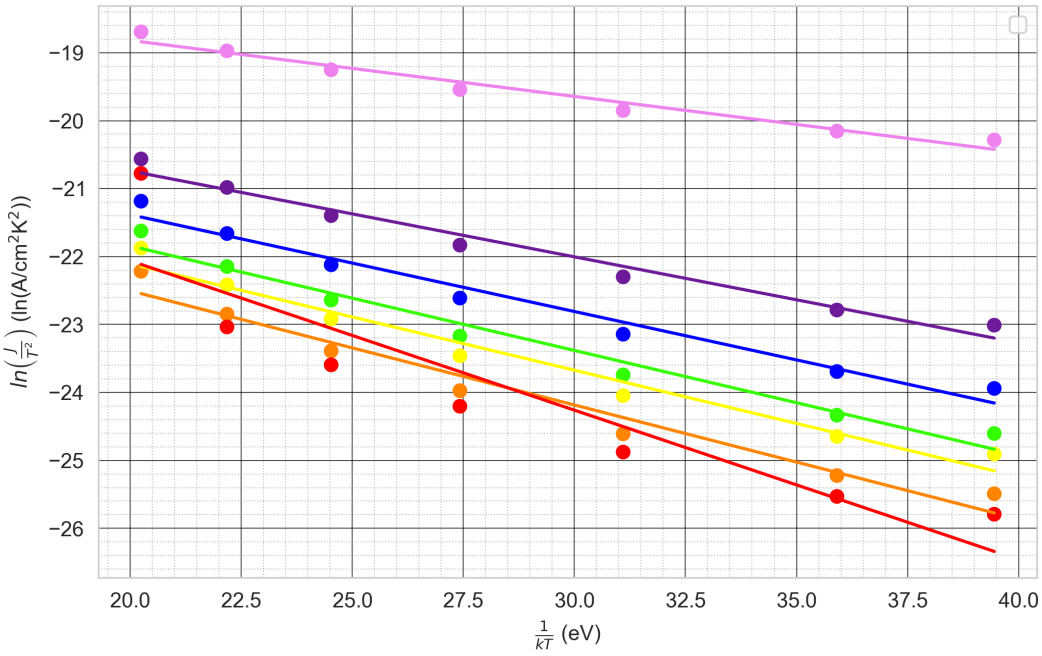

Figure 3.27 A conventional Richardson plot for the various channel widths tested (Sample D, 50 V range).

emission effects, leading to deviations from the expected LTLM trends. Such effects would also manifest as variations in the extracted Richardson constant, suggesting additional transport mechanisms beyond simple thermionic emission [21, 49].

Further analysis is provided by figure 3.27 and table 3.5, in which the 50 V measurements as processed in a Richardson plot are summarised. The effective Schottky barrier height as observed in this case is significantly lower than for the 10 V measurements, reducing from ~ 0.150 eV to ~ 0.082 eV for the shortest channel spacing of ~ 2.8 µm. This is most likely due to image force barrier lowering of the Schottky contacts [58, 67]. This is also a natural consequence of equation 3.21, as the barrier height is dependent upon the measured current, but the derivation extends from the classical point charge derivation of image force effects for a metal contacting a semiconductor. Section 2.4.1 contains a further exploration of the image force effect and how this reduces the Schottky barrier to thermionic emission for differing electric field strengths.

Channel (µm)	Barrier (eV)	$A*_{eff}$ ($\mathrm{A\,cm^{-2}\,K^{-2}}$)	R^2
2.803	0.0824	3.49e-08	0.9670
4.862	0.1265	1.24e-08	0.9729
6.945	0.1425	8.95e-09	0.9731
9.029	0.1539	7.09e-09	0.9727
11.110	0.1567	5.77e-09	0.9710
13.150	0.1681	4.86e-09	0.9651
15.130	0.2200	2.14e-08	0.8304

Table 3.5 Extracted parameters from the Richardson plot for sample D at 50 V.

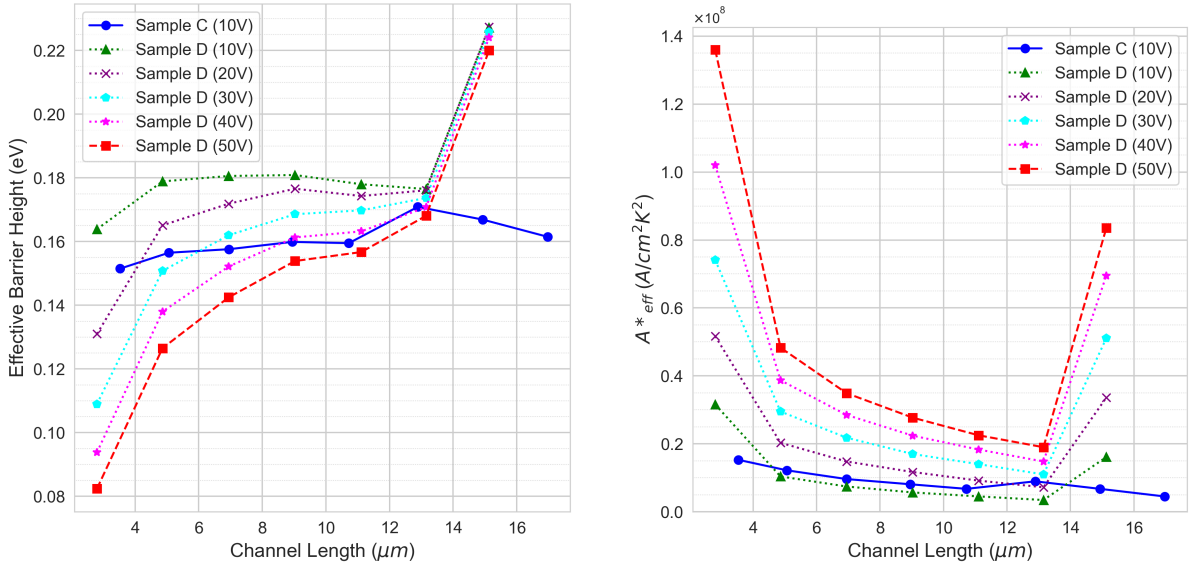

(a) The measured values for the barrier heights as a function of the linear TLM channel length.

(b) The measured values for the Richardson constant as a function of the linear TLM channel length.

Figure 3.28 (a) Effective barrier height vs. linear TLM channel length demonstrating that there are different observed barrier heights as a function of channel length, due to additional current transport effects. (b) Effective Richardson constant vs. linear TLM channel length, showing that the non-constant barrier height may be due to the addition of field-effect emission processes.

Additional complexity may be considered as a result of the "low-temperature" nature of the diamond in the temperature range studied here. This may introduce a temperature dependency for the barrier height, which can be written as [58]:

$$\phi_B(T) = \phi_B(0) - \xi T \tag{3.23}$$

where ξ is a proportionality constant. Given the good linear fits overall for the Richardson plots, this is not considered any further, but it remains as a possible complicating factor in these results.

The smallest channel of sample D at 50 V bias presents an effective barrier height of ~ 0.08 eV, while the largest channel was ~ 0.22 eV. Similarly, there is an inverse proportionality between the channel length and the observed Richardson constant for both samples, with sample C's Richardson constant consistently an order of magnitude lower

than sample D. This is represented visually in figure 3.28, as the relationship between the effective Richardson constant and the channel length for all data is quite complex.

3.4.4. TLM Results

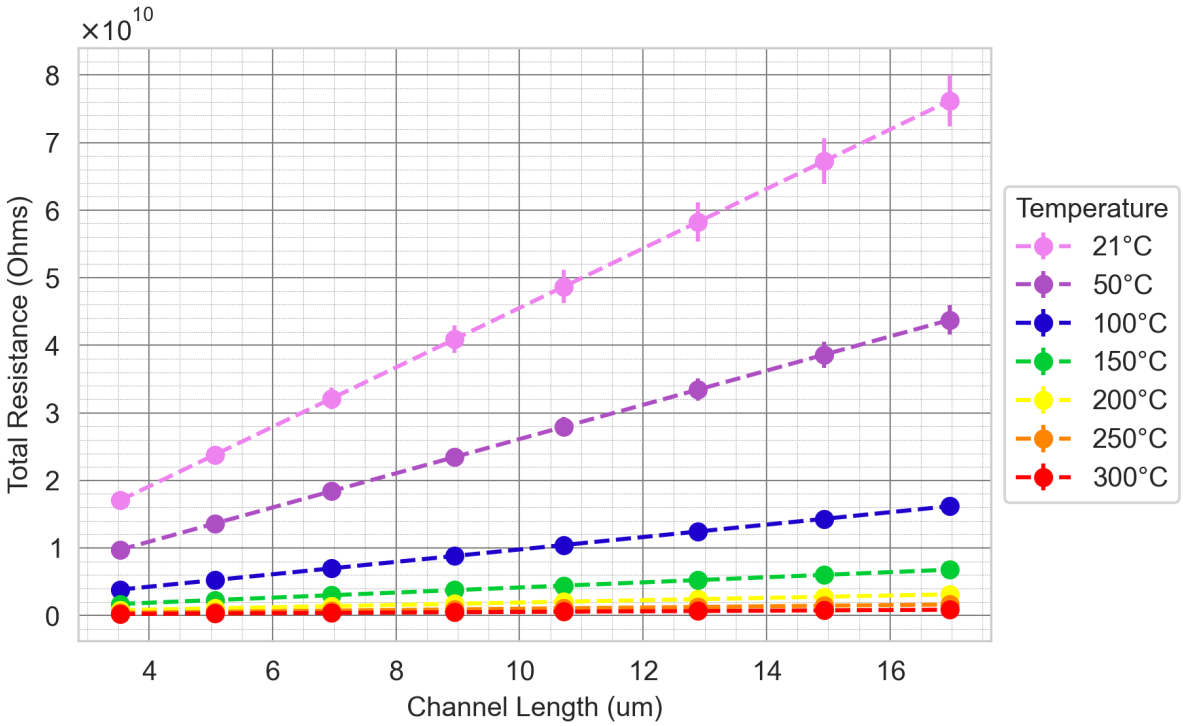

Figure 3.29 Sample C - the channel spacing vs measured total resistance for all temperatures (±10 V).

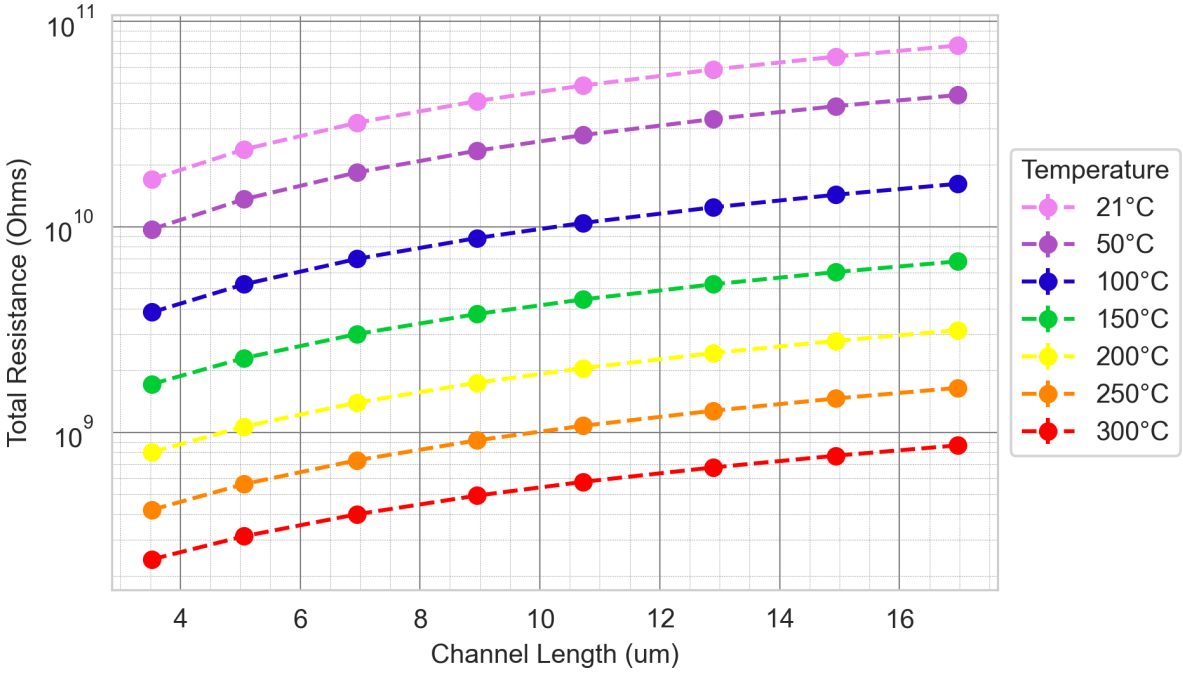

Figure 3.30 Sample C - the channel spacing vs log scale measured total resistance for all temperatures (±10 V).

T°C	R_{sh} ($\Omega/\square$)	ρ_s ($\Omega \cdot cm$)	ρ_c ($\Omega \cdot cm^2$)	R^2
21	$1.10 \times 10^{+12}$	$1.32 \times 10^{+08}$	$4.72 \times 10^{+05}$	9.95×10^{-01}
50	$6.33 \times 10^{+11}$	$7.60 \times 10^{+07}$	$2.51 \times 10^{+05}$	9.93×10^{-01}
100	$2.30 \times 10^{+11}$	$2.76 \times 10^{+07}$	$1.88 \times 10^{+05}$	9.91×10^{-01}
150	$9.44 \times 10^{+10}$	$1.13 \times 10^{+07}$	$1.21 \times 10^{+05}$	9.49×10^{-01}
200	$4.35 \times 10^{+10}$	$5.22 \times 10^{+06}$	$5.81 \times 10^{+04}$	9.64×10^{-01}
250	$2.28 \times 10^{+10}$	$2.74 \times 10^{+06}$	$3.06 \times 10^{+04}$	9.69×10^{-01}
300	$1.16 \times 10^{+10}$	$1.39 \times 10^{+06}$	$2.43 \times 10^{+04}$	9.28×10^{-01}

Table 3.6 The summarised extracted parameters via LTLM on sample C for a 10 V range.

Table 7.2 presents the summary of LTLM analysis for sample C. At room temperature, a specific contact resistivity of 472 kΩcm^2 is observed, reducing to 24.3 kΩcm^2 at 300°C. This is paired with a phosphorous doped diamond resistivity ranging from 132 MΩcm to 1.39 MΩcm.

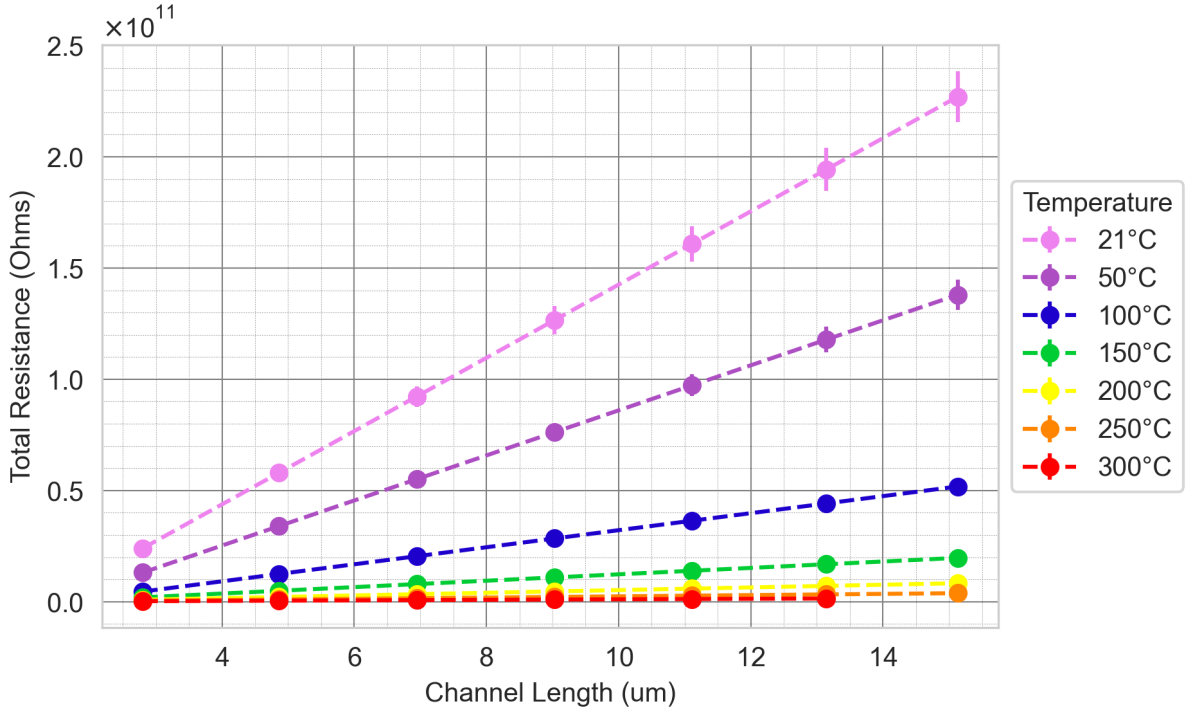

Figure 3.31 Sample D - the channel spacing vs measured total resistance for all temperatures (±10 V).

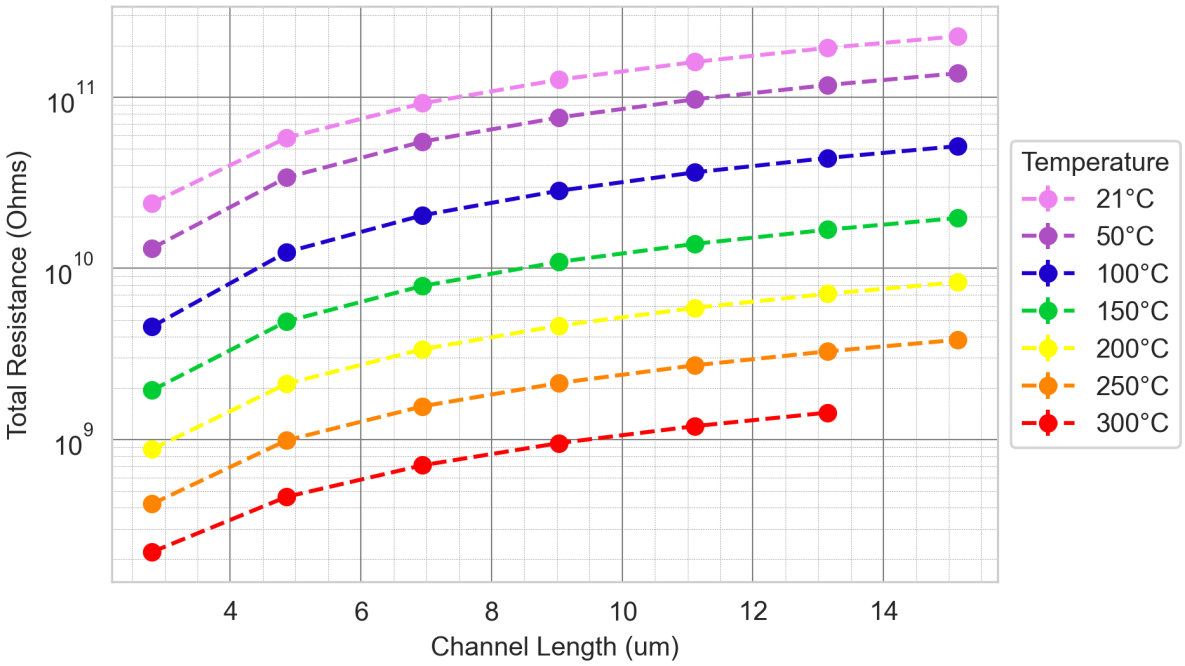

Figure 3.32 Sample D - the channel spacing vs log scale measured total resistance for all temperatures (±10 V).

T°C	R_{sh} ($\Omega/\square$)	ρ_s ($\Omega \cdot cm$)	ρ_c ($\Omega \cdot cm^2$)	R^2
21	$4.12 \times 10^{+12}$	$4.94 \times 10^{+08}$	$6.91 \times 10^{+06}$	9.84×10^{-01}
50	$2.53 \times 10^{+12}$	$3.04 \times 10^{+08}$	$4.77 \times 10^{+06}$	9.89×10^{-01}
100	$9.58 \times 10^{+11}$	$1.15 \times 10^{+08}$	$1.93 \times 10^{+06}$	9.93×10^{-01}
150	$3.60 \times 10^{+11}$	$4.32 \times 10^{+07}$	$6.55 \times 10^{+05}$	9.92×10^{-01}
200	$1.50 \times 10^{+11}$	$1.81 \times 10^{+07}$	$2.53 \times 10^{+05}$	9.92×10^{-01}
250	$6.90 \times 10^{+10}$	$8.28 \times 10^{+06}$	$1.10 \times 10^{+05}$	9.93×10^{-01}
300	$2.94 \times 10^{+10}$	$3.53 \times 10^{+06}$	$3.42 \times 10^{+04}$	9.84×10^{-01}

Table 3.7 The summarised extracted parameters via LTLM on sample D for a 10 V range.

Table 7.3 presents the summary of LTLM analysis for sample D. At room temperature, a specific contact resistivity of 6910 $k\Omega cm^2$ is observed, reducing to 34.0 $k\Omega cm^2$ at 300°C. This is paired with a phosphorous doped diamond resistivity ranging from 132 $M\Omega cm$ to 1.39 $M\Omega cm$.

3.4.5. XPS Analysis

Further to the SIMS analysis of films grown for one hour, X-Ray Photo-electron Spectroscopy (XPS) measurements were performed on a sample that had been used for a four hour deposition of highly phosphorous doped material. This is sample E in table 7.1. An additional sample included in this batch of doped diamond growth was then used for circular-TLM measurements, to compare highly phosphorous doped diamond films grown in as close to identical conditions as possible. The growth duration was chosen to be 4 hours based on the previous observation via SIMS of a growth rate of 0.3 $\mu m h^{-1}$,

with the aim being the production of a ~ 1 µm thick surface layer. This would ensure that any conduction measured through the phosphorous doped diamond film would be comparable to other work in this area, with conduction through a doped layer on the scale of hundreds of nanometres, implying a bulk conduction process rather than any surface transfer doping [10, 48]. Note, that for all data presented here, the XPS data comes from just below the sample surface. This is due to an original planned experiment of depth profiling, hence ion beam bombardment was used to etch away the diamond surface and attempt to etch through the phosphorus doped surface layer. However, it was observed that despite a predicted depth of 3 µm being reached, no change in the XPS spectra was observed beyond the initial change from surface characterisation and then the cleaned, sub surface characterisation. This was backed up by AFM and attempts to resolve the depth of the etched region via optical profilometry failing to measure any etched region in the diamond surface. Hence, the sub-surface spectra are presented without depth profiling attempted, with the observation from additional characterisation that the "sub-surface" spectra may only represent a clean diamond surface spectra.

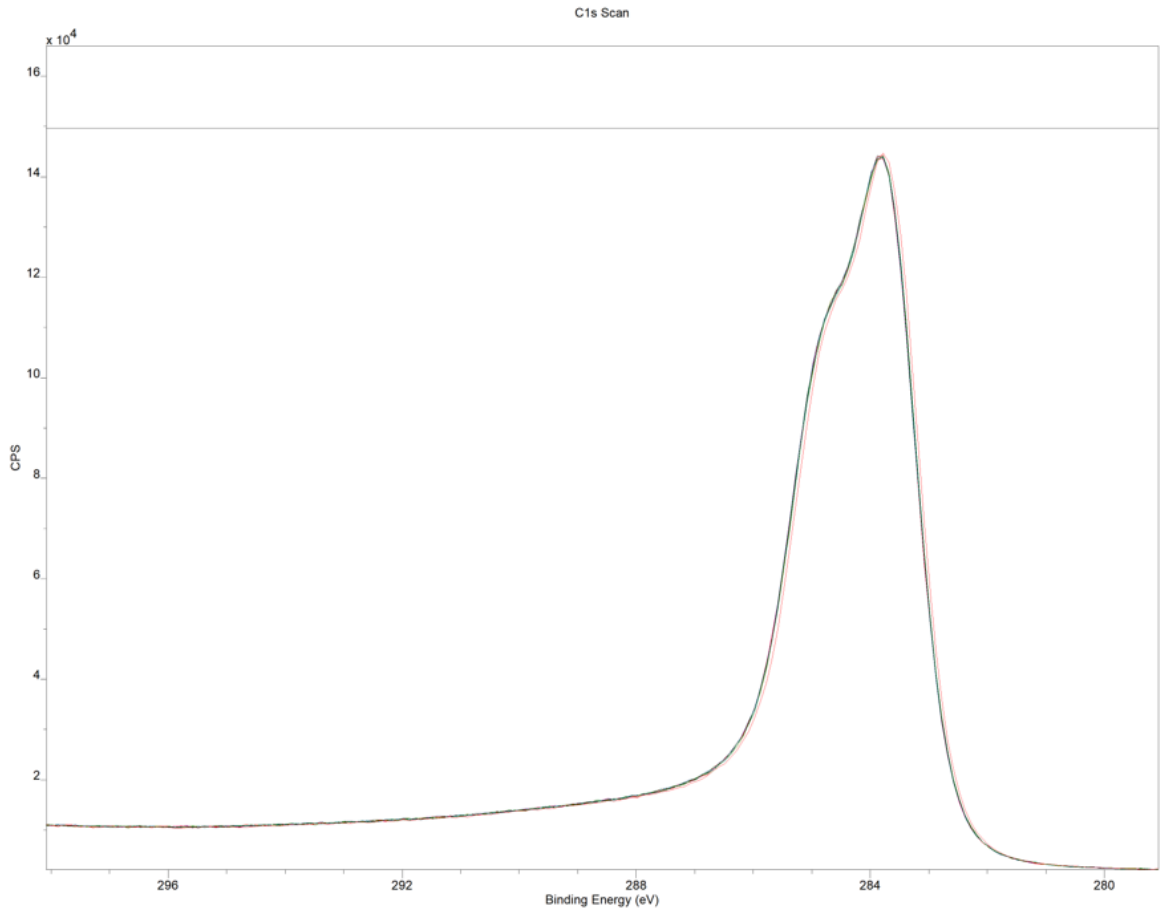

Figure 3.33 XPS - The C1s scan range.

In figure 3.33, the XPS data taken for the theoretical C1s peak region are shown. Note that the counts per second (CPS) for the peak closely correlating with the sp^3 C1s 284.8 eV peak [16] is at around 14×10^4 CPS. The slight side peak visible can be decomposed to

reveal that it is centred very closely to the sp^2 binding energy of 284.2 eV, indicating a significant degree of amorphous carbon in the phosphorous doped diamond surface layer [16].

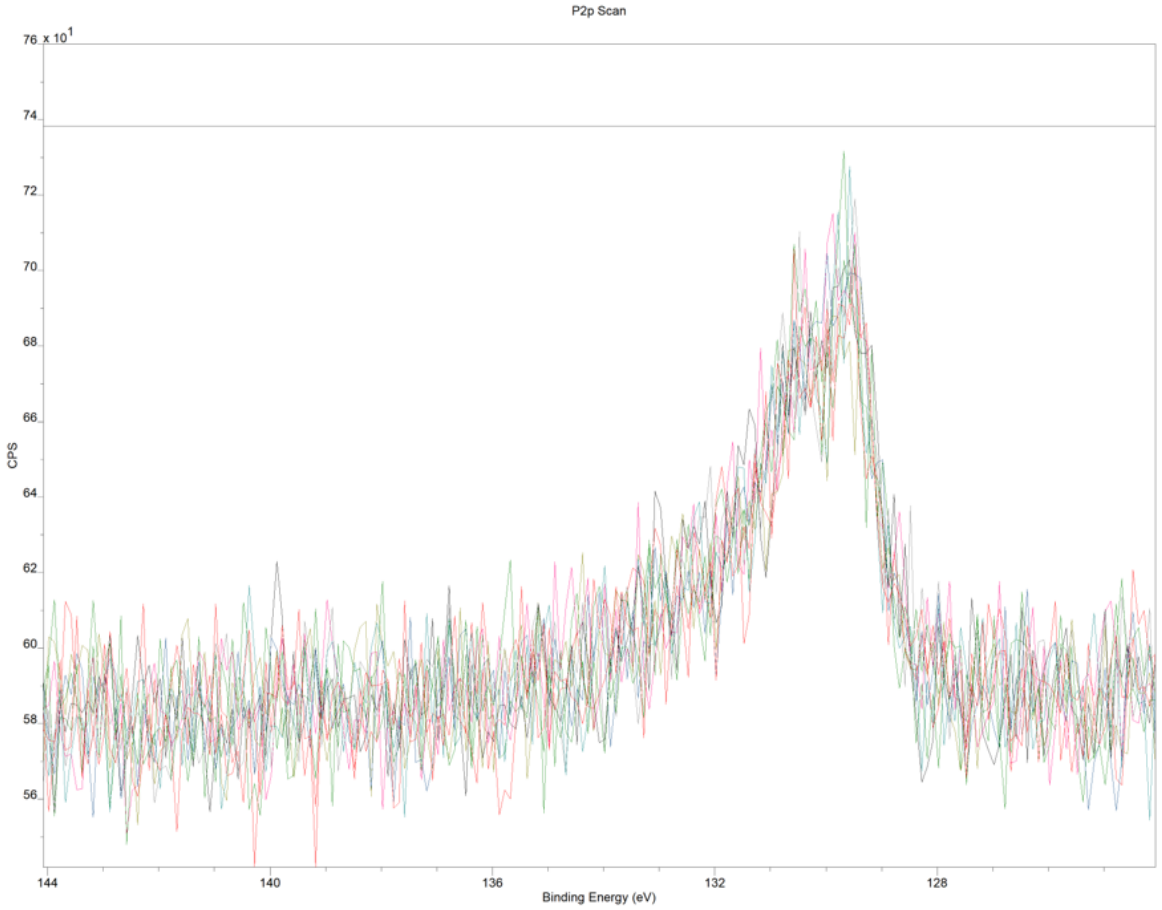

Figure 3.34 XPS - The P2p scan range.

Figure 3.34 shows the XPS data taken for the binding energy region corresponding to the C-P bond of 132.6 eV and the P-O bond of 133.6 eV [79]. While these data are difficult to decompose, the order of magnitude for CPS due to phosphorous bonds can be read as approximately 680 CPS. As the scale of CPS with these datasets is calibrated prior to the measurements being taken, these CPS measurements can be taken as a relative scale of carbon to phosphorous atomic concentrations. There is a factor of 200 difference between the P2p peak shown here and the C1s peak observed in figure 3.33. Hence, it is observed that there is approximately a concentration of 0.5% phosphorous within the crystal lattice. Given the density of carbon atoms within the crystal lattice is 1.76×10^{23} at cm^{-3}, it is estimated that there is a phosphorous concentration of up to 8.8×10^{20} at cm^{-3} in the surface of this sample. This can be interpreted as an upper bound estimate. Comparison of the integrated areas below the peaks indicates that the true estimate based on this data is closer to 1.4×10^{20} at cm^{-3}, which is very similar to that observed via SIMS analysis on a different sample.

3.5. Circular Transfer Length Method (CTLM)

3.5.1. CTLM Theory

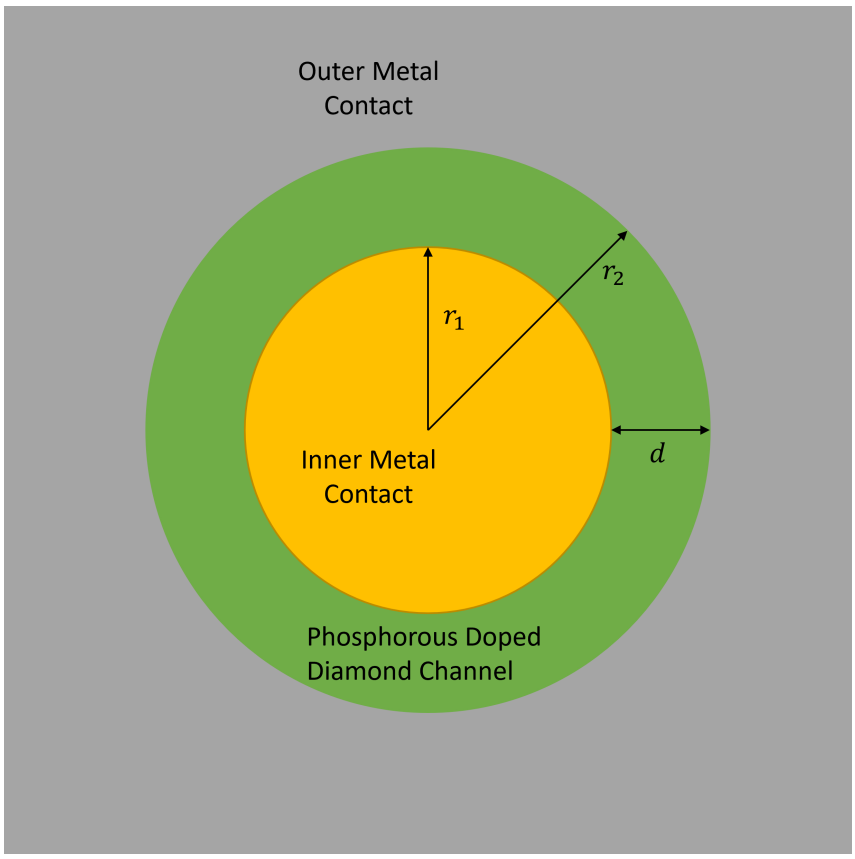

Figure 3.35 The CTLM structure as used in this work.

Generally, given equal sheet resistivities under the metal contacts and within the channel spacing, total resistance in CTLM is given by [3]:

$$R_T = \frac{R_{sh}}{2\pi}\left[\frac{L_T}{L}\frac{I_0\left(\frac{L}{L_T}\right)}{I_1\left(\frac{L}{L_T}\right)} + \frac{L_T}{L+d}\frac{K_0\left(\frac{L}{L_T}\right)}{K_1\left(\frac{L}{L_T}\right)} + \ln\left(1+\frac{d}{L}\right)\right] \tag{3.24}$$

where R_s is the sheet resistance of the semiconductor layer and L_T is the transfer length (discussed in section 2.1.3.1), I and K are used in this case to denote the modified Bessel functions of the first order [55, 47]. Also note that in this equation, the radius of the central contact is denoted as L for consistency with source literature, rather than r, as will be used later. When the radius $L >> d$, the Bessel function ratios of $\frac{I_0}{I_1}$ and $\frac{K_0}{K_1}$ tend to unity and R_T takes the form [58]:

$$R_T = \frac{R_{sh}}{2\pi}\left[\frac{L_T}{L} + \frac{L_T}{L+d} + \ln\left(1+\frac{d}{L}\right)\right] \tag{3.25}$$

Then, given sufficient sizes of circular contacts such that $L >> d$, this equation is further simplified into:

$$R_T = \frac{R_{sh}}{2\pi L}(d+2L_T)C \tag{3.26}$$

where C is a correction factor introduced to account for non-linearity at increasing channel spacings in the resulting R_T vs d plotting [9], defined as:

$$C = \frac{L}{d}\ln\left(1+\frac{d}{L}\right) \tag{3.27}$$

However, instead of assuming $L >> d$, as this is rarely the case for small contact geometries, the correction factor can instead be incorporated directly into the general equation. While original circular methods used a constant outer radius and variable inner radius [58, 35], usage of a constant sum of inner $L = r_1$ and outer $(L+d) = r_2$ radii can be used to rewrite the general form of R_T.

$$R_T = \frac{R_{sh}}{2\pi}\left(L_T\left(\frac{1}{r_1}+\frac{1}{r_2}\right)+\ln\frac{r_2}{r_1}\right) \tag{3.28}$$

As noted in previous work by Kato et al. [31, 30], this can hence be rearranged to form a direct linear function of total resistance. This is done by considering the definition of transfer length $L_T = \sqrt{\frac{\rho_c}{R_{sh}}}$. When the inner and outer electrode radii $r_1 + r_2$ are constant, depicted by figure 3.35, the inner radius can be written as:

$$r_1 = r_0 - \frac{d}{2} \tag{3.29}$$

and the outer radius similarly is given by:

$$r_2 = r_0 + \frac{d}{2} \tag{3.30}$$

allowing for the total resistance R_T between circular electrodes to follow a linear relationship to the spacing (d) of said electrodes:

$$d = r_2 - r_1 \tag{3.31}$$

With these definitions, the general equation is rewritten as:

$$R_T = \frac{R_{sh}}{2\pi}\left(L_T\left(\frac{1}{r_0-\frac{d}{2}}+\frac{1}{r_0+\frac{d}{2}}\right)+\ln\frac{r_2}{r_1}\right) \tag{3.32}$$

this is rearranged and uses a Taylor series expansion to obtain the approximation:

$$R_T \approx \frac{R_{sh}}{2\pi r_0}(2L_T + d) \tag{3.33}$$

which can also be written in the linear slope-intercept form $y = mx + c$:

$$R_T = \frac{R_{sh}}{2\pi r_0}d + \frac{L_T R_s}{\pi r_0} \tag{3.34}$$

allowing for the linear fitting of measured R_T for different spacings d to extract the gradient of $m = \frac{R_{sh}}{2\pi r_0}$ and intercept of $c = \frac{L_T R_s}{\pi r_0}$. By utilising the relationship of transfer

length to specific contact resistivity and sheet resistance it can then be derived that the specific contact resistivity is given by:

$$\rho_c = \frac{c^2 \pi r_0}{2m} \tag{3.35}$$

Hence, by using the geometry constant r_0, it is possible to use a linear plot of R_T against channel spacing d to derive the sheet resistance and specific contact resistivity. There are several advantages to this methodology over LTLM in the case of phosphorous-doped diamond. First and foremost is the primary motivation for circular TLM structures: the removal of the error caused by current flow around the contact edges in cases where the LTLM contacts are not as wide as the substrate surface itself. In the absence of isolation (e.g., mesa etching), this error is exacerbated as current can flow around the contacts rather than through the intended channel. This error is further increased as ρ_c decreases or R_{sh} increases [45].

One of the key advantages of CTLM theory over LTLM is that of simplicity in fabrication. LTLM structures rely primarily upon etching of material to form "mesa steps," which then prevent the leakage of current around the channel formed between adjacent contacts. While this has been performed for diamond characterisation via inductively coupled plasma etching (ICP) [13], it is also common practice to instead rely upon alternative geometric structures, such as circular contacts, which do not allow for leakage current to flow around the specified channels. With two concentric rings as electrical contacts, the channel length between any two nearest points of the contacts remains that of the intended channel length, with no fringe effect paths available.

Spacing $d = r_2 - r_1$ µm	$r_2 + r_1$ µm	r_2 µm	r_1 µm
2	100	51	49
4	100	52	48
6	100	53	47
8	100	54	46
10	100	55	45
12	100	56	44
14	100	57	43
16	100	58	42
18	100	59	41

Table 3.8 Design of CTLM

3.5.2. Double Schottky CTLM

Further to the general CTLM theory, special consideration must also be given to the double Schottky nature of these contacts, due to the Fermi-level pinning of metal contacts on the diamond surface. This phenomenon occurs because the Fermi level of the metal

aligns with a fixed energy level in the diamond, creating a Schottky barrier regardless of the metal's work function. As discussed further in section 3.5.4.4, this maintains a Schottky barrier despite careful selection of metal work functions and carbide formation via annealing. In many early publications which examine this topic in the case of phosphorous doped diamond and the formation of metal contact to such substrates, the voltage ranges examined are large enough to significantly reduce the impact of this barrier on a typical IV plot. It is only in the lower voltage ranges, where the specific contact resistivity is a significant parasitic power draw, that these Fermi-level pinned Schottky barriers produce a large effect.

When the resulting double Schottky structure is applied to CTLM theory, the contact resistance R_c includes a nonlinear term R_N and the conventional linear term of R_L. This can also be expressed as the nonlinear voltage V_N. Expressed as a function V of the current I:

$$V(I) = R_C I + R_{bulk} I = R_L I + V_N(I) + V_N(-I) + R_{bulk} I \tag{3.36}$$

where $R_{bulk} = R_{sh} \frac{d}{2\pi r_0}$ is the bulk resistance of the doped semiconductor layer (representing the resistance of the diamond substrate itself) and the term $R_L = R_{sh} \frac{2L_L}{2\pi r_0}$ with L_L coming from the linear contribution to the transfer length. The transfer length L_L represents the distance over which the current transitions from the metal contact to the semiconductor. The expressions of $V_N(I)$ or $V_N(-I)$ give the voltage applied to both the forward and reverse side interfaces respectively. Under a low bias, both the forward and reverse currents will be limited by that of the Schottky barriers. With heavy doping, a reverse current will flow even in the low voltage range, as well as a forward current. This is due to the tunneling effect, which becomes significant in heavily doped semiconductors. The IV characteristics of a TLM experiment can then be measured as a function of d with:

$$V(I,d) = \frac{2L_L R_{sh} I}{2\pi r_0} + V_N(I) + V_N(-I) + \frac{R_{sh} d}{2\pi r_0} I \tag{3.37}$$

To include the nonlinear terms such as $V_N(I)$, a constant current I_0 condition can be used to separate the bulk resistance and contact resistance. This approach simplifies the analysis by fixing the current and observing the voltage response. Hence, the contact voltage as defined by the first three terms in equation 3.37, can be specified as independent of the spacing d. The total resistance as a function of constant current ($I = I_0$) and spacing is then defined thusly:

$$R_T(I_0,d) = \frac{V(I_0,d)}{I_0} = \frac{2L_L R_{sh}}{2\pi r_0} + \frac{V_N(I_0) + V_N(-I_0)}{I_0} + \frac{R_{sh} d}{2\pi r_0} \tag{3.38}$$

From this equation, plotting the total resistance as a function of d for specific I_0 will reveal the contact resistance $R_{L+N}(I_0)$ and transfer length L_{L+N}, including linear and nonlinear parts, from the slope and the d-intercept respectively. The slope of the plot corresponds to the bulk resistance, while the intercept provides information about the

contact resistance. This is also expressed as:

$$R_{L+N}(I_0) = \frac{2L_L}{R_{sh}2\pi r_0} + \frac{V_N(I_0) + V_N(-I_0)}{I_0} \tag{3.39}$$

$$2L_{L+N} = \frac{2\pi r_0 R_{L+N}(I_0)}{R_{sh}} \tag{3.40}$$

which can then be related in the general TLM formula to the specific contact resistivity:

$$\rho_c(I_0) = R_{sh}L_{L+N}^2 \tag{3.41}$$

where the voltage V_C applied to both electrodes of the TLM structure can be described similarly as a function of I_0:

$$V_C(I_0) = R_{L+N}(I_0)I_0 \tag{3.42}$$

Generally, it is possible to ignore the nonlinear terms of $V_N(I)$ and $V_N(-I)$ as they are significantly smaller than the linear term $V_L = R_L I$ for ohmic contacts to standard semiconductors. However, in the case of phosphorous doped diamond with Fermi-level pinned Schottky barriers present for both electrodes in the TLM structure, the Schottky (non-linear) terms cannot be ignored. This is because the Schottky barriers dominate the current-voltage characteristics at low voltages, making the nonlinear terms critical for accurate analysis.

3.5.3. Ti/Au Contacts

(Sample F from table 7.1 - for reference.) In this study, Titanium/Gold (Ti/Au) CTLM contacts were fabricated by the candidate to allow for more direct comparison of these contacts with that of the literature quoted values. The substrate used for the experiment was a mechanically polished, high-pressure high-temperature (HPHT) diamond sample similar to that used for the LTLM contacts, with an orientation of 111 and dimensions of approximately 2 mm in width/length and 0.5 mm in depth. A homoepitaxial heavily phosphorous doped layer was grown on this substrate with the same recipe as for the two previous TLM samples (C and D), however the growth duration was increased to 4 hours, allowing for a thicker surface layer of approximately 1.2 µm to be grown. Samples E and G were also included in this same growth phase, and sample E was previously used in XPS measurements to confirm that despite the longer growth time, the surface layer maintained the previously established concentration of phosphorous at around $1 \times 10^{20}\text{cm}^{-3}$.

The Ti/Au contacts were structured in a circular Transfer Length Method (TLM) configuration as previously outlined. Standard photolithography was performed, with e-beam deposition of 30 nm/100 nm Ti/Au followed by a lift off process using N-Methyl-2-pyrrolidone. All lithography in this work was performed by the candidate at Newcastle University. The resulting structure is shown in figure 3.36. The full lithography mask was designed to replicate the pattern used in [30] and [46], with channel spacings in

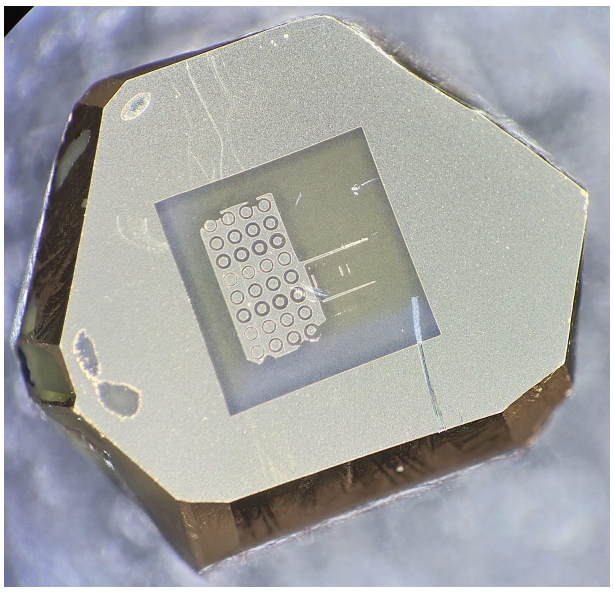

Figure 3.36 Sample F, as seen under a wide-field optical microscope following photolithography.

the range of 2–18 µm. Additional contacts were intended to be present for Hall-effect measurements, however significant edge bead issues with the photolithography process resulted in a sub-optimal resulting metal pattern. This also resulted in an overall lower resolution of effective feature sizes, with the smallest channel spacing (of the contacts that were suitably circular, with minimal defects) observed to be approximately 13 µm, rather than the intended 2 µm. Hence, the experimental range of channel lengths was between 13–30 µm as measured via AFM characterisation as detailed in the following sections, for channels that were visually observed via optical microscopy to be of high quality relative to the contacts available for usage. This was determined primarily upon the circularity of the contacts, with contacts that had significant sharp edges determined to be difficult to use in a CTLM experiment. Following preliminary electrical measurements, the contacts were annealed at a temperature of 500 degrees Celsius in high vacuum for 10 minutes. This annealing temperature was selected based on a review of the literature, with temperatures both above and below 500 °C being a common choice for annealing Ti/Au contacts. Please see section (come back here, theory section on annealing) for more information on annealing conditions.

Of crucial importance for CTLM methodology is the exact determination of channel length, and the sum of radii. To examine these quantities as patterned on sample F, AFM characterisation was performed by the candidate, at Newcastle University.

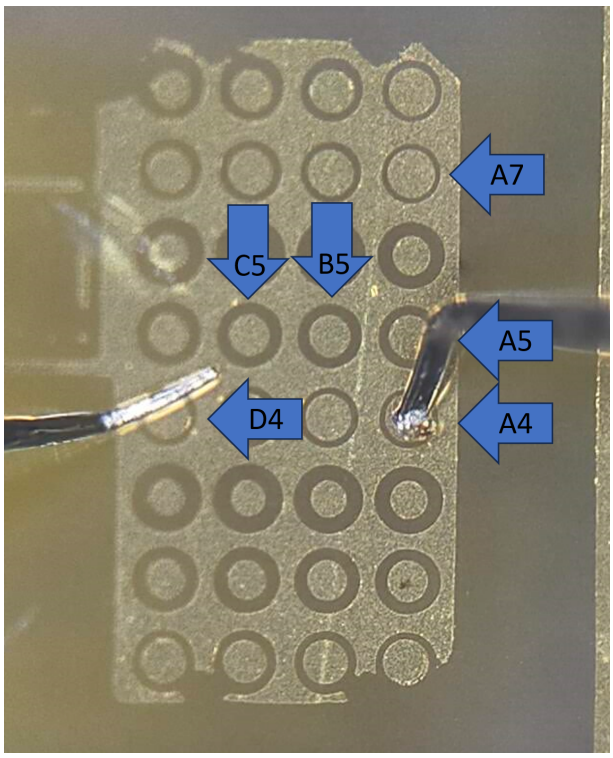

Figure 3.37 The circular contacts used in electrical characterisation on sample F, as seen under an optical microscope during pre-annealing testing.

Figure 3.37 provides a view of the circular contacts as seen during preliminary electrical characterisation. Contacts used for the following CTLM sections are labelled according to their relative grid positions. Six contacts in particular were chosen to provide a good range of channel spacings, with all six presenting a good circular inner contact geometry when examined via AFM, as shown in the following section of AFM imaging.

3.5.3.1. Annealing Temperature Selection and Rationale

In selecting the optimal annealing temperature for the formation of Ti/Au contacts on phosphorous-doped diamond, various studies were reviewed, each investigating different growth conditions, techniques, and parameters.

Author	Year	Temperature (°C)	Time	Atmosphere	Metals Used
Koizumi [38]	1997	600	5 min	Vacuum	Ti
Teraji [70]	2000	600	10 min	Vacuum	Ti/Au
Suzuki [66]	2004	700	10 min	N_2	Ti/Pt/Au
Kato [30]	2009	420	30 min	Ar	Ti/Pt/Au
Matsumoto [46]	2014	420	30 min	Ar	Ti/Pt/Au
Grotjohn [20]	2014	700	60 min	-	Ti/Pt/Au
Wang [74]	2022	420	10 min	Ar	Ti/Pt/Au
Valappil [73]	2023	450	15 min	Ar	Ti/Mo/Au

Table 3.9 Annealing Conditions for Various Studies

Table 3.9 provides a summary of the annealing conditions used for ohmic contact formation via the generation of a TiC interface for several relevant papers. Also, the two

LTLM samples of annealing conditions 850°C for 30 minutes and 600°C for 300 minutes must also be considered. Based on the delamination issues, and the lack of clear ohmic contacts with the high temperature LTLM devices, a slightly lower temperature of 500°C, along with a shorter annealing time of 10 minutes was chosen instead. This is still a higher temperature than a few of the literature examples, but it is otherwise quite comparable to the well established reange of annealing conditions for ohmic contacts.

3.5.3.2. AFM Scans of CTLM Channels

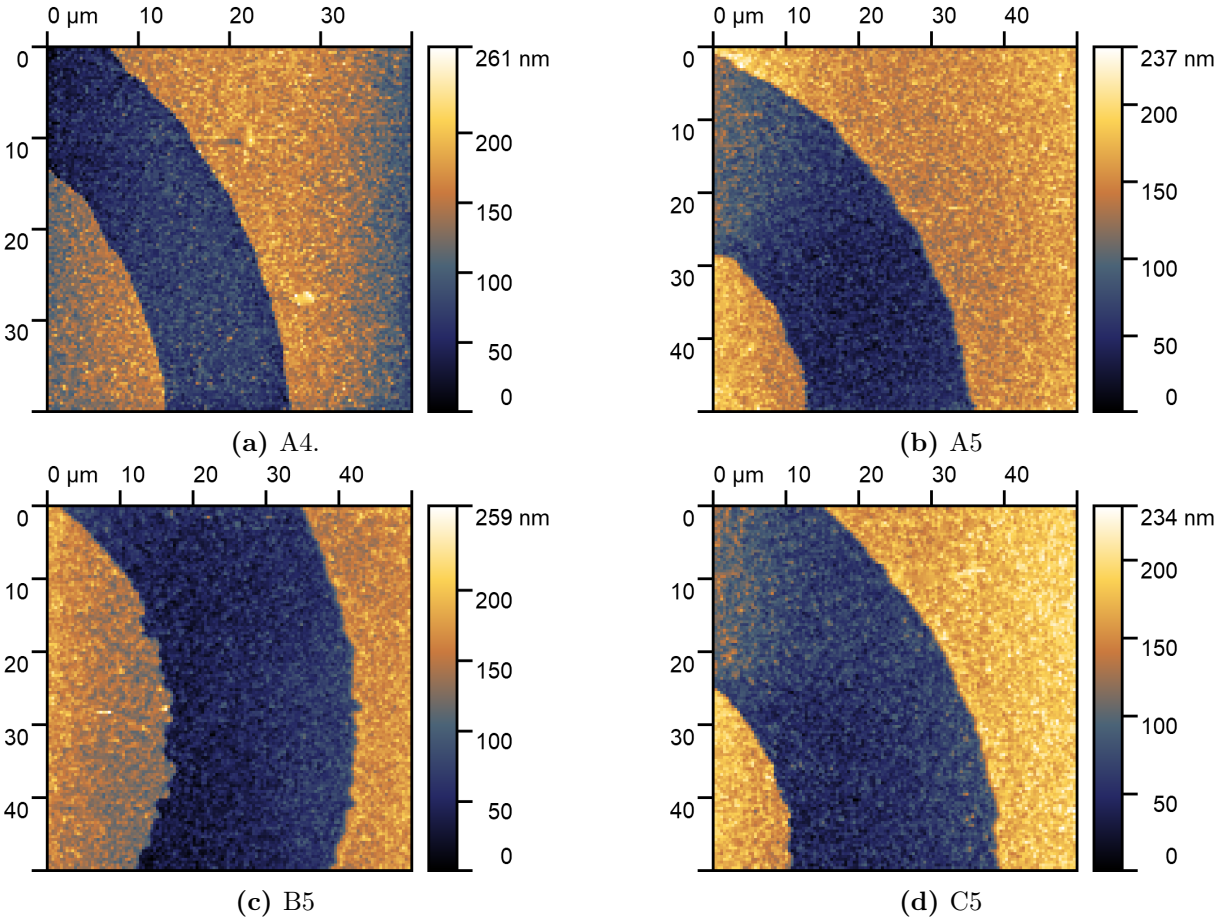

(a) A4. **(b)** A5

(c) B5 **(d)** C5

Figure 3.38 Post-anneal AFM scans of the channels marked as A4, A5, B5 and C5 in figure 3.37.

Figure 3.38 shows a collection of the AFM scans used to examine the viability of the CTLM structures and to determine the effective channel spacing. It was generally observed that the metal contacts formed smooth edges, with only a few notable examples of sharper defects, as in figure 3.38c. Due to the sharp points visible in AFM scans, the channel spacing was determined by averaging three differing lines across the channel.

Table 3.10 summarises the measured channel spacings, and compares them to the intended channel spacings. Three differing lines of measurement for the channel spacing are used, with standard deviation calculated. The standard deviation directly correlates with the smoothness of the contact edges, and hence reveals which contacts had more

Contact	d_1 µm	d_2 µm	d_3 µm	d_{int} µm	d_{avg} µm	σ_{d} µm
A7	13.3	13	13.3	2.0	13.2	0.10
A4	13.9	13.6	13.7	2.0	13.7	0.09
D4	20	19.9	19.7	6.0	19.9	0.09
A5	22.8	21.5	21.6	8.0	22.0	0.42
B5	25	24.5	23.8	10.0	24.4	0.35
C5	28.3	27.9	28.1	12.0	28.1	0.12

Table 3.10 AFM measurements of channel spacing compared to intended spacing.

irregularities. While the overall measured channel spacings are significantly larger than the intended channel spacings (d_{int}), there is still a suitable range of channels for CTLM plotting. Another concern was in the consistency of $r_1 + r_2$, which is a more difficult parameter to measure directly. In an attempt to characterise it based upon the AFM data collected, arc lengths were used to estimate r_1 and r_2, with the additional benefit of providing another measure of the channel spacing. AFM was chosen over scanning electron microscopy (SEM) for topological characterisation due to its superior ability to provide high-resolution, three-dimensional surface profiles, which are critical for accurately measuring channel spacing and contact edge smoothness [33]. While SEM offers excellent imaging capabilities, it is less suited for quantitative height measurements and surface roughness analysis, which are essential for this study.

3.5.3.3. Arc Length Channel Spacing

Due to the limited scan areas of typical AFM scans, the full diameter of the CTLM structures in question were not measured directly by AFM. Instead, sections that represent approximately a quarter of the circular channel were measured for all channels, as previously demonstrated in section 3.5.3.2. While suitable for multiple measurements of the channel spacing, assuming that the chosen section is sufficient to represent the whole contact, this does limit the ability to confirm radii of the metal contacts. Hence, an approach based upon arc lengths was taken to provide more insight.

In figure 3.39, the measurements needed for determining the radii of both circles is depicted with a simple diagram. The calculation used is [63]:

$$r_{1,2} = \frac{c_{1,2}}{8h_{1,2}} + \frac{h_{1,2}}{2} \tag{3.43}$$

which can be derived naturally with trigonometry. $c_{1,2}$ and $h_{1,2}$ are the lengths and heights of chords 1 and 2 respectively, both of which can be obtained via the AFM scans which only provide a small section of the inner and outer circular contacts.

Application of equation 3.43 to the AFM scans was performed by taking three separate chords for both the circular metal contacts and the outer metal contacts. Chords were taken such that a chord of maximum length, followed by two different chords of smaller length were fitted to these circles. This allows for calculation of an average chord length,

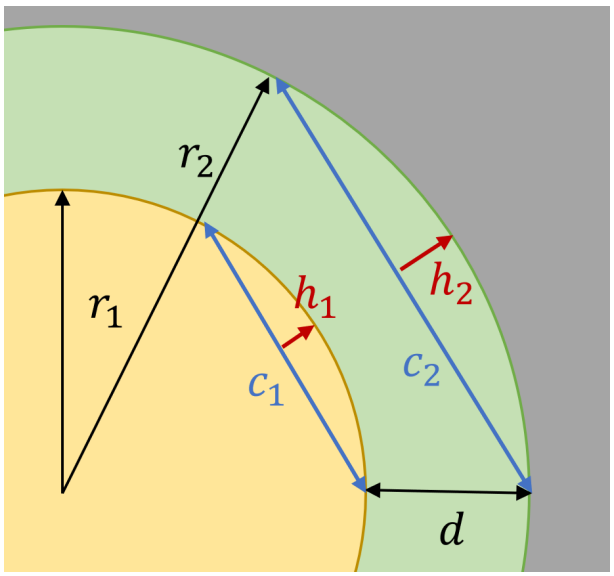

Figure 3.39 A diagram of the relevant measurements used for determining the radii from chord lengths and heights.

Contact	$r_{1,\text{avg}}$ µm	σ_{r_1} µm	$r_{2,\text{avg}}$ µm	σ_{r_2} µm	$r_{1,avg}+r_{2,avg}$ µm	r_2-r_1 µm
A7	47.3	1.4	60.6	0.5	107.9	13.4
A4	46.0	1.9	60.0	0.7	105.9	14.0
D4	39.3	2.4	58.6	0.7	97.9	19.3
A5	38.3	0.6	60.8	0.4	99.0	22.5
B5	41.5	0.8	65.5	1.3	107.0	24.0
C5	36.4	2.1	67.5	0.2	103.9	31.1

Table 3.11 Summary of chord length analysis for radii and channel length extraction.

as well as the average chord height, which can then be used to calculate the estimated radii. The results of this methodology are presented in table 3.11, with the standard deviations of both radii also included. Finally, the calculated channel spacing $d = r_2 - r_1$ is included, which presents slightly different values to that measured by direct measurements of the channel spacing. However, these values are in agreement with the direct measurements that were summarised in table 3.10. While the calculated sum of radii ($r_{1-} + r_{2-a}$) does vary between the differing contacts, the standard deviation is calculated to be 3.9. This is hence 3.9% of the intended constant radii sum (100 µm), indicating that despite the larger than designed channel spacing, the radii sum is moderately consistent. A more consistent radii sum would be preferable, as this weakens the confidence in CTLM results, but photolithography using this sample was quite challenging.

It is believed that the deviation of patterned metal when compared to the lithographic mask is due primarily to a significantly thicker photoresist layer than intended. This is a result of using a spin-coater with a small, non-circular sample. It is a common disadvantage of spin-coating samples, with a poor thickness homogeneity due to edge-bead effects negatively affecting the resulting lithographic pattern [43, 75]. An ideal lithographic methodology may involve the usage of spray-coating for small samples such as used here, as this method of photoresist application is ideal for arbitrarily shaped substrates [80].

However, this was unavailable at the time of experimental testing. To alleviate the issues with edge beading, a slightly higher rpm than standard of 6000 rpm was utilised in the spin coating of sample F, though the difference from samples coated at a spin speed of 4200 rpm was marginal, with all samples including sample F as patterned showing significant edge beading effects. With the channel spacings as determined via direct measurement of the channels, backed up indirectly via the chord length methodology, CTLM analysis via electrical characterisation before and after annealing was performed.

3.5.4. Comparison of Pre and Post anneal electrical data

The device's electrical characteristics were evaluated using two probe stations, the Keithley 4200A and the Cascade B1500. I-V sweeps were performed at various voltage ranges, starting from low voltages and gradually increasing up to maximum biases of ±200 V.

3.5.4.1. I-V Plots

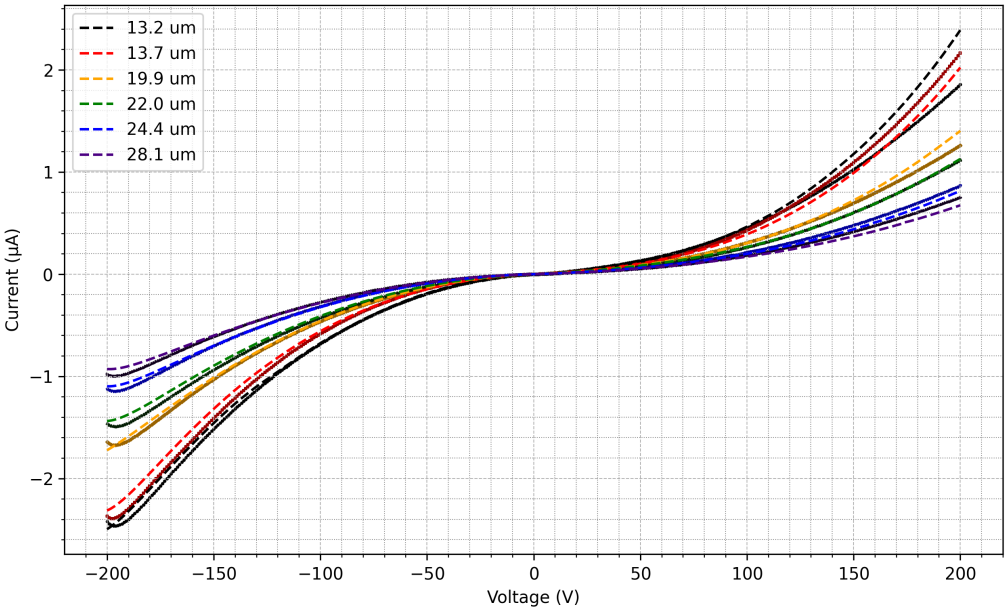

Figure 3.40 I-V data for the full bias range (±200 V), across the selected channels. Pre-anneal data is indicated by scatter points, and post-anneal is shown with dashed lines.

Figure 3.40 shows the linear IV characteristics of all 6 of the selected CTLM channels. The channel lengths as determined via direct measurement of the channel are indicated for the related data in the legend. A dashed line of a darker shade than that of the corresponding pre-anneal data is used to indicate the post-anneal data. The data generally reflects the measured channel spacings, with the highest currents observed for the lowest channel spacings and the lowest currents for the highest channel spacings. Error in the y axis is assumed to be determined via the probe station calibration, which is substantially lower

than that of the currents observed here, at around 100 pA. As a result, error bars are not visible in the current. Note that for the circular contacts, this figure cannot be normalised as was the case for LTLM structures as in section 3.4.1.2, and is provided as a reference for the further CTLM analysis, typical for studies involving this device structure [30, 46].

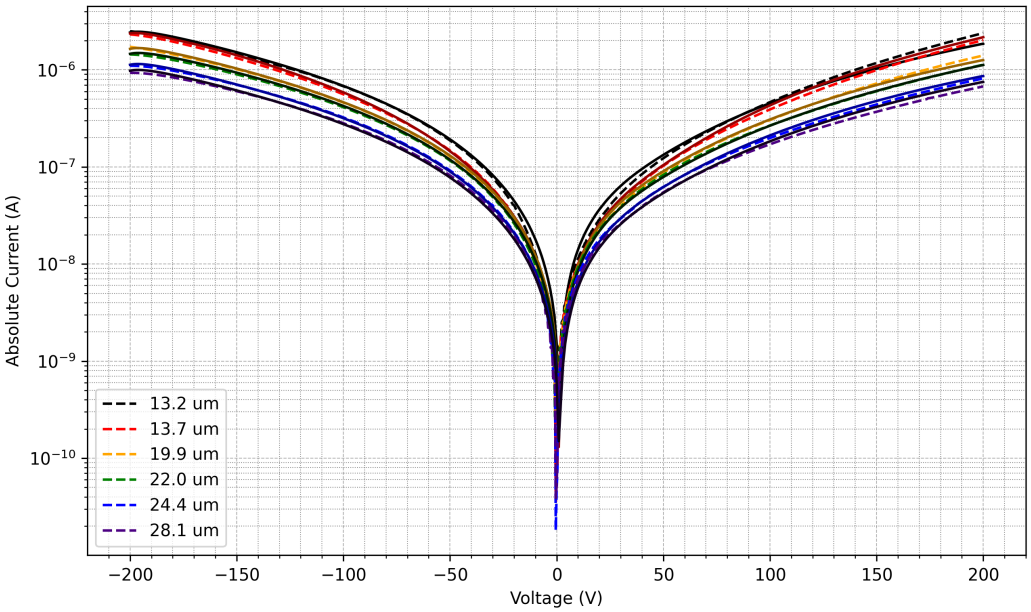

Figure 3.41 I-V data for the full bias range (±200 V), across the selected channels. Pre-anneal data is indicated by solid lines, and post-anneal is shown with dashed lines. Logarithmic current scale.

Figure 3.41 shows the log scale plot of IV data as measured across the 6 selected CTLM channels. Post-anneal data is indicated with dashed lines, while the pre-anneal scatter presents as a solid line. The log plot of IV data further reinforces that the observed resistance appears to directly correlate with the measured channel spacings. While the 13.2 and 13.7 µm channels are difficult to distinguish from one another, this may be due to the possibility of the shortest electrical path not quite matching the measured channel spacings. An error of up to ±0.4 µm based on the standard deviation of measurements as presented in table 3.10 would account for this visible overlap in measured resistance.

3.5.4.2. d-R Plots

A key parameter that must be considered fully in the plotting of total resistance against the channel spacing is that of the constant current condition. As described in section 3.5.1, the constant current condition I_0 is a necessary step in order to separate the bulk and contact resistances of these CTLM structures. The resistances measured in figures 3.40 and 3.41 are significantly higher than that of comparable studies on highly phosphorous doped diamond, which is likely due to the resistivity of phosphorous doped material in use for this work in combination with the larger than intended channel spacings. As a result,

the constant current conditions used by Matsumoto et al. [46] are impossible to duplicate, and a range of values that fit these data better can instead be used. It is impossible to use CTLM analysis without acknowledging the Schottky nature of the junction and non-linear nature of specific contact resistivity, as is ordinarily done in CTLM experiments on wide-bandgap semiconductors [76].

In this section, the methodology of CTLM is employed with differing constant current conditions to produce linear plots of total resistance against channel spacing. The use of constant current conditions ensures that the voltage drop across the contacts and the bulk material can be separated, allowing for accurate extraction of the contact resistance (R_c) and specific contact resistivity (ρ_c). By fixing the current, the nonlinear contributions from the Schottky barriers are also accounted for, which is critical for accurate characterisation of wide-bandgap semiconductors like phosphorous-doped diamond. A full range of constant current conditions are applied, which span the IV characteristics of section 3.5.4.1 from relatively low voltages to near 200 V. A maximum current condition of 1 µA was chosen as this is the highest current that was measured across the largest channel spacings tested. A minimum constant current condition of 10 nA represents some of the lowest voltages applied to the channels, and hence is very noisy in comparison the higher voltage measurements, with the IV data perhaps being taken from voltages at which neither of the Schottky barriers created by the metal contacts are in a forward bias mode of current flow. As outlined in section 3.5.3.2, the channel spacing is determined by three differing AFM measurements across the circular channel, with a maximum standard deviation of ±0.4 µm. As a slight overestimate, horizontal error bars of ±0.5 µm will be used in the plotting of total resistance against channel size.

Figure 7.3 shows the CTLM plot of constant current condition -1 µA. The negative current is taken to allow for a constant current magnitude of 1 µA to be taken for all channels. As can be determined via the IV plots of section 3.5.4.1, this represents the measurements taken in the voltage region of approximately 150–200 V. At these high voltages, it is apparent that the data represent a strongly biased double Schottky structure, with only a slight asymmetry that may be attributable to the differing areas of Schottky contacts. The data for pre and post annealing are both plotted in figure 7.3, as indicated by the legend. A notable trend is the slight increase of total measured resistance for the post-anneal data, other than for the lowest channel lengths. It is unclear why the annealing process has not resulted in a reduction in contact resistance, reducing the total resistance of all channel lengths. This will be explored further in section 3.5.4.4, as the trivial expectation of TiC formation through annealing leading to a lower specific contact resistivity is well established in boron doped diamond devices. The R^2 value of the pre and post anneal linear fits in figure 7.3 are 0.975 and 0.960 respectively. The calculated values for the specific contact resistivity ρ_c are 462 $\Omega\,\mathrm{cm}^2$ and 577 $\Omega\,\mathrm{cm}^2$ for pre and post annealing. The corresponding sheet resistivities are 186 $\mathrm{k}\Omega\,\mathrm{cm}$ and 182 $\mathrm{k}\Omega\,\mathrm{cm}$, given sheet resistivities $\rho_s = R_{sh}t$ where t is the thickness of the phosphorous doped surface layer,

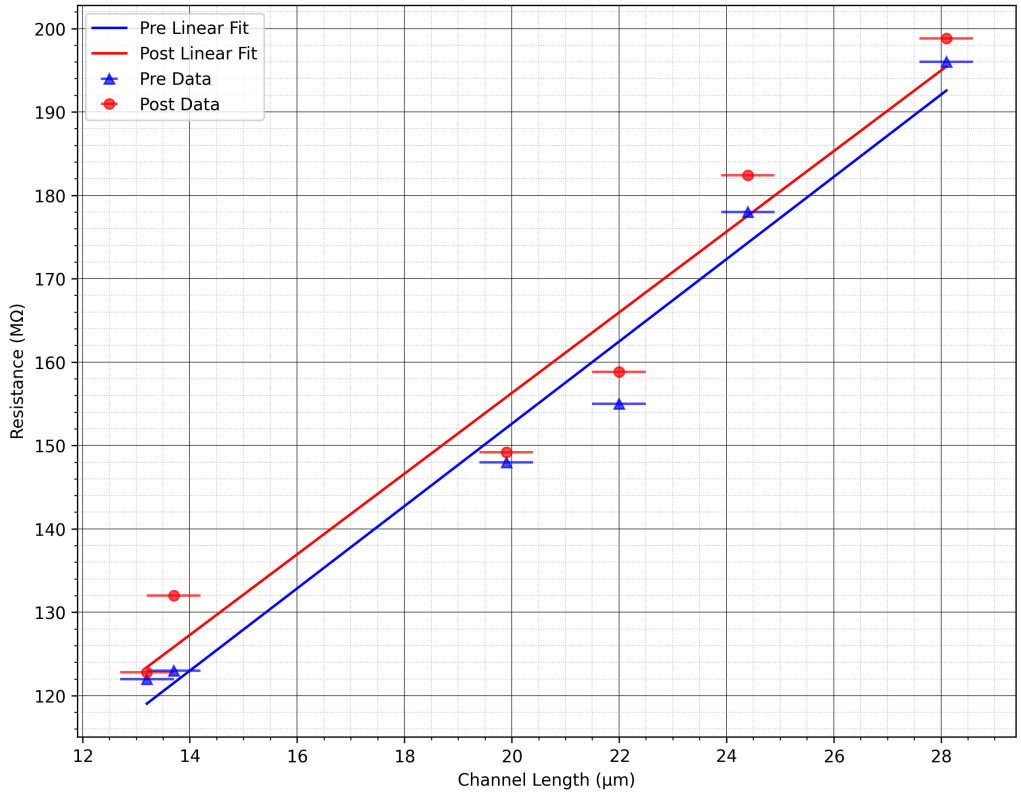

Figure 3.42 Comparison of both pre/post annealing d-R data for $I_0 = -1 \times 10^{-6}$ A, across the selected channels.

estimated at 1.2 µm. The close agreement of ρ_s between annealing conditions, compared to the notable increase of ρ_c, is intriguing, implying that the methodology is correctly identifying the change in contacts and unchanging phosphorous doped channel.

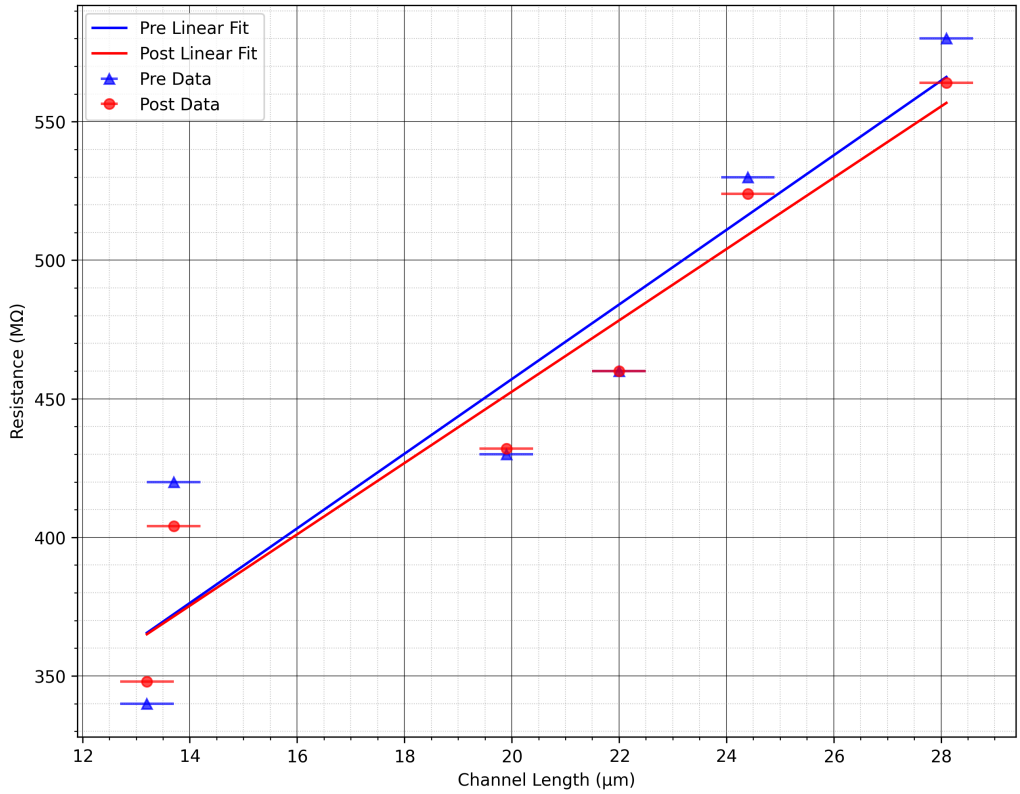

Figure 3.43 Comparison of both pre/post annealing d-R data for $I_0 = -1 \times 10^{-7}$ A, across the selected channels.

Figure 3.43 shows the CTLM plot of constant current condition -100 nA. The exact voltages required for this value correspond to approximately 30–60 V from the smallest to largest channel spacings used. In contrast to the higher current condition of 1 µA, the linear fit is of a lower quality with R^2 values for the pre and post anneal data of 0.874 and 0.926 respectively. As the reduced constant current condition requires examination of a lower potential bias region, the reduction in linearity observed here may be attributable to a lack of forward biasing in Schottky contacts formed between the Ti/Au contacts and the highly phosphorous doped diamond. The calculated values of ρ_c are 2.06 kΩ cm^2 and 2.32 kΩ cm^2 for pre and post anneal conditions respectively. Corresponding ρ_s are 508 kΩ cm and 485 kΩ cm. In contrast to the higher constant current condition of -1 µA, there is a more notable discrepancy between the sheet resistivities, with the post anneal resistivity $\sim 4.5\%$ lower than that of the pre anneal resistivity. Given the reduced R^2 values for the linear fits here, it is expected that this is due to random error, and not indicative of a real change in the phosphorous doped diamond channel. The significantly higher specific contact resistivities are a natural consequence of taking resistance measurements from a lower voltage bias, as the Schottky contacts formed here are not in a linear conduction regime.

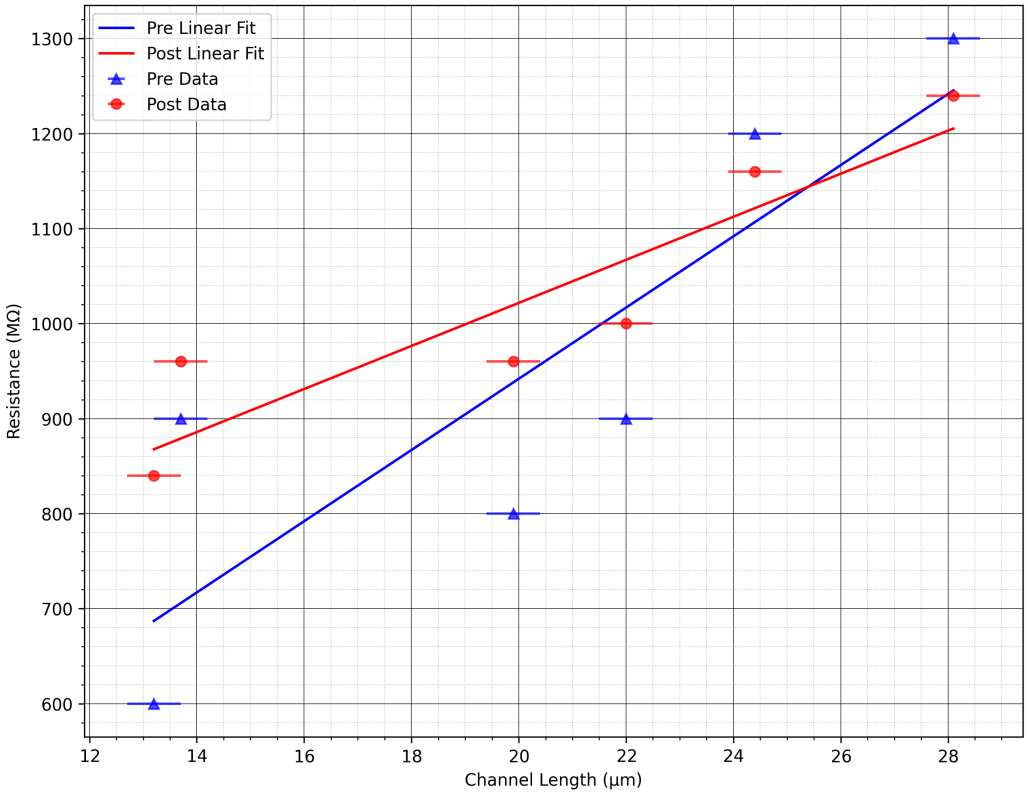

Figure 3.44 Comparison of both pre/post annealing d-R data for $I_0 = -1 \times 10^{-8}$ A, across the selected channels.

Finally, figure 3.44 shows the CTLM plot of constant current condition -10 nA. This represents a magnitude of approximately 1 V bias across the metal contacts. While it is possible to apply linear fitting to these data, the resulting R^2 values are 0.732 and 0.832 for the pre and post anneal conditions respectively, representing a significant drop in linearity for this low potential bias. The calculated specific contact resistivities ρ_c are 775 $\Omega\,cm^2$ and 11.2 $k\Omega\,cm^2$ for the pre and post anneal contacts respectively. Additionally, the sheet resistivities are 1.41 $M\Omega\,cm$ and 854 $k\Omega\,cm$. As has already been noted, the linear fits to these data are quite speculative, and so there is not much physical meaning to be interpreted from these figures. However, it can be generally observed that the specific contact resistivity is increasing for lower constant current conditions, and this is what should be expected for the calculation of ρ_c across a double Schottky junction such as that seen here.

Anneal	I_0 (nA)	ρ_s (kΩcm)	ρ_c (kΩcm^2)	R^2
Pre	-1000	186	0.462	0.975
Post	-1000	182	0.577	0.960
Pre	-100	508	2.06	0.874
Post	-100	485	2.32	0.926
Pre	-10	1410	0.775	0.732
Post	-10	854	11.2	0.832

Table 3.12 Comparison of electrical parameters before and after annealing.

Following the theoretical description given earlier, the phosphorous doped diamond and specific contact resistivities are given in table 3.12. The residuals are also given for clarity in the reliability of these calculations. The first significant observation must be in the deterioration of reliability at lower current values, with the linear fit for spacing-resistance plots becoming significantly less reliable. This can also be interpreted as less confidence in the fit for lower voltage ranges, since the constant current condition of $I_0 = 1$ nA is only true in the region immediately adjacent to 0 V relative to the higher constant current values, which are found at higher applied voltages. Note that while it is convenient to study the negative current region in particular due to the slightly larger currents allowing for a full range from 10–1000 nA, one may question if the positive currents produce the same response. As the relationship between constant current condition and specific contact resistivity or the resistivity of the sheet is unclear with the data presented thus far, further analysis was performed to shed light on this topic.

3.5.4.3. CTLM Overall Trends

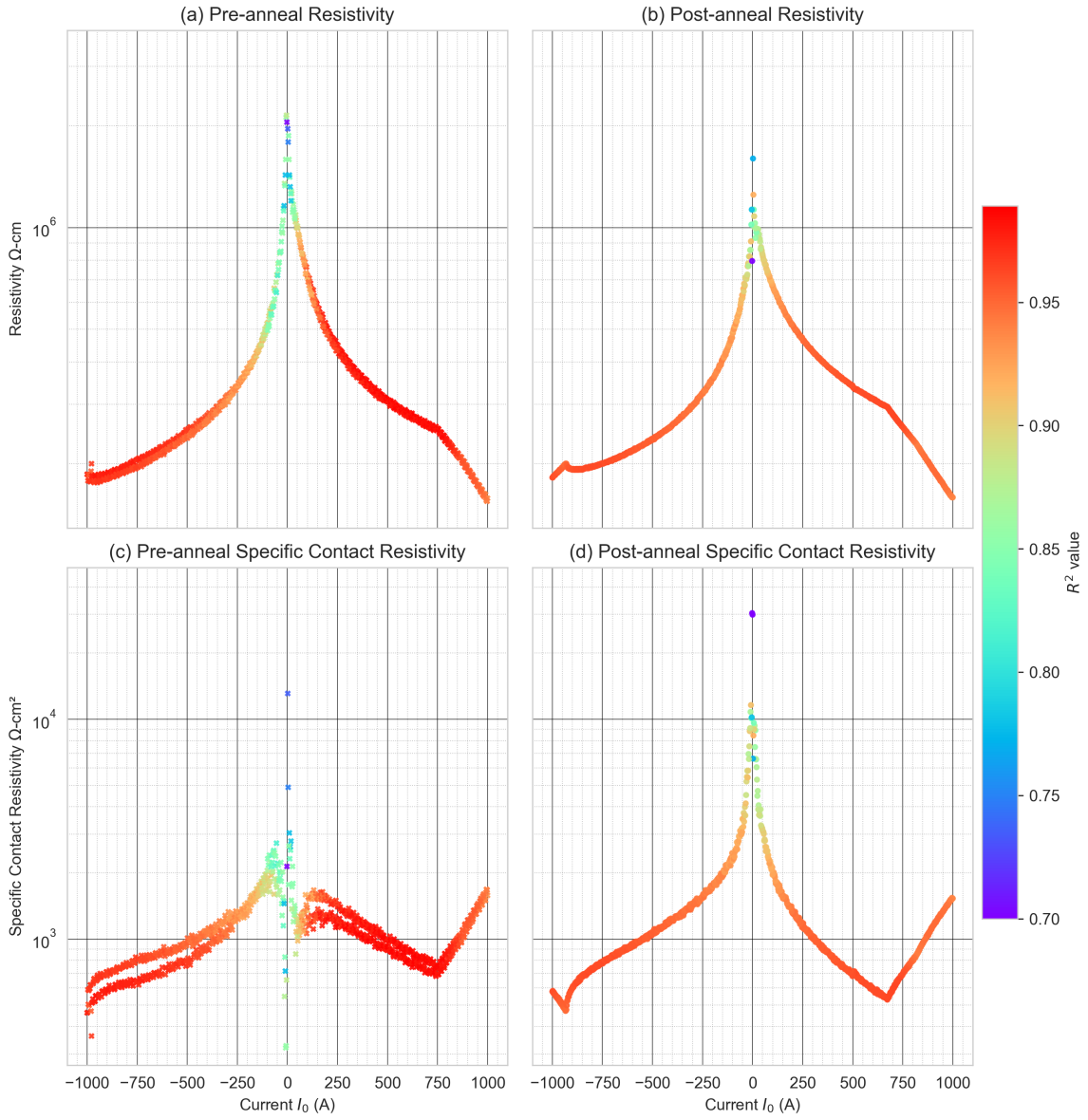

Figure 3.45 A full comparison of pre and post annealing on the specific contact resistivity and the observed resistivity of phosphorous doped diamond.

Figure 7.4 provides a visual examination of the CTLM data, separating the data for ease of comparison. In addition to the resistivity and specific contact resistivity plots, a colour scale based on the corresponding R^2 value is used to help indicate the data which shows a poor linear fit when used for CTLM analysis. One important note is regarding the clear split between two separate lines of scatter points in figure c, this was initially believed to be due to oversampling of the electrical data. The potential issue lies in the usage of 500 evenly spaced data points between 0.1–1000 nA. As the measured current will most likely differ from any given constant current condition point, an absolute difference comparison was used to find the closest current values. In the case of figure c, this appears to result in two adjacent lines. However, subsequent tests of this methodology, using far fewer

data points, reveal much the same double line formation of scatter points. Hence, this is an odd pattern to observe within the pre-anneal specific contact resistivity. Further to this anomaly is the clear asymmetry between positive and negative constant currents. In particular, there is a sharp bend upwards at the $I_0 = 750$ nA mark in ρ_c for both the pre and post anneal case. This trend is also reflected in figures a and b, where a shoulder is visible at the same current value. While the data is understandably noisy at very close to 0 A, this is not the case for the 750 nA feature, with consistently high R^2 values in this region. Finally, another small feature is noted in the negative constant current region, which appears to mirror that of the 750 nA feature. It is possible that this represents a real physical change in the devices as they are being tested, though it should also be noted that these features are consistent between the pre and post anneal testing.

Finally, comparison can be made to the work of Matsumoto et al. [46] who applied this analysis with a constant current condition of $I_0 = 50$ µA, which corresponded to an applied voltage in the region of 5 V. With the constant current condition of $I_0 = 0.1 - -1$ µA, it is possible to conduct the same analysis despite the significant difference in observed total resistance. Matsumoto et al. observed a sheet resistance of 910 kΩ and a specific contact resistivity of $1.46 \Omega\,\mathrm{cm}^2$, for Ti based electrodes. If the near maximum current drawn of -1 µA is used for comparison, the contacts tested here displayed a phosphorous doped channel of approximate resistivity 184 $\mathrm{k}\Omega\,\mathrm{cm}$, corresponding to a sheet resistance with phosphorous doped thickness ~ 1 µm of 1.84 GΩ and specific contact resistivity of $462\ \Omega\,\mathrm{cm}^2$. The factor of 2000 difference between the sheet resistances is quite notable, indicating that while the phosphorous doped surface layer here is conductive, it is significantly less conductive than ostensibly comparable samples.

3.5.4.4. Annealing at 500 °C *and Contact Degradation*

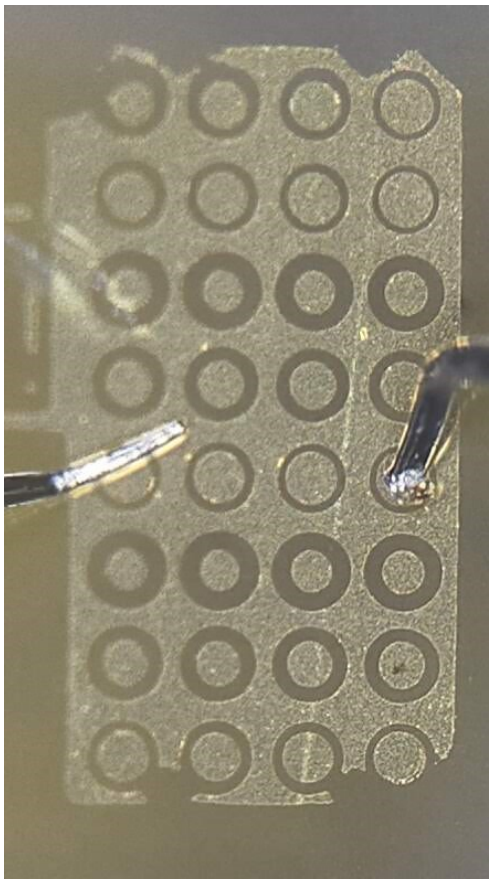

Figure 3.46 The CTLM structure pre-anneal.

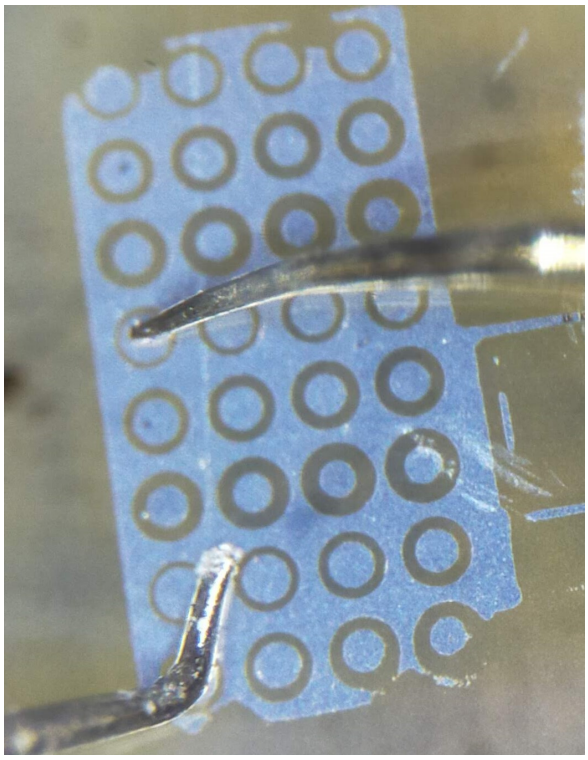

Figure 3.47 The CTLM structure post-anneal.

The annealing process at 500 °C led to observable changes in the physical properties of the Ti/Au contacts. Initially, the contacts exhibited a gold colour (figure 3.46), typical of the gold layer. However, after annealing, the colour changed to a silver-like appearance (figure 3.47). This transformation could be attributed to the formation of gold nano-droplets during the annealing process, which might have exposed the underlying titanium layer [34].

Despite this physical transformation, the annealing process did not lead to any significant improvements in the electrical contact between the titanium layer and the phosphorus-doped diamond substrate. The specific contact resistivity remained much the same with the -1000 nA measurement of 186 and 184 $\Omega\,\mathrm{cm}^2$ for the pre and post anneal data respectively, suggesting that the annealing process at the chosen temperature and duration did not significantly enhance the ohmic nature of the contacts.

Over time, the contacts demonstrated further degradation. After a couple of months of exposure to ambient air, the contacts were found to be completely resistant to electrical contact. This could be due to oxidation of the exposed titanium layer, a process that impedes the flow of electric current once a complete layer of titanium dioxide has formed [12]. These results highlight the challenges associated with the stability and durability of

Ti/Au contacts on phosphorus-doped diamond substrates. More robust and stable ohmic contacts are required to realise the full potential of diamond-based electronic devices, especially for samples that do not display sheet resistivities that may be expected for highly doped samples.

References

[1] Eslam Abubakr et al. "Laser-induced novel ohmic contact formation for effective charge collection in diamond detectors". In: *Materials Science in Semiconductor Processing* 139 (Mar. 2022), p. 106370. DOI: 10.1016/j.mssp.2021.106370. URL: https://doi.org/10.1016/j.mssp.2021.106370.

[2] Giovanni Alfieri, Lukas Kranz, and Andrei Mihaila. "Phosphorus-Related Complexes and Shallow Doping in Diamond". In: *physica status solidi (RRL) - Rapid Research Letters* 12.4 (Jan. 2018), p. 1700409. DOI: 10.1002/pssr.201700409. URL: https://doi.org/10.1002/pssr.201700409.

[3] E Ajith Amerasekera and Charvaka Duvvury. *ESD in Silicon Integrated Circuits*. en. 2nd ed. Chichester, England: John Wiley & Sons, Apr. 2002.

[4] Shenda M. Baker, George R. Rossman, and John D. Baldeschwieler. "Observation of surface charge screening and Fermi level pinning on a synthetic, boron-doped diamond". In: *Journal of Applied Physics* 74.6 (Sept. 1993), pp. 4015–4019. DOI: 10.1063/1.354445. URL: https://doi.org/10.1063/1.354445.

[5] Bhaswar Baral, Simon S. M. Chan, and Richard B. Jackman. "Cleaning thin-film diamond surfaces for device fabrication: An Auger electron spectroscopic study". In: *Journal of Vacuum Science & Technology A* 14.4 (July 1996), pp. 2303–2307. ISSN: 0734-2101. DOI: 10.1116/1.580063. eprint: https://pubs.aip.org/avs/jva/article-pdf/14/4/2303/12007445/2303_1_online.pdf. URL: https://doi.org/10.1116/1.580063.

[6] Purushottam Chakraborty. "Ultra-high depth resolution SIMS for the interface analysis of complex low-dimensional structures". In: *Nuclear Instruments and Methods in Physics Research Section B: Beam Interactions with Materials and Atoms* 266.8 (Apr. 2008), pp. 1858–1865. ISSN: 0168-583X. DOI: 10.1016/j.nimb.2007.12.084. URL: http://dx.doi.org/10.1016/j.nimb.2007.12.084.

[7] Yigang Chen et al. "Ohmic contacts on p-type homoepitaxial diamond and their thermal stability". In: *Semiconductor Science and Technology* 20.8 (July 2005), pp. 860–863. DOI: 10.1088/0268-1242/20/8/041. URL: https://doi.org/10.1088/0268-1242/20/8/041.

[8] Chunmin Cheng et al. “Ab-initio study of Schottky barrier heights at metal-diamond (1 1 1) interfaces”. In: *Applied Surface Science* 615 (Apr. 2023), p. 156329. ISSN: 0169-4332. DOI: 10.1016/j.apsusc.2023.156329. URL: http://dx.doi.org/10.1016/j.apsusc.2023.156329.

[9] J Colvin. “ESD failure analysis methodology”. In: *Microelectronics Reliability* 38.11 (Nov. 1998), pp. 1705–1714. ISSN: 0026-2714. DOI: 10.1016/s0026-2714(98)00173-5. URL: http://dx.doi.org/10.1016/S0026-2714(98)00173-5.

[10] Kevin G. Crawford et al. “Surface transfer doping of diamond: A review”. In: *Progress in Surface Science* 96.1 (Feb. 2021), p. 100613. ISSN: 0079-6816. DOI: 10.1016/j.progsurf.2021.100613. URL: http://dx.doi.org/10.1016/j.progsurf.2021.100613.

[11] Dhruba Das and M.S. Ramachandra Rao. “Effect of phosphorus ion implantation on electrical conductivity and local lattice distortions in diamond”. In: *Diamond and Related Materials* 128 (Oct. 2022), p. 109212. ISSN: 0925-9635. DOI: 10.1016/j.diamond.2022.109212. URL: http://dx.doi.org/10.1016/j.diamond.2022.109212.

[12] Rajib Das, Vibhav Ambardekar, and Partha Pratim Bandyopadhyay. “Titanium Dioxide and Its Applications in Mechanical, Electrical, Optical, and Biomedical Fields”. In: *Titanium Dioxide - Advances and Applications*. IntechOpen, Mar. 2022. DOI: 10.5772/intechopen.98805. URL: http://dx.doi.org/10.5772/intechopen.98805.

[13] M. De Feudis et al. “Ohmic graphite-metal contacts on oxygen-terminated lightly boron-doped CVD monocrystalline diamond”. In: *Diamond and Related Materials* 92 (Feb. 2019), pp. 18–24. ISSN: 0925-9635. DOI: 10.1016/j.diamond.2018.12.009. URL: http://dx.doi.org/10.1016/j.diamond.2018.12.009.

[14] “Doping and semiconductor characterizations”. In: *Power Electronics Device Applications of Diamond Semiconductors*. Elsevier, 2018, pp. 99–189. DOI: 10.1016/b978-0-08-102183-5.00002-9. URL: https://doi.org/10.1016/b978-0-08-102183-5.00002-9.

[15] Integrated Systems Engineering. *TCAD Release 7.5 User’s Manual*. Zurich, Switzerland, DESSIS, ISE. 2001. URL: http://www.ise.ch/.

[16] De Fang et al. “Calibration of Binding Energy Positions with C1s for XPS Results”. In: *Journal of Wuhan University of Technology-Mater. Sci. Ed.* 35.4 (Aug. 2020), pp. 711–718. ISSN: 1993-0437. DOI: 10.1007/s11595-020-2312-7. URL: http://dx.doi.org/10.1007/s11595-020-2312-7.

[17] Alexandre Fiori et al. “Improved depth resolution of secondary ion mass spectrometry profiles in diamond: A quantitative analysis of the delta-doping”. In: *Thin Solid Films* 557 (Apr. 2014), pp. 222–226. ISSN: 0040-6090. DOI: 10.1016/j.tsf.2013.10.076. URL: http://dx.doi.org/10.1016/j.tsf.2013.10.076.

[18] E. Gheeraert et al. "Low temperature excitation spectrum of phosphorus in diamond". In: *Diamond and Related Materials* 10.3–7 (Mar. 2001), pp. 444–448. ISSN: 0925-9635. DOI: 10.1016/s0925-9635(00)00408-8. URL: http://dx.doi.org/10.1016/S0925-9635(00)00408-8.

[19] Jonathan P. Goss, Richard J. Eyre, and Patrick R. Briddon. *Theoretical Models for Doping Diamond for Semiconductor Applications*. Aug. 2008. DOI: 10.1002/9783527623174.ch8. URL: https://doi.org/10.1002/9783527623174.ch8.

[20] T.A. Grotjohn et al. "Heavy phosphorus doping by epitaxial growth on the (111) diamond surface". In: *Diamond and Related Materials* 44 (Apr. 2014), pp. 129–133. DOI: 10.1016/j.diamond.2014.02.009. URL: https://doi.org/10.1016/j.diamond.2014.02.009.

[21] Siyu Guo et al. "Detailed investigation of TLM contact resistance measurements on crystalline silicon solar cells". In: *Solar Energy* 151 (July 2017), pp. 163–172. ISSN: 0038-092X. DOI: 10.1016/j.solener.2017.05.015. URL: http://dx.doi.org/10.1016/j.solener.2017.05.015.

[22] Erik H Hauri et al. "Microanalysis of 13C, 15N, and N abundances in diamonds by secondary ion mass spectrometry". In: *Chemical Geology* 185.1–2 (Apr. 2002), pp. 149–163. ISSN: 0009-2541. DOI: 10.1016/s0009-2541(01)00400-4. URL: http://dx.doi.org/10.1016/S0009-2541(01)00400-4.

[23] Tatsuya Iwasaki et al. "Formation of ohmic contacts on semiconducting diamond grown by chemical vapour deposition". In: *Diamond and Related Materials* 3.1–2 (Jan. 1994), pp. 30–34. ISSN: 0925-9635. DOI: 10.1016/0925-9635(94)90026-4. URL: http://dx.doi.org/10.1016/0925-9635(94)90026-4.

[24] Wiebke Janssen et al. "Substitutional phosphorus incorporation in nanocrystalline CVD diamond thin films: Substitutional phosphorus incorporation in nanocrystalline CVD diamond thin films". In: *physica status solidi (RRL) - Rapid Research Letters* 8.8 (June 2014), pp. 705–709. ISSN: 1862-6254. DOI: 10.1002/pssr.201409235. URL: http://dx.doi.org/10.1002/pssr.201409235.

[25] Holly M. Johnson et al. "Cleaning diamond surfaces via oxygen plasma inhibits the formation of a TiC interface". In: *Diamond and Related Materials* 126 (June 2022), p. 109058. ISSN: 0925-9635. DOI: 10.1016/j.diamond.2022.109058. URL: http://dx.doi.org/10.1016/j.diamond.2022.109058.

[26] Yūki Katamune et al. "Heavy phosphorus doping of diamond by hot-filament chemical vapor deposition". In: *Diamond and Related Materials* 134 (Apr. 2023), p. 109789. DOI: 10.1016/j.diamond.2023.109789. URL: https://doi.org/10.1016/j.diamond.2023.109789.

[27] Yūki Katamune et al. “n-Type doping of diamond by hot-filament chemical vapor deposition growth with phosphorus incorporation”. In: *Applied Physics A* 126.11 (Oct. 2020). DOI: 10.1007/s00339-020-04060-w. URL: https://doi.org/10.1007/s00339-020-04060-w.

[28] Hiromitsu Kato, Satoshi Yamasaki, and Hideyo Okushi. “Carrier compensation in (001) n-type diamond by phosphorus doping”. In: *Diamond and Related Materials* 16.4–7 (Apr. 2007), pp. 796–799. ISSN: 0925-9635. DOI: 10.1016/j.diamond.2006.11.085. URL: http://dx.doi.org/10.1016/j.diamond.2006.11.085.

[29] Hiromitsu Kato, Satoshi Yamasaki, and Hideyo Okushi. “n-type doping of (001)-oriented single-crystalline diamond by phosphorus”. In: *Applied Physics Letters* 86.22 (May 2005), p. 222111. ISSN: 0003-6951. DOI: 10.1063/1.1944228. eprint: https://pubs.aip.org/aip/apl/article-pdf/doi/10.1063/1.1944228/14642781/222111_1_online.pdf. URL: https://doi.org/10.1063/1.1944228.

[30] Hiromitsu Kato et al. “Characterization of specific contact resistance on heavily phosphorus-doped diamond films”. In: *Diamond and Related Materials* 18.5 (2009). Proceedings of Diamond 2008, the 19th European Conference on Diamond, Diamond-Like Materials, Carbon Nanotubes, Nitrides and Silicon Carbide, pp. 782–785. ISSN: 0925-9635. DOI: https://doi.org/10.1016/j.diamond.2009.01.033. URL: https://www.sciencedirect.com/science/article/pii/S0925963509000363.

[31] Hiromitsu Kato et al. “Low specific contact resistance of heavily phosphorus-doped diamond film”. In: *Applied Physics Letters* 93.20 (Nov. 2008). ISSN: 1077-3118. DOI: 10.1063/1.3005639. URL: http://dx.doi.org/10.1063/1.3005639.

[32] Hiromitsu Kato et al. “n-type diamond growth by phosphorus doping on (0 0 1)-oriented surface”. In: *Journal of Physics D: Applied Physics* 40.20 (Oct. 2007), pp. 6189–6200. DOI: 10.1088/0022-3727/40/20/s05. URL: https://doi.org/10.1088/0022-3727/40/20/s05.

[33] Ryosuke Kizu et al. “Comparison of SEM and AFM performances for LER reference metrology”. In: *Metrology, Inspection, and Process Control for Microlithography XXXIV*. Ed. by Ofer Adan and John C. Robinson. SPIE, Mar. 2020, p. 21. DOI: 10.1117/12.2551468. URL: http://dx.doi.org/10.1117/12.2551468.

[34] Alla Klimovskaya et al. “Study of the formation processes of gold droplet arrays on Si substrates by high temperature anneals”. In: *Nanoscale Research Letters* 6.1 (Feb. 2011). ISSN: 1556-276X. DOI: 10.1186/1556-276x-6-151. URL: http://dx.doi.org/10.1186/1556-276X-6-151.

[35] J.H. Klootwijk and C.E. Timmering. “Merits and limitations of circular TLM structures for contact resistance determination for novel III-V HBTs”. In: *Proceedings of the 2004 International Conference on Microelectronic Test Structures (IEEE Cat. No.04CH37516)*. ICMTS-04. IEEE. DOI: 10.1109/icmts.2004.1309489. URL: http://dx.doi.org/10.1109/ICMTS.2004.1309489.

[36] T. Kociniewski et al. "MOCVD doping technology for phosphorus incorporation in diamond: Influence of the growth temperature on the electrical properties". In: *Diamond and Related Materials* 16.4 (2007). Proceedings of Diamond 2006, the 17th European Conference on Diamond, Diamond-Like Materials, Carbon Nanotubes, Nitrides and Silicon Carbide, pp. 815–818. ISSN: 0925-9635. DOI: https://doi.org/10.1016/j.diamond.2006.12.032. URL: https://www.sciencedirect.com/science/article/pii/S0925963506005437.

[37] T. Kociniewski et al. "n-type CVD diamond doped with phosphorus using the MOCVD technology for dopant incorporation". In: *physica status solidi (a)* 203.12 (2006), pp. 3136–3141. DOI: https://doi.org/10.1002/pssa.200671113. eprint: https://onlinelibrary.wiley.com/doi/pdf/10.1002/pssa.200671113. URL: https://onlinelibrary.wiley.com/doi/abs/10.1002/pssa.200671113.

[38] S. Koizumi et al. "Growth and characterization of phosphorous doped {111} homoepitaxial diamond thin films". In: *Applied Physics Letters* 71.8 (Aug. 1997), pp. 1065–1067. DOI: 10.1063/1.119729. URL: https://doi.org/10.1063/1.119729.

[39] Satoshi Koizumi, Christoph Nebel, and Milos Nesladek. *Physics and applications of CVD Diamond*. en. Ed. by Satoshi Koizumi, Christoph Nebel, and Milos Nesladek. Weinheim, Germany: Wiley-VCH Verlag, Aug. 2008.

[40] Satoshi Koizumi, Tokuyuki Teraji, and Hisao Kanda. "Phosphorus-doped chemical vapor deposition of diamond". In: *Diamond and Related Materials* 9.3 (2000), pp. 935–940. ISSN: 0925-9635. DOI: https://doi.org/10.1016/S0925-9635(00)00217-X. URL: https://www.sciencedirect.com/science/article/pii/S092596350000217X.

[41] L.D. LANDAU and E.M. LIFSHITZ. "THE GIBBS DISTRIBUTION". In: *Statistical Physics*. Elsevier, 1980, pp. 79–110. ISBN: 9780080570464. DOI: 10.1016/b978-0-08-057046-4.50010-5. URL: http://dx.doi.org/10.1016/B978-0-08-057046-4.50010-5.

[42] B. B. Li et al. "Measurement of the substitutional nitrogen activation energy in diamond films". In: *Applied Physics Letters* 73.6 (Aug. 1998), pp. 812–814. DOI: 10.1063/1.122010. URL: https://doi.org/10.1063/1.122010.

[43] Qiuyu Liu et al. "Influence of Airflow Disturbance on the Uniformity of Spin Coating Film Thickness on Large Area Rectangular Substrates". In: *Coatings* 12.9 (Aug. 2022), p. 1253. ISSN: 2079-6412. DOI: 10.3390/coatings12091253. URL: http://dx.doi.org/10.3390/coatings12091253.

[44] F. Lloret et al. "High phosphorous incorporation in (100)-oriented MP CVD diamond growth". In: *Diamond and Related Materials* 133 (Mar. 2023), p. 109746. ISSN: 0925-9635. DOI: 10.1016/j.diamond.2023.109746. URL: http://dx.doi.org/10.1016/j.diamond.2023.109746.

[45] J. Maserjian and N. Zamani. “Behavior of the Si/SiO2 interface observed by Fowler-Nordheim tunneling”. In: *Journal of Applied Physics* 53.1 (Jan. 1982), pp. 559–567. ISSN: 1089-7550. DOI: 10.1063/1.329919. URL: http://dx.doi.org/10.1063/1.329919.

[46] Tsubasa Matsumoto et al. “Reduction of n-type diamond contact resistance by graphite electrode”. In: *physica status solidi (RRL) – Rapid Research Letters* 8.2 (Nov. 2013), pp. 137–140. ISSN: 1862-6270. DOI: 10.1002/pssr.201308252. URL: http://dx.doi.org/10.1002/pssr.201308252.

[47] N.W. McLachlan. *Bessel Functions for Engineers*. Oxford University Press, 1954. ISBN: 1124148620.

[48] Winfried Mönch. *Electronic Properties of Semiconductor Interfaces*. Springer Berlin Heidelberg, 2004. ISBN: 9783662069455. DOI: 10.1007/978-3-662-06945-5. URL: http://dx.doi.org/10.1007/978-3-662-06945-5.

[49] Inyong Moon et al. “Analytical measurements of contact resistivity in two-dimensional WSe2 field-effect transistors”. In: *2D Materials* 8.4 (Aug. 2021), p. 045019. ISSN: 2053-1583. DOI: 10.1088/2053-1583/ac1adb. URL: http://dx.doi.org/10.1088/2053-1583/ac1adb.

[50] V. Mortet et al. “Characterization of boron doped diamond epilayers grown in a NIRIM type reactor”. In: *Diamond and Related Materials* 17.7-10 (July 2008), pp. 1330–1334. DOI: 10.1016/j.diamond.2008.01.087. URL: https://doi.org/10.1016/j.diamond.2008.01.087.

[51] V. Mortet et al. “Effect of substrate crystalline orientation on boron-doped homoepitaxial diamond growth”. In: *Diamond and Related Materials* 122 (Feb. 2022), p. 108887. DOI: 10.1016/j.diamond.2022.108887. URL: https://doi.org/10.1016/j.diamond.2022.108887.

[52] Ryota Ohtani et al. “Large improvement of phosphorus incorporation efficiency in n-type chemical vapor deposition of diamond”. In: *Applied Physics Letters* 105.23 (Dec. 2014). DOI: 10.1063/1.4903779. URL: https://doi.org/10.1063/1.4903779.

[53] Marie-Amandine Pinault-Thaury et al. “Attractive electron mobility in (113) n-type phosphorus-doped homoepitaxial diamond”. In: *Carbon* 175 (Apr. 2021), pp. 254–258. DOI: 10.1016/j.carbon.2021.01.011. URL: https://doi.org/10.1016/j.carbon.2021.01.011.

[54] Alfred G. Redfield. “Electronic Hall Effect in Diamond”. In: *Physical Review* 94.3 (May 1954), pp. 526–537. ISSN: 0031-899X. DOI: 10.1103/physrev.94.526. URL: http://dx.doi.org/10.1103/PhysRev.94.526.

[55] G.K. Reeves. “Specific contact resistance using a circular transmission line model”. In: *Solid-State Electronics* 23.5 (May 1980), pp. 487–490. ISSN: 0038-1101. DOI: 10.1016/0038-1101(80)90086-6. URL: http://dx.doi.org/10.1016/0038-1101(80)90086-6.

[56] Sung-Gi Ri et al. “Electrical and optical characterization of boron-doped (111) homoepitaxial diamond films”. In: *Diamond and Related Materials* 14.11-12 (Nov. 2005), pp. 1964–1968. DOI: 10.1016/j.diamond.2005.06.032. URL: https://doi.org/10.1016/j.diamond.2005.06.032.

[57] Sung-Gi Ri et al. “Fermi level pinning-free interface at metals/homoepitaxial diamond (111) films after oxidation treatments”. In: *Applied Physics Letters* 92.11 (Mar. 2008). ISSN: 1077-3118. DOI: 10.1063/1.2892658. URL: http://dx.doi.org/10.1063/1.2892658.

[58] Dieter K Schroder. *Semiconductor material and device characterization*. en. 3rd ed. Wiley - IEEE. Chichester, England: Wiley-Blackwell, Jan. 2006.

[59] Yusuke Shirakawa et al. “Hall Effect Measurement and Band Bending Calculation of Hydrogenated Diamond Film Grown by Chemical Vapor Deposition”. In: *Japanese Journal of Applied Physics* 36.6R (June 1997), p. 3414. ISSN: 1347-4065. DOI: 10.1143/jjap.36.3414. URL: http://dx.doi.org/10.1143/JJAP.36.3414.

[60] I. Stenger et al. “Electron mobility in (100) homoepitaxial layers of phosphorus-doped diamond”. In: *Journal of Applied Physics* 129.10 (Mar. 2021). DOI: 10.1063/5.0044326. URL: https://doi.org/10.1063/5.0044326.

[61] I. Stenger et al. “Impurity-to-band activation energy in phosphorus doped diamond”. In: *Journal of Applied Physics* 114.7 (Aug. 2013), p. 073711. ISSN: 0021-8979. DOI: 10.1063/1.4818946. eprint: https://pubs.aip.org/aip/jap/article-pdf/doi/10.1063/1.4818946/15118921/073711_1_online.pdf. URL: https://doi.org/10.1063/1.4818946.

[62] I. Stenger et al. “Impurity-to-band activation energy in phosphorus doped diamond”. In: *Journal of Applied Physics* 114.7 (2013), p. 073711. DOI: 10.1063/1.4818946. eprint: https://doi.org/10.1063/1.4818946. URL: https://doi.org/10.1063/1.4818946.

[63] Babylonian Student. *YBC 7289 and the Babylonian Method of Calculating the Square Root of 2*. Babylonian Numeration System with Base 60, Old Babylonian period, buried in the ground. Babylonian tablet YBC 7289, interpreted by Dennis Ramsey, showing calculation of the square root of 2. Held in the Babylonian Collection of Yale University. circa 1800 BCE.

[64] N. Mohasin Sulthana et al. “Studies on tuning surface electronic properties of hydrogenated diamond by oxygen functionalization”. In: *Diamond and Related Materials* 128 (Oct. 2022), p. 109284. ISSN: 0925-9635. DOI: 10.1016/j.diamond.2022.109284. URL: http://dx.doi.org/10.1016/j.diamond.2022.109284.

[65] Mariko Suzuki et al. “Electrical characteristics of n-type diamond Schottky diodes and metal/diamond interfaces”. In: *physica status solidi (a)* 203.12 (Sept. 2006), pp. 3128–3135. DOI: 10.1002/pssa.200671124. URL: https://doi.org/10.1002/pssa.200671124.

[66] Mariko Suzuki et al. “Electrical characterization of phosphorus-doped n-type homoepitaxial diamond layers by Schottky barrier diodes”. In: *Applied Physics Letters* 84.13 (Mar. 2004), pp. 2349–2351. ISSN: 0003-6951. DOI: 10.1063/1.1695206. eprint: https://pubs.aip.org/aip/apl/article-pdf/84/13/2349/10203590/2349_1_online.pdf. URL: https://doi.org/10.1063/1.1695206.

[67] S.M. Sze and Kwok K. Ng. *Physics of Semiconductor Devices*. Wiley, Apr. 2006. DOI: 10.1002/0470068329. URL: https://doi.org/10.1002/0470068329.

[68] T. Tachibana, J. T. Glass, and R. J. Nemanich. “Effect of surface hydrogen on metal-diamond interface properties”. In: *Journal of Applied Physics* 73.2 (Jan. 1993), pp. 835–842. ISSN: 1089-7550. DOI: 10.1063/1.353322. URL: http://dx.doi.org/10.1063/1.353322.

[69] Nephi Temahuki et al. “New Process for Electrical Contacts on (100) N-type Diamond”. In: *physica status solidi (a)* 214.11 (Nov. 2017), p. 1700466. DOI: 10.1002/pssa.201700466. URL: https://doi.org/10.1002/pssa.201700466.

[70] T. Teraji, S. Koizumi, and H. Kanda. “Ohmic Contacts for Phosphorus-Doped n-Type Diamond”. In: *physica status solidi (a)* 181.1 (2000), pp. 129–139. DOI: https://doi.org/10.1002/1521-396X(200009)181:1<129::AID-PSSA129>3.0.CO;2-O. eprint: https://onlinelibrary.wiley.com/doi/pdf/10.1002/1521-396X%28200009%29181%3A1%3C129%3A%3AAID-PSSA129%3E3.0.CO%3B2-O. URL: https://onlinelibrary.wiley.com/doi/abs/10.1002/1521-396X%28200009%29181%3A1%3C129%3A%3AAID-PSSA129%3E3.0.CO%3B2-O.

[71] Tokuyuki Teraji et al. “Ohmic Contact Formation for N-Type Diamond by Selective Doping”. In: *Japanese Journal of Applied Physics* 42.8A (Aug. 2003), p. L882. DOI: 10.1143/JJAP.42.L882. URL: https://dx.doi.org/10.1143/JJAP.42.L882.

[72] Norio Tokuda et al. “Influence of substrate misorientation on the surface morphology of homoepitaxial diamond (111) films”. In: *physica status solidi (a)* 213.8 (Mar. 2016), pp. 2051–2055. DOI: 10.1002/pssa.201600082. URL: https://doi.org/10.1002/pssa.201600082.

[73] Sreenath Mylo Valappil et al. “Corrosion-Resistive and Low Specific Contact Resistance Ohmic Contacts to Semiconducting Diamonds Using Nanocarbon Electrodes”. In: *physica status solidi (a)* 220.3 (Jan. 2023), p. 2200627. DOI: 10.1002/pssa.202200627. URL: https://doi.org/10.1002/pssa.202200627.

[74] Juan Wang et al. “Vertical Diamond Trench MOS Barrier Schottky Diodes With High Breakdown Voltage”. In: *IEEE Transactions on Electron Devices* 69.11 (Nov. 2022), pp. 6231–6235. ISSN: 1557-9646. DOI: 10.1109/ted.2022.3206178. URL: http://dx.doi.org/10.1109/TED.2022.3206178.

[75] David E. Weidner and Soroosh Mahmoodi. "Reduction of edge beading defects on rectangular substrates using a rotation about an axis perpendicular to the spin axis". In: *Physics of Fluids* 35.10 (Oct. 2023). ISSN: 1089-7666. DOI: 10.1063/5.0167174. URL: http://dx.doi.org/10.1063/5.0167174.

[76] Wojciech Wojtasiak et al. "AlGaN/GaN High Electron Mobility Transistors on Semi-Insulating Ammono-GaN Substrates with Regrown Ohmic Contacts". In: *Micromachines* 9.11 (Oct. 2018), p. 546. ISSN: 2072-666X. DOI: 10.3390/mi9110546. URL: http://dx.doi.org/10.3390/mi9110546.

[77] S Yamanaka et al. "Low-compensated boron-doped homoepitaxial diamond films". In: *Diamond and Related Materials* 9.3-6 (Apr. 2000), pp. 956–959. DOI: 10.1016/s0925-9635(99)00212-5. URL: https://doi.org/10.1016/s0925-9635(99)00212-5.

[78] Hongchao Yang, Yandong Ma, and Ying Dai. "Progress of structural and electronic properties of diamond: a mini review". In: *Functional Diamond* 1.1 (Jan. 2021), pp. 150–159. ISSN: 2694-1120. DOI: 10.1080/26941112.2021.1956287. URL: http://dx.doi.org/10.1080/26941112.2021.1956287.

[79] Kunpeng Yu et al. "Effects of phosphorus dopingviaMn3P2on diamond growth along the (100) surfaces". In: *CrystEngComm* 21.44 (2019), pp. 6810–6818. ISSN: 1466-8033. DOI: 10.1039/c9ce01257e. URL: http://dx.doi.org/10.1039/C9CE01257E.

[80] Liming Yu et al. "Spray Coating of Photoresist for 3D Microstructures with Different Geometries". In: *Journal of Physics: Conference Series* 34 (Apr. 2006), pp. 937–942. ISSN: 1742-6596. DOI: 10.1088/1742-6596/34/1/155. URL: http://dx.doi.org/10.1088/1742-6596/34/1/155.

[81] Sen Zhang et al. "Surface potential pinning study for oxygen terminated IIa diamond". In: *Carbon* 205 (Mar. 2023), pp. 69–75. ISSN: 0008-6223. DOI: 10.1016/j.carbon.2023.01.021. URL: http://dx.doi.org/10.1016/j.carbon.2023.01.021.

[82] E. Zinner. "Depth profiling by secondary ion mass spectrometry". In: *Scanning* 3.2 (Jan. 1980), pp. 57–78. ISSN: 1932-8745. DOI: 10.1002/sca.4950030202. URL: http://dx.doi.org/10.1002/sca.4950030202.

[83] Ramiz Zulkharnay, Gulnur Zulpukarova, and Paul W. May. "Oxygen-terminated diamond: insights into the correlation between surface oxygen configurations and work function values". In: *Applied Surface Science* 658 (June 2024), p. 159776. ISSN: 0169-4332. DOI: 10.1016/j.apsusc.2024.159776. URL: http://dx.doi.org/10.1016/j.apsusc.2024.159776.

Chapter 4. Characterisation of Laser Processed Phosphorous Doped Diamond

4.0.1. Disclosure of Collaborative Content

In this chapter, the growth of phosphorous doped diamond, as well as the procurement of diamond substrates was performed by the industrial partner Evince technology. Laser writing of graphitic phases within the diamond samples was performed by Ravi Shivaraman in Oxford, in collaboration with Patrick Salter of the same department. The design used for the laser writing was conceived wholly by the candidate, with all subsequent electrical and material characterisation (such as fluorescence and AFM) performed by the candidate with one exception being that of Raman characterisation, which was conducted by SAgE Analytical with the candidates active participation.

4.1. Introduction

4.1.1. Summary of Previous Experimental Work

Chapter 3 examines the formation of conventional metal contacts to heavily phosphorous doped diamond, via annealed titanium-based contacts. The literature best-case value for the specific contact resistivity with titanium contacts is $10^{-3}\ \Omega\,\mathrm{cm}^2$ [29]. The contacts formed in this work, both in the CTLM and LTLM experiments and under different annealing conditions, differ markedly from these examples. With LTLM samples, the specific contact resistivity was measured to be 472 and 494 $\mathrm{k}\Omega\,\mathrm{cm}^2$, with a resistivity of the phosphorous doped film of 132 and 464 $\mathrm{M}\Omega\,\mathrm{cm}$ for samples C and D respectively at 10 V. For sample F and the CTLM results, at a constant current condition of -100 nA, a specific contact resistivity of around 2.1 $\mathrm{k}\Omega\,\mathrm{cm}^2$ and resistivity of around 490 $\mathrm{k}\Omega\,\mathrm{cm}$ was measured. Following these observations, it was clear that an alternative approach must be taken to form superior ohmic contacts on these samples which are sufficient to allow for competitiveness between diamond based power devices and current best case values on standard materials. For example, SiC is able to achieve extremely low resistance ohmic contacts below $1 \times 10^{-7}\ \Omega\,\mathrm{cm}^2$ [31].

4.1.2. Improved Contacts to Diamond Devices

Novel approaches to the formation of ohmic contacts with n-type diamond are an ongoing area of research, with unique orientation and substrate dependent methodologies being

developed. For instance, Temahuki et al. [44] demonstrated the ability of Ni-catalysed etching to provide pyramidal (111) oriented pits for a heavily phosphorous doped overgrowth layer. This method provides both geometrically enhanced emitter-type structures, as well as a greater phosphorous concentration than what is otherwise obtainable on a (100) oriented substrate, hence producing significantly improved contacts than other contacts to n-type (100) substrates without micro-structures. For (111) oriented substrates, the formation of metal contacts has been studied and often used throughout the literature. While much work in this area treats these metal contacts as ohmic in nature due solely to the nature of the heavy n-type doping and subsequent formation of titanium carbide contacts, unique approaches to further reducing this specific contact resistivity can be seen in [29] and [48, 47]. In the first such case, thermal graphitisation of the diamond surface is used to provide an additional intermediate layer for the formation of ohmic contacts, achieving an order of magnitude reduction in the specific contact resistivity when compared to the titanium carbide contacts [29]. In the more recent work by Valappil et al., coaxial arc plasma deposition (CAPD) is used to form nanocarbon electrodes which show a similar order of magnitude improvement over the conventional titanium contacts.

One technique that has not yet been utilised for the reduction in specific contact resistivity on heavily phosphorous doped diamond is that of laser processing for the purpose of graphitisation. Laser processing offers numerous advantages over the procedures of nanocarbon CAPD, or thermal graphitisation, such as the ability to directly pattern working contacts without standard photolithography steps, the ability to write 3D structures such as wires passing through the diamond substrate for diamond detectors [6], and the ability to also create waveguides within the diamond substrates through modification of the local refractive index [11]. While unrelated to power electronic applications, it is also worth noting that this process can also be used to generate point defects within diamond substrates, which can be used to generate single negatively charged nitrogen-vacancy (NV^-) centres, and have a wide array of potential applications in magnetometry [22], single photon sources [4], quantum centres [49], etc [10]. The combination, or specific usage of any of these key features allows for a large range of device structures to be fabricated by laser graphitisation processes. For a complete review of laser graphitisation, please see section 2.3.

4.1.3. Field Effect Emission

A device structure that may particularly benefit from 3D laser graphitisation is that of the cold-cathode type structure. As described in the seminal work by Spindt et al. [40], it is possible to induce cold-field effect emission with sufficiently sharp (geometrically enhanced) structures. This structure was then proposed to be used in conjunction with the negative electron affinity of hydrogen-terminated diamond [18], allowing for lower applied voltages to generate practical electron sources that could compete with thermionic emitters. Significant issues with this design structure arise during the fabrication of such structures,

due in large part to the etching process and overgrowth of heavily n-type diamond. Parallels could be drawn between the fabrication of these structures and the work of [44], where a random distribution of Ni-etched pits are overgrown with heavily phosphorous doped diamond, and finally contacted with standard Ti/Au contacts. However, the fabrication of emitters as in Geis et al [18]. requires the emitters to be fabricated such that the tips are perpendicular and very close to the surface of the diamond emitters. Any spacing between the tip of the cathode-emitter and the hydrogen terminated diamond surface will result in a large potential difference drop between the cathode and the anode, reducing the effective field strength at the tip and hence significantly affecting the field effect emission of such a device. In practice, this narrow spacing is extremely difficult to achieve via etching, as dislocations or other defects in the diamond substrate will generate fault lines for the etching process, drastically altering the etching rate. Several alternative approaches have been attempted in recent history. Significantly, several devices have been suggested which attempt to either create sharp diamond cathodes [12], etching back substrates [35], or utilising designs that allow for carbon nanotubes to be employed. There is a notable overlap in device designs that attempt to fabricate emitters based on diamond and graphite [30, 34], carbon nanotubes [13], diamond-like carbon layers [19], amorphous carbon [15], or diamondoid monolayers [52], all of which were designed prior to the development of 3D laser graphitisation processes. Ultimately, all such devices present insufficient properties or flaws, and this area of research is ongoing.

4.1.4. Laser Written Geometrically Enhanced Emitters

A natural proposition for 3D micron scaled laser graphitised wires within diamond such as that demonstrated within [41] is that of cold-cathode type devices. While a practical device that can compete with either one of the aforementioned designs or silicon-based devices is ambitious, as the phosphorous doped CVD growth of diamond and the laser graphitisation processes continue to mature, future devices which make use of these capabilities to generate cold-cathode structures with only one laser processing step may start to appear achievable. This would eliminate the need for many of the processing steps such as the deposition of Ti-C based ohmic contacts, or the need for various etching steps and differing metal depositions to produce sufficient gate electrodes in the triode structure. It also addresses the issue of thin electronic grade diamond samples being required for a suitably narrow region between the emitters and the hydrogen terminated diamond surface, which brings about a host of practical processing concerns. Also note that the requirement of electronic grade diamond for carefully controlled, reliable etching procedures is also tentatively eliminated, as the priority can instead be given to high quality phosphorous doped diamond substrates, benefiting the reduction of Schottky barrier height at the graphite/diamond interface. An additional benefit of such devices would be that of the reduction in cost for suitable diamond substrates, as electronic grade material remains a rare product moving into 2025.

Hence, experimental work was planned by the candidate to examine both the effect of laser processing for the purpose of reduced specific contact resistivity ohmic contacts, and to also explore the possibility of laser written structures utilising an emitter type design.

4.1.5. Laser Graphitised Device Design

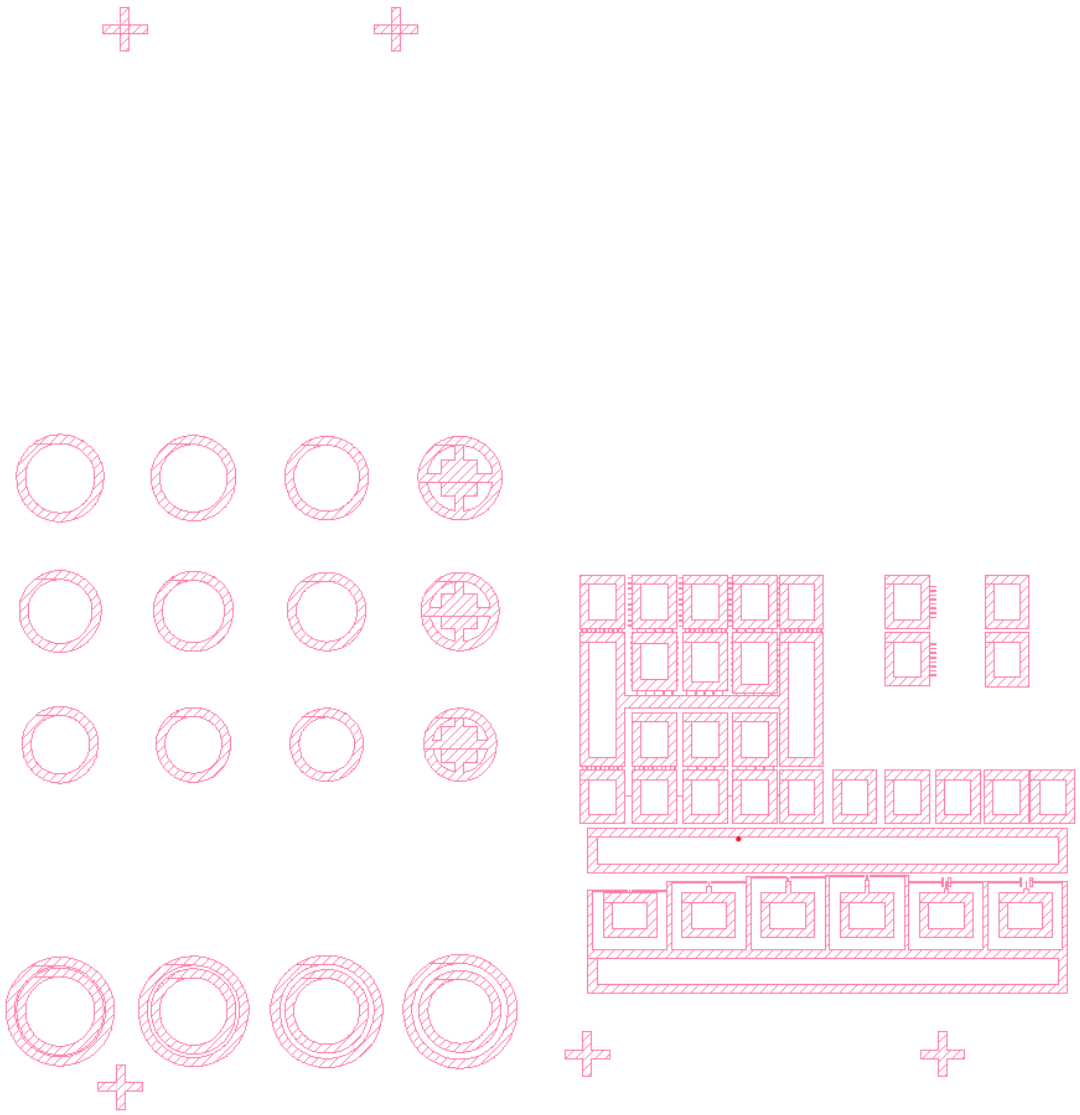

Figure 4.1 An overview of the laser graphitisation design, including alignment markers for potential photolithography steps and various device structures as described in this section.

To test the reduction of specific contact resistivity via laser processing and the preliminary concept of laser graphitised emitters, the laser graphitisation layout as shown in figure 4.1 was designed by the candidate. Various strategies were employed to allow for the testing of various specific features. Of particular note are the LTLM structures, CTLM structures and the emitter array seen as an array of rectangular contacts. This allowed for some redundancy in the devices, and the direct comparison between different devices. The best example of this is between the LTLM array, which is a simple rectangular arrangement of contacts with channel spacings between 2–9 µm, and the emitter arrays, which had

similar rectangular contacts to the LTLM array, but with protruding emitters between the two contacts. The comparison between planar contacts and these geometrically enhanced contacts can then be compared to look for signs of field effect emission due to the sharp emitter features.

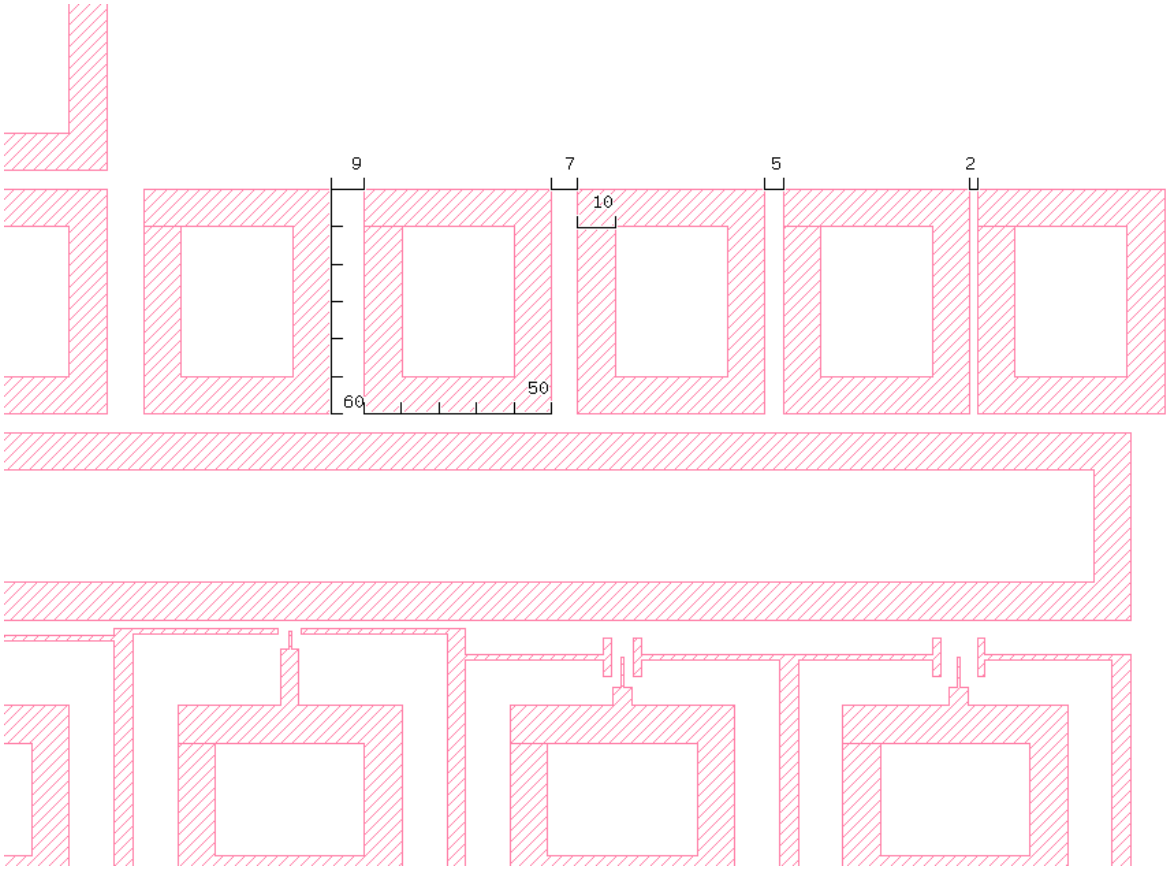

Figure 4.2 A close up of the LTLM design, including scale measurements of relevant feature sizes for clarity.

4.2. Laser Graphitisation Fabrication

Laser graphitisation of diamond surfaces allows for significant advancement in the fabrication of diamond-based electronic devices. This technique leverages focused laser beams to convert specific regions of the diamond substrate into graphitic material, facilitating the creation of conductive pathways and contacts essential for device functionality. Precise control over the graphitisation process enables the fabrication of complex structures, such as wires and contact pads, with tailored electrical properties. For a full review of this technique, see chapter 2.3. The laser fabrication of the following sample as tested in this chapter was performed at Oxford University in collaboration with Patrick Salter and Ravi Shivaraman, using the mask designed by the candidate.

4.2.1. Laser Fabrication Processing

The laser graphitisation process employs a state-of-the-art Pharos laser system, operating at a wavelength of 515 nm. This system is characterised by its high repetition rate of 10 kHz, which is crucial for achieving consistent graphitisation across the targeted areas. The choice of objective lens and the adjustment of laser pulse energy play significant roles in defining the morphology and conductivity of the graphitised structures.

4.2.1.1. Laser Parameters and Setup

The fabrication of graphitic wires and contact pads utilised objective lenses with numerical apertures (NA) of 0.75 and 0.5, respectively. The higher pulse energy facilitated by the 0.75 NA objective lens is preferred for creating wider wires, while the 0.5 NA lens is suited for processing the contact pads. Notably, the sequence in which these components are fabricated; starting with the contact pads before the wires, was observed during initial processing to influence the wire morphology, particularly near the pads. This suggests that the local thermal and structural changes induced by the pad fabrication can affect subsequent graphitisation steps.

4.2.1.2. Calibration of Pulse Energy

The precise calibration of pulse energy is critical for optimising the graphitisation process. Although initial settings were based on angular adjustments of the waveplate, detailed calibration is necessary to correlate these settings with specific pulse energies. This calibration ensures that the laser energy delivered to the diamond surface is precisely controlled, minimising damage to surrounding areas while maximising the quality and conductivity of the graphitic structures.

4.2.1.3. Limitations

The laser graphitisation process, while highly effective for creating conductive pathways in diamond, is subject to several limitations that impact the precision and consistency of the fabricated structures. These limitations arise from both the inherent properties of the laser system and the physical constraints of the graphitisation or amorphous carbon generation process. Hence, in this section the following topics are discussed in further detail: the laser spot size and resolution, laser power and thermal effects, defect density and graphitisation efficiency, lithography alignment and overlay accuracy, scalability and throughput.

Laser Spot Size and Resolution The minimum feature size achievable with laser graphitisation is limited by the laser spot size, which is determined by the wavelength of the laser and the numerical aperture of the objective lens. For the Pharos laser system used in this work, the spot size is on the order of a few micrometres [36]. This limits the

resolution of the graphitised structures, particularly for devices requiring sub-micrometre features, such as field-effect transistors or nanoscale interconnects. The diffraction-limited minimum spot size for femtosecond lasers is typically around 1–2 micrometres, which restricts the ability to create nanoscale features without advanced beam shaping techniques or nonlinear absorption effects [43, 27, 1, 2, 37]. The minimum conductive wire thickness of 400 nm as demonstrated in previous studies [41] was used to define a minimum feature size of 500 nm, ensuring that the effective resistivity of written material would be sufficiently low enough to provide a conductive pathway.

Laser Power and Thermal Effects The graphitisation process relies on the precise delivery of laser energy to the diamond surface. However, variations in laser power or fluctuations in pulse energy can lead to inconsistent graphitisation depths and morphologies [51]. Additionally, excessive laser power can cause thermal damage to the surrounding diamond lattice, leading to unintended graphitisation or cracking [21, 51]. This is particularly problematic for devices with closely spaced features, where thermal diffusion can affect adjacent structures [50]. Femtosecond lasers, while minimising thermal effects compared to nanosecond or picosecond lasers, still generate localised heating that can alter the diamond's structural integrity [1]. The challenge lies in balancing the laser fluence to achieve sufficient graphitisation without inducing thermal damage.

Defect Density and Graphitisation Efficiency The efficiency of the graphitisation process is highly dependent on the defect density within the diamond lattice. As discussed in section **??**, graphitisation is seeded by pre-existing defects or inclusions [51]. In high-quality, low-defect diamond substrates, the graphitisation process may be less efficient, requiring higher laser fluences or multiple passes to achieve the desired conductivity [41]. This can increase the risk of thermal damage and reduce the overall yield of the fabrication process. The presence of intrinsic defects, such as nitrogen vacancies or substitutional impurities, significantly lowers the ablation threshold and enhances graphitisation efficiency [1]. However, in high-purity diamonds, the lack of such defects necessitates higher laser fluences, which can lead to uncontrolled graphitisation and surface roughness [9].

Lithography Alignment and Overlay Accuracy The alignment of laser graphitised structures with pre-existing features, such as metal contacts or doped regions, is critical for device functionality [26]. However, the lack of integrated lithography capabilities in the laser system limits the alignment accuracy. Misalignment between graphitised features and other device components can lead to poor electrical contact or device failure. This limitation highlights the need for improved alignment techniques or hybrid fabrication approaches that combine laser graphitisation with conventional lithography. The paper by Ali et al. [1] discusses the challenges of achieving precise alignment in femtosecond laser micromachining, particularly for complex device architectures. Advanced alignment systems, such as real-time monitoring and feedback control, are being developed to address

this issue, but they remain an area of ongoing research. A specific issue addressed by the team at Oxford for this project was the slight misalignment angle of the [1 1 1] oriented surface, perhaps due to the polishing process following diamond growth. This was addressed via refocusing of the laser spot to account for the change in elevation as the fabrication was undertaken, resulting in an evenly written surface structure.

Scalability and Throughput The laser graphitisation process is inherently serial, with each feature being written sequentially. This limits the scalability of the technique for large-area devices or high-throughput fabrication. While the high repetition rate of the Pharos laser system (10 kHz) mitigates this issue to some extent, the process remains time-consuming for complex devices with numerous graphitised features. Parallel processing techniques or the use of multiple laser beams could address this limitation in future work. Femtosecond laser systems with high repetition rates (up to several MHz) and multi-beam setups are being explored to improve throughput [1]. However, these systems require precise synchronisation and beam control to maintain machining quality, which remains a significant technical challenge.

Despite these limitations, laser graphitisation remains a powerful tool for fabricating diamond-based electronic devices. The ability to create conductive pathways directly within the diamond lattice, without the need for additional materials or complex processing steps, offers significant advantages for applications requiring high thermal conductivity, chemical inertness, and radiation hardness. Future improvements in laser technology, alignment techniques, and process control are expected to further enhance the capabilities of this fabrication method [1, 2].

4.2.1.4. Significance of Laser Processing Parameters

Finally, the choice of laser parameters, including the repetition rate, pulse energy, and objective lens, directly impacts the efficiency and outcome of the graphitisation process. These parameters determine the depth, width, and electrical properties of the graphitic structures, influencing the performance of the final diamond-based devices. It is also important to note that the sample used here is different to that found in previous studies [41], [37], the samples are (1 1 1) oriented HPHT substrates, with a highly phosphorous doped surface layer of ~ 1.2 µm thickness, whereas work in the literature is performed on (1 0 0) oriented, undoped CVD substrates.

This subsection has outlined the foundational aspects of the laser graphitisation fabrication process, highlighting the critical role of laser parameters in achieving desired structural and electrical characteristics. Further characterisation techniques, such as AFM, PL, and Raman spectroscopy, are used to provide deeper insights into the quality and properties of the graphitised diamond, which will be discussed in the subsequent sections.

4.2.2. AFM Characterisation

AFM was used to provide broad overviews of the resulting structures following the fabrication at Oxford. These scans allowed for the examination of key features such as trench depth, surface roughness, and the overall morphology of the laser-graphitised regions.

4.2.2.1. AFM Rationale

AFM was chosen to characterise the surface topology of the laser-graphitised devices due to its ability to provide precise three-dimensional topographical data, including depth measurements, which are critical for understanding the graphitised trenches and contact structures. While scanning electron microscopy (SEM) excels in lateral characterisation and high-resolution imaging of surface features, it does not provide the same level of vertical resolution or quantitative height information as AFM. The ability of AFM to measure surface roughness, step heights, and trench depths directly was deemed essential for this study, even though it may not fully exploit the lateral imaging capabilities of SEM. This choice was driven by the need for detailed topological characterisation, which is crucial for evaluating the quality and consistency of the laser-written structures.

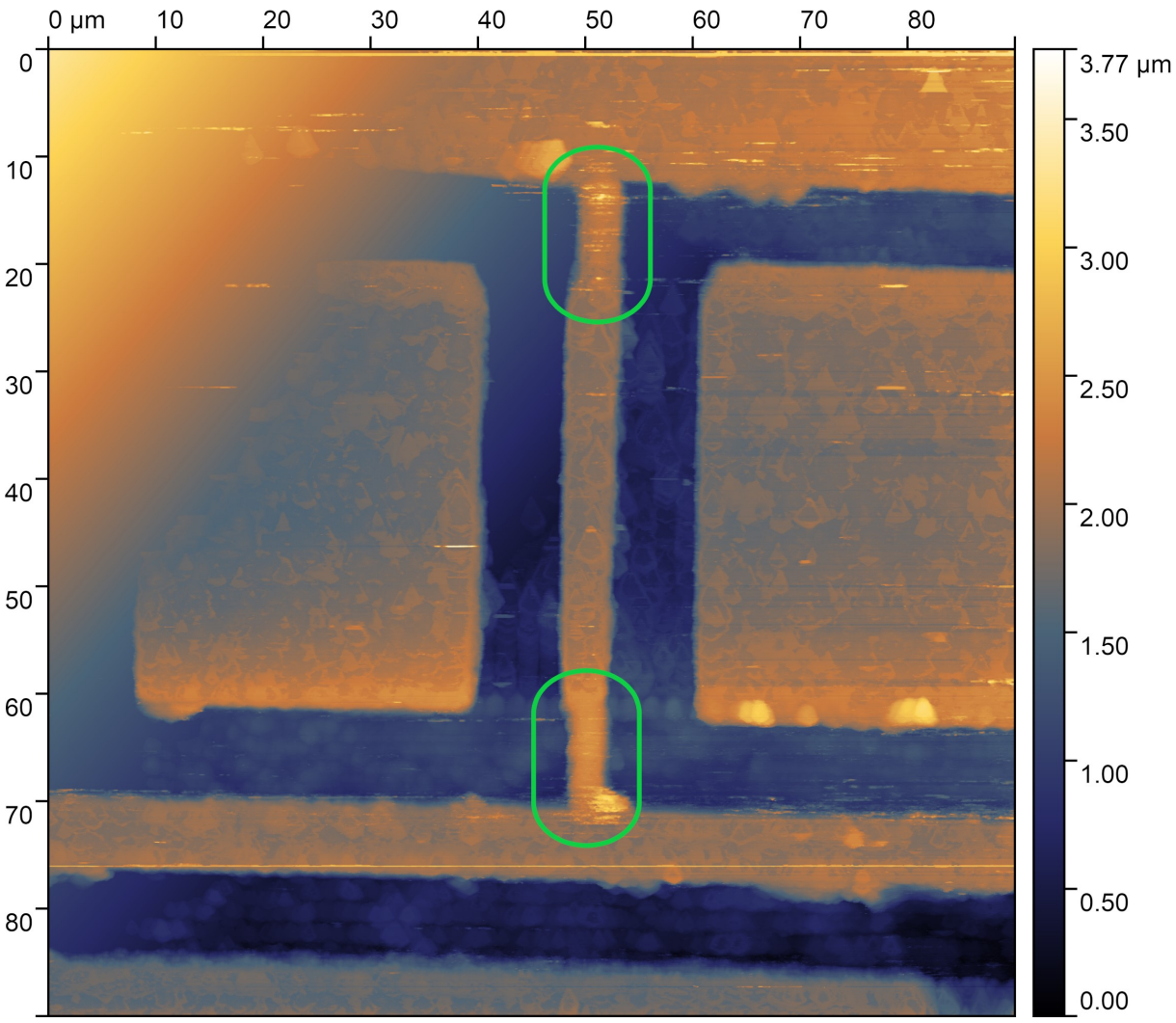

Figure 4.3 A large area AFM scan of the LTLM channel that was designed to have a spacing of 2 µm.

Figure 4.3 shows a broad scan of the LTLM contacts that were designed to have a spacing of 2 µm. The top left corner of this scan experienced a systematic error, visible as a raised blur. Preliminary low resolution scans of this region did not contain this error, and it can hence be identified as a scanning error unrelated to the sample. Otherwise, the scan managed to achieve a generally high level of detail, despite the 90 µm square area being close to the maximum scan area for the XE-150 system. Of note is the slightly inconsistent channel length between the two rectangular contacts, presented in the exact centre of the figure. At the top and bottom of the contacts, marked by the green capsules, the channel is visibly squeezed in, with the rest of the channel presenting a thicker separation. It is also possible to see that the laser graphitisation has etched down into the diamond surface on the order of 1 µm. This presented a concern that the laser graphitisation process may have etched through the active, phosphorous doped layer of 1.2 µm, with thin graphite walls on the edges of the ablated regions providing electrical contact, in contrast to the intended block of graphitic material in full proximity to the phosphorous doped channel.

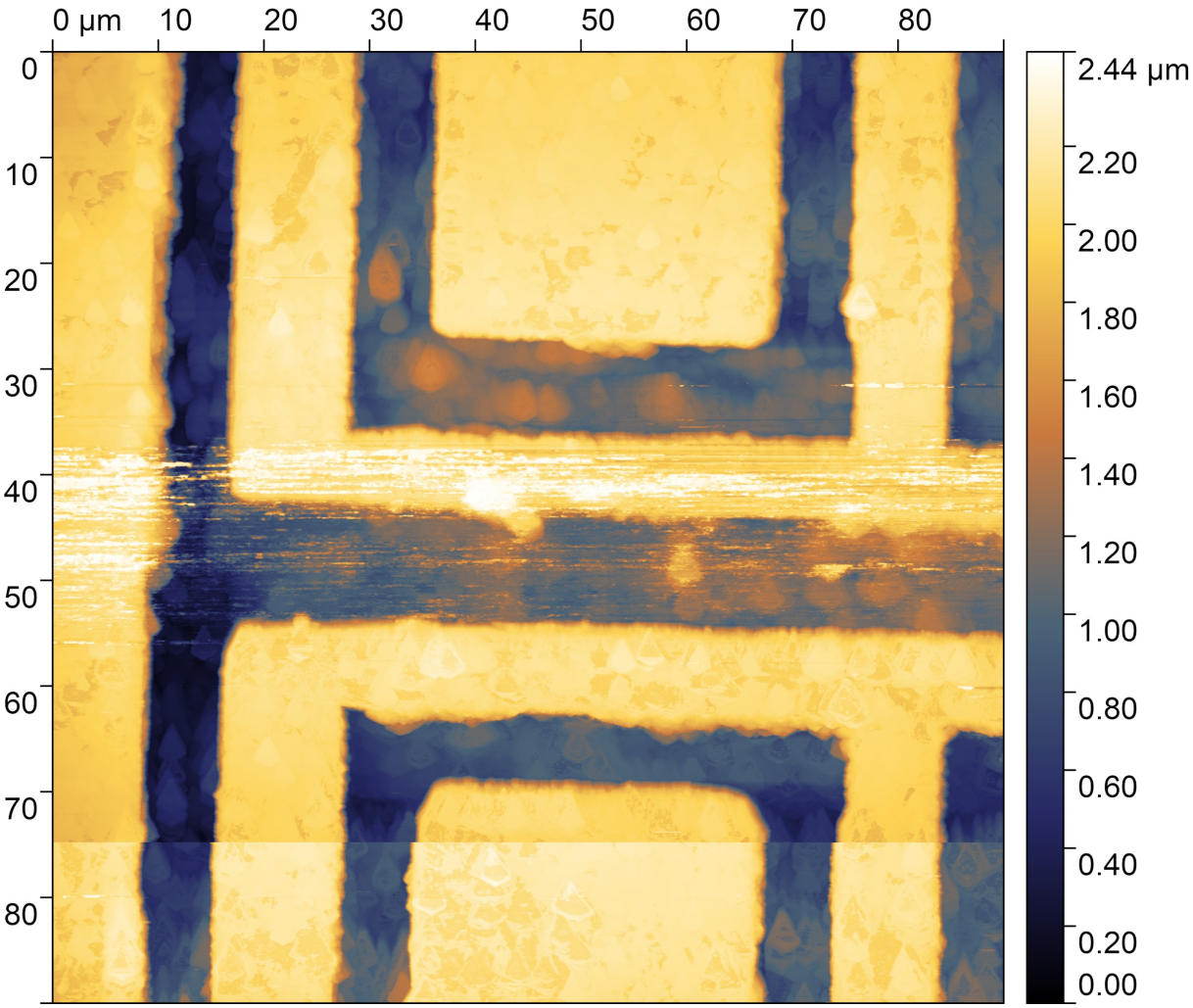

Figure 4.4 A large area AFM scan of the wider graphitised surface wire, with adjacent contacts for emitter array testing.

Figure 4.4 displays a portion of the control surface wire that was included in the graphitisation design for calibration purposes. This surface wire had a designed thickness of 14 µm, to allow for preliminary testing of the written graphite resistivity. While this large scale AFM scan suffers from some noise in the centre of the scan region, it does provide another view of the as written structures, and how they deviate from the design with specific topological features apparent on the sides of the contact wires. The laser written contacts are observed to be up to approximately 2 µm deep relative to the diamond surface, with steep walls at the side of the written trenches.

4.2.2.2. Trench Wall Steepness and AFM Tip Profile

It is important to note one detail in particular of the AFM scans, that of the graphitised trench steepness, or the profile of the trench walls. For the purpose of examining the large area AFM scans, it is necessary to consider more precisely the observed steepness of the written contacts and the possible impact of the AFM tip itself. Figure 4.5 shows a typical ACTA probe as were used in these scans, utilising a rectangular Si cantilever, a pyramidal tip of height 14–16 µm and radius of curvature 6 µm. The exact dimensions of the AFM tip may differ from probe to probe, but the pyramidal tip may have had some impact on the observed steepness of etched trenches due to the widening of the base away from the tip.

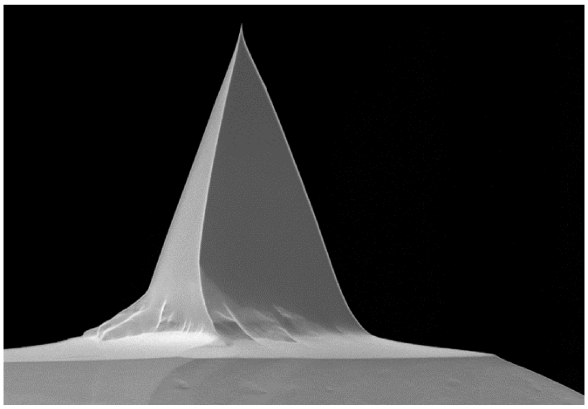

Figure 4.5 An SEM scan of a typical ACTA tip, as provided in the technical specifications sheet by Applied NanoStructures Inc.

In NC-AFM, D-AFM or C-AFM, when the tip passes from the diamond surface into the trench, it will quickly descend, with the rate of descent determined primarily by the chosen drive in the Z-scanner. This is then recorded as an incline and less steep wall, with the exact slope being determined by the scan rate if the tip is in relative free-fall after leaving the diamond surface. Equally, when the tip is instead passing from the trench and encounters the trench wall, it may detect the wall itself well beyond the point of the tip coming into contact, due to the pyramidal base meeting the wall first. The piezoelectric system will hence raise the tip, as it detects the side wall with the pyramidal base as for the tip. In this situation, the scan rate may also lead to the risk of direct collision between the pyramidal base and the sidewall, ultimately leading to damage of the AFM tip.

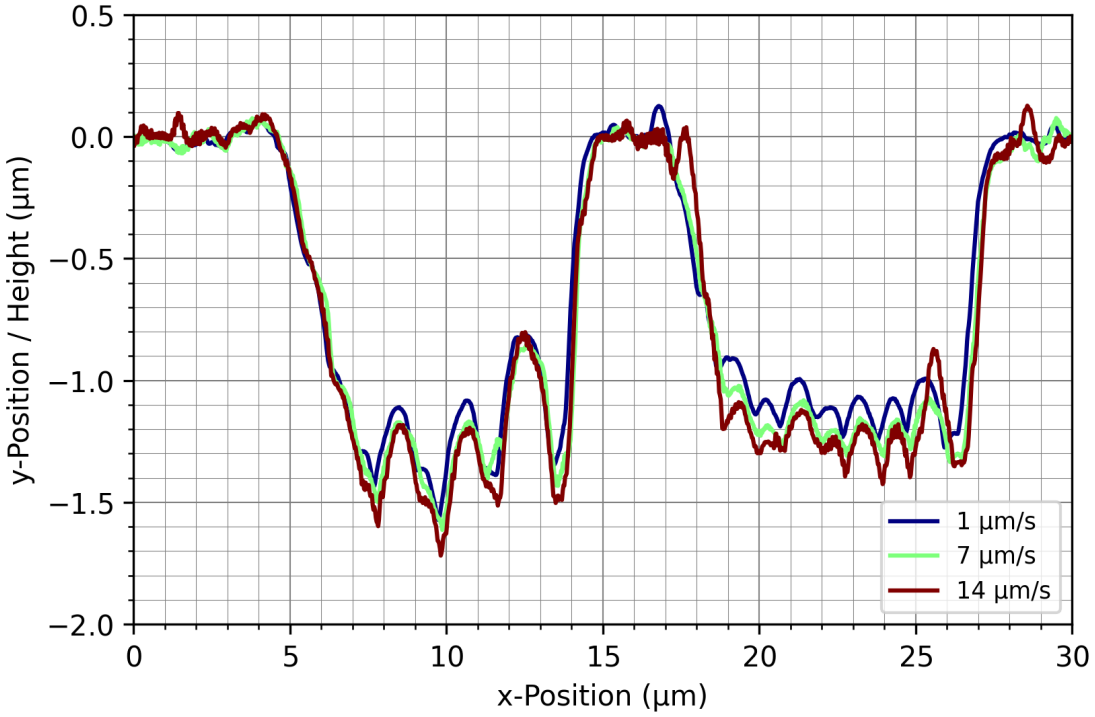

Figure 4.6 A comparison of three different NC-AFM scan rates on a laser graphitised trench structure. The data are planarised based on the first and last data points, to represent the estimated diamond surface level.

Figure 4.6 has a few notable features which demonstrate this process when using NC-AFM. First, all three scan rates have distinct peaks and troughs as they pass through the laser graphitised channels. The sharp, triangular troughs perhaps directly reflect the triangular AFM tip in action when it meets a sharp drop in the z-axis. Second, it is clear that the direction of the scan impacts the observed edges of the graphitised trenches. In this figure, the scan is passing from the left to the right. While the first trench appears to have a relatively low slope, with agreement between all three scan rates, the descent into the second trench has a notable discrepancy between the two lower scan rates and the highest included scan rate of 15 $\mu m s^{-1}$. In contrast, the walls as seen by the ascending AFM tip are in relative agreement, as they all encounter the wall and must ascend very quickly to ensure that the tip does not impact the wall. It is also notable that the observed trench depth decreases as a function of the AFM scan rate, indicating that at the lowest scan rates the system is better recognising the correct altitude of the tip, as it has time to adjust based on the specific features within the channels.

4.2.2.3. Further AFM Scans

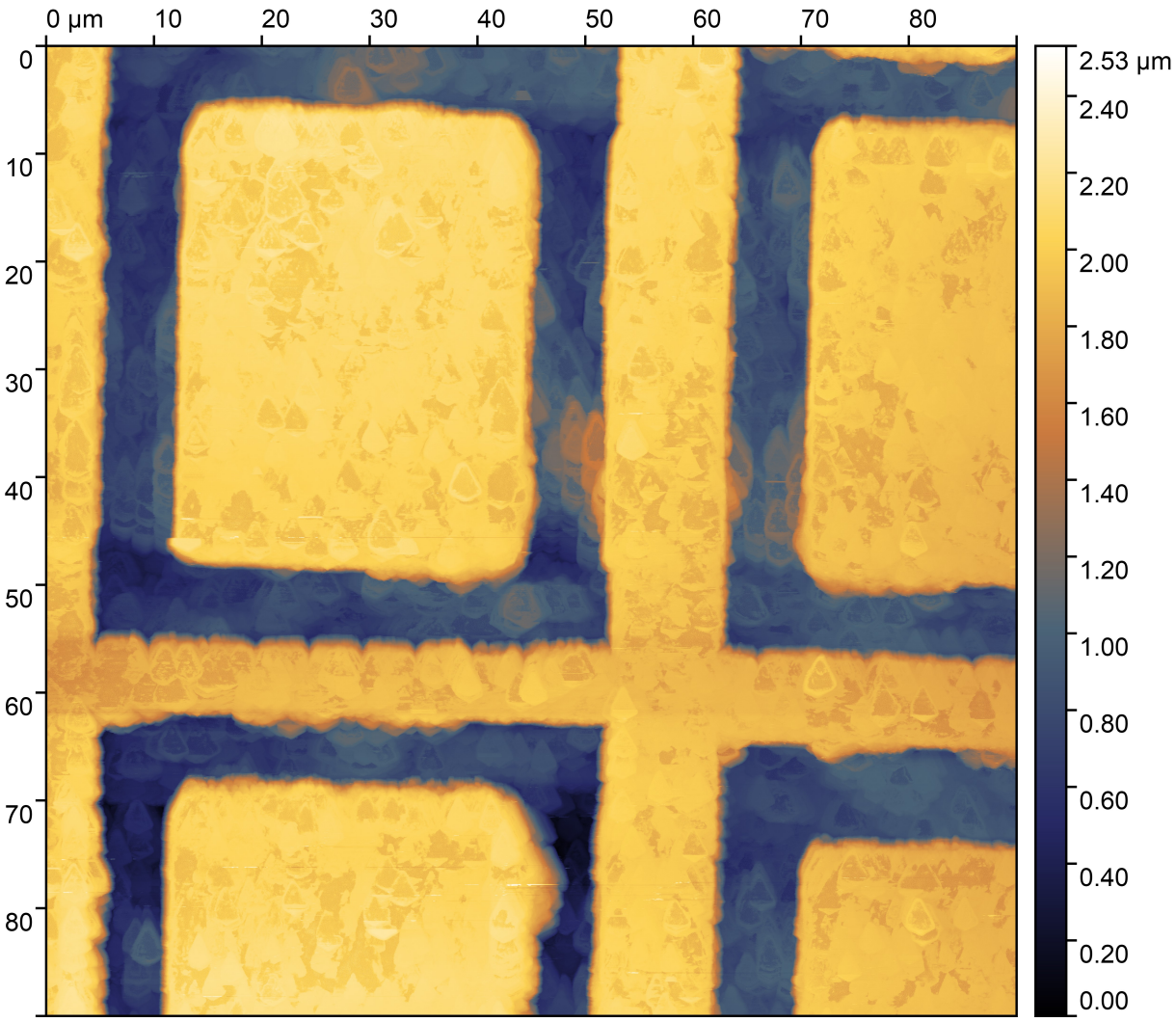

Figure 4.7 A large area AFM scan of emitter array AF that was used for electrical characterisation.

Figure 4.7 shows a large area AFM scan that was taken to examine the effective topology of an emitter array type structure as written via laser graphitisation. In this figure, almost the entirety of contact A (top left) is visible, with contact F directly below (bottom left). In-between these two contacts, extending downwards from contact A, the beginnings of the laser written wire structures are just about visible as depressions in the topology. This also provides another general view of the laser writing process and the sometimes inconsistent structures that are written on the diamond surface. In some places, there are very noticeable protrusions from the sidewalls into the otherwise rectangular etched contact structures. As this is purely a topological scan, this hence displays a lack of ablation in these regions, perhaps due to a lack of graphitisation processes, lower laser absorption, or other changes in the writing process. Similarly, some areas within the contact structures appear to have a greater depth than the majority of written area, perhaps due to a greater

absorption of laser power in these specific regions, or perhaps more readily graphitised and subsequently ablated diamond.

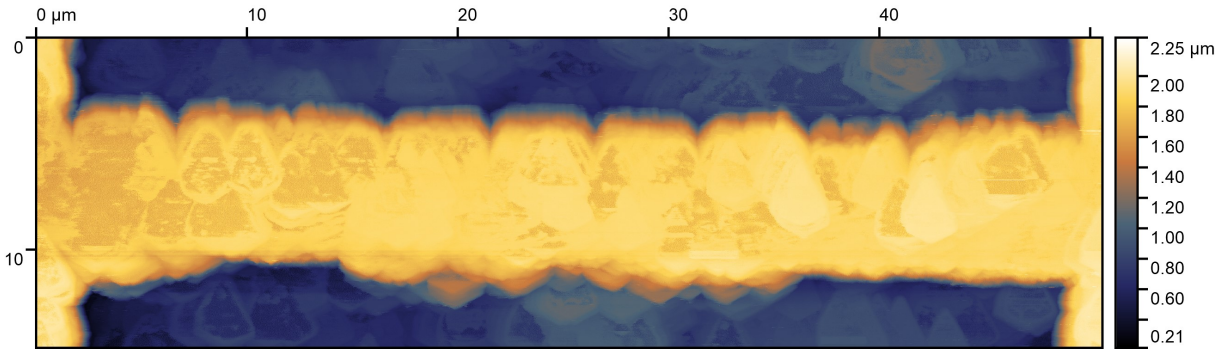

Figure 4.8 A cropped AFM scan of emitter array AF that was used for electrical characterisation.

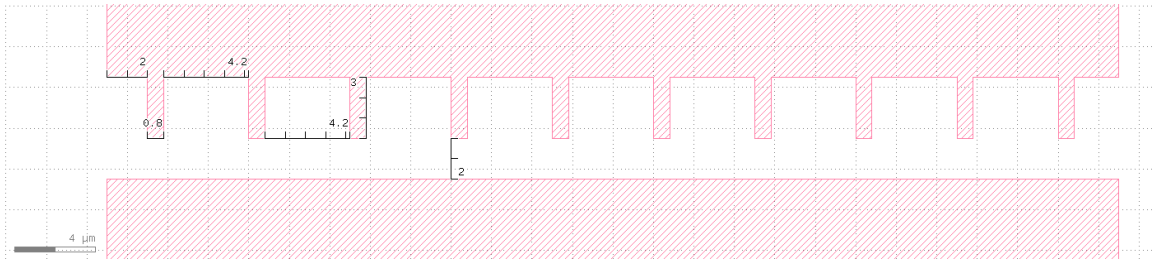

Figure 4.9 A cropped view of the AF emitter array design, with feature size measurements provided.

For clarity, the region between contacts A (upper) and F (lower) is cropped down and expanded in figure 4.8. When compared directly with the designed array in figure 4.9, the topology does not directly reveal the presence of 0.8 µm width emitter wires extending down towards contact F. However, it is possible to see what may be the very start of all but the two outer emitter wires, with notable triangular depressions extending nearly as deep as the larger width contact structures.

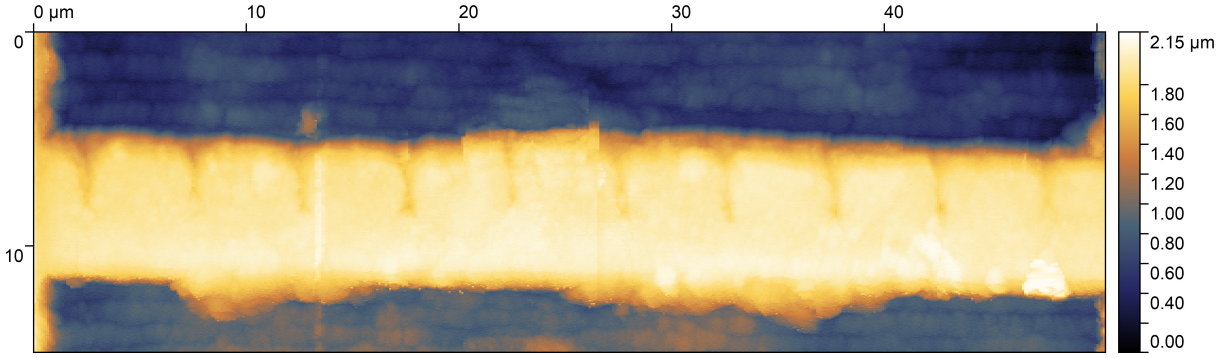

Figure 4.10 A cropped AFM scan of the CH emitter array, with scan direction parallel to the emitter wires (y-axis).

Figure 4.10 shows another of the emitter array structures that were fabricated on the diamond surface. In contrast to the unclear topology observed with array AF, array CH appears to clearly demonstrate the presence of ablated diamond, and hence the fabrication

of emitter wires leading down from contact C into the channel towards contact H. As observed in the wider AFM scans, the intended rectangular contact design for contact H in particular displays some deformation, with notable incongruities along the top of the graphitised region. The success of this AFM scan in displaying topographical results may be attributed to the y-axis scan direction, which is the fast direction. Based on the general observation from scan rate testing that higher scan rates will tend to show a lower slope of descent, and a higher angle of ascent, one clear practical approach to accurately detecting sub-micron thickness graphitised wires is to scan along the length of the emitter, rather than across the width. This ensures that the tip does not need to descend into the emitter channel, and instead as it passes down from the contact region, it will tend to only require a raised elevation as it progresses. When running in the reverse direction (up from contact H), again only one clear descent is necessary to enter the emitter channel, where the tip then remains as it passes down the channel. Hence, the slow scan rate direction is then across the width of the emitters, and is best able to detect any change in topology. A further detail with this approach is that this requires a suitable pixel density, as the number of pixels across the width of the emitter channel directly translates to the number of points along the length of the emitter where the tip will travel, measuring the depth of ablated material. Hence, in this example with a fast scan rate of 7.5 $\mu m\,s^{-1}$ and a raw scan size of 62 µm x 15 µm, to observe emitter widths of 0.8 µm, the effective pixel width must be below 0.4 µm to ensure that the AFM tip does indeed enter the graphitised emitter channel, in a near central location. For this scan a pixel width of ~ 0.24 µm appears to have been sufficient to positively identify ablation related to the formation of graphitised emitters, especially combined with the slow scan rate direction and the top-down AFM tip pass scan direction.

The design of emitter array CH was otherwise very similar to AF, with 10 emitter cathodes of width 0.8 µm spaced 4.2 µm apart across the 60 µm contact structure (C). The only difference was in the cathode-anode spacing, due to a slight shortening of the emitter wire, which in the case of AF was 2 µm, and for CH was 2.5 µm. Preliminary low resolution AFM scans indicated that array CH was one of the clearest examples of the intended emitter structure, and so this was selected for electrical characterisation alongside AF.

4.2.3. Fluorescence Characterisation

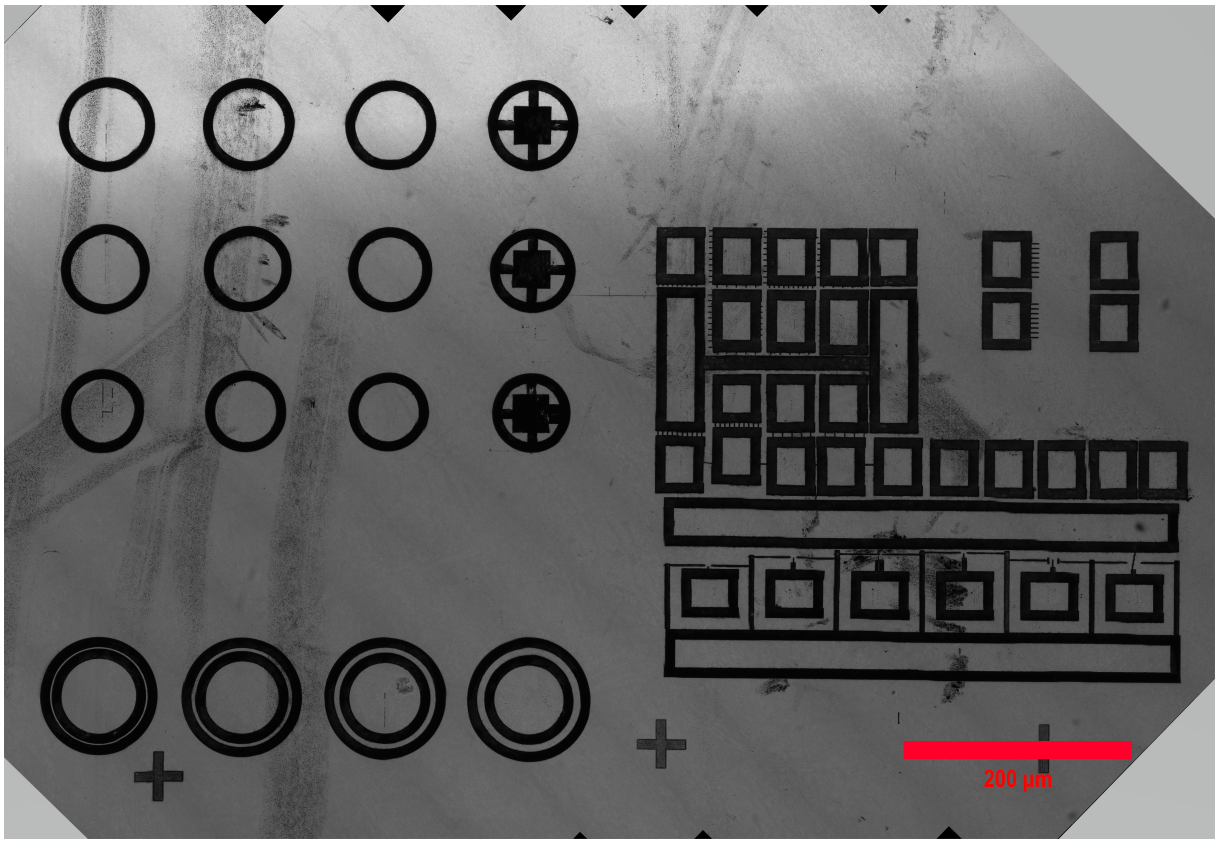

Figure 4.11 An overview of the laser graphitised structure as seen using a backlit 488 nm light source and mapping with a confocal microscope.

One possible source of material characterisation is that of fluorescence. Figure 4.11 shows the optical overview provided by the Zeiss LSM 800 system, providing a grouped map of confocal scans that allows for near-diffraction-limited imaging across the entirety of the laser-written structures. The images provided by this system allow for good optical comparisons with the topological AFM measurements, with the change in observed 488 nm absorbance due to the graphitisation or amorphisation of carbon perhaps providing a more reliable picture of how well the fabrication of the thinnest laser treated features have formed. Further to this, diamond fluorescence centres offer a unique examination of the composition of diamond defects. In particular, it should be expected that HPHT samples such as those used for the substrates in the current work will have a large concentration of singly substitutional nitrogen, aka C-centres. This imparts the deep yellow-orange colour as is typical for HPHT samples when seen by the naked eye, and is a substantial factor in the characteristic fluorescence of HPHT grown diamonds.

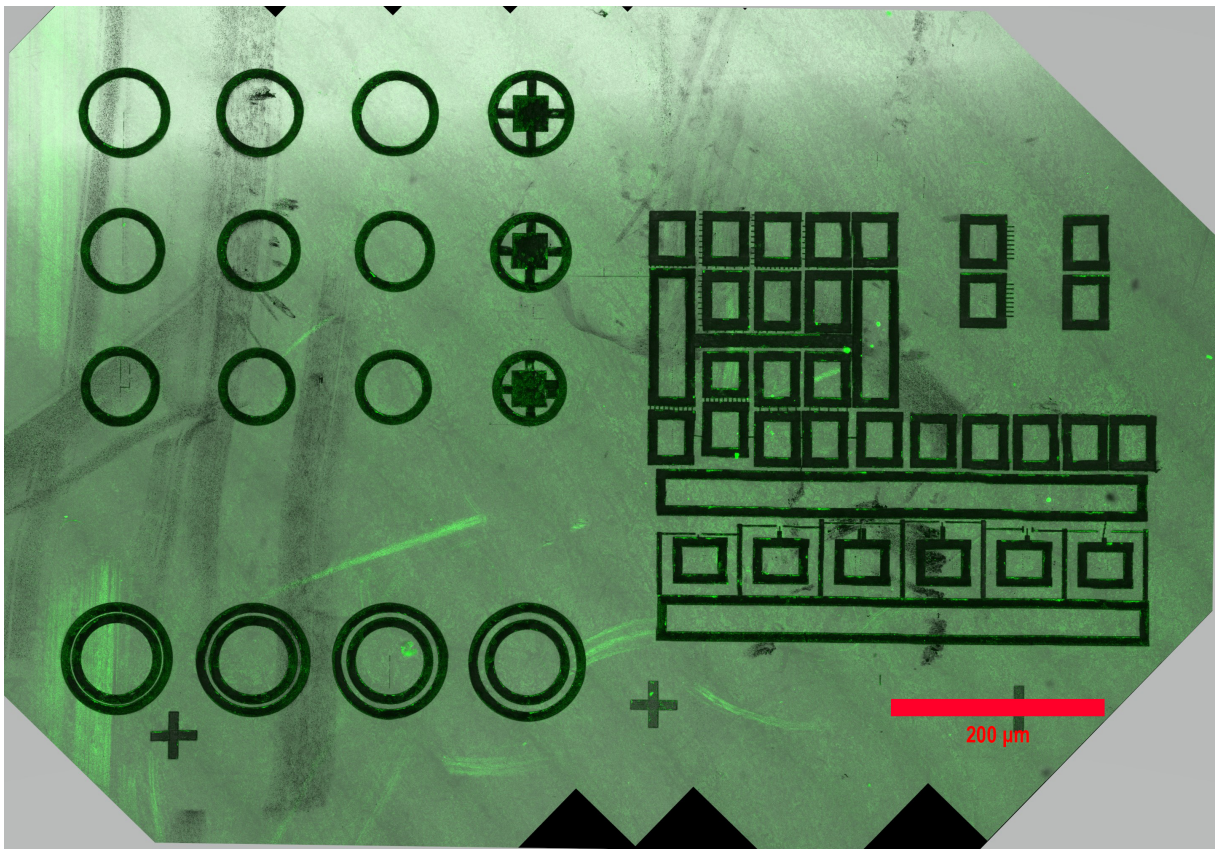

Figure 4.12 A confocal microscope mapping overview of the laser written structures as seen using a backlit 488 nm light source. The green false colour is provided by fluorescence using an excitation laser of 408 nm.

Figure 7.5 shows the overlay of a false colour (green) fluorescence scan with excitation laser 408 nm onto the original 488 nm absorption imaging from figure 4.11. A few observations can be made regarding this experiment, beginning with the clear background fluorescence throughout the sample. This is due to the substrate itself, as is expected for a typical HPHT sample [14, 54]. However, while the background fluorescence has a reasonably steady profile, there are significant deviations visible.

4.2.3.1. Source of Fluorescence

During the setup of the fluorescence imaging shown in this section, a sweep of the fluorescence emission spectrum was performed by utilising the range of colour filters available in the Zeiss LSM 800 system. The available colour filters thus provided an estimate of the wavelength of fluorescence emission within 20 nm ranges, and showed that the most significant wavelength detection was within the 500–520 nm range. The exact defects responsible for the fluorescence that is concentrated on the laser processed portions cannot be determined precisely with the collected data presented here. The exact defect emission wavelengths can differ due to temperature differences, crystal strain and excitation wavelength, making exact identification difficult even under ideal circumstances [23] though more recent applications of machine learning statistical methods allow for much lower error rates [20].

Despite the challenge in defect identification, one possibility that must be considered for the observed regions of intense fluorescence at the edges of laser processing is that of etching through the phosphorous doped surface layer to allow for more light emission from the substrate underneath. This is unlikely, as the AFM appears to show an inverse correlation with the fluorescent laser processed diamond and the height. That is to say that the regions which display discolouration (darkening) and hence an increased concentration of amorphous carbon without deep etching through the phosphorous doped layer also appear to have fluorescent regions in certain locations.

The incorporation of nitrogen into the HPHT grown substrate in the absence of a nitrogen getter is largely dependent upon growth facets, with the growth sectors {1 1 1} containing the highest concentrations of nitrogen [24]. This leads to a clear pattern of colour corresponding to a change in optically active defects, with the sample used for laser graphitisation in this case being no exception to this growth process. A notable observation from figure 7.5 was that of a relatively uniform background fluorescence, alongside the non-uniform, concentrated fluorescence of the laser processed devices. This also implies that the larger concentration of C centres leading to visible colouration of growth facets has not altered the concentration or distribution of fluorescing colour centres within the diamond, though the possibility of fluorescence being due to organic molecules etc cannot be excluded entirely based on this analysis alone.

Defect Type	**Excitation (nm)**	**Fluorescence (nm)**
N3V	365 (LW)	415, 440 (1)
H3 (NVN^0)	365 (LW)	503, 530 (1), 510 (3,4)
H4 (N_4V_2)	365 (LW)	496, 520 (1,3)
480 nm band	365 (LW), varies	480, varies (1), ∼540 (3)
NV^0	532	575 (ZPL) (1,2)
NV^-	532	637 (ZPL) (1,2)
Unknown	Not specified	370-380 (Newly observed) (2)
3H Split interstitial ⟨100⟩	Not specified	504–510, 532 (Paired bands) (2,5)

Table 4.1 Overview of defects in HPHT diamonds, excitation wavelengths (long wave LW, short wave SW), and specific fluorescence wavelengths as discussed in (1) [14], (2) [7], (3) [39], (4) [38], (5) [20].

Table 4.1 provides a general overview of defects observed in diamond fluorescence spectroscopy. This represents only a small sub-sample of the many identified fluorescent defects and a couple of unidentified defects to help illustrate the number of unknowns within this spectroscopic analysis. While effort has been made to associate the observed fluorescence wavelength with the excitation wavelength, this is a parameter which is less commonly reported in full, and so the usage of a 408 nm laser does complicate the direct comparison to literature values. Of particular note for HPHT samples is the general identification of fluorescence when exposed to SW-UV [14, 39], in contrast to the LW dependent fluorescence of natural diamonds. Identification of the exact colour centres responsible for this fluorescence varies from sample to sample, however NV centres of

various charge states are the most likely candidate for the HPHT samples used in this work. Additional defects which should not have appreciable concentrations are included to give a broader overview of diamond fluorescence, with the H3 aggregate in particular providing one potential colour centre in the range observed by the spectroscopic estimate provided with the Zeiss LSM 800 system. This is despite the expectation of a lack of nitrogen aggregation in typical (111) HPHT diamond due to the growth process itself [8]. Another possibility is the unintentional introduction of NV colour centres via laser processing [10], which may then be possible to see around laser processing for device manufacturing.

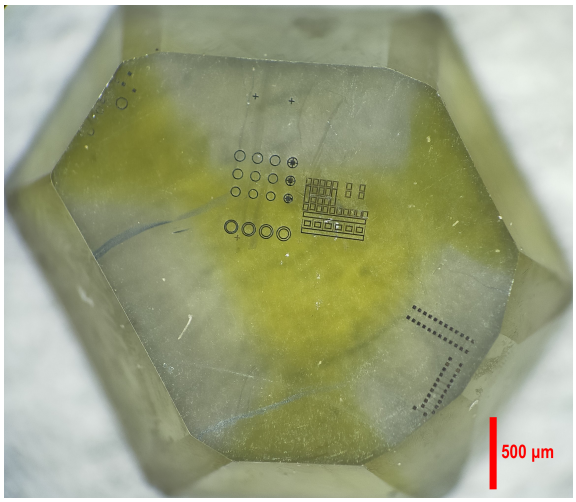

(a) Typical frontal white LED illumination.

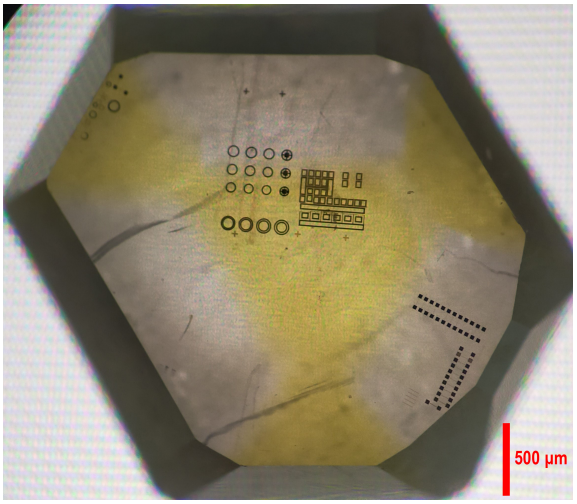

(b) Back-lighting provided by a RGB array.

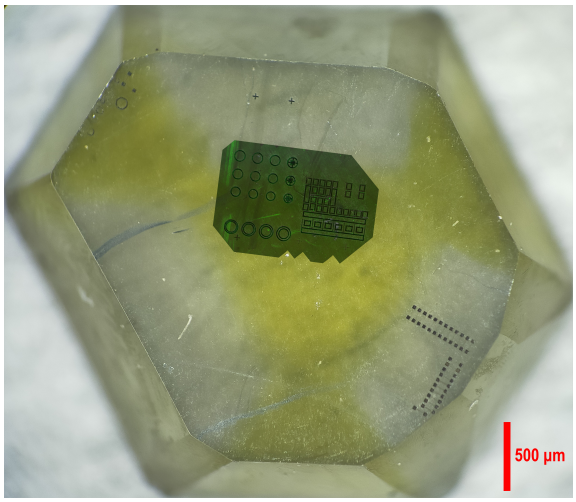

(c) Frontal illumination and fluorescence overlay.

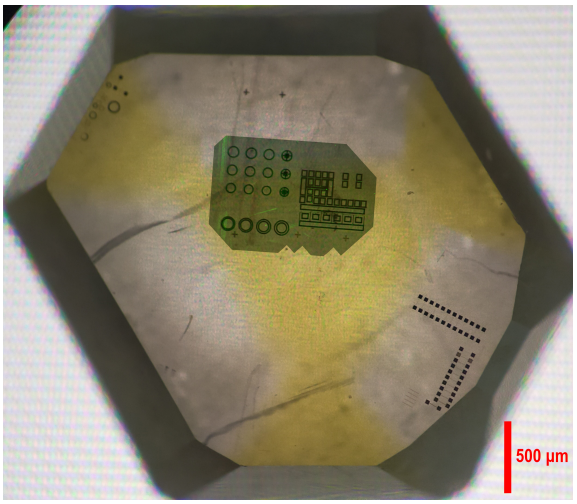

(d) Back-lighting and fluorescence overlay.

Figure 4.13 Sample G as seen with a 3.6X magnification optical microscope, either direct front facing light or back-lighting, and the fluorescence imaging overlaid on these two images of differing lighting.

Figure 4.13 includes two different approaches to taking optical images of the sample at a macroscopic scale, to demonstrate the visually apparent growth sectors within the HPHT sample. Back-lighting has a significant impact on the clarity and colour of the different growth sectors, as seen in figures 4.13b, 4.13d. In particular, a change in the

substrate background colour can be observed near the top of the laser processed region, and it is possible to pick out the differing growth regions from the HPHT seed crystal.

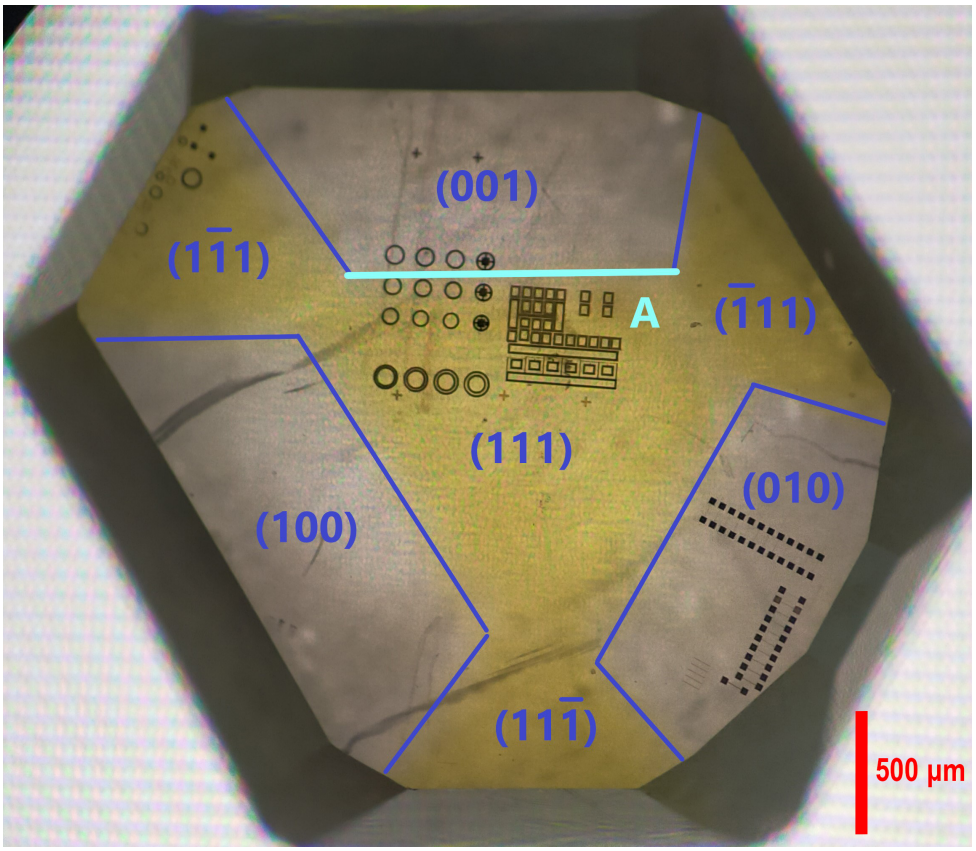

Figure 4.14 An annotated version of the back-lit optical microscope image to highlight growth sectors and the significant change in colouration running through the laser processed region.

Figure 4.14 provides an annotated form of figure 4.13b, to clarify the relevant growth sectors and also highlight the distinct change in colour centres that is observed across line A. Comparisons to the fluorescence reveal that the background fluorescence does not change significantly in density despite this change in absorbed/transmitted light.

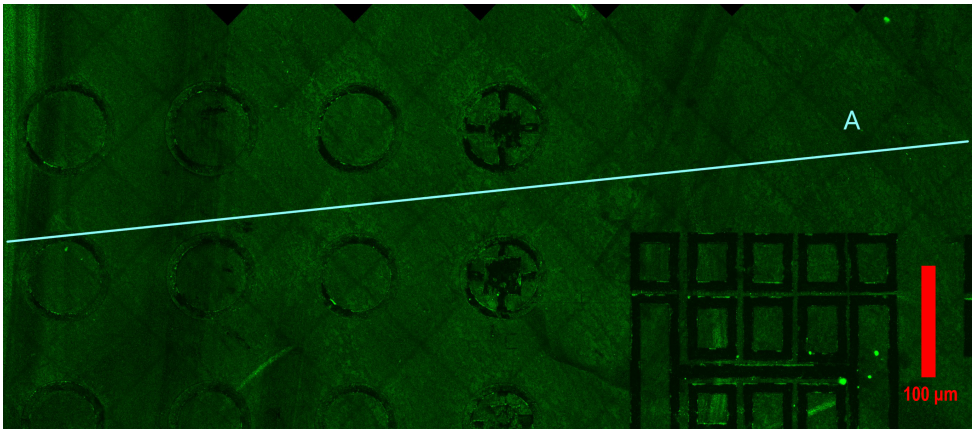

Figure 4.15 A section of the fluorescence microscopy.

In figure 4.15, the section around line A from figure 4.14 is presented to highlight the lack of background growth sector specificity in the observed, relatively constant background

fluorescence. The estimated location of the optically observed growth sector change and subsequent change in nitrogen content is indicated by line A.

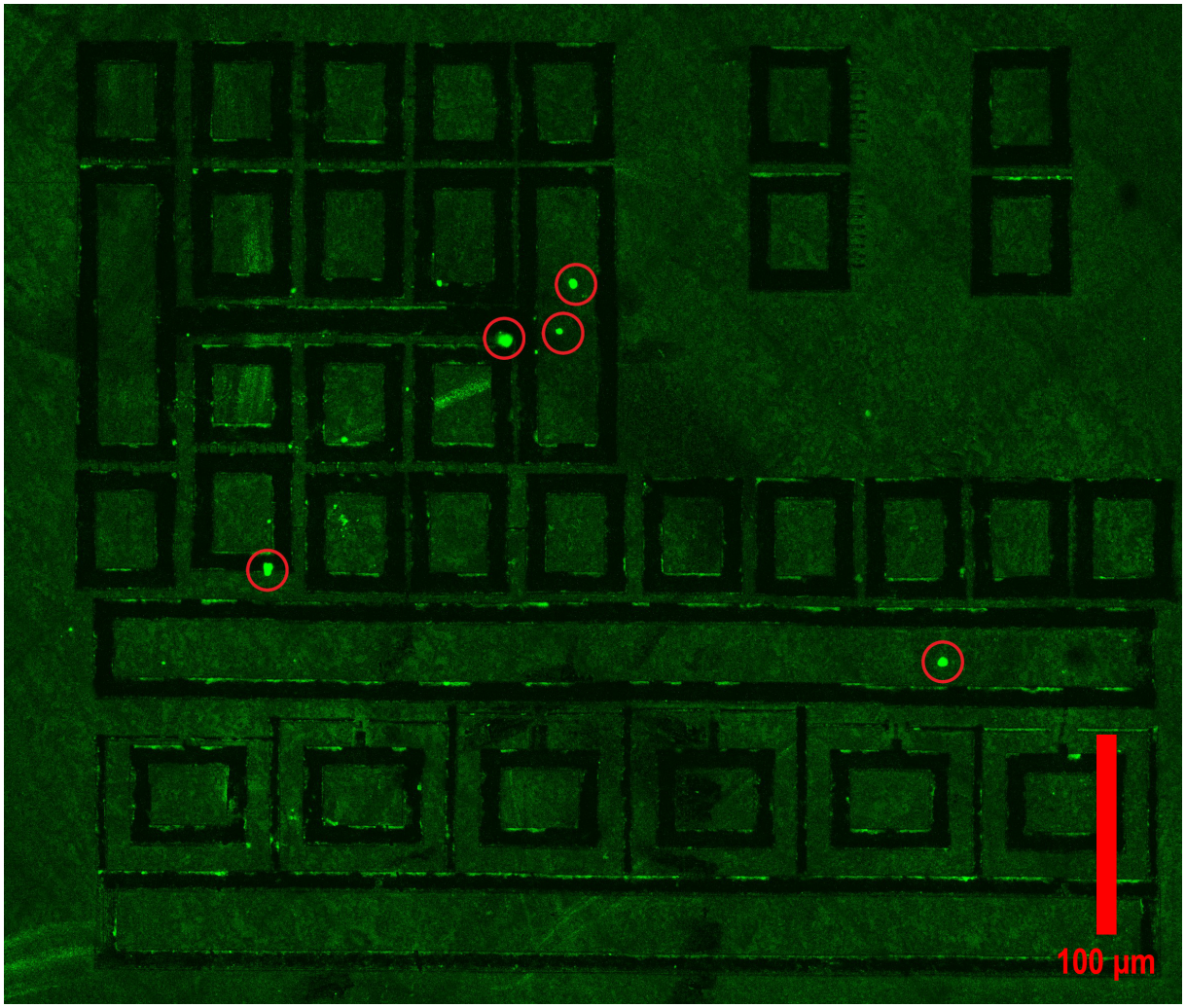

Figure 4.16 A cropped down form of the fluorescent track only, demonstrating the non-uniformity of fluorescence concentrations.

Figure 4.16 takes a closer look at the laser processed region of the sample, with only the fluorescence track from the confocal microscopy represented in this image. Note that while the effective spectroscopic analysis of colour filtering did reveal a fluorescence peak in the region of 500–520 nm, the green colouration of the fluorescence is a false colour applied to all detected fluorescence used to aid in contrast and the actual colouring may differ. Some fluorescence appears to be present on the surface of the diamond sample, marked by the red circles. In select locations it appears to be on the edge of the laser processed material and yet it is also on the unaltered diamond surface. Due to this inconsistency, it is assumed that this fluorescence is neither due to the substrate or the laser processing, and is likely caused by organic surface contamination despite solvent cleaning steps.

Position (cm^{-1})	Typical FWHM (cm^{-1})	Assignment
1332	5–10	first-order diamond Raman line
1355	250	sp^2 (D peak)
1575	100	sp^2 (G peak)

Table 4.2 Raman peaks of interest in diamond and carbon related materials [32, 46].

4.2.4. Raman Characterisation

As outlined in section 2.1.3.3, raman microscopy provides an effective tool for examining the composition of diamond samples. Table 4.2 summarises the relevant peaks of interest for diamond, with the general deconvolution of CVD diamond raman spectra into a diamond line and the D or G modes of amorphous carbon. The relative intensity of diamond to D or G signals is strongly dependent upon excitation wavelength, with the exact mechanisms behind this likely linked to resonance enhancement of the sp^3 component and decreasing resonance in the sp^2 component [32]. Another noteworthy point on excitation wavelength is that the typical rising background seen with excitation sources such as the green argon ion laser at 514.5 nm is commonly attributed to strong photoluminescence from nitrogen-vacancy defects [17]. The laser wavelengths used can be varied depending upon the application, but background subtraction allows for visible peaks even in the case of high background photoluminescence. A laser wavelength of 532 nm was used with the LabRam HR-800 Jobin Yvon at the SAgE analytical facility for the purposes of characterising the laser processed device structures and heavily phosphorous doped surface layer.

One other relevant consideration for raman spectroscopy of samples which have two components, such as amorphous carbon, is the relative polarisability of the components. π bonds formed by sp^2 hybridised carbons have a higher polarisability than that of the σ bonds within sp^3 hybridised carbon, which results in a larger raman cross-section [53]. Additionally, π bonds are resonantly enhanced with visible excitation lasers while σ bonds are not. This tends to lead to a dominance of sp^2 signal in samples where even low ($\sim 20\%$) fractions of sp^2 material is present [16]. To summarise, for single crystal diamond the position and FWHM of the diamond line, and relative intensity of the diamond line to the G and D peaks are used as crude measures of crystallinity [5]. This is due to single crystal diamond only displaying the first order diamond line while grain boundaries in polycrystalline films will produce varying intensities of D and G peaks depending upon the grain sizes [3]. At the extreme of pure graphite, only the crystalline G peak remains, while in all other forms of graphitic materials the disorder D peak appears [46].

4.2.4.1. Amorphous Carbon

Amorphous carbon (a-C) is made up of unstructured mixtures of sp^3 and sp^2 hybridised carbon. The properties of such material is dependent upon the ratio of sp^3 and sp^2 bonding, with amorphous carbon films of high sp^3 content forming a harder material which is more

transparent and of higher resistivity than of materials with high sp^2 content [42]. Films of high sp^3 content are also highly stressed [28], and are hence more likely to delaminate from the substrate surface. Amorphous carbon films can also be hydrogenated, which is quite common for CVD grown films [33]. These hydrogenated amorphous carbon films are softer, more stable, and will tend to be more transparent than hydrogen-free films. There is also a variable range hopping conduction mechanism between clusters of hydrogenated sp^2 carbon in amorphous carbon films which may represent a possible conductive path in the case of laser processed diamond [45].

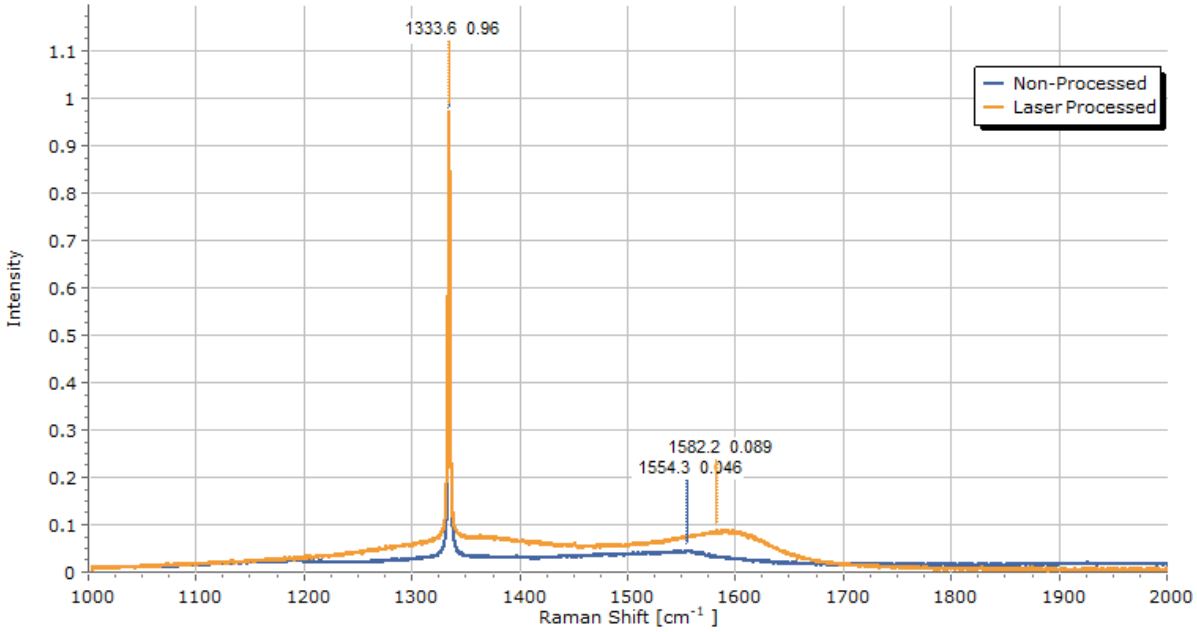

Figure 4.17 Relative intensities of raman spectra for untreated and laser-treated portions of sample G. The spectra are normalised such that the sp^3 peak for both examples is set to 1.

Material Type	Raman Shift (cm^{-1})	Relative Intensity	FWHM (cm^{-1})
Non-Processed	1334	1.00	2.24
Non-Processed	1554.3	0.08	63.81
Laser Processed	1333.6	0.99	2.28
Laser Processed	1582.2	0.12	29.53

Table 4.3 Raman spectrum data comparing non-processed and laser-processed materials.

In figure 4.17, two different raman spectra are plotted, which represent a portion of the sample that has been laser processed, and another region which was well away from any laser processing on the phosphorous doped diamond surface. The exact location used for the laser processed region is indicated by the red square in figure 4.18, which was chosen due to the large radius of laser processed material that surrounds the centre point. While it is not possible to guarantee that the laser spot will only be absorbed and otherwise interact with the visibly darkened, laser affected region of diamond, this location was chosen to maximise any sp^2 raman signal.

The "Non-Processed" region was strategically chosen on the opposite side of the diamond sample (on the same face with a phosphorous doped surface layer), away from any laser-written areas. However, due to the optical transparency of diamond, it remains a slim possibility that any sp^2 raman signal from this location may be due to a distant, laser processed portion.

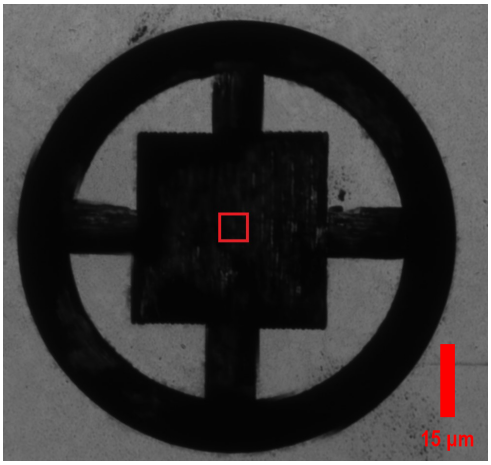

Figure 4.18 A 488 nm confocal microscope image of the raman area, showing the section of the sample under investigation.

As shown in figure 4.17 and table 4.3, there is a shift in what may be considered the G peak, rising from a small hump that may be attributable to the highly phosphorous grown surface layer, to a moderate peak in the raman spectra of laser processed material. Both spectra show a small shift in the 1332 cm^{-1} diamond peak, and they also have a similar FWHM for this line. While there is a visible difference between these two raman spectra, it is difficult to say that the laser processed material represents highly graphitised material, especially compared to the relative shifts that are typical for laser modified diamond [25, 43]. However, the rise in G peak does indicate a change in the material structure due to the laser processing, in accordance with a rise in sp^2 carbon content.

References

[1] Bakhtiar Ali, Igor V. Litvinyuk, and Maksym Rybachuk. “Femtosecond laser micromachining of diamond: Current research status, applications and challenges”. In: *Carbon* 179 (July 2021), pp. 209–226. ISSN: 0008-6223. DOI: 10.1016/j.carbon.2021.04.025. URL: http://dx.doi.org/10.1016/j.carbon.2021.04.025.

[2] Bakhtiar Ali et al. “Laser-Induced Graphitization of Diamond Under 30 fs Laser Pulse Irradiation”. In: *The Journal of Physical Chemistry Letters* 13.12 (Mar. 2022), pp. 2679–2685. ISSN: 1948-7185. DOI: 10.1021/acs.jpclett.2c00429. URL: http://dx.doi.org/10.1021/acs.jpclett.2c00429.

[3] P.K. Bachmann et al. “Raman and X-ray studies of polycrystalline CVD diamond films”. In: *Diamond and Related Materials* 3.11–12 (Nov. 1994), pp. 1308–1314. ISSN: 0925-9635. DOI: 10.1016/0925-9635(94)90143-0. URL: http://dx.doi.org/10.1016/0925-9635(94)90143-0.

[4] Juliane Bahe et al. “A single photon source based on NV centers in diamond nanocrystals”. In: *CLEO/Europe - EQEC 2009 - European Conference on Lasers and Electro-Optics and the European Quantum Electronics Conference*. IEEE, June 2009, pp. 1–1. DOI: 10.1109/cleoe-eqec.2009.5192205. URL: http://dx.doi.org/10.1109/CLEOE-EQEC.2009.5192205.

[5] J.J. Bennett et al. "Inhomogeneities across boron-doped nanocrystalline diamond films". In: *Carbon Trends* 15 (June 2024), p. 100353. ISSN: 2667-0569. DOI: 10.1016/j.cartre.2024.100353. URL: http://dx.doi.org/10.1016/j.cartre.2024.100353.

[6] C. Bloomer et al. "A single-crystal diamond X-ray pixel detector with embedded graphitic electrodes". In: *Journal of Synchrotron Radiation* 27.3 (Mar. 2020), pp. 599–607. ISSN: 1600-5775. DOI: 10.1107/s160057752000140x. URL: http://dx.doi.org/10.1107/S160057752000140X.

[7] A.G. Burachenko et al. "Luminescence spectra of diamonds containing nitrogen-vacancy and interstitial photoactive centers". In: *Journal of Luminescence* 237 (Sept. 2021), p. 118214. ISSN: 0022-2313. DOI: 10.1016/j.jlumin.2021.118214. URL: http://dx.doi.org/10.1016/j.jlumin.2021.118214.

[8] R.C. Burns et al. "Growth of high purity large synthetic diamond crystals". In: *Diamond and Related Materials* 8.8–9 (Aug. 1999), pp. 1433–1437. ISSN: 0925-9635. DOI: 10.1016/s0925-9635(99)00042-4. URL: http://dx.doi.org/10.1016/S0925-9635(99)00042-4.

[9] G.B.J. Cadot et al. "Investigation of the microstructure change due to phase transition in nanosecond pulsed laser processing of diamond". In: *Carbon* 127 (Feb. 2018), pp. 349–365. ISSN: 0008-6223. DOI: 10.1016/j.carbon.2017.10.030. URL: http://dx.doi.org/10.1016/j.carbon.2017.10.030.

[10] Yu-Chen Chen et al. "Laser writing of coherent colour centres in diamond". In: *Nature Photonics* 11.2 (Dec. 2016), pp. 77–80. ISSN: 1749-4893. DOI: 10.1038/nphoton.2016.234. URL: http://dx.doi.org/10.1038/nphoton.2016.234.

[11] Arnaud Courvoisier, Martin J. Booth, and Patrick S. Salter. "Inscription of 3D waveguides in diamond using an ultrafast laser". In: *Applied Physics Letters* 109.3 (July 2016). ISSN: 1077-3118. DOI: 10.1063/1.4959267. URL: http://dx.doi.org/10.1063/1.4959267.

[12] Jimmy L. Davidson et al. *Diamond Trode Devices with a Diamond Microtip Emitter.* United States Patent No. US 7,256,535 B2. Patent number: US 7,256,535 B2. Aug. 2007.

[13] Steven Dimitrijevic, James C. Withers, and Raouf O. Loutfy. *Diamond/Diamond-Like Carbon Coated Nanotube Structures for Efficient Electron Field Emission.* United States Patent No. US 6,882,094 B2. Patent number: US 6,882,094 B2. Apr. 2005.

[14] Sally Eaton-Magana, James E. Shigley, and Christopher M. Breeding. "Observations on HPHT-Grown Synthetic Diamonds: A Review". In: *Gems &; Gemology* 53.3 (Nov. 2017), pp. 262–284. ISSN: 0016-626X. DOI: 10.5741/gems.53.3.262. URL: http://dx.doi.org/10.5741/GEMS.53.3.262.

[15] Steven Falabella. *Amorphous-Diamond Electron Emitter*. United States Patent No. US 6,204,595 B1. Patent number: US 6,204,595 B1. Mar. 2001.

[16] Andrea Carlo Ferrari and John Robertson. "Raman spectroscopy of amorphous, nanostructured, diamond–like carbon, and nanodiamond". In: *Philosophical Transactions of the Royal Society of London. Series A: Mathematical, Physical and Engineering Sciences* 362.1824 (Sept. 2004). Ed. by Andrea C. Ferrari and Jhon Robertson, pp. 2477–2512. ISSN: 1471-2962. DOI: 10.1098/rsta.2004.1452. URL: http://dx.doi.org/10.1098/rsta.2004.1452.

[17] J. Filik. "Raman Spectroscopy: A Simple, Non-destructive Way to Characterise Diamond and Diamond-like Materials". In: *Spectroscopy Europe* 17.5 (2005), p. 10.

[18] M. W. Geis, J. C. Twichell, and T. M. Lyszczarz. "Diamond emitters fabrication and theory". In: *Journal of Vacuum Science; Technology B: Microelectronics and Nanometer Structures Processing, Measurement, and Phenomena* 14.3 (May 1996), pp. 2060–2067. ISSN: 1520-8567. DOI: 10.1116/1.588986. URL: http://dx.doi.org/10.1116/1.588986.

[19] Arvind Goel et al. *Electrically Tunable Low Secondary Electron Emission Diamond-Like Coatings and Process for Depositing Coatings*. United States Patent No. US 6,486,597 B1. Patent number: US 6,486,597 B1. Nov. 2002.

[20] M.F. Hardman et al. "Evaluating the defects in CVD diamonds: A statistical approach to spectroscopy". In: *Diamond and Related Materials* 130 (Dec. 2022), p. 109508. ISSN: 0925-9635. DOI: 10.1016/j.diamond.2022.109508. URL: http://dx.doi.org/10.1016/j.diamond.2022.109508.

[21] Anming Hu et al. "Femtosecond pulsed laser deposition and optical properties of diamond-like amorphous carbon films embedded with sp-bonded carbon chains". In: *Diamond and Related Materials* 17.7–10 (July 2008), pp. 1643–1646. ISSN: 0925-9635. DOI: 10.1016/j.diamond.2008.03.024. URL: http://dx.doi.org/10.1016/j.diamond.2008.03.024.

[22] Kasper Jensen, Pauli Kehayias, and Dmitry Budker. "Magnetometry with Nitrogen-Vacancy Centers in Diamond". In: *High Sensitivity Magnetometers*. Springer International Publishing, Sept. 2016, pp. 553–576. ISBN: 9783319340708. DOI: 10.1007/978-3-319-34070-8_18. URL: http://dx.doi.org/10.1007/978-3-319-34070-8_18.

[23] Daniel C Jones et al. "Multidimensional luminescence microscope for imaging defect colour centres in diamond". In: *Methods and Applications in Fluorescence* 8.1 (Nov. 2020), p. 014004. ISSN: 2050-6120. DOI: 10.1088/2050-6120/ab4eac. URL: http://dx.doi.org/10.1088/2050-6120/ab4eac.

[24] H. Kanda. "Large diamonds grown at high pressure conditions". In: *Brazilian Journal of Physics* 30.3 (2000), pp. 482–489. ISSN: 0103-9733. DOI: 10.1590/s0103-97332000000300003. URL: http://dx.doi.org/10.1590/S0103-97332000000300003.

[25] T.V Kononenko et al. "Ablation of CVD diamond with nanosecond laser pulses of UV–IR range". In: *Diamond and Related Materials* 7.11–12 (Dec. 1998), pp. 1623–1627. ISSN: 0925-9635. DOI: 10.1016/s0925-9635(98)00198-8. URL: http://dx.doi.org/10.1016/S0925-9635(98)00198-8.

[26] T.V. Kononenko et al. "Femtosecond laser microstructuring in the bulk of diamond". In: *Diamond and Related Materials* 18.2–3 (Feb. 2009), pp. 196–199. ISSN: 0925-9635. DOI: 10.1016/j.diamond.2008.07.014. URL: http://dx.doi.org/10.1016/j.diamond.2008.07.014.

[27] V V Kononenko et al. "Photoinduced graphitization of diamond". In: *Laser Physics Letters* 12.1 (2015), p. 016101. DOI: 10.1088/1612-2011/12/1/016101. URL: https://doi.org/10.1088/1612-2011/12/1/016101.

[28] F. C. Marques and R. G. Lacerda. "Hardness and stress of amorphous carbon films deposited by glow discharge and ion beam assisting deposition". In: *Brazilian Journal of Physics* 30.3 (2000), pp. 527–532. ISSN: 0103-9733. DOI: 10.1590/s0103-97332000000300008. URL: http://dx.doi.org/10.1590/S0103-97332000000300008.

[29] Tsubasa Matsumoto et al. "Reduction of n-type diamond contact resistance by graphite electrode". In: *physica status solidi (RRL) – Rapid Research Letters* 8.2 (Nov. 2013), pp. 137–140. ISSN: 1862-6270. DOI: 10.1002/pssr.201308252. URL: http://dx.doi.org/10.1002/pssr.201308252.

[30] Tomio Ono et al. *Cold Cathode for Discharge Lamp Having Diamond Film*. United States Patent No. US 7,423,369 B2. Patent number: US 7,423,369 B2. Sept. 2008.

[31] Yue Pan et al. "Investigating extremely low resistance ohmic contacts to silicon carbide using a novel test structure". In: *Micro/Nano Materials, Devices, and Systems*. Ed. by James Friend and H. Hoe Tan. SPIE, Dec. 2013. DOI: 10.1117/12.2033910. URL: http://dx.doi.org/10.1117/12.2033910.

[32] Steven Prawer and Robert J. Nemanich. "Raman spectroscopy of diamond and doped diamond". In: *Philosophical Transactions of the Royal Society of London. Series A: Mathematical, Physical and Engineering Sciences* 362.1824 (Nov. 2004), pp. 2537–2565. ISSN: 1471-2962. DOI: 10.1098/rsta.2004.1451. URL: http://dx.doi.org/10.1098/rsta.2004.1451.

[33] J. Robertson. "Electronic processes in hydrogenated amorphous carbon". In: *Journal of Non-Crystalline Solids* 198–200 (May 1996), pp. 615–618. ISSN: 0022-3093. DOI: 10.1016/0022-3093(95)00775-x. URL: http://dx.doi.org/10.1016/0022-3093(95)00775-X.

[34] Tadashi Sakai et al. *Cold Cathode and Cold Cathode Discharge Device*. United States Patent Application Publication No. US 2004/0178712 A1. Publication number: US 2004/0178712 A1. Sept. 2004.

[35] Naoshi Sakuma, Tomio Ono, and Tadashi Sakai. *Manufacturing Method of a Diamond Emitter Vacuum Micro Device*. United States Patent No. 6,103,133. Patent number: 6,103,133. Aug. 2000.

[36] Patrick S. Salter et al. "High resolution structural characterisation of laser-induced defect clusters inside diamond". In: *Applied Physics Letters* 111.8 (Aug. 2017). ISSN: 1077-3118. DOI: 10.1063/1.4993118. URL: http://dx.doi.org/10.1063/1.4993118.

[37] Patrick S. Salter et al. "Laser Engineering Nanocarbon Phases within Diamond for Science and Electronics". In: *ACS Nano* 18.4 (Jan. 2024), pp. 2861–2871. ISSN: 1936-086X. DOI: 10.1021/acsnano.3c07116. URL: http://dx.doi.org/10.1021/acsnano.3c07116.

[38] Olga A. Shenderova et al. "Review Article: Synthesis, properties, and applications of fluorescent diamond particles". In: *Journal of Vacuum Science & Technology B, Nanotechnology and Microelectronics: Materials, Processing, Measurement, and Phenomena* 37.3 (Apr. 2019). ISSN: 2166-2754. DOI: 10.1116/1.5089898. URL: http://dx.doi.org/10.1116/1.5089898.

[39] James E. Shigley and Christopher M. Breeding. "Optical Defects in Diamond: A Quick Reference Chart". In: *Gems & Gemology* 49.2 (Aug. 2013), pp. 107–111. ISSN: 0016-626X. DOI: 10.5741/gems.49.2.107. URL: http://dx.doi.org/10.5741/GEMS.49.2.107.

[40] C. A. Spindt et al. "Physical properties of thin-film field emission cathodes with molybdenum cones". In: *Journal of Applied Physics* 47.12 (Dec. 1976), pp. 5248–5263. ISSN: 1089-7550. DOI: 10.1063/1.322600. URL: http://dx.doi.org/10.1063/1.322600.

[41] Bangshan Sun, Patrick S. Salter, and Martin J. Booth. "High conductivity microwires in diamond following arbitrary paths". In: *Applied Physics Letters* 105.23 (Dec. 2014). ISSN: 1077-3118. DOI: 10.1063/1.4902998. URL: http://dx.doi.org/10.1063/1.4902998.

[42] M. Suzuki, T. Ohana, and A. Tanaka. "Tribological properties of DLC films with different hydrogen contents in water environment". In: *Diamond and Related Materials* 13.11–12 (Nov. 2004), pp. 2216–2220. ISSN: 0925-9635. DOI: 10.1016/j.diamond.2004.06.023. URL: http://dx.doi.org/10.1016/j.diamond.2004.06.023.

[43] M. S. Komlenok et al. T. V. Kononenko M. Meier. "Microstructuring of diamond bulk by IR femtosecond laser pulses". In: *Appl. Phys. A.* 90 (2008), pp. 645–651. DOI: 10.1007/s00339-007-4350-9. URL: https://link.springer.com/article/10.1007/s00339-007-4350-9.

[44] Nephi Temahuki et al. "New Process for Electrical Contacts on (100) N-type Diamond". In: *physica status solidi (a)* 214.11 (Nov. 2017), p. 1700466. DOI: 10.1002/pssa.201700466. URL: https://doi.org/10.1002/pssa.201700466.

[45] Masashi Tomidokoro et al. "Electrical Conduction Properties of Hydrogenated Amorphous Carbon Films with Different Structures". In: *Materials* 14.9 (May 2021), p. 2355. ISSN: 1996-1944. DOI: 10.3390/ma14092355. URL: http://dx.doi.org/10.3390/ma14092355.

[46] F. Tuinstra and J. L. Koenig. "Raman Spectrum of Graphite". In: *The Journal of Chemical Physics* 53.3 (Aug. 1970), pp. 1126–1130. ISSN: 1089-7690. DOI: 10.1063/1.1674108. URL: http://dx.doi.org/10.1063/1.1674108.

[47] Sreenath Mylo Valappil et al. "Corrosion-Resistive and Low Specific Contact Resistance Ohmic Contacts to Semiconducting Diamonds Using Nanocarbon Electrodes". In: *physica status solidi (a)* 220.3 (Jan. 2023), p. 2200627. DOI: 10.1002/pssa.202200627. URL: https://doi.org/10.1002/pssa.202200627.

[48] Sreenath Mylo Valappil et al. "Nanocarbon ohmic electrodes fabricated by coaxial arc plasma deposition for phosphorus-doped diamond electronics application". In: *AIP Advances* 12.8 (Aug. 2022), p. 085007. DOI: 10.1063/5.0093470. URL: https://doi.org/10.1063/5.0093470.

[49] F.C. Waldermann et al. "Creating diamond color centers for quantum optical applications". In: *Diamond and Related Materials* 16.11 (Nov. 2007), pp. 1887–1895. ISSN: 0925-9635. DOI: 10.1016/j.diamond.2007.09.009. URL: http://dx.doi.org/10.1016/j.diamond.2007.09.009.

[50] C. Z. Wang et al. "Laser-Induced Graphitization on a Diamond (111) Surface". In: *Phys. Rev. Lett.* 85 (19 2000), pp. 4092–4095. DOI: 10.1103/PhysRevLett.85.4092. URL: https://link.aps.org/doi/10.1103/PhysRevLett.85.4092.

[51] Hongrui Wang et al. "Study of the dynamics of the graphitization in diamond induced by high repetition rate fs laser". In: *Optics Communications* 565 (Aug. 2024), p. 130639. ISSN: 0030-4018. DOI: 10.1016/j.optcom.2024.130639. URL: http://dx.doi.org/10.1016/j.optcom.2024.130639.

[52] Wanli Yang et al. *Diamondoid Monolayers as Electron Emitters*. United States Patent No. US 8,569,941 B2. Patent number: US 8,569,941 B2. Oct. 2013.

[53] Claire Chunjuan Zhang et al. "Raman Spectroscopy Characterization of Amorphous Coke Generated in Industrial Processes". In: *ACS Omega* 7.3 (Jan. 2022), pp. 2565–2570. ISSN: 2470-1343. DOI: 10.1021/acsomega.1c03456. URL: http://dx.doi.org/10.1021/acsomega.1c03456.

[54] Jiahui Zhao et al. "Phosphorescence and donor-acceptor pair recombination in laboratory-grown diamonds". In: *Physical Review B* 108.16 (Oct. 2023). ISSN: 2469-9969. DOI: 10.1103/physrevb.108.165203. URL: http://dx.doi.org/10.1103/PhysRevB.108.165203.

Chapter 5. Laser Processing for Ohmic Contacts

As demonstrated in sections 4.2.3 and 4.2.4 via various microscopy techniques, the laser processing of a highly phosphorous doped surface layer on a (1 1 1) oriented sample has resulted in a clear change in the diamond crystal structure following the intended design of electronic devices. AFM characterisation has shown that the topographical features vary in the ablation associated with this processing. The fluorescent behaviour of these features is noteworthy, indicating that while this material absorbs visible light as expected for diamond with broken sp^3 bonds, its optical properties differ from those of other laser-processed regions. While the models for this fluorescence remain speculative, the primary concern is that of the electrical characteristics, and whether or not the features of ablation and fluorescence impact the function of electrical devices created using this processing step. To that end, the electrical characterisation presented here follows a bottom-up approach, starting with tests on surface-written wires to confirm ohmic behaviour, indicative of the breakdown of diamond's sp^3 bonds. Subsequent tests on a TLM type structure and an emitter structure further explore this behaviour, and attempt to utilise this property.

5.1. Testing of Surface Graphitic Wires

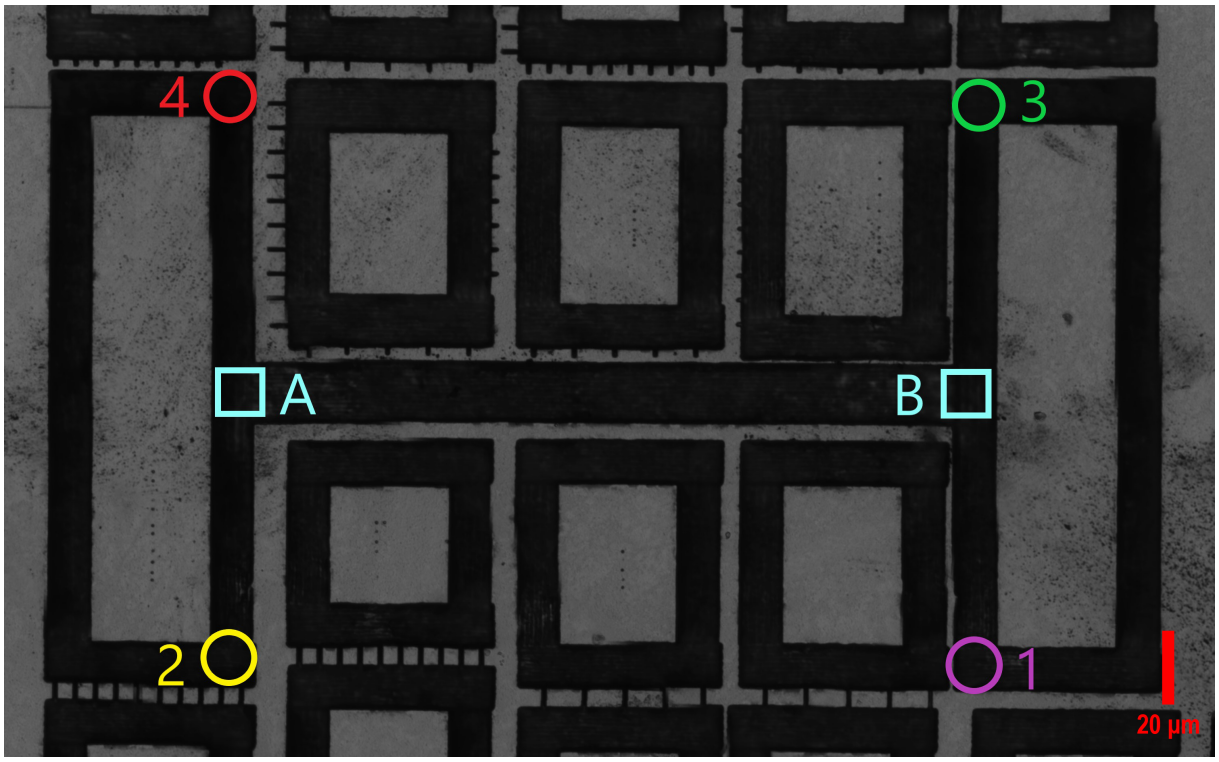

Figure 5.1 The I-shaped laser processed conductivity test structure.

Figure 5.1 shows the simple wire structure that was designed to allow for preliminary electrical characterisation. The annotated shapes indicate the positions of six different electrical probe positions that were used to make contact with the laser processed diamond surface. For reference, these are labelled such that the two aqua squares A and B represent the first set of electrical trials, followed by the circles used for the second set of trials which are labelled 1–4 starting from the bottom right and increasing in the anti-clockwise direction.

As indicated in figure 5.2, the top 10 µm wide wires have a length of 70.5 µm, and the bottom wire has a length of 65.5 µm. This slight difference in path length should result in a reduced resistance in the situation where the induced current is measured across probes 1 and 2, when compared to probes 3 and 4. Note that the 14 µm cross-bar wire has a length of 174 µm when measured from the edges of the 10 µm wires. This substantial length allows for a relatively large distance of laser processed wire to be tested, with the additional benefit of a change in width allowing for comparison with the slightly narrower 10 µm wires.

5.1.1. Electrical Probe Placement Error Estimation

One detail worth including at this stage is a discussion of the electrical probe tips that were used to make contact to the laser processed wires. Standard micro-probes usually have tip radii of the order of 10 µm, and naturally, trying to make good contact with wires that are 10 µm in width is a challenging prospect, especially due to the ablation of material in the centre of the wire. It would be exceedingly difficult to reliably place tips with a diameter greater than that of the surface features in the correct place. Tip placement relies upon the tip curvature and surface topology, which as previously noted is that of surface trenches, of smaller widths than that of the optically observed laser processed wires. It is physically impossible to place such a large tip into the trench, and contact would only be made on the very edges of the probe tip, reducing the surface area of the contact significantly and potentially inducing a large contact resistance if no good contact is formed. For that reason, probe tips with a full tip diameter of 10 µm were used to make contact to the surface wire structures directly. The circles used to represent the probe positions in figure 5.1 hence show a rough approximation of the size of the tips used in the electrical characterisation, with radii at 5 µm.

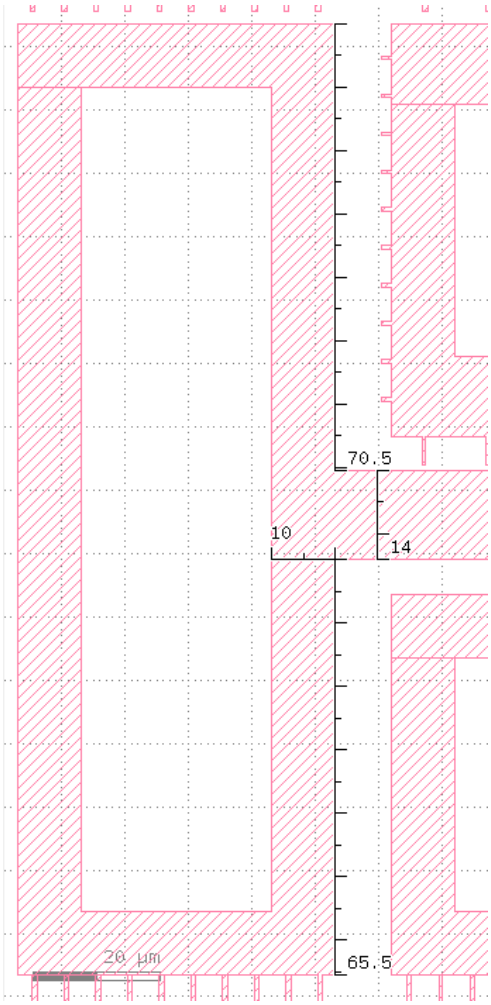

Figure 5.2 A snippet of the design for the wire testing region.

Despite great care in the positioning of these micro-tips, it is also important to note that the exact positioning of the probes relative to the wires being measured is an important source of error. The exact length of wires under investigation is a crucial variable for the calculation of measured resistivity and conductivity across differing wires. Hence, the variation of micron-scale positioning must be accounted for. The minimum potential error in electrical path length may be given by 2× the tip radii, which is ±10 µm. This is the minimum due to the tip radii themselves, but also sets a lower bound for the potential of inexact placements during the experimental process itself, as the probe tips may not necessarily be ideally situated in the locations marked on figure 5.1. While the placements were aided by an optical microscope, the precision and reliability with micropositioners establishes a hard limit of ±5 µm per probe tip. In particular for these smaller than average probe tip radii, the identification of physical contact was challenging to observe, with any additional force applied to the probe leading to significant bending of the probe tip and subsequent translation of the probe tip along the wire. Larger tip radii allows for

a probe tip with greater resistance to deformation, but as previously discussed the tip radii was strategically chosen to allow for the best possible contacts to be made to 10 µm wide wires, leading to this potential error in placement but reducing the issue of contact formation itself.

Electrical Path	Path Length (µm)
A-B	164
1-3	140
2-4	140
1-2	295
3-4	305
1-4	301
3-2	301

Table 5.1 Summary of electrical path lengths and the corresponding error due to probe placement. The error in path length is taken as ±10.

Table 5.1 provides a brief summary of the electrical path lengths between the different probe locations. The standard minimum error is more notable for the shortest electrical paths, such as A-B or 1-3, 2-4, when it is expressed as a percentage error of the path length. However, by taking this into account the conclusions of electrical measurements taken between these probe locations can be considered fairly.

5.1.2. Laser Writing Thickness

One final detail is necessary to consider the effective resistivity of the laser processed surface wires – that of the thickness of these processed regions. A full overview of the laser processing technique is outlined more fully in section 2.3, however the salient point regarding laser treated thickness can be estimated based on key studies in which the structure of laser processed diamond samples are examined via techniques such as TEM [17], SEM [2] and interference based microscopy techniques following the removal via oxidation of graphitic material [13]. Despite the topological complications induced by ablation during the laser processing technique, it is reasonable to estimate based on this prior work that the thickness of material in which a graphitisation or general sp^3 bond breaking process has occurred is likely to be relatively continuous, with only small variations on average across the laser treated region. With consideration of the literature that is comparable to the laser processing performed to create these device structures [13, 10, 12], a simple assumption that will allow for further analysis of the electrical properties of laser written wires is to take an estimated thickness of 500 nm for the effective thickness. This then represents material that may be considered to contain graphitised phases of carbon. This is consistent with the photographitisation/thermal graphitisation process that is described in section 2.3, though it must be stated that the exact thickness of the graphitised material will be a function of position along the wire, and it is unlikely to be completely uniform.

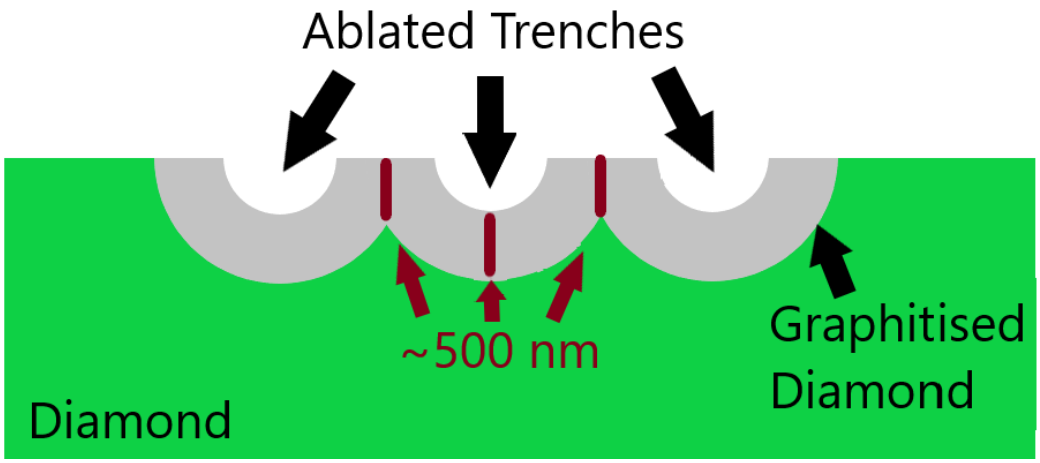

Figure 5.3 A simple ablation model to demonstrate the approximate thickness of graphitic material.

A rudimentary model of the thickness approximation is represented in figure 5.3. There are a few complications that must be acknowledged with such a model. First, the order in which the laser processing is performed will affect the photographitisation/thermal graphitisation process itself, with additional ablation occurring when laser treatment is applied adjacent to a point which already has a significant degree of graphitisation. This may be one of the most significant reasons as to why the profile of laser treated surface wires shows one deep topological trench, with a roughness that may then be due to the individual ablation regions.

Second, the spacing between adjacent laser spots will naturally change the ablation regions, and surface topology, with knock on effects for the graphitised region of interest. If laser spots are kept very close together, then the semi-circles representing ablated trenches in figure 5.3 will overlap, with a non-trivial local thickness of the graphitised region in these regions of overlap.

Thirdly, the photographitisation process is quite dependent upon defects as the origin of sp^3 bond breaking [11], in material which contains said defects. There are multiple defects that could have formed the origin of such photo-induced graphitisation, such as at the interface between the HPHT substrate and CVD grown heavily phosphorous doped diamond film [22], within the CVD grown layer itself due to the growth conditions used for highly phosphorus doped material [6], and the HPHT substrate itself due to the nitrogen content and likely high density of twinning or stacking faults [1, 20]. Hence, the origin of photographitisation is difficult to ascertain in such a substrate, and this may lead to a small amount of variance in the depth at which the sp^2 seeds are formed. The relative consistency of the topological scans demonstrated thus far indicates that despite these complications in a more precise model of the thickness of graphitised material, the ablation within the wider wires where multiple passes of laser processing has occurred is reasonably consistent. This removes the third point from relevance, as the exact positioning of the photo-induced graphitisation process need not be considered a large factor.

While the first and second points still hold, comparison to previous work indicates that while there may be some variability in the local thickness of laser graphitised layers, the approximate thickness of 500 nm should provide a reasonable estimate of the resistivity of these layers. At minimum, there should not be any points within the laser written wires where there is a thickness substantially thinner than 500 nm, with large deviations likely to be slightly thicker than this estimate.

5.1.3. Conductive Wire Testing - 14 micron width

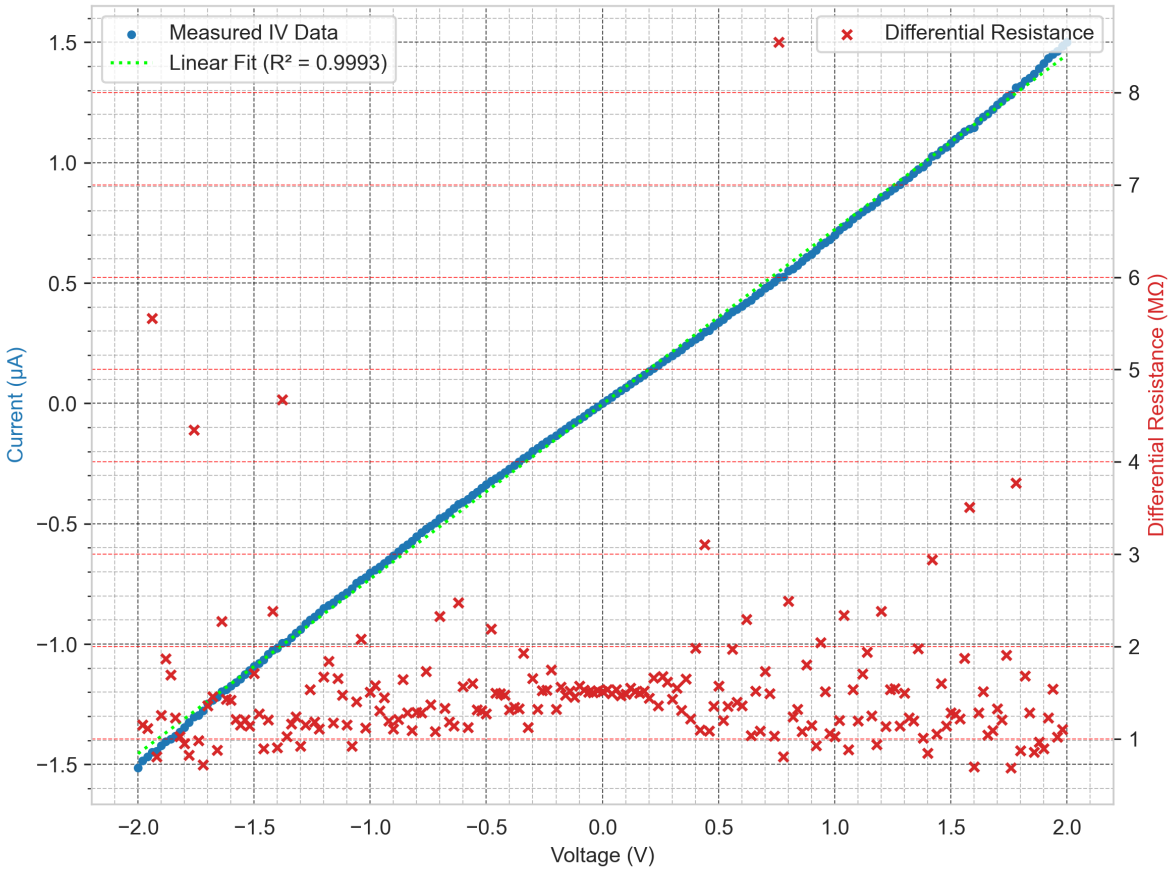

Figure 5.4 The first set of electrical measurements across the 14 µm wire structure via probe locations A and B.

The first set of electrical measurements were carried out between probe positions A and B as shown in figure 5.1. The linear IV plot is shown in figure 5.4, and shows a good ohmic relationship in the low voltage region of ± 2 V ($R^2 = 0.9993$). This line of best fit corresponds to a measured total resistance of 1.34 MΩ. A full set of electrical measurements were taken from this starting point, increasing up to an absolute potential bias of 100 V applied at probe A, with probe B held at ground. Figure 5.4 also displays the differential resistance between consecutive data points, further demonstrating the ohmic quality of this wire.

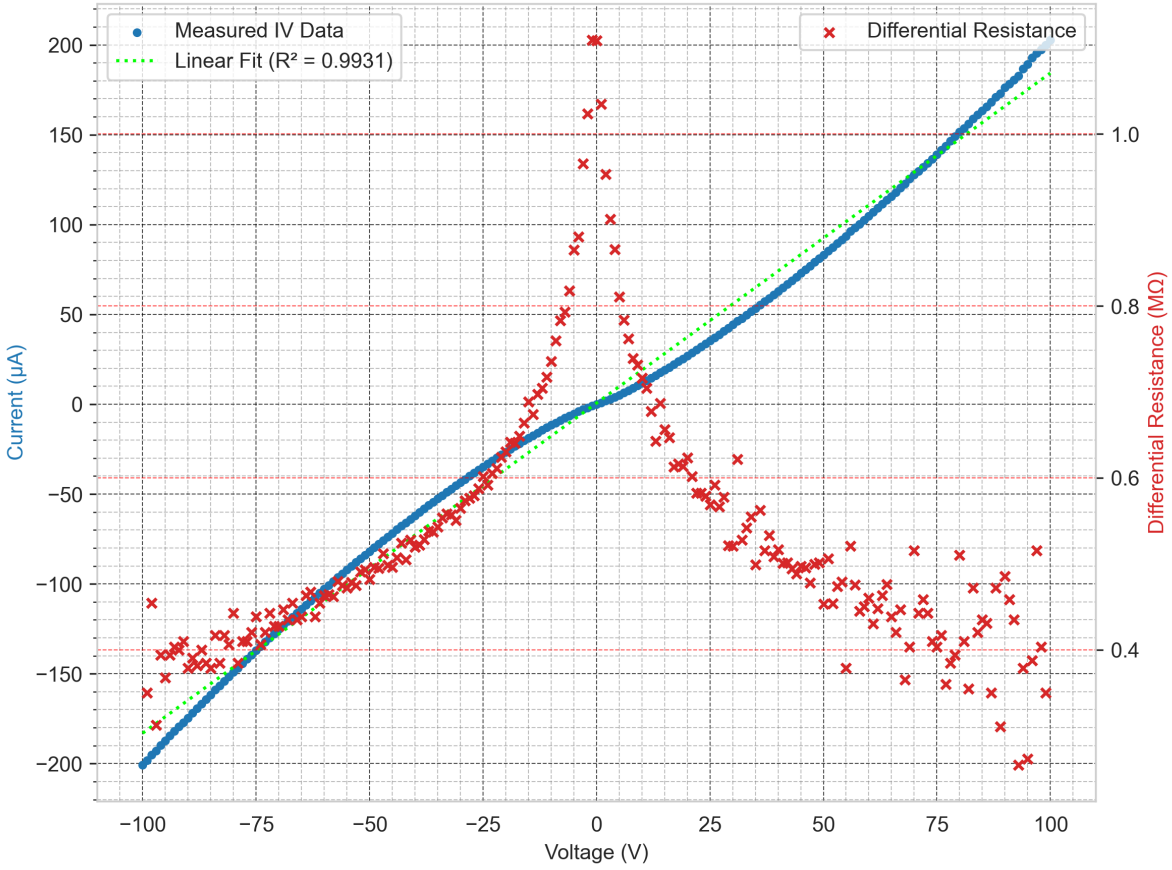

Figure 5.5 A ±100 V set of electrical measurements across the 14 µm wire structure via probe locations A and B.

Voltage (V)	Total Resistance (MΩ)	Diff. in Resistance (kΩ)	Absolute % Diff.	R^2
2	1.38	14.9	1.08%	0.9993
5	1.21	−19.8	1.64%	0.9964
10	0.992	−16.1	1.62%	0.9925
20	0.771	11.6	1.50%	0.9930
40	0.629	6.18	0.98%	0.9914
60	0.589	16.8	2.85%	0.9933
80	0.571	−14.0	2.45%	0.9937
100	0.544	−5.57	1.02%	0.9931

Table 5.2 Total resistance, difference in positive vs negative resistances, the absolute percentage difference, and total R^2 for various voltage ranges.

Figure 5.5 shows the electrical characteristics when measured with a potential bias of ±100 V. In contrast to the lower voltage range, a Schottky behaviour can be observed. The linear fit yields an R^2 value of 0.9931, and a measured total resistance for this linear fit of 0.544 MΩ. One valuable thing to consider with these characteristics is the potential for asymmetry in the measured resistance, and how this may change as the voltage range changes. To examine this briefly, table 5.2 collects the calculated difference in resistance between the positive and negative regions, which may be expressed as $R_{\text{diff}} = R_+ - R_-$, and also shows the percentage difference between the absolute value of R_{diff} and the resistance

as calculated from the full fit for the dataset $\left(\frac{|R_{\text{diff}}|}{R_{\text{total}}} \times 100\%\right)$. The results indicate that the data are well regarded as symmetric in nature, with only minor absolute % differences between the resistance as measured from the positive and negative voltage regions. There doesn't appear to be any clear correlation between the change in sign for $R_{(diff)}$ and the voltage range used, though it is also difficult to state that this is due to noise or other such error in the measurements, since the absolute % difference changes across the voltage range used.

The examination of symmetry will be explored further with the electrical characterisation of emitter structures, due to the possibility of one-way diodes being created through the geometric field enhancement and subsequent field effect emission. However, in this case, both probes A and B are placed on what is ostensibly material containing enough graphitic phase carbon to allow for near-ohmic conductivity. The observation of an inconsistent asymmetry may indicate some change in the structure of sp^2 phase carbon under the application of electrical bias, or potentially a more exotic phase of carbon such as a diaphitic structure. This will be explored further later in this chapter.

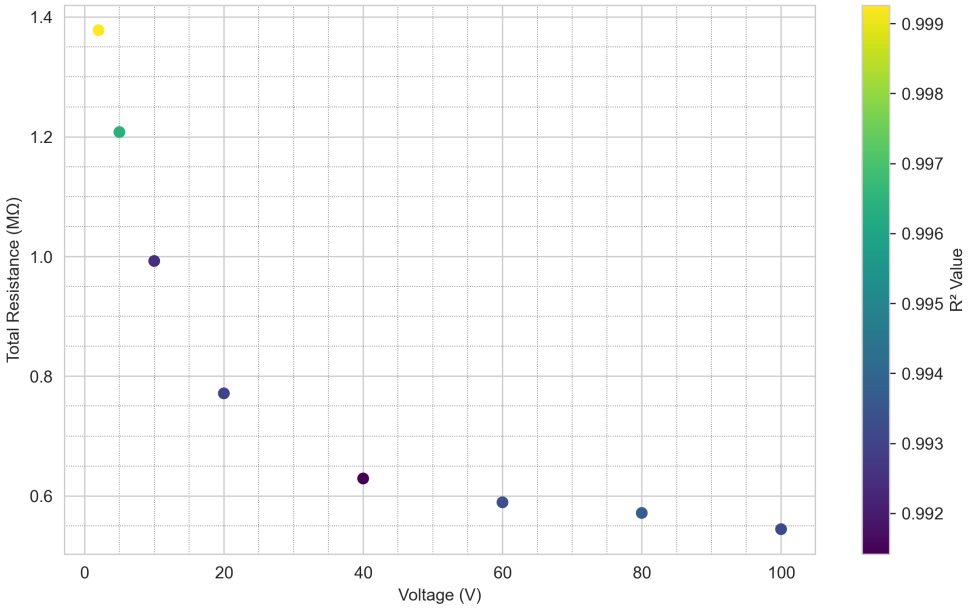

Figure 5.6 The full voltage range and their corresponding total resistances as measured across probes A and B.

Figure 5.6 displays the full range of measured total resistances based on the voltage range used. A colour scale is used to represent the changing R^2 value as the IV characteristics trend towards a Schottky-like behaviour at higher voltage ranges, deviating from the linear fit applied for the calculation of resistance.

Table 5.3 shows the resulting resistivity and conductivity as measured across the various voltage ranges between probes A and B. Immediate comparisons could be made to typical conductivity values for graphite, which, when parallel to the basal plane are typically

Voltage (V)	Resistivity (Ωcm)	Conductivity (S/m)	Conductivity Error (S/m)
2	5.88	17.0	1.04
5	5.16	19.4	1.18
10	4.24	23.6	1.44
20	3.29	30.4	1.85
40	2.68	37.2	2.27
60	2.51	39.8	2.43
80	2.44	41.0	2.50
100	2.32	43.0	2.62

Table 5.3 Voltage vs. resistivity, conductivity, and a conductivity error of 6.1% for this wire.

reported to have values of 2–4×10^5 $\mathrm{S\,m^{-1}}$, and perpendicular to the basal plane are closer to 333 $\mathrm{S\,m^{-1}}$ [16]. The best reported conductivity here at a bias of 100 V is of 43.0 $\mathrm{S\,m^{-1}}$, approximately 8 times smaller than that of the perpendicular graphite conductivity value. This is a significantly higher conductivity than that of the diamond substrate itself as measured via LTLM and CTLM in chapter 3 on another sample with a heavily phosphorous doped surface layer grown under the same conditions as for this sample. However, it is difficult to infer the dominant form of carbon allotrope that is present, especially when the concept of electrical percolation within composite materials is considered as in [15]. The recent application of complex network theory to electrical conduction mechanisms in nanostructure assemblies allows for a wide range of conduction types, even in materials that at first appear to be discontinuous [25]. Hence, the reduced resistivity observed in laser treated diamond that contains a larger content of sp^2 bonded carbon would appear to show that, despite not being a truly "graphitic" wire that acts as a metal, with conductivity similar to that of bulk graphite, enough electrically conductive material is present to allow for ohmic conductivity, albeit with a higher resistance than might be expected.

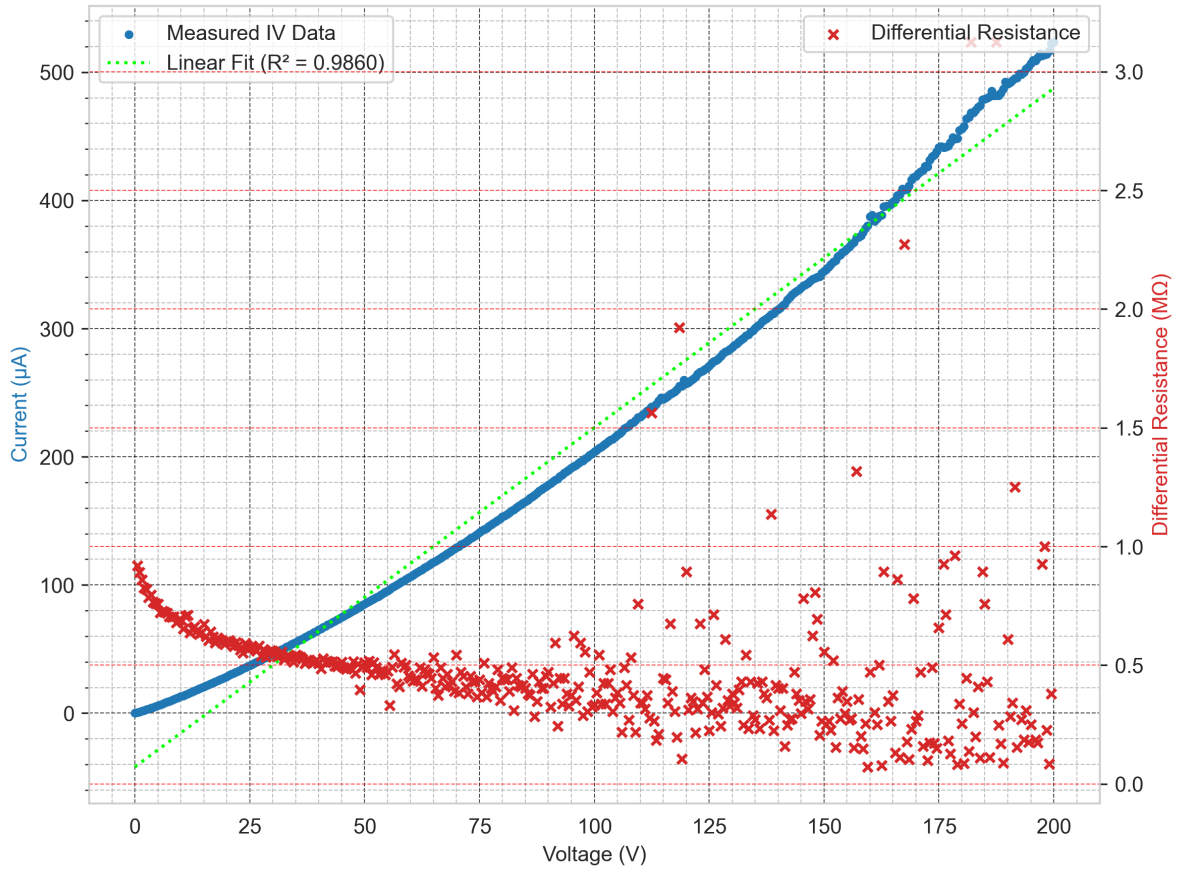

Figure 5.7 A set of electrical measurements across the 14 µm wire structure via probe locations A and B, reaching up to 200 V.

Voltage (V)	Resistivity (Ωcm)	Conductivity (S/m)	Conductivity Error (S/m)
4	4.06	24.6	1.50
10	3.51	28.5	1.74
20	3.07	32.6	1.99
40	2.64	37.9	2.31
60	2.38	42.0	2.56
80	2.20	45.4	2.77
100	2.09	47.8	2.92
120	1.99	50.3	3.07
140	1.89	52.8	3.22
160	1.80	55.5	3.39
180	1.73	57.9	3.53
200	1.61	62.0	3.78

Table 5.4 Total voltage sweep vs. resistivity, conductivity, and a conductivity error of 6.1% for the wire.

Next, higher voltage testing was performed, which continued the same observations as outlined in table 5.3. An example of a 200 V sweep is shown in figure 5.7, with a linear fit corresponding to a measured resistance of 3.78×10^5 Ω plotted alongside the raw data. The Schottky-like behaviour continues to grow in significance at these higher voltages, with more deviation from the linear fit visible. However, the effective conductivity continues in

much the same trend as before, with a conductivity of 62 $\mathrm{S\,m^{-1}}$ from the linear fit. This is represented in figure 5.7 by the decrease in differential resistance at higher voltages.

Table 5.4 gives the full set of higher voltage data between probes A and B. This set of measurements was performed with fresh probe tips and a complete reset of the experimental setup, to ensure that the results were not dependent upon an unknown error related to the previous set of result. Similar to the previous measurements, the conductivity at a bias of 10 V was around 28.5 ± 1.7 $\mathrm{S\,m^{-1}}$. One notable difference with these measurements is the setting of the ground probe to a negative bias, rather than holding it at ground. This allowed for a wider range of potential biases to be explored with the electrical probe station, but prevented the previous estimation of asymmetrical differences in absolute current values for negative vs positive electrical biases.

5.1.4. Conductive Wire Testing - 10 microns

In the previous section, the calculation of effective conductivity for the large (14 µm) laser processed wire is set out as for the measurements taken between probe locations A and B. Further measurements were taken at probe locations 1–4, following the electrical measurements of A–B. One small detail, which was noticed during the testing of A–B was that following multiple voltage sweeps at higher potential differences, the observed conductivity appeared to decrease marginally across multiple sweeps. However, testing the following day was able to achieve similar results to that set out in table 5.3. Regardless, it is worth examining the measurements between probe locations 1-4 and 2-3 separately, as these wires were otherwise untested in the previous conductivity measurements between probes A and B. They also have a different wire thickness of 10 µm, and so it may be natural to expect a higher resistivity. The comparative values of the wires are 3.57×10^{-8} m for the 10 µm wires and 4.27×10^{-8} m for the 14 µm wire. Hence, if the wires do indeed follow the trivial calculation of resistivity using an estimated thickness of 500 nm, it is expected that these thinner wires will show a conductivity that is approximately 16% lower than that of the 14 µm wires.

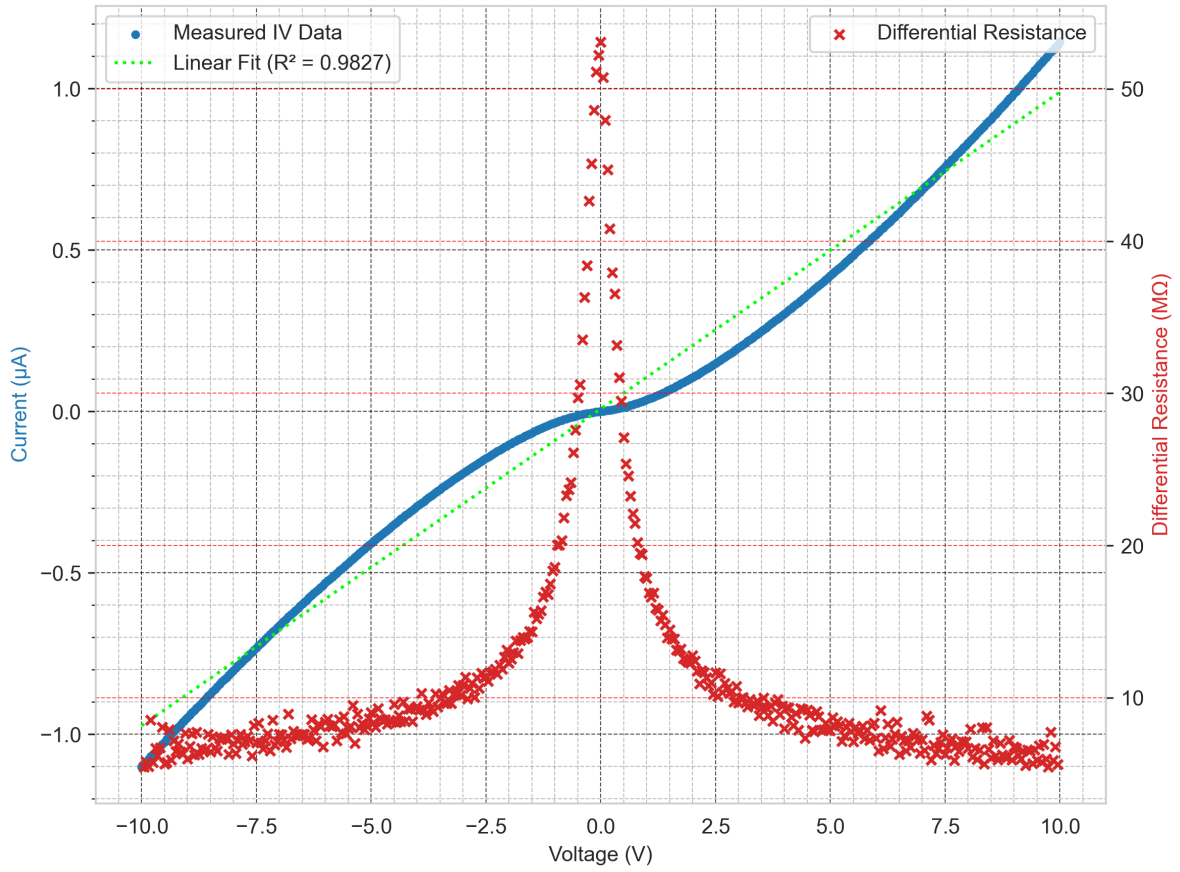

Figure 5.8 The first electrical characteristics between probe positions 1 and 3.

Figure 5.8 shows the first measured IV characteristics of the 10 µm wire between probe positions 1 and 3. Of particular importance is the reduced absolute current relative to the thicker wire measurements, and also the clear Schottky behaviour, even given the lower bias range applied in this case. It was unclear initially if this behaviour was due to the wire itself at this stage in the experimental process. The differential resistance as plotted reflects this rise in Schottky behaviour at low voltages.

Voltage (V)	Resistivity (Ωm)	Conductivity (S/m)	Conductivity Error (S/m)
2	0.796	1.25	0.0895
10	0.364	2.75	0.196

Table 5.5 Resistivity, conductivity, and errors for the wire between probes 1 and 3.

Table 5.5 provides a summary of the relevant conductivity data for the laser written wire between probe positions 1 and 3. The 10 V conductivity of approximately 2.75 ± 0.20 µm is significantly lower than the final 14 µm value of $28.5 \pm 1.7\ \mathrm{S\,m^{-1}}$.

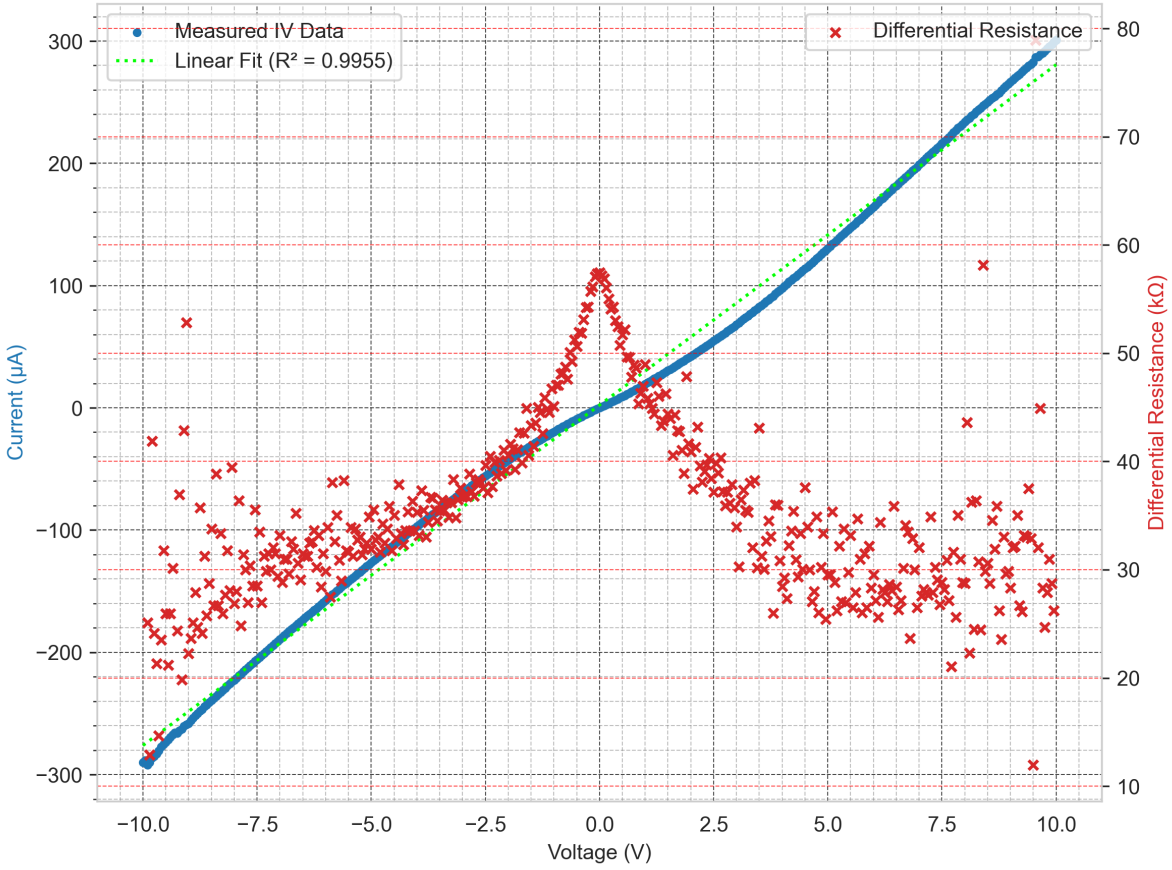

Figure 5.9 The average electrical characteristics between probe positions 2 and 4.

In figure 5.9, the IV measurements between probe positions 2 and 4 are plotted. This wire showed a significant jump in absolute current measurements, with the peak current reaching approximately 300 µA, in stark contrast to the previous measurements on both the comparable 1-3 wire and also the measurements across the 14 µm. The associated differential resistance is similarly lower by a few orders of magnitude.

Voltage (V)	Resistivity (Ωcm)	Conductivity (S/m)	Conductivity Error (S/m)
2	0.203	492	35.1
10	0.128	780	55.7

Table 5.6 Resistivity, conductivity, and errors for the wire between probes 2 and 4.

In the same style as for the previous table of results for the wire between probes 1 and 3, table 5.6 shows the conductivity data for the 10 µm wire between probes 2 and 4. At 10 V the conductivity of this wire was measured to be approximately $780 \pm 1.3\ \mathrm{S\,m^{-1}}$, a factor of 284 increase in conductivity over the previous wire. This is also markedly higher than that of the 14 µm wire, with a factor of 27 increase in conductivity (for conductivity taken at 10 V in the 14 µm wire).

Following these results, it was apparent that repetition of the electrical characterisation was a necessity, as the drastic change in conductivity between different probe locations indicated that there may be some issues with making direct contact to the as processed

laser written wires. Hence, the experimental procedure was repeated, with fresh probe tips and great care to ensure that the probe locations were as centrally located as physically possible to maximise the contacts formed. Several measurements performed with all 4 possible combinations of probe locations indicated that probe 3 in particular was the issue with the previous measurements.

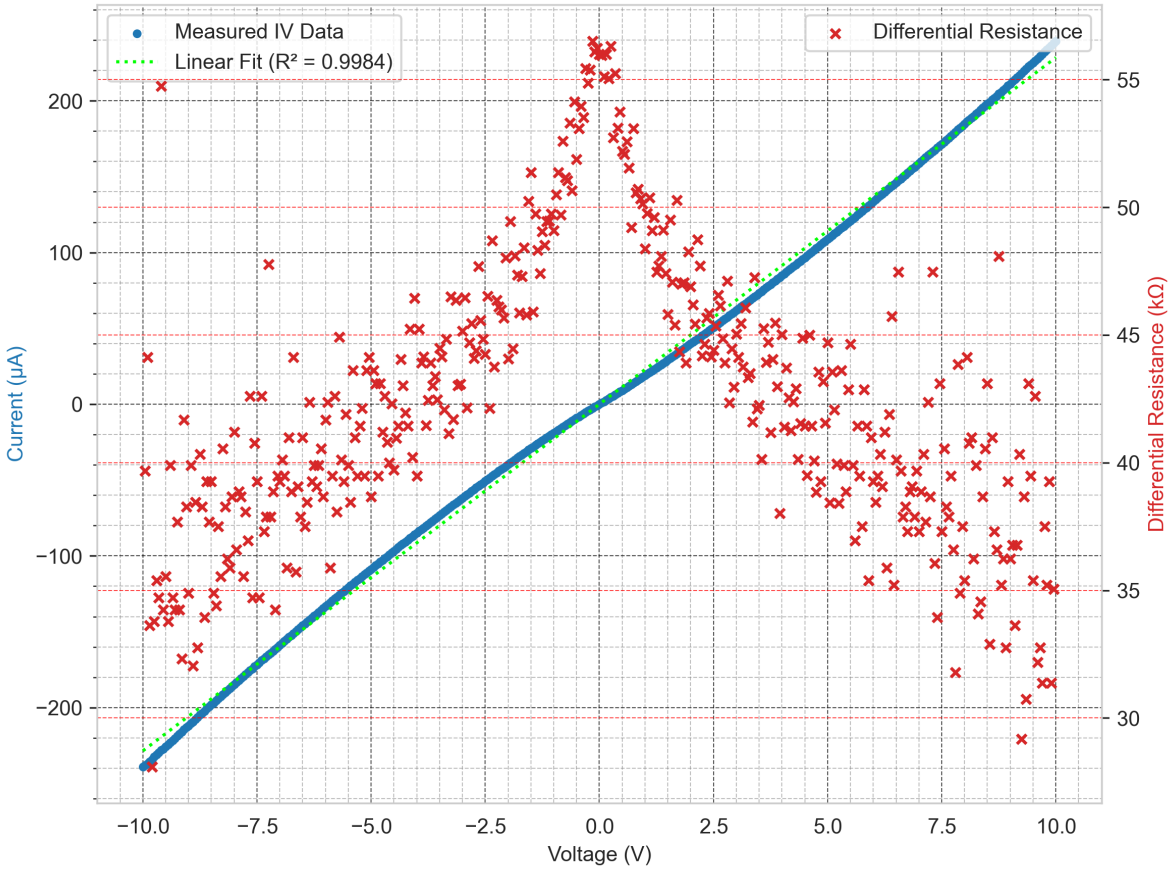

Figure 5.10 The average electrical characteristics between probe positions 1 and 3 - repeated.

Figure 5.10 shows the results of repeating this experiment with fresh probe tips and having had another standard solvent clean prior to making contact. The characteristics when contrasted to the previous data shown in figure 5.8 are significantly more ohmic in nature, with the linear fit of R^2 value 0.9984 vs the previous fit of 0.9827 providing some quantification of this trend. As for

Voltage (V)	Resistivity (Ωcm)	Conductivity (S/m)	Conductivity Error (S/m)
2	0.223	449	32.1
10	0.156	640	45.7

Table 5.7 Resistivity, conductivity, and errors for the wire between probes 1 and 3 - repeated.

The summary of further electrical measurements between probes 1 and 3 is given in table 5.7. Measurements between all 4 replaced probes were performed to confirm that none of the probes had a defective contact in this experimental setup, and the wire between positions 2 and 4 showed a similar conductivity to the previous results, at $749 \pm 53.5\ \mathrm{S\,m^{-1}}$.

Further to this, a final complete replacement of electrical probes was performed to verify the order of magnitude of current being reported here, and this was in agreement. Therefore, it was concluded that the contacts in this setup were no longer the cause of any discrepancy between the measured wire conductivities.

5.1.5. Conductive Wire Testing - 10 and 14 microns

In the previous two sections, the experiments performed on the wire testing structure as shown in figure 5.1 were used to establish the observed electrical conductivities of the 10 and 14 µm wires. Several further sets of measurements were taken across the structure, as previously alluded to in the verification that the original contact formed by probe 3 was relatively poor compared to the other 3 points of electrical contact. While the measurements across the full span of the structure are more difficult to use for precise calculation of the effective conductivities involved due to the two differing wire widths, the observations thus far point to the thicker 14 µm wire having a conductivity approximately 30 times lower than that of the 10 µm wires. Hence, it is reasonable to assume that when electrical measurements are taken across the full span of the testing structure (such as between probes 1-2, 1-4 and 3-2, 3-4), the dominant resistance will likely be that of the 14 µm wire, despite the additional 10 µm wire paths.

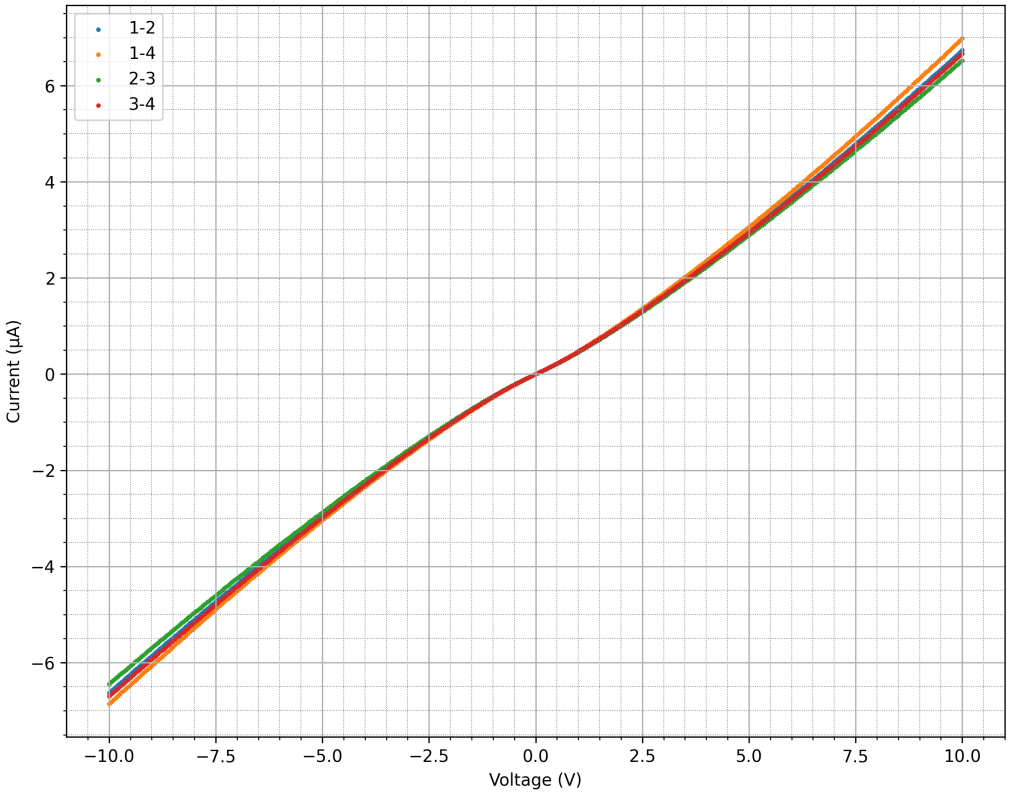

Figure 5.11 The average IV characteristics across all four possible paths utilising the full wire test structure.

Figure 5.11 shows the overlay of all four differing sets of electrical measurements taken across the 14 µm wire via probes located on the 10 µm wires. It is difficult to see the dataset corresponding to the IV data between probes 1-2, as it very tightly follows the data for probes 3-4. Otherwise, there are only minor differences in the measured conductivities between these locations on the wire structure, and all four sets of measurements are in good agreement, despite the slight differences in wire lengths (1-2 $\sim$ 295 µm, 1-4/2-3 $\sim$ 301 µm, 3-4 $\sim$ 305 µm).

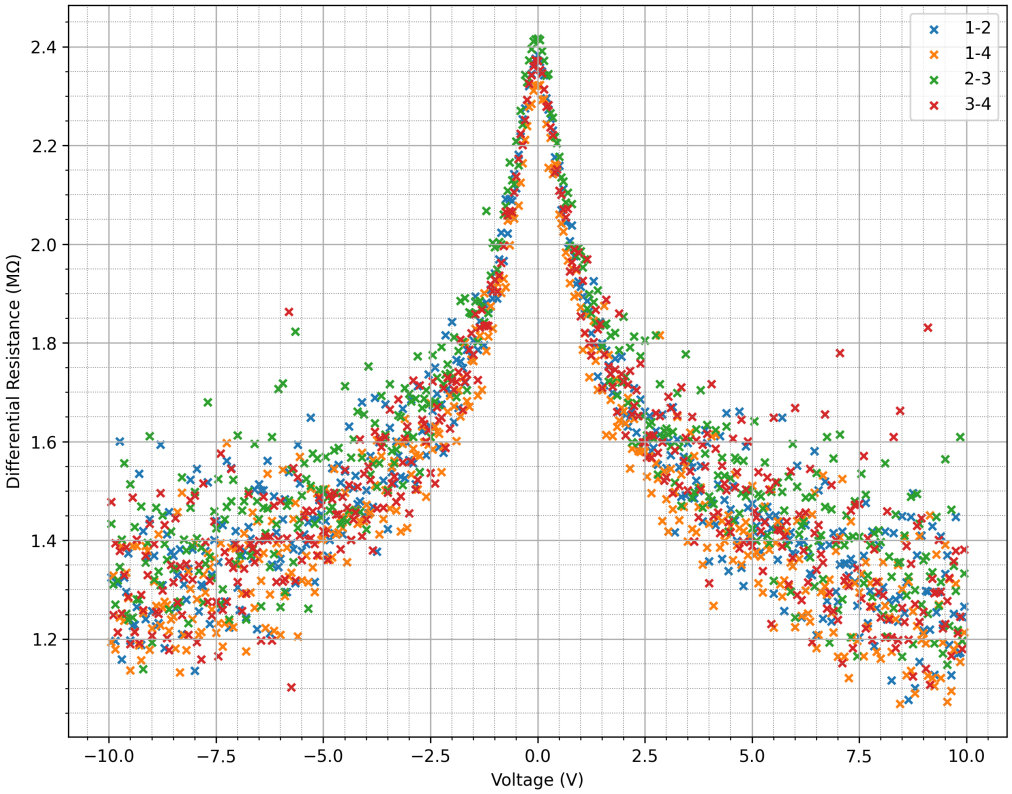

Figure 5.12 The average differential resistance across all four possible paths utilising the full wire test structure.

Figure 5.12 shows an overlay of all four differential resistance plots across the test structure. Similar to the observations in figure 5.11, the electrical characteristics are consistent across all paths. However, at higher voltages, a notable spread in differential resistance values is observed. This variability might be attributed to the differing number of data points per sweep, with 1000 data points typically collected in most sweeps, and a minimum of 400 in others. More consistent sampling across sweeps, and increasing the number of data points, is likely to enhance the precision and reduce the variability of the results. Each IV sweep was performed three times, spaced by a minimum of 10 seconds between each sweep to mitigate any effects of residual charge build-up, ensuring that the measurements reflect the true resistance of the wire without interference from transient electrical effects.

In table 5.8, the various electrical measurements across all four different "cross" configurations. Note that the calculation of resistivity and hence conductivity in this table uses an average wire width of 12 µm (in the first half), to provide an estimate for comparison with previous measurements across single wires. These measurements can be interpreted as three separate resistors in series, utilising wires that were characterised individually in the lower half of the table. All four electrical paths showed a reasonable similarity, with

Path	Resistance (MΩ)	Resistivity (Ωcm)	Conductivity (S/m)	Error (S/m)
1-2	1.58	3.21	31.1	2.22
1-4	1.53	3.05	32.7	2.34
3-2	1.63	3.25	30.8	1.06
3-4	1.58	3.11	32.2	1.09
A-B	0.992	4.24	23.6	1.44
1-3	0.0438	0.156	640	45.7
2-4	0.0370	0.132	756	54.0

Table 5.8 Summary of electrical measurements at 10 V for different probe configurations.

the potential error due to probe positioning potentially negating the slight differences observed. The lower half of the table provides the final measurements for each individual wire section, which highlights again the dominance of the resistance caused by the 14 µm wire.

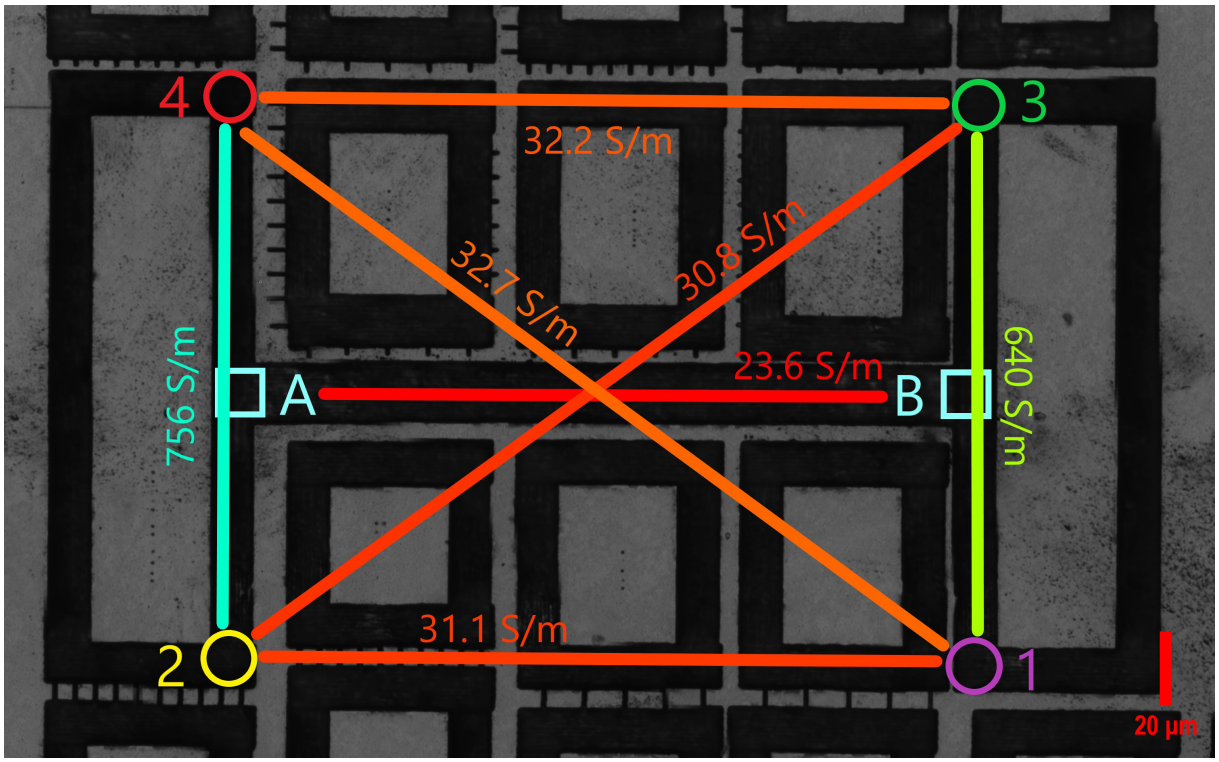

Figure 5.13 A simplified summary of the electrical characterisation of wire structures, as observed at 10 V.

Figure 5.13 provides a visual representation of the electrical measurements performed to determine the effectiveness of laser writing in creating ohmic wire structures. A colour spectrum is used with the simplified straight line connections to show the relative conductivities for the differing paths. The most noteworthy conclusion from these measurements was that the 10 µm wires were not merely ohmic, but were in fact significantly more ohmic than what was presumed to be the most electrically conductive structure in the design (the 14 µm wide wire). While there are some slight differences in the conductive paths that utilise both the cross bar and the thinner wires, the differences are not significant enough with the error analysis to conclude that any particular parts of the wires were

more or less conductive. This is represented by the slight shift from red-orange that is present in the straight line connections used to represent these electrical paths. The only clear difference was between the two 10 µm wires, which showed an 18% conductivity improvement in the leftmost wire between points 4-2, when compared to the rightmost wire between points 3-1.

5.1.6. Comparison to Graphite

With the measured conductivities following a number of assumptions regarding the geometric properties of the laser written wires, it is now a reasonable step to compare these values to what might be expected from ideal graphite wires. Then, it is possible to ask what the geometry of these graphite wires must be to match the measured resistances. It is inferred that the thickness of such a pure graphite wire must follow:

$$t = \frac{L}{\sigma R W} \tag{5.1}$$

Using a low estimate of the basal plane conductivity for typical graphite ($\sim 2 \times 10^5$ S m^{-1} [16], and by comparing to the measured resistance for the highest calculated conductivity of 756 S m^{-1} (path 2-4, as outlined in table 5.8), the effective thickness of such an ideal wire is calculated to be 1.89 nm in thickness. While the inter-atomic spacing between graphene sheets within graphite is a strong function of temperature and also depends upon the stacking sequence, typical inter-layer spacings are of the order of 0.355 nm [16]. Hence, a low estimate of basal plane conductivity for ideal graphite indicates an effective wire of only ~ 5 layers of thickness.

If instead, conduction is considered perpendicular to the basal plane of ~ 300 S m^{-1} [16], and again the highest calculated conductivity wire is used as a resistance reference point, the effective thickness of this wire is calculated to be 1.26 µm. This is not too surprising, since the assumption of thickness 0.5 µm was used in the calculation of conductivity 756 S m^{-1} for this wire originally. It does however confirm that for the electrical characteristics as performed on the 10 µm wide wires, graphite-like conductivity over a wire thickness that is reasonable does appear to be observed. Indeed the conductivity is more than 2 times higher when it is assumed that the thickness is 0.5 µm, which as discussed in section 5.1.2 represents a fair estimate based on literature values. Much thicker than 1 µm is unlikely, though further studies on laser graphitisation of diamond may help to elucidate the mechanisms determining the depth at which conductive material is generated, be that in the form of graphitic, diaphitic, or segregated areas of sp^2 bonding in a percolative network, as well as the interplay between these materials in conductors.

Finally, for the case of lower conductivity, such as that for the wire between points A-B, considering graphitic conduction perpendicular to the basal plane of ~ 300S m^{-1} [16], the effective thickness for the measured resistance is 39.4nm. It is certainly possible that the assumption of relatively uniform graphitised material may be significantly incorrect

in this wire, with some narrow conductive paths leading to the observed resistance. However, this is at least mildly odd, implying that despite the wire being significantly wider, the conductive path formed is substantially more inconsistent in thickness to the degree that the additional width is irrelevant. This is perhaps another indicator that the conductive material formed by this process cannot be simply regarded as "graphitic", despite the successful application of such a descriptor to the thinner wires. Instead, it must be considered that such conduction is due to electrical percolation and nanostructure assemblies as described by complex network theory [15, 25]. Broken type 2 diaphite is another likely contender in such poorly conducting material, with recent work examining the shift between ohmic and semiconducting material due to differing laser parameters highlighting the potential for such broken conductive paths to transition from ohmic type 1 diaphite wires to highly resistive type 2 diaphite wires [18].

Usage of the low estimated conductivity for in-plane graphite leads to an effective thickness of 59 pm when the values for path A-B are used again, around 7 times thinner than that of typical measured thicknesses of single graphene layers [19]. This provides further confirmation that on the scale from a thin highly conductive layer of sp2 bonded carbon, to very thick, poorly conducting amorphous carbon containing sp^2 bonding, it must necessarily be well away from the edge case of a single graphene layer providing the bulk of observed conductivity. It is impossible to rule out a "broken islands" structure of graphene conductivity, but this is again leading to a complex network theory or electrical percolation model. In which case, it is more likely that layers of graphene are not the cause of conductivity.

Regardless of the exact geometric and material model underlying the observed conductive paths, these conductive paths are sufficient to provide electrical wires embedded within the diamond surface. The contact between such wires and the phosphorous doped diamond surface layer may now be considered.

5.2. LTLM Structure

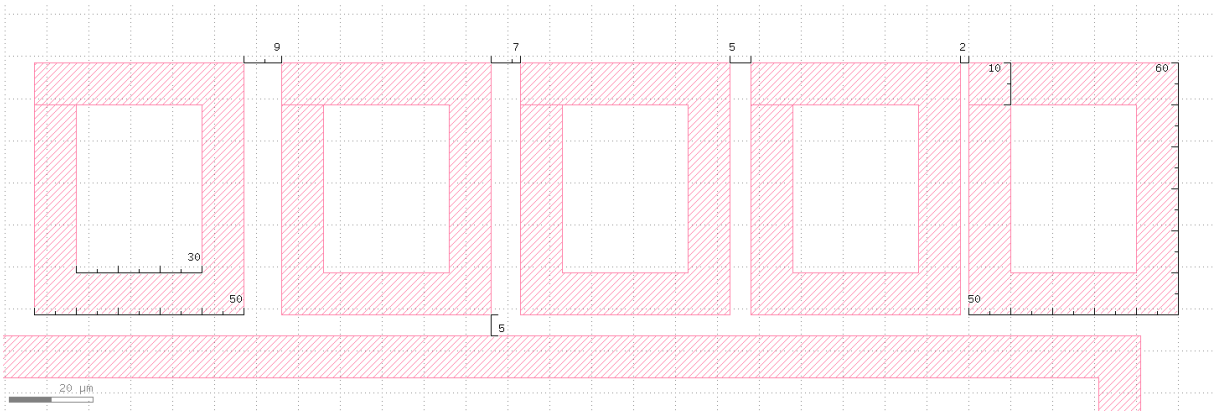

Figure 5.14 The design of a LTLM structure for laser processing.

As established in section 5.1.6, the electrical conductivity of the wires is sufficient to proceed with testing of diamond devices manufactured with these wires. In particular, one of the intended device structures is that of emitters, or emitter arrays. However, before testing such devices, it is important to have a baseline of comparison, which in practical terms results in a simple LTLM structure, as that will provide a test of "emitter-less" devices. This has the additional benefit of providing a comparison to conventional Ti-based ohmic contacts, which rely on annealing to generate a TiC interlayer for the reduction of Schottky barrier height and the subsequent reduction in specific contact resistivity. Figure 5.14 shows the designed structure of this LTLM-type setup. Four channel lengths between 2–9 µm are included, with simple rectangular wires providing the effective contacts. As shown in section 4.2.2, the channel width as measured via topological surveys shows some error in particular locations. It is important to examine these contacts prior to any LTLM analysis, due to the potential for significant deviation from the intended device structure.

5.2.1. LTLM Microscopy

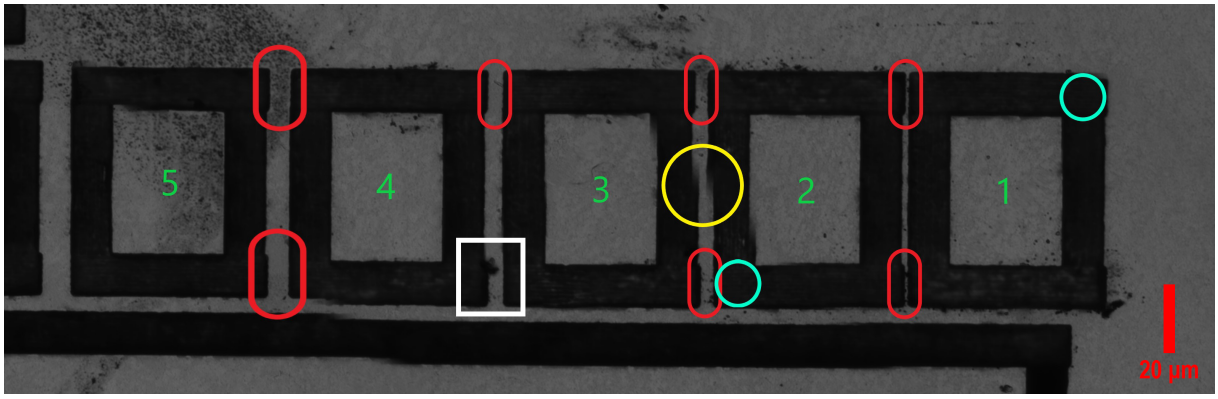

Figure 5.15 The LTLM laser written structure as observed via confocal microscopy with a 488 nm light source. Annotated numbers indicate the contact label.

Figure 5.15 shows the laser processed device structure as seen via confocal microscopy, utilising a 488 nm back-light. The different electrical wires used to form effective contact regions are labelled 5–1 from left to right. Red capsules are used to highlight corners of the contacts where it appears that a slight overshoot relative to the vertical wires has occurred. In the case of the channel between contacts 2-1, this results in what appears to be a potential overlap at this scale between the contacts in laser written graphitic content. In the case of the other channels it simply produces a small region at the corners where visible narrowing occurs. The yellow circle indicates what appears to be a slight mismatch in the vertical wires at the edges of contact 3 and 2. On contact 3, the wire appears to fade away to transparent diamond moving upwards and out of this circle, while on contact 2 the wire at the edge of the contact appears to similarly fade into transparency moving downwards. The net result is a region in the centre of the circle in particular where the channel appears to have its narrowest point, and significantly wider regions before the

corners. Finally a white square highlights what appears to be an amorphous blob on the bottom right corner of contact 4. It is unclear if this is due to the laser writing, or if it is contamination on the surface of the diamond. A region of small, soot-like contamination appears in various locations of this image, particularly near contact 5. It is possible that this is graphitic material due to ablation during the laser processing, which has not been removed in the subsequent solvent cleaning steps. Other possibilities, such as absorbance of the back-lighting within the substrate itself, may be considered via examination of other microscopy imaging utilising a top-down light source.

A final detail included in figure 5.15 is that of the cyan circles on contacts 2 and 1. These represent the two probe locations which were used for electrical characterisation across the 2 µm channel. Similar positions were used for the rest of the LTLM channels, with the right-most probe being located on the upper right corner of the contact structure and the left-most contact positioned on the lower left corner of the corresponding contact. This was done to ensure as much consistency as possible with the electrical measurements, as changing the relative positions of the probes on the contacts beween channels would change the resistance due to the 10 µm wire resistivity. As previously established, the 10 µm wires demonstrate the highest electrical conductivity, so the voltage drop across these wires should be minimal in comparison to the phosphorous doped diamond channel. However, this factor cannot be overlooked and is considered in the analysis of electrical measurements.

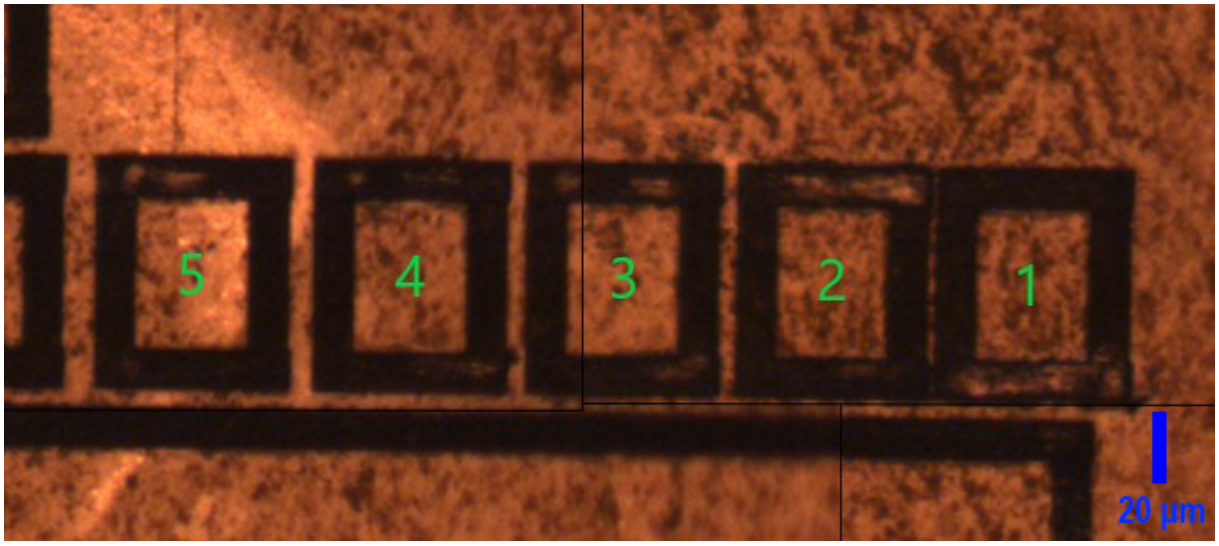

Figure 5.16 The LTLM laser written structure as observed via optical microscopy with a white light source.

Figure 5.16 shows a tiled image of the LTLM structure, as seen with a standard optical microscope (air immersion). The resolution of this image is significantly lower than that of the back-lit microscopy shown in figure 5.15, but it provides another visual comparison of the LTLM structure. In particular, the concentration of absorbent soot-like contamination near contact 5 is now visible as a reflective region on the surface of the sample, in contrast to the other areas which are not reflective.

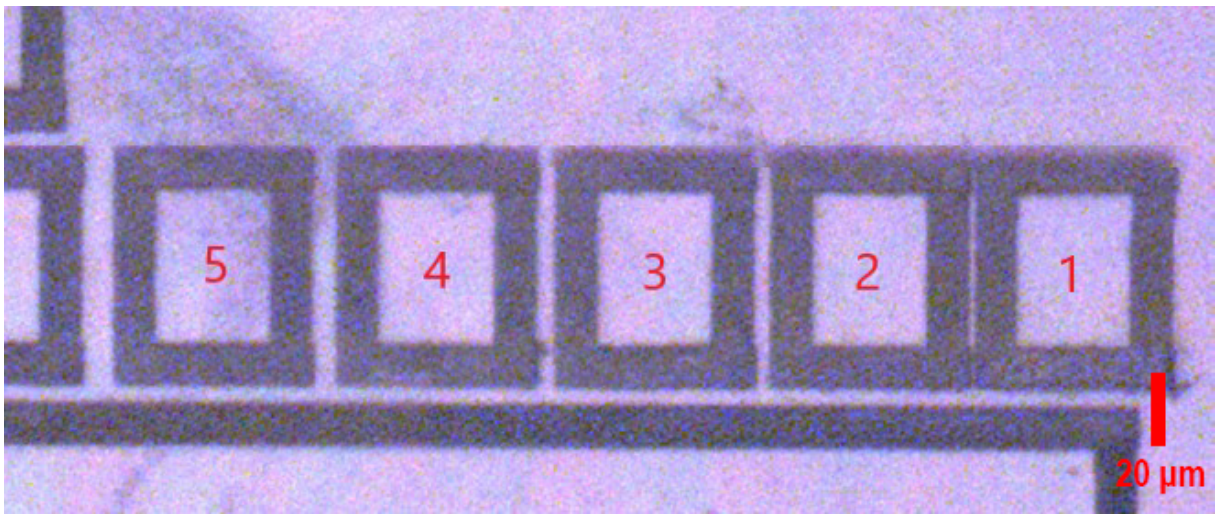

Figure 5.17 The LTLM laser written structure as observed via optical microscopy with a back-lit white light source.

Figure 5.17 provides a white back-lit image of the LTLM devices, using the same optical microscope as for the top-down white light source imaging in figure 5.16. Similar to that of the 488 nm back-lit confocal microscopy of figure 5.15, the soot-like contamination around contact 5 is seen to absorb a fraction of the white light source. It is notable that in contrast to the complete absorption of 488 nm light, this region does appear to have some transparency in the visible light range. However, given the significant disparity in optical resolution with this image, it is still possible that these particles are strongly absorbing the full visible light range. Regardless, this provides further comparative optical imaging for a qualitative examination of the device structures.

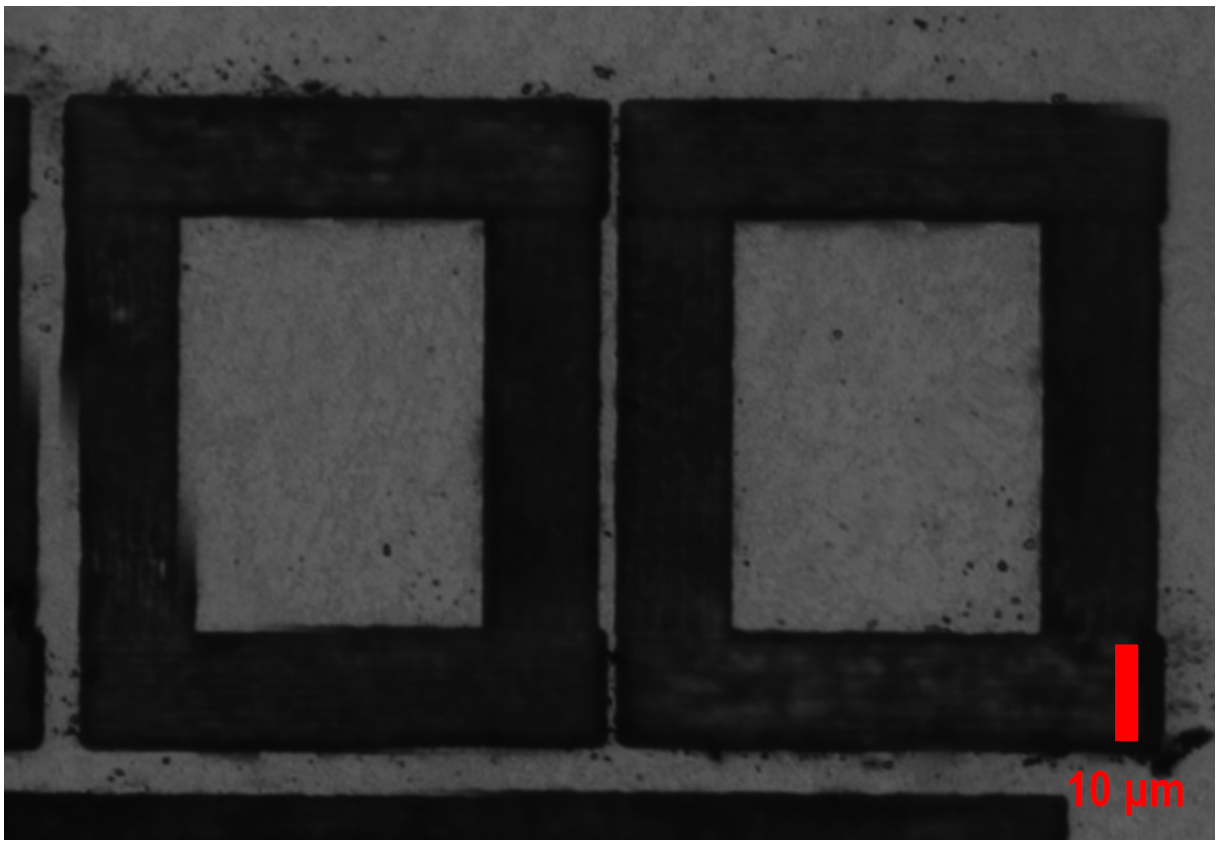

Figure 5.18 Contacts 2-1 of the LTLM structure, more closely examined via 488 nm confocal microscopy.

Figure 5.18 provides a view of contacts 2-1, as viewed via 488 nm confocal microscopy. At this scale the limit due to diffraction is starting to become evident, since the estimated limit of spatial resolution for the oil-immersion confocal microscope used is 200 nm with the 488 nm laser used.

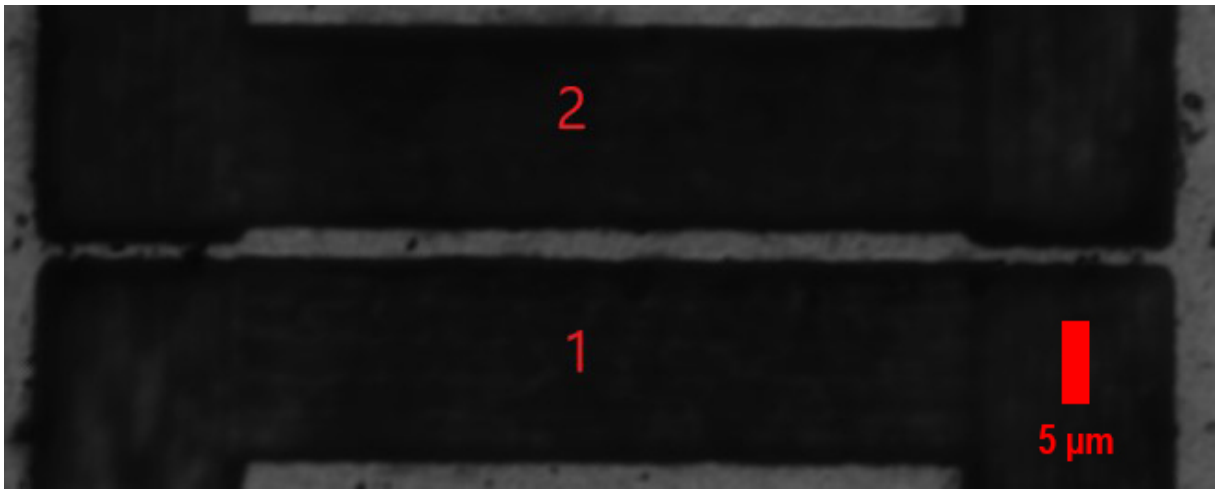

Figure 5.19 Contacts 2-1 of the LTLM structure, at the optical limit via 488 nm confocal microscopy.

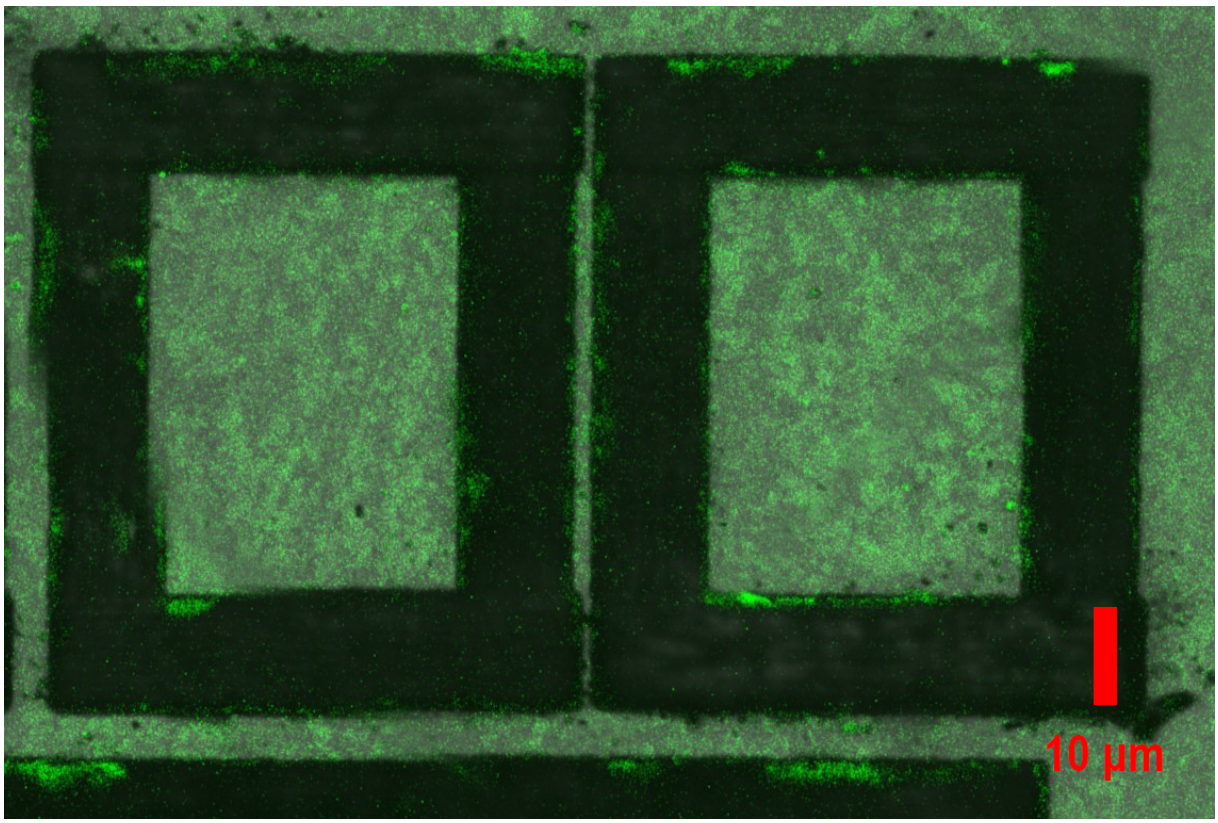

Figure 5.20 Contacts 2-1 of the LTLM structure, more closely examined via 488 nm confocal microscopy with 408 nm excited fluorescence.

In figure 5.20, the fluorescence due to an excitation laser of 408 nm is overlaid onto the 488 nm confocal microscope imaging of figure 5.19. While the source of any fluorescence is speculative, this provides another view of the laser written LTLM electrical contacts.

One noteworthy conclusion that is drawn from these high spatial resolution optical images of the contacts is that the slight overshoot observed at the corners of each contact appears to be touching at the bottom of the channel between contacts 2-1. At minimum, the spatial resolution of 200 nm is insufficient to resolve a clear spacing between the contacts in this region. As has been previously discussed in this chapter, the exact composition of laser processed wires and the resulting electrical characteristics could vary quite widely. While there is a visual "short" between the two contacts, if the dark material seen in this region is highly resistive, then the effective channel width may well still approach that of the designed 2 µm. While electrical characteristics indicating an intact semiconducting channel will help to disprove the existence of any electrical short, it is important to consider that the material connecting these two contacts may still be a semiconducting allotrope of carbon, but it may no longer be that of highly phosphorous doped diamond. This may distort the results if it is less resistive than that of the diamond channel, but still appear as though it is a semiconducting channel.

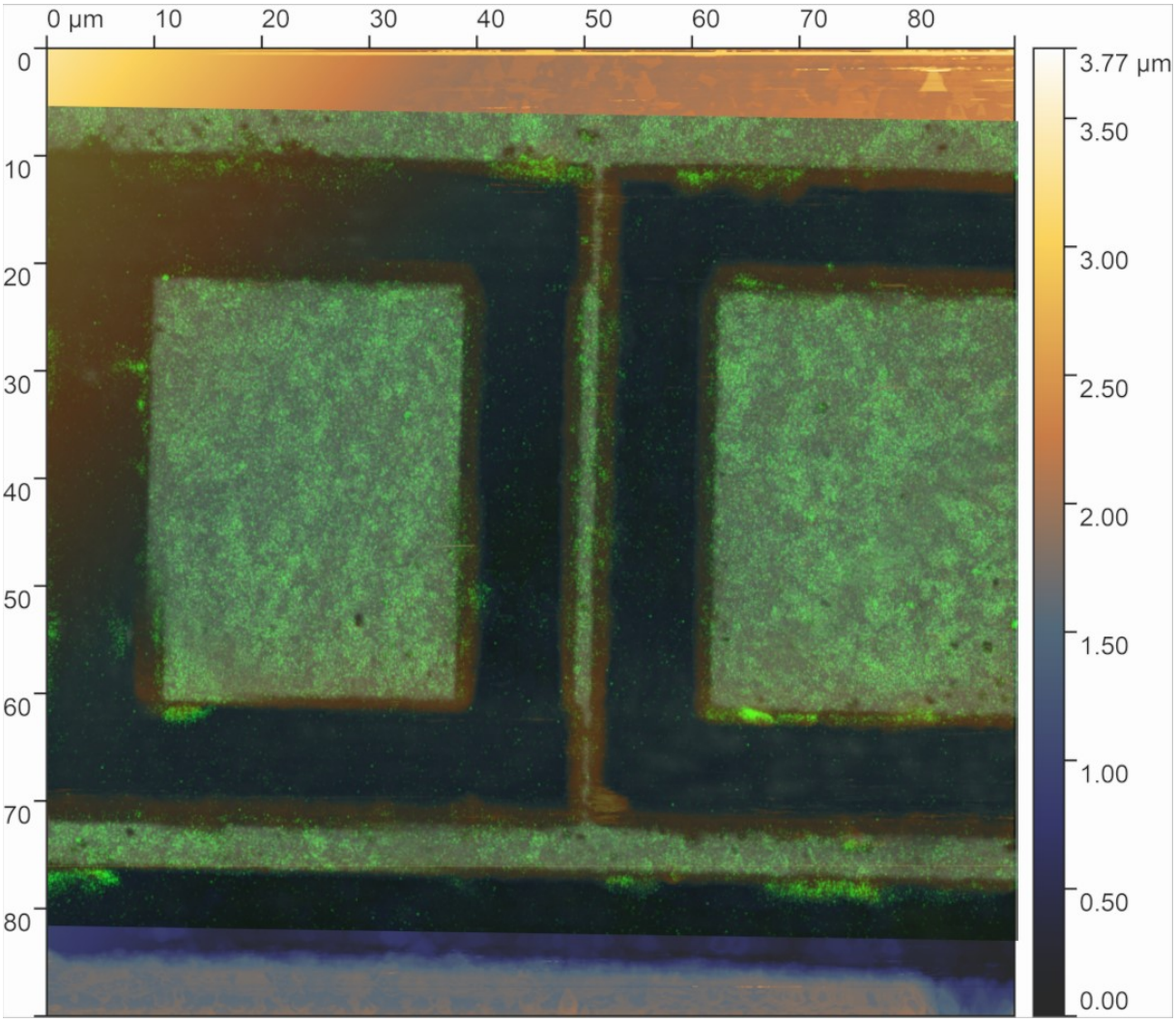

Figure 5.21 Contacts 2-1 of the LTLM structure, viewed as a combination of AFM, optical microscopy and fluorescence.

In figure 5.21, an overlay of the oil-immersion fluorescent microscopy is fitted to the AFM characterisation taken for these two LTLM contacts. The fluorescent microscope imaging has had the transparency adjusted such that the deep blue used for the height associated with the bottom of the trenches is visible enough to observe the topological map. Note that while the visual inspection of these contacts reveals a link between the laser written wires in the lower portion of the channel, the topology reveals a clear lack of ablation in this region. This may have implications for the relative concentration of graphitic material present in the channel, as a lack of ablation will correlate with lower laser power or fluence [7, 13]. While the optically transparent diamond has been altered, a speculative conclusion may be that this material is unlikely to be highly graphitic, and hence much more resistive or at least semiconducting in nature. For the AFM topology only please see figure 4.3.

5.2.2. 2 Micron Channel IV Characteristics and LTLM Assumptions

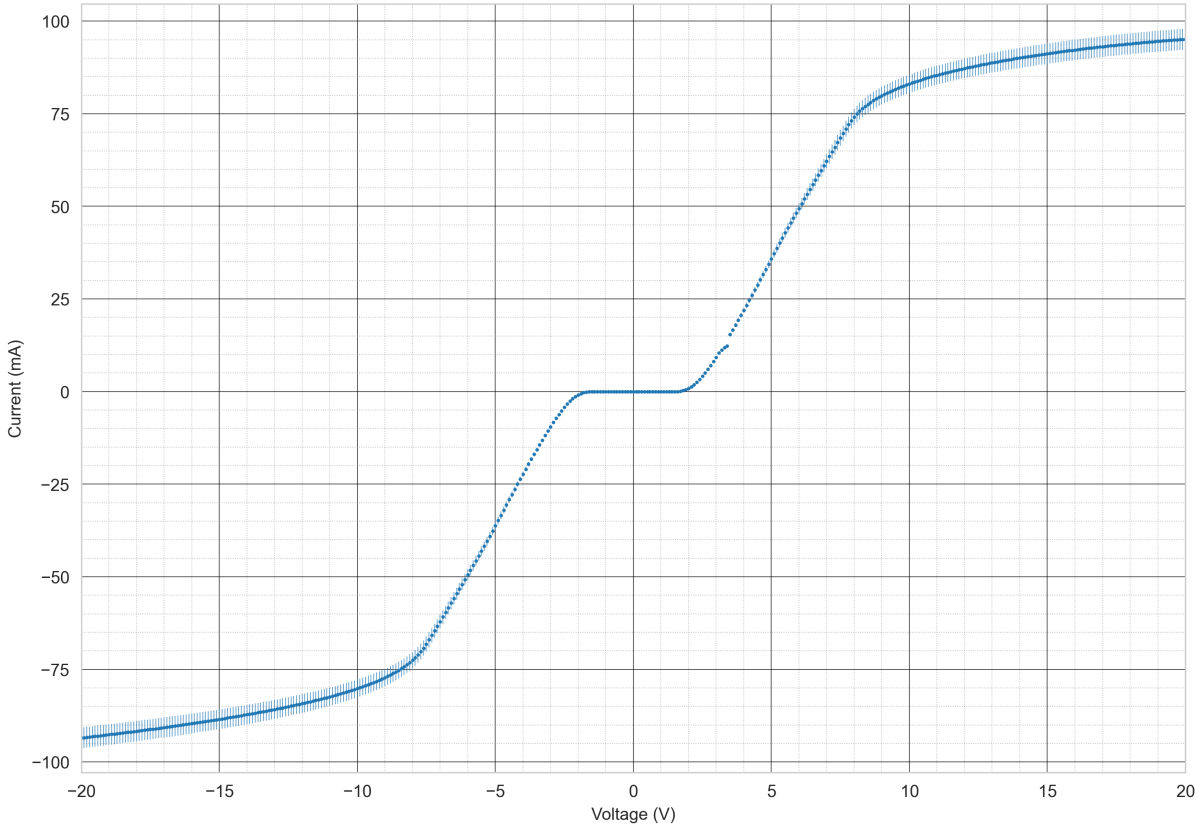

Figure 5.22 A linear plot of the averaged IV characteristics across contacts 2-1. Error bars corresponding to a systematic error of 5% are plotted.

Figure 5.22 shows the results of several trials of IV measurements across the channel between contacts 2-1. Several qualitative remarks can be made about the relationship displayed here, particularly in contrast to the previous experiments performed by the candidate using metal contacts and a LTLM structure in chapter 3. Error bars of 5% are included to account for the spread of data points observed between repeat attempts, and are hence a high estimate of systematic error based on the results themselves.

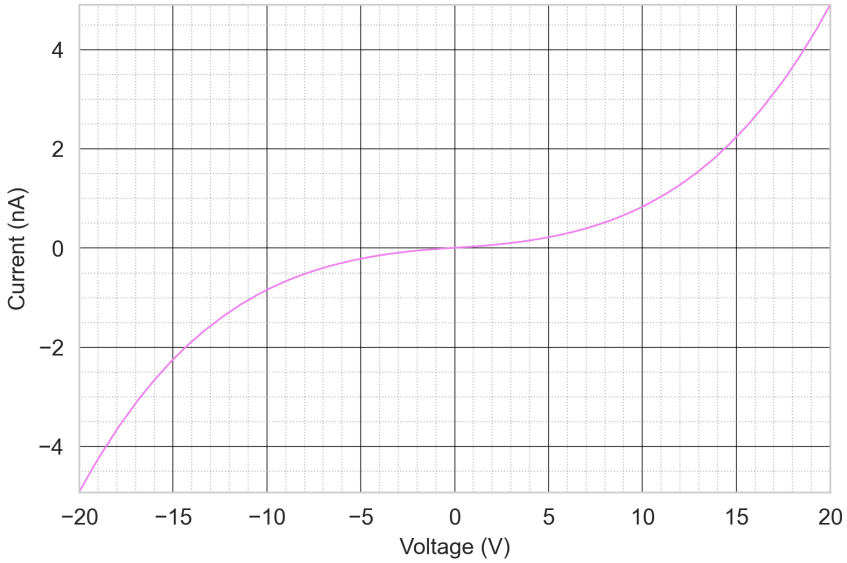

Figure 5.23 A linear plot of the measured room temperature IV characteristics across the 2.8 µm LTLM channel for sample D (annealed Ti/Pt/Au contacts).

Figure 5.23 provides a visual reference to sample D, which also used a LTLM device structure for IV characterisation. The phosphorous doped diamond film on sample D was thinner than sample G's, at ∼0.3 µm against the laser processed ∼1.2 µm layer. If the only significant factor at play was the thickness of said phosphorous doped layer, with the resistivity remaining the same, then it would be expected that the measured resistance is a factor of 4 lower in the thicker sample. Given that at a bias of 20 V, across a 2.8µm channel, sample D had a measured current of ∼5 nA and sample G with similar conditions and a ∼2 µm channel had a measured current of ∼93 mA, there is an obvious 10^7 magnitude shift in resistance which must be accounted for. There is also a clear change in behaviour from that of a single Schottky barrier, to what might represent a double Schottky barrier. As noted in the microscopy of channel 2-1, the observed channel width may differ from the designed 2 µm. However, even if the effective channel length is closer to 0.5 µm alongside the known difference in thickness, this presents a geometrical factor of 16 in the observed resistance. Naturally, it is also possible to consider the resistivity as measured via CTLM, which presented a value of $\sim 15\ \Omega\,\mathrm{cm}$ with constant current condition of 1 µA. The direct comparative work of Matsumoto et al. [14] gives a value of $\sim 9 \times 10^{-3}\ \Omega\,\mathrm{cm}$ at a constant current condition of 50 µA for similarly doped material. This methodology hence indicated that the majority of the measured resistance was due to the metal contacts, agreeing by and large with the two LTLM samples (C and D). The exact measurements of specific contact resistivity and resistivity do raise questions regarding the quality of metal contacts and homogeneity of highly phosphorous doped diamond, but the key concurring factor with metal contacts on phosphorous doped diamond is that of the extremely high specific contact resistivity that has been observed over a range of annealing conditions. Hence, while the geometry of this laser processed

LTLM is largely intended to provide a benchmark for the emitter arrays, a key takeaway from the comparison of IV characteristics represented by figures 5.22 and 5.23 may be that the laser written structure is now providing a significantly reduced specific contact resistivity, even prior to the application of LTLM methodology. There are numerous assumptions that must be made to apply the quantitative methodology of the LTLM method in this case, with the channel length, local resistivity, contact wire conductivity and laser written geometry all factors that may affect the results. Be that as it may, the application of LTLM methodology was employed to provide a more direct comparison between metal contacts and laser written contacts.

5.2.3. LTLM

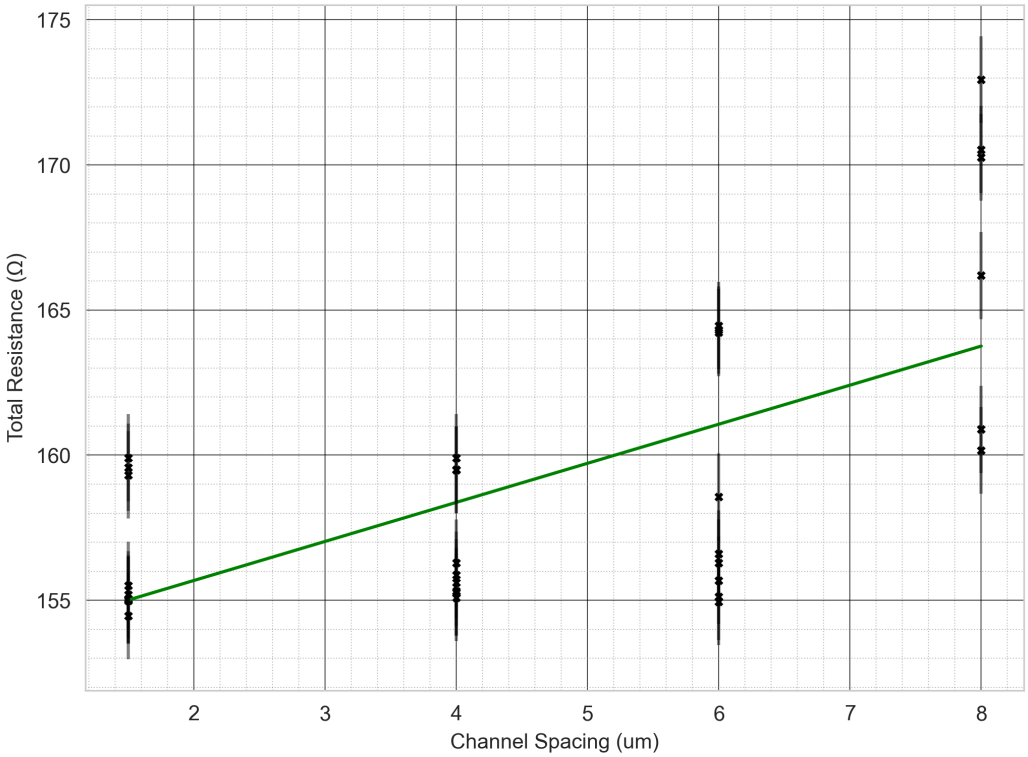

Figure 5.24 A linear plot of the total measured resistance against LTLM channel spacing at 5 V, with a line of best fit. Error bars of ±1.5 Ω are plotted based on the spread of data observed within each set of IV sweeps, and represent a high estimate of the systematic error.

Figure 5.24 shows the results of several rounds of LTLM experiments. One notable detail is the usage of slightly different channel spacings (1.5, 4, 6, 8 µm) when compared to the designed spacings (2, 5, 7, 9 µm respectively). This reduction of channel spacing was implemented to better reflect the observed topology of laser written devices, but while the data themselves better match these spacings, this is a difficult measurement to take from the given characterisation techniques and remains as an assumption to allow for plotting.

Further to this, the low total resistance observed across all channels is a challenging result to reconcile with the previous wire measurements. This will be explored further in the following sections.

Despite the linear fit seen in figure 5.24 having an R^2 value of 0.39, the extracted specific contact resistivity is $5.5 \times 10^{-5}\ \Omega\,cm^2$, representing the lowest specific contact resistivity to highly phosphorous doped diamond of any devices presented in the literature. It is important to note the voltage at which this set of data are obtained, 5 V. This is a reasonable estimate of the linear, forward bias region of one of the two Schottky barriers, but the linear IV characteristics for all channel spacings reflect the lack of comparison to that of ohmic contacts around the 0 V region.

5.2.4. Line of Best Fit and LTLM Parameters

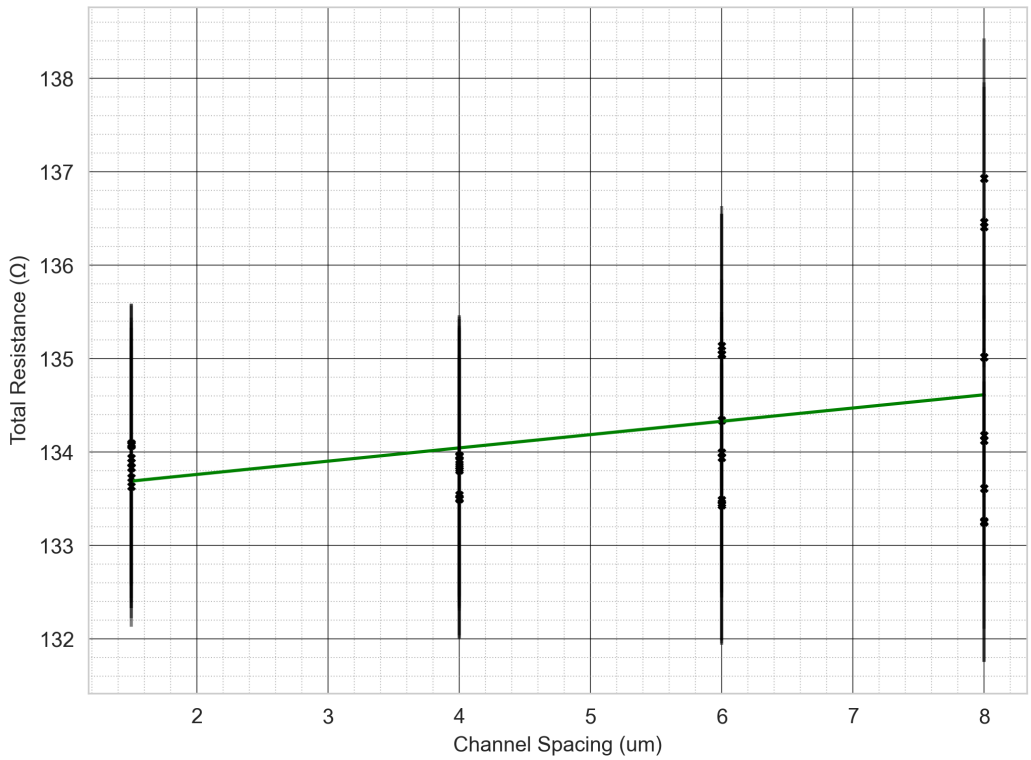

Figure 5.25 A linear plot of the total measured resistance against LTLM channel spacing at 10 V, with a line of best fit. Error bars of ±1.5 Ω are plotted based on the spread of data observed within each set of IV sweeps, and represent a high estimate of the systematic error.

Figure 5.25 shows the LTLM plot for resistance data collected at a potential bias of 10 V. The line of best fit in this case is very poor, with an R^2 value of 0.15. The measured resistance has been lowered relative to the 5 V measurements for all channel lengths, which may be due to the voltage-dependent conductivity of laser processed wires.

As seen, when the LTLM methodology is applied to differing voltages, the resulting line of best fit can change quite dramatically in quality relative to the data. However, while the specific values of the total measured resistance do generally reduce at higher voltages, the rough trendlines observed in figures 5.24 and 5.25 are still present. It is also worth noting that any line which passes through the LTLM data presented here will have similar orders of magnitude for the specific contact resistivity and sheet resistance/resistivity, regardless of the resulting R^2 value.

This allows for some speculative comparison to be made to work such as Valappil et al. [24, 23], who demonstrated nanocarbon specific contact resistivitys of $1 \times 10^{-3}\ \Omega\,cm^2$ for the voltage range of 5–10 V. Matsumoto et al [14] demonstrated thermally graphitised CTLM specific contact resistivitys of $0.9\ \Omega\,cm^2$, notably at around the 2 V mark. Finally, previous literature values such as that of Kato et al [8] at $2 \times 10^{-3}\ \Omega\,cm^2$ may also be considered, though this publication did not use the constant current condition necessary for CTLM methodology.

The error present with any linear fit in figure 5.24 prevents any conclusive comparison to be made with these examples, as a linear fit to these data is speculative at best. A useful consideration may be the range of linear fits that are possible given this dataset, as the specific contact resistivity estimation of $1 \times 10^{-5}\ \Omega\,cm^2$ is two orders of magnitude lower to comparable contacts made using nanocarbon or thermally graphitised contacts on highly phosphorous doped material.

Another consideration is the possibility of the electrical contacts deteriorating over time, or with consecutive electrical measurements. The data used for figure 5.24 spans multiple days, with repeat measurements on those days. While a good degree of repeatability was observed throughout the experimental process, the similarity between total measured resistances across the range of channels does raise questions concerning the source of any error. Although data that were likely affected by poor contact placement have already been discarded, the factor of variable conductivity within the wires themselves, and the potential impact of this upon the graphite/diamond/graphitic structure formed, is more difficult to quantify. Finally, the discrepancy between the measured resistance across LTLM contacts and the wire test structures must be considered.

5.2.5. Missing Resistance

As previously stated in section 5.2.2, the IV characteristics of the LTLM structure were performed with an observation of repeatability between differing days and across all four channel spacings. However, testing of emitter structures revealed a significantly lower base current, of the order of µA. This is in line with the previous electrical measurements across wire testing structures in section 5.1, and hence the LTLM measurements require further exploration.

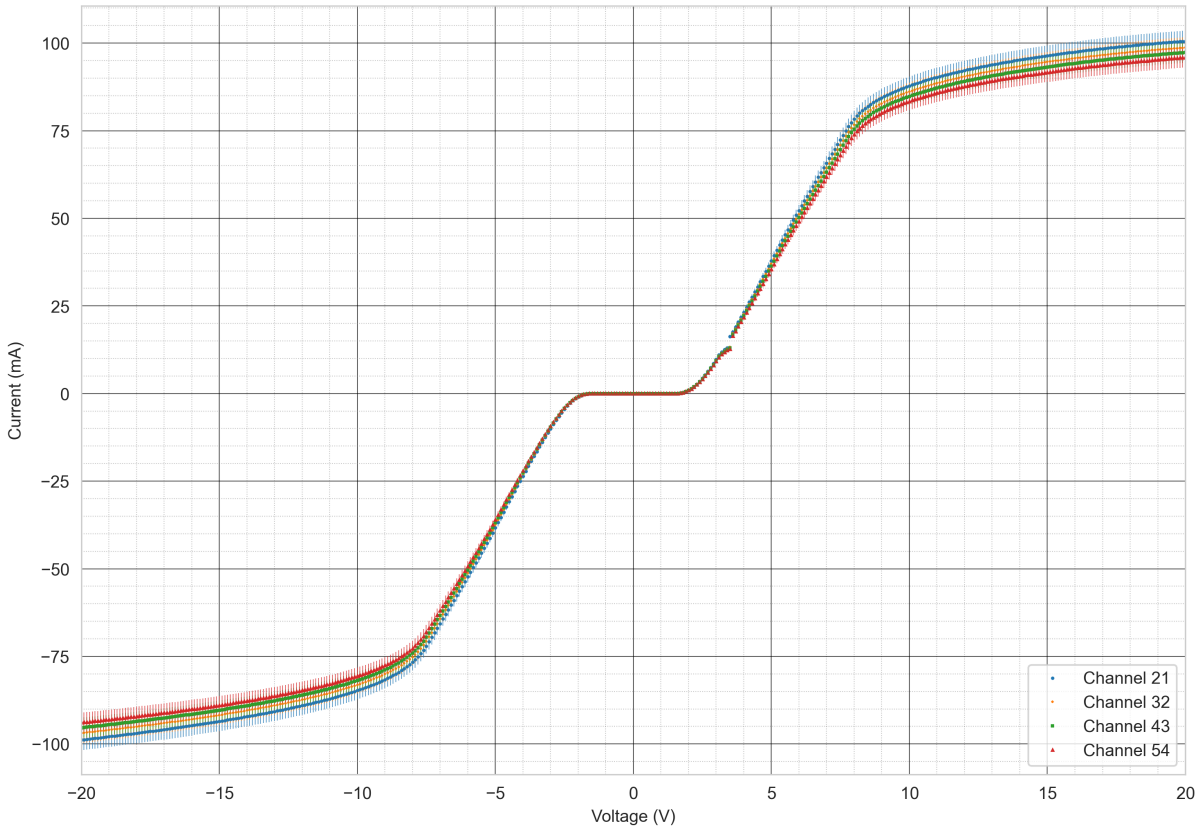

Figure 5.26 A linear plot of the averaged IV characteristics across all channel spacings with percentage error bars of 5%.

Figure 5.26 shows the full range of IV characteristics for the LTLM structure. Each channel was swept at least 12 times, ranging from ±1 V, to ±20 V, with the average data presented in the figure. A simplified circuit diagram of the structure, as it was tested, may resemble a series of parallel resistors, along with the channel resistor. Taking an average value of resistivity for the 10 µm wires of 0.14 Ω cm, and estimating the distance via the two conductive paths from the probe to the LTLM channel as 162 µm, thickness 0.5 µm, the predicted pair of resistors for each contact wire are 21 kΩ. Given a channel spacing of 4 µm, with resistivity of phosphorous doped diamond as quantified by CTLM at 15 Ω cm, thickness 1.2 µm and contact width 60 µm, it can be expected for the channel resistance to be approximately 340 kΩ. This is represented by figure 5.27.

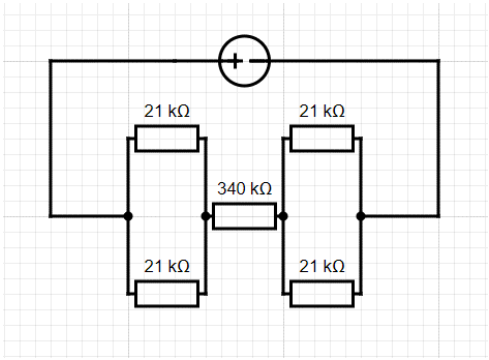

Figure 5.27 A circuit diagram of the expected LTLM structure for a 4 µm channel.

This resistance is not reflected in the LTLM data, despite further experiments on emitter structures following this expectation well. As this is the case for all LTLM data collected in this set of experiments, which involved at minimum two days of data collection, it is unclear why this is the case. The data point towards an unintended conduction channel being responsible for the observed IV characteristics, despite control experiments ensuring that

no conductive channel was present without the probes actively in contact with the LTLM test structure, as is standard practice. Furthermore, the same probes and experimental setup were used to provide testing data on wire structures, with no issues identified with any of those electrical sweeps or the data in follow-up analysis. Despite these checks, the LTLM data presented here must be considered to be affected by a systematic error, due to the large discrepancy in observed resistance and the resistance of all other test structures.

Finally, with the benefit of additional data through emitter testing and another LTLM experiment that will be presented in the following sections, a more realistic peak current value may be expected at the 3 µA level for channel spacings comparable to that of the LTLM structure. While this is certainly not a full TLM methodology, if the current observed in all of the LTLM measurements presented here were affected by a factor of 10^5 shift due to an unknown systematic error, then the actual specific contact resistivity would be approximately 1 $\Omega\,\mathrm{cm}^2$. This is the same order of magnitude that was observed via thermal graphitisation [14], and would place laser processing firmly among the established methods of reducing specific contact resistivity to highly phosphorous doped diamond, even given the lower resistivity previously measured on these samples using CTLM which will make any ohmic contacts harder to form.

5.3. Second Round Of LTLM

As it was established in section 5.2.5 that the collected LTLM data had an inexplicable systematic error following measurements of emitter structures, a fresh set of measurements were taken with new micro-probes and another solvent clean. To ensure that these data would have a higher reliability, the additional step of taking measurements under illumination and in complete darkness was undertaken. The intention of this, along with a more thorough experimental process overall was to ensure that the IV data was both repeatable and also sensible in the context of phosphorous doped diamond samples.

5.3.0.1. Light/Dark Experimental Setup

In the following experimental analysis, light is used to refer to the condition in which the sample was illuminated by a 100 lumen LED, positioned directly above the sample window. Dark is used to refer to the condition of when the sample window was covered by a blocking cover. While the exact intensity of light at the sample surface was unknown, this was considered sufficient to test if direct illumination had any effect on the electrical characteristics.

5.3.0.2. IV Characteristics (Light/Dark)

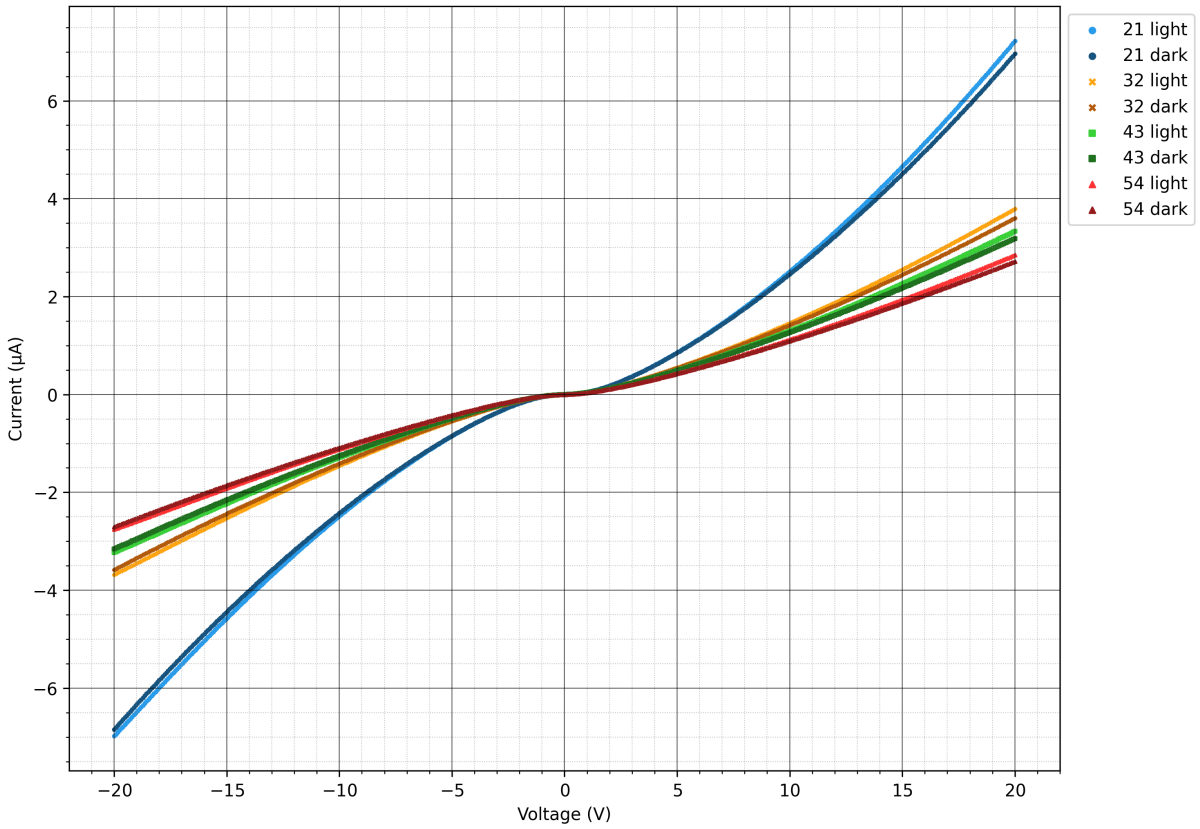

Figure 5.28 A linear plot of the averaged IV characteristics across all channel spacings, ±20 V, under bright illumination or in darkness. The contact width in this experiment was 60 µm.

Figure 5.28 shows the full set of IV characteristics taken during this second run of LTLM measurements. Each set of scatter points represents 3 datasets, averaged together with 501 data points. The same probe positions as for the previous LTLM measurements were used. Lighter and darker colours are used to help provide a visual difference between the light and dark datasets respectively, which diverge in a consistent manner. The reduction of measured total resistance under illumination provides a clear indication of semiconducting properties, with the conductive path expected to be within the phosphorous doped diamond surface layer. The observed current matches the conclusions drawn from the previous LTLM testing, with the correct order of magnitude as expected for contacts of $\sim 1\ \Omega\,\mathrm{cm}^2$ beyond the low voltage region. Note that in contrast to the previous LTLM IV plots which had 5% error bars to account for the spread of datapoints observed during testing, the data in this figure were observed to be highly repeatable and the error can instead be presumed to be close to the limit imposed by that of the B1500 probe station. As calibrated, this is below 1 nA, approaching 1 pA, and is hence not visible in the plots of currents as error bars. Please see section 3.4.1.2 for discussion of contact length normalisation, as the data presented here represents the measured IV properties only.

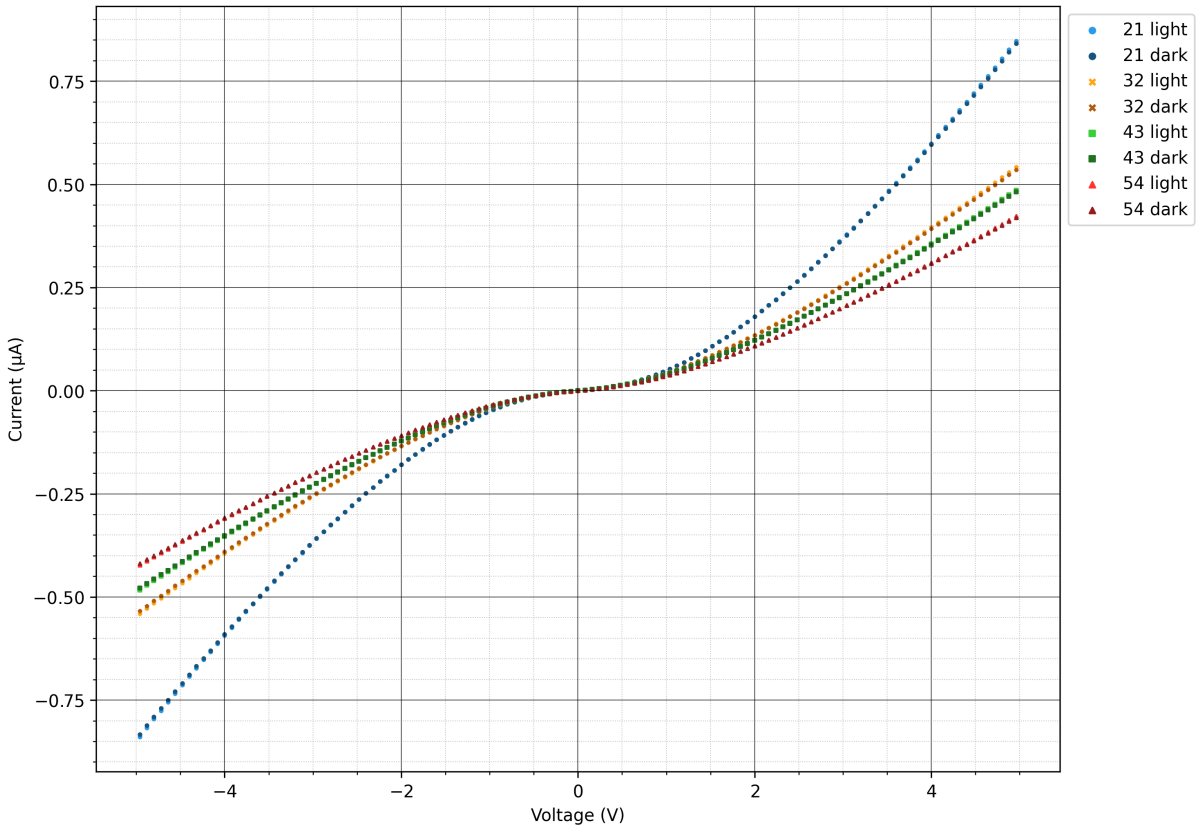

Figure 5.29 A linear plot of the averaged IV characteristics across all channel spacings, ±5 V, under bright illumination or in darkness.

In figure 5.29, the low voltage region in particular is plotted. At this scale, it is difficult to see the marginal reduction in resistance due to illumination relative to the dark characteristics. It is also considered that the 501 datapoints used for these sweeps are adequate to resolve the low voltage region, which may be defined as ±1 V. Further sampling would provide more certainty for comparisons between channels, but the potential for error due to micro-probe positioning negates the slight gains in precision that could be obtained with higher datapoints. Within this bias region, neither of the double Schottky barriers are sufficiently biased to overcome the Schottky barrier heights. As for figure 5.28, the channels are ordered in measured resistance as should be expected, 2-1, 3-2, 4-3 and 5-4, in order of ascending channel spacings.

5.3.1. LTLM Characteristics (Light/Dark)

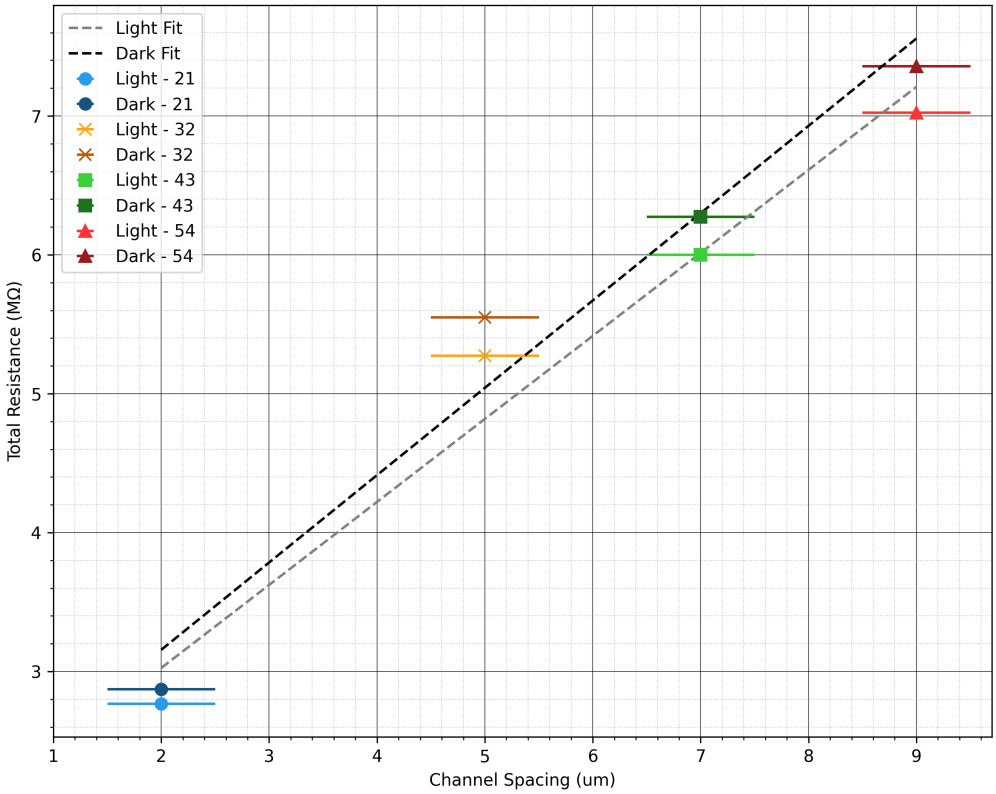

Figure 5.30 A LTLM plot of the total measured resistance against LTLM channel spacing at 20 V, with lines of best fit for both the illuminated and dark datasets. Uncertainties due to the error associated with current measurements are not possible to see at this scale, ±0.5 µm horizontal error bars are plotted.

Parameter	Light	Dark
R^2	0.969	0.966
R_c (kΩ)	915	949
R_s (MΩ/□])	35.9	37.7
ρ_c (Ω cm^2)	0.659	0.683
L_t (µm)	1.53	1.51
ρ_s (Ω cm)	4300	4530

Table 5.9 LTLM Parameters at 20 V for light and dark conditions.

Figure 7.6 shows the results of plotting the total measured resistance at 20 V against the designed channel spacing (2, 5, 7 and 9 µm), with the data taken both under a bright light source and also in complete darkness represented. Error bars of ±0.5 µm are plotted to account for the possible deviation of channel spacing as observed via optical characterisation. The extracted parameters are summarised in table 5.9.

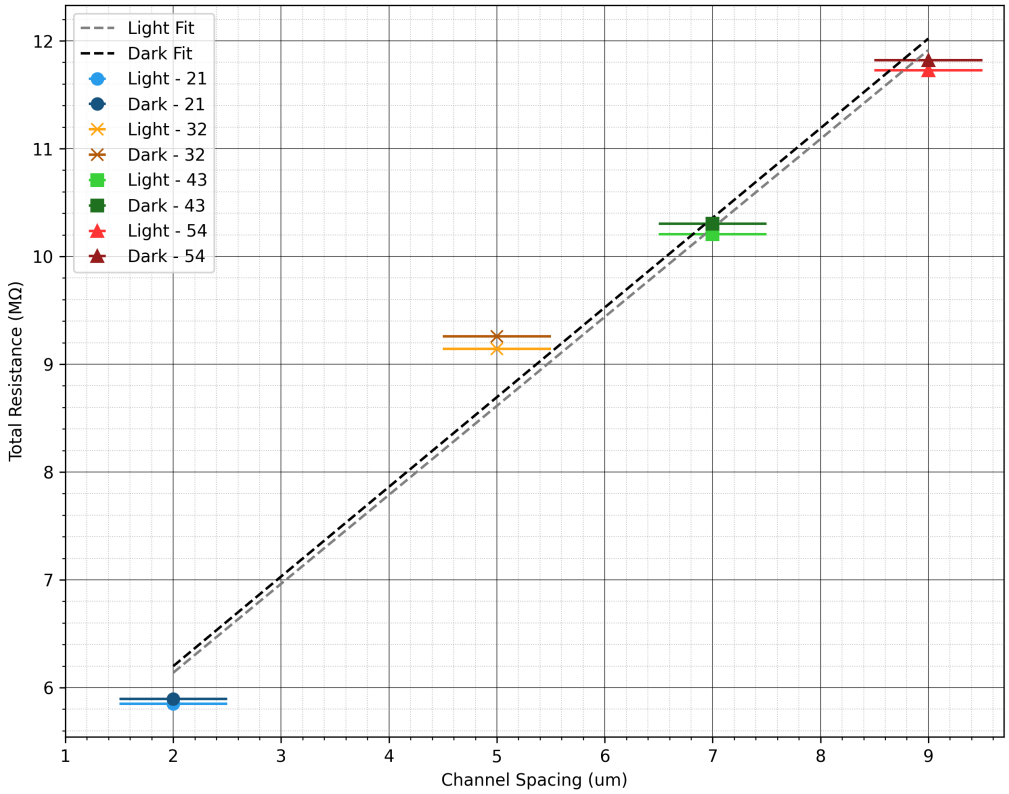

Figure 5.31 A LTLM plot of the total measured resistance against LTLM channel spacing at 5 V, with lines of best fit for both the illuminated and dark datasets. Uncertainties due to the error associated with current measurements are not possible to see at this scale, ±0.5 µm horizontal error bars are plotted.

Parameter	Light	Dark
R^2	0.978	0.976
R_c (kΩ)	2244	2268
R_s (MΩ□$^{-1}$)	49.5	49.9
ρ_c (Ω cm^2)	1.62	1.63
L_t (µm)	2.72	2.73
ρ_s (Ω cm)	5940	5990

Table 5.10 LTLM Parameters at 5 V for light and dark conditions.

Figure 5.31 shows a LTLM plot for total resistance as measured at an applied bias of 5 V against the designed channel spacing (2, 5, 7 and 9 µm), with the data taken under both a bright light source and also in complete darkness represented. Error bars of ±0.5 µm are plotted to account for the possible deviation of channel spacing as observed via optical characterisation. The extracted parameters are given in table 5.10. The change in specific contact resistivity is quite natural, as it may be interpreted as mostly being due to the image force barrier lowering of the forwardly biased Schottky barrier in the

double Schottky structure [21, 3]. There is the additional factor of greater donor ionisation under increasing electric field strengths that may also be considered as a factor, since the majority of substitutional phosphorous dopants are effectively frozen out at room temperature [9, 5, 4]. The concentration of dopants is a key factor in the formation of conventional ohmic contacts on semiconductors, and this may hence be visible here.

5.3.2. Voltage Dependent specific contact resistivity

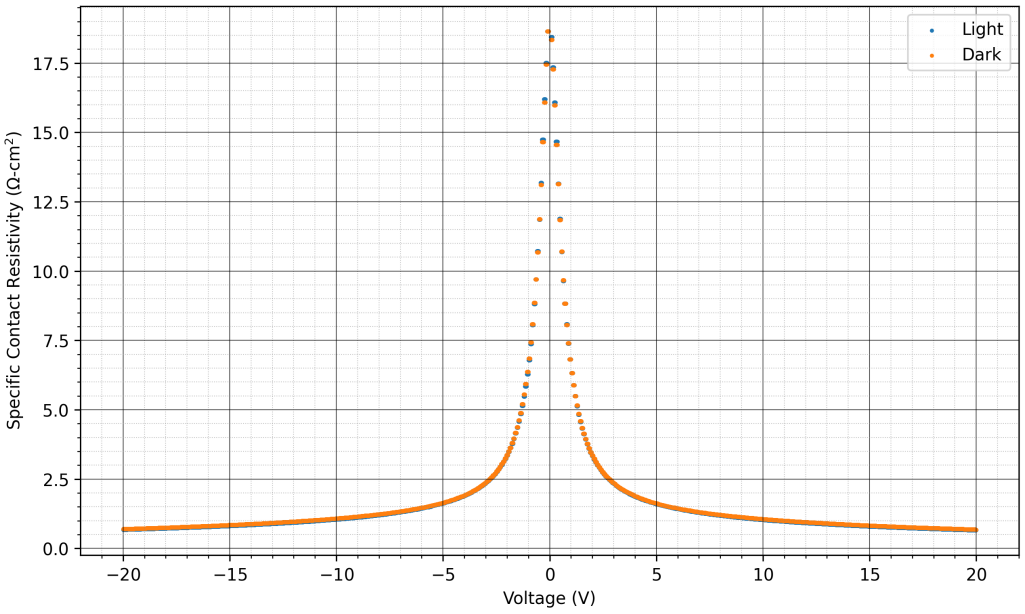

Figure 5.32 A plot of the measured specific contact resistivity as a function of applied voltage, sampling the full range of IV characteristics.

Finally, figure 5.32 provides a visual representation for the dependence of specific contact resistivity upon the applied voltage across the device. Notably, even in the very low voltage region approaching 0 V, the specific contact resistivity remains below 20 $\Omega\,\mathrm{cm}^2$. This is quite unexpected, as the IV characteristics would initially indicate that the low voltage region has a very high resistance. Instead, it is clear that the double Schottky structure here allows for a measurable level of leakage current even without either contact being in the forward bias mode of operation. The difference between measurements taken under direct illumination and in complete darkness are difficult to pick apart in figure 5.32, but there is a mean difference between the light and dark data of $-0.0228\ \Omega\,\mathrm{cm}^2$, with a variance of $0.0003\ \Omega^2\,\mathrm{cm}^4$. The negative mean difference indicates that the dark specific contact resistivity is higher than that of the well lit measurements, and the variance is low enough to consider the majority of data in this voltage range to agree with this mean difference. For a final check, a comparison between all pairs of data-points was conducted to find any dark values which were less than that of the light measurements.

All such values are contained within the ±1.08 V range, as could be expected based on the divergence of IV characteristics beyond 1 V.

Throughout all of the data presented for the second round of LTLM measurements, the error can be estimated via the previously discussed estimates of error via exact probe positioning on the laser processed wires. The systematic error present for these measurements is estimated to be approaching the limit imposed by the B1500 probe station, which is well below even 1% of the currents measured here.

References

[1] John C. Angus et al. "Twinning and faceting in early stages of diamond growth by chemical vapor deposition". In: *Journal of Materials Research* 7.11 (Nov. 1992), pp. 3001–3009. ISSN: 2044-5326. DOI: 10.1557/jmr.1992.3001. URL: http://dx.doi.org/10.1557/JMR.1992.3001.

[2] K.K. Ashikkalieva et al. "Internal structure and conductivity of laser-induced graphitized wires inside diamond". In: *Diamond and Related Materials* 128 (Oct. 2022), p. 109243. ISSN: 0925-9635. DOI: 10.1016/j.diamond.2022.109243. URL: http://dx.doi.org/10.1016/j.diamond.2022.109243.

[3] V. Aubry and F. Meyer. "Schottky diodes with high series resistance: Limitations of forward I-V methods". In: *Journal of Applied Physics* 76.12 (Dec. 1994), pp. 7973–7984. ISSN: 1089-7550. DOI: 10.1063/1.357909. URL: http://dx.doi.org/10.1063/1.357909.

[4] N Donato et al. "Diamond power devices: state of the art, modelling, figures of merit and future perspective". In: *Journal of Physics D: Applied Physics* 53.9 (Dec. 2019), p. 093001. ISSN: 1361-6463. DOI: 10.1088/1361-6463/ab4eab. URL: http://dx.doi.org/10.1088/1361-6463/ab4eab.

[5] Nazareno Donato and Florin Udrea. "Static and Dynamic Effects of the Incomplete Ionization in Superjunction Devices". In: *IEEE Transactions on Electron Devices* 65.10 (Oct. 2018), pp. 4469–4475. ISSN: 1557-9646. DOI: 10.1109/ted.2018.2867058. URL: http://dx.doi.org/10.1109/TED.2018.2867058.

[6] T.A. Grotjohn et al. "Heavy phosphorus doping by epitaxial growth on the (111) diamond surface". In: *Diamond and Related Materials* 44 (Apr. 2014), pp. 129–133. DOI: 10.1016/j.diamond.2014.02.009. URL: https://doi.org/10.1016/j.diamond.2014.02.009.

[7] Sandor Holly et al. "Precision shaping of a diamond surface by using interferometrically controlled laser-ablation method". In: *SPIE Proceedings*. Ed. by Vitali I. Konov and Victor G. Ralchenko. SPIE, Oct. 1998. DOI: 10.1117/12.328196. URL: http://dx.doi.org/10.1117/12.328196.

[8] Hiromitsu Kato et al. "Characterization of specific contact resistance on heavily phosphorus-doped diamond films". In: *Diamond and Related Materials* 18.5 (2009). Proceedings of Diamond 2008, the 19th European Conference on Diamond, Diamond-Like Materials, Carbon Nanotubes, Nitrides and Silicon Carbide, pp. 782–785. ISSN: 0925-9635. DOI: https://doi.org/10.1016/j.diamond.2009.01.033. URL: https://www.sciencedirect.com/science/article/pii/S0925963509000363.

[9] S. Koizumi et al. "Growth and characterization of phosphorous doped {111} homoepitaxial diamond thin films". In: *Applied Physics Letters* 71.8 (Aug. 1997), pp. 1065–1067. DOI: 10.1063/1.119729. URL: https://doi.org/10.1063/1.119729.

[10] T.V. Kononenko et al. "Femtosecond laser microstructuring in the bulk of diamond". In: *Diamond and Related Materials* 18.2–3 (Feb. 2009), pp. 196–199. ISSN: 0925-9635. DOI: 10.1016/j.diamond.2008.07.014. URL: http://dx.doi.org/10.1016/j.diamond.2008.07.014.

[11] V V Kononenko et al. "Photoinduced graphitization of diamond". In: *Laser Physics Letters* 12.1 (Dec. 2014), p. 016101. ISSN: 1612-202X. DOI: 10.1088/1612-2011/12/1/016101. URL: http://dx.doi.org/10.1088/1612-2011/12/1/016101.

[12] V V Kononenko et al. "Photoinduced graphitization of diamond". In: *Laser Physics Letters* 12.1 (2015), p. 016101. DOI: 10.1088/1612-2011/12/1/016101. URL: https://doi.org/10.1088/1612-2011/12/1/016101.

[13] Vitalii V Kononenko et al. "Effect of the pulse duration on graphitisation of diamond during laser ablation". In: *Quantum Electronics* 35.3 (Mar. 2005), pp. 252–256. ISSN: 1468-4799. DOI: 10.1070/qe2005v035n03abeh002900. URL: http://dx.doi.org/10.1070/QE2005v035n03ABEH002900.

[14] Tsubasa Matsumoto et al. "Reduction of n-type diamond contact resistance by graphite electrode". In: *physica status solidi (RRL) – Rapid Research Letters* 8.2 (Nov. 2013), pp. 137–140. ISSN: 1862-6270. DOI: 10.1002/pssr.201308252. URL: http://dx.doi.org/10.1002/pssr.201308252.

[15] David S. McLachlan, Michael Blaszkiewicz, and Robert E. Newnham. "Electrical Resistivity of Composites". In: *Journal of the American Ceramic Society* 73.8 (Aug. 1990), pp. 2187–2203. ISSN: 1551-2916. DOI: 10.1111/j.1151-2916.1990.tb07576.x. URL: http://dx.doi.org/10.1111/j.1151-2916.1990.tb07576.x.

[16] Hugh O. Pierson. "Graphite Structure and Properties". In: *Handbook of Carbon, Graphite, Diamonds and Fullerenes*. Elsevier, 1993, pp. 43–69. DOI: 10.1016/b978-0-8155-1339-1.50008-6. URL: http://dx.doi.org/10.1016/B978-0-8155-1339-1.50008-6.

[17] Patrick S. Salter et al. "High resolution structural characterisation of laser-induced defect clusters inside diamond". In: *Applied Physics Letters* 111.8 (Aug. 2017). ISSN: 1077-3118. DOI: 10.1063/1.4993118. URL: http://dx.doi.org/10.1063/1.4993118.

[18] Patrick S. Salter et al. “Laser Engineering Nanocarbon Phases within Diamond for Science and Electronics”. In: *ACS Nano* 18.4 (Jan. 2024), pp. 2861–2871. ISSN: 1936-086X. DOI: 10.1021/acsnano.3c07116. URL: http://dx.doi.org/10.1021/acsnano.3c07116.

[19] Cameron J Shearer et al. “Accurate thickness measurement of graphene”. In: *Nanotechnology* 27.12 (Feb. 2016), p. 125704. ISSN: 1361-6528. DOI: 10.1088/0957-4484/27/12/125704. URL: http://dx.doi.org/10.1088/0957-4484/27/12/125704.

[20] Hitoshi Sumiya, Katsuko Harano, and Kenji Tamasaku. “HPHT synthesis and crystalline quality of large high-quality (001) and (111) diamond crystals”. In: *Diamond and Related Materials* 58 (Sept. 2015), pp. 221–225. ISSN: 0925-9635. DOI: 10.1016/j.diamond.2015.08.006. URL: http://dx.doi.org/10.1016/j.diamond.2015.08.006.

[21] S.M. Sze and Kwok K. Ng. *Physics of Semiconductor Devices*. Wiley, Apr. 2006. DOI: 10.1002/0470068329. URL: https://doi.org/10.1002/0470068329.

[22] A. Tallaire et al. “Dislocations and impurities introduced from etch-pits at the epitaxial growth resumption of diamond”. In: *Diamond and Related Materials* 20.7 (July 2011), pp. 875–881. ISSN: 0925-9635. DOI: 10.1016/j.diamond.2011.04.015. URL: http://dx.doi.org/10.1016/j.diamond.2011.04.015.

[23] Sreenath Mylo Valappil et al. “Corrosion-Resistive and Low Specific Contact Resistance Ohmic Contacts to Semiconducting Diamonds Using Nanocarbon Electrodes”. In: *physica status solidi (a)* 220.3 (Jan. 2023), p. 2200627. DOI: 10.1002/pssa.202200627. URL: https://doi.org/10.1002/pssa.202200627.

[24] Sreenath Mylo Valappil et al. “Nanocarbon ohmic electrodes fabricated by coaxial arc plasma deposition for phosphorus-doped diamond electronics application”. In: *AIP Advances* 12.8 (Aug. 2022), p. 085007. DOI: 10.1063/5.0093470. URL: https://doi.org/10.1063/5.0093470.

[25] Heming Yao et al. “Modelling electrical conduction in nanostructure assemblies through complex networks”. In: *Nature Materials* 19.7 (Apr. 2020), pp. 745–751. ISSN: 1476-4660. DOI: 10.1038/s41563-020-0664-1. URL: http://dx.doi.org/10.1038/s41563-020-0664-1.

Chapter 6. Testing of Laser Written Emitters and Simulations

6.1. Emitter Sharpness

In designing the emitter-type structures, the plausibility of measuring field effect emission was examined via electrostatic finite element modelling (FEM) in Comsol Multiphysics. The most critical factor to consider in these simulations was that of the effective cathode tip. Previous work in Oxford has demonstrated conductive graphite wires going down to 400 nm in diameter [35], however the creation of sharp emitters depends upon the cross-sectional area presented at the very end of such a wire. Simple electrostatic simulations were created to estimate the magnitude of the normal electric field experienced by wires ranging from rectangular in appearance with very sharp corners, to wires with the corners tapered off to such a degree that the radius of curvature aligns with the wire diameter. Following these electrostatic models, implementation of Fowler-Nordheim type field-effect emission with a Murphy-Good approximation was implemented to estimate the emitted current corresponding to the normal electric field on the cathodes [9, 17, 7].

Figure 6.1 The emitter structures of emitter array C-H, as closely examined as possible via oil immersion, 488 nm confocal microscopy.

Figure 6.1 shows the laser written emitter structures of interest in emitter structure C-H. While initial modelling was performed without this characterisation, the composition of effective conducting material may differ from the optically distinct profiles formed here. While the diffraction limit is evident on close examination of the emitter structures, further characterisation via experiments utilising conductive atomic force microscopy, or perhaps Kelvin probe force microscopy may provide a much sharper view of the as written emitter tip profiles due to their ability to map the electrical properties that influence field effect emission [19, 20].

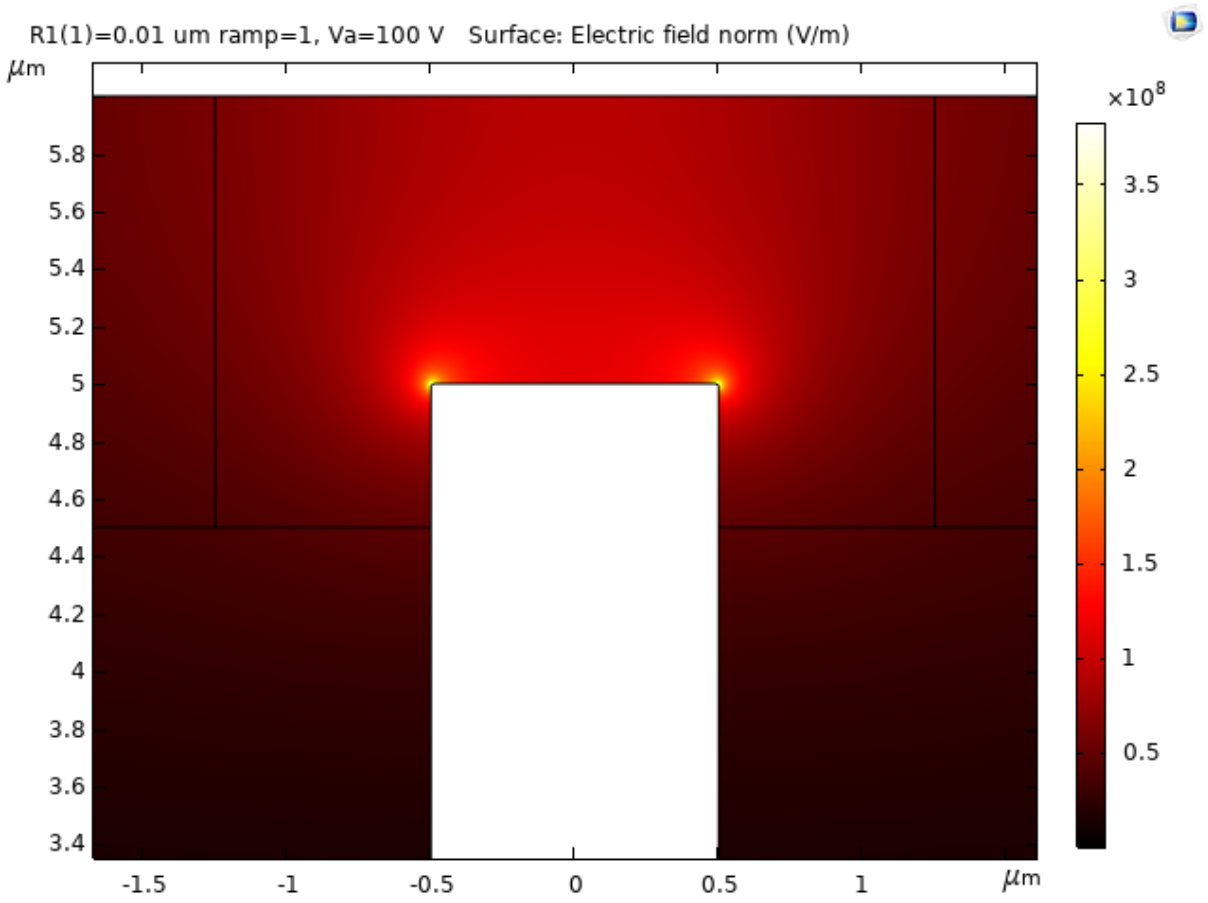

Figure 6.2 Electrostatic modelling of a surface graphitic wire with diameter 1 µm and corner radii of 0.01 µm.

Figure 6.2 illustrates the electrostatic profile of a surface graphitic wire of diameter 1 µm, which has very sharp corners which have radii of curvature of 0.01 µm. The 2D model is performed with a thickness of 1 µm. Note the intensely localised electric field at the corners of the wire, reaching above 3.5×10^8 V m^{-1}, with significantly lower normal electric fields across the rest of the wire. In this model, the cathode is held at 0 V, while the anode is held at 100 V. The cathode-anode spacing is 1 µm. The segmented sections visible (black lines) indicate different regions of meshing, with a very dense mesh used for the region immediately surrounding the tip of the emitter to better resolve the sharper features.

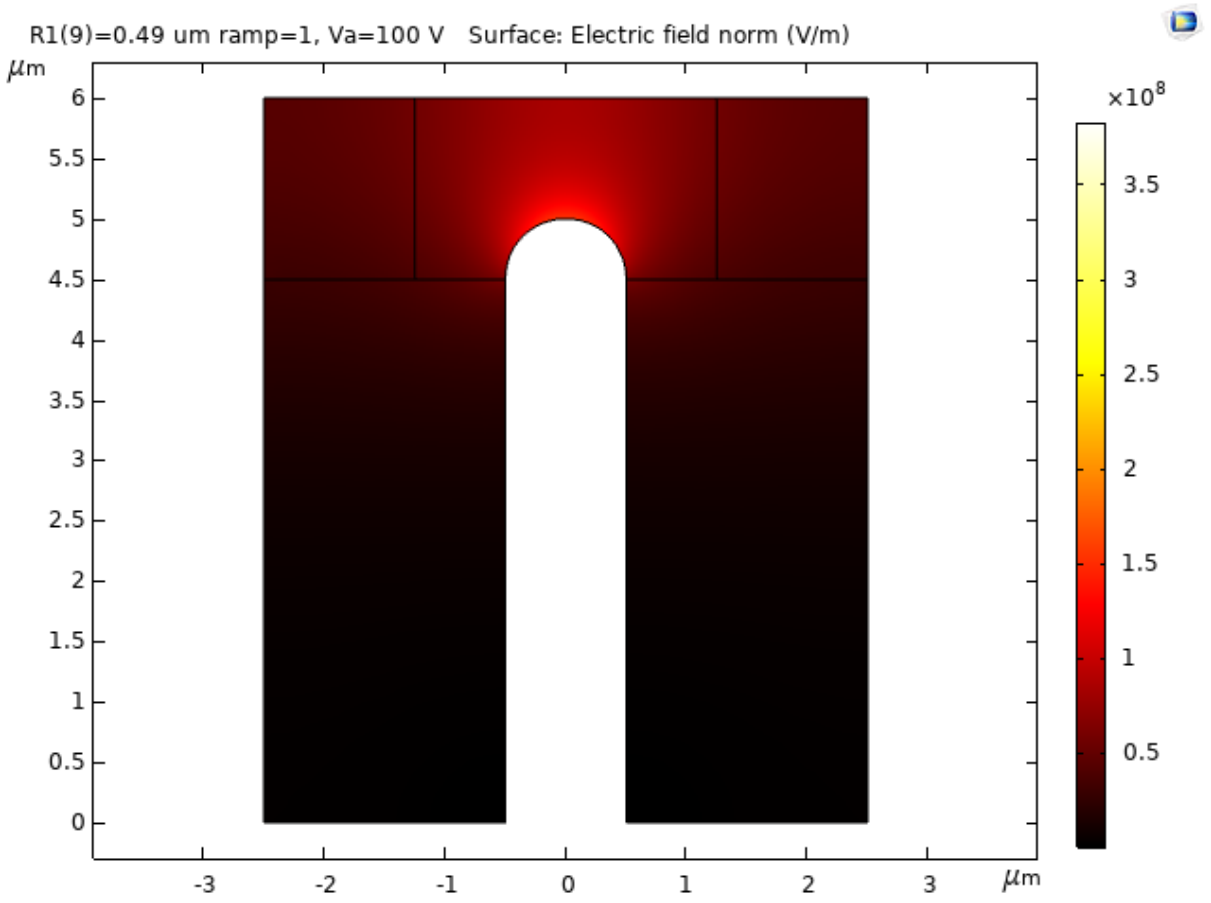

Figure 6.3 Electrostatic modelling of a surface graphitic wire with diameter 1 µm and corner radii of 0.49 µm.

Figure 6.3 demonstrates the electrostatic profile of a surface graphitic wire of diameter 1 µm, which has corners of radii 0.49 µm. The 2D model is performed with a thickness of 1 µm. Note that in contrast to figure 6.2, the wire in this model has corner radii which are very close to the radius of the wire, resulting in a nearly semi-circular end to the wire. The resulting normal electric field is significantly more diffuse than in the low radii example, with a peak at the very end of the wire corresponding to around 1.5×10^8 V m^{-1}. In this model, the cathode is held at 0 V, while the anode is held at 100 V. The cathode-anode spacing is 1 µm. The segmented sections that are partially visible (black lines) indicate different regions of meshing, with a very dense mesh used for the region immediately surrounding the tip of the emitter to better resolve the sharper features.

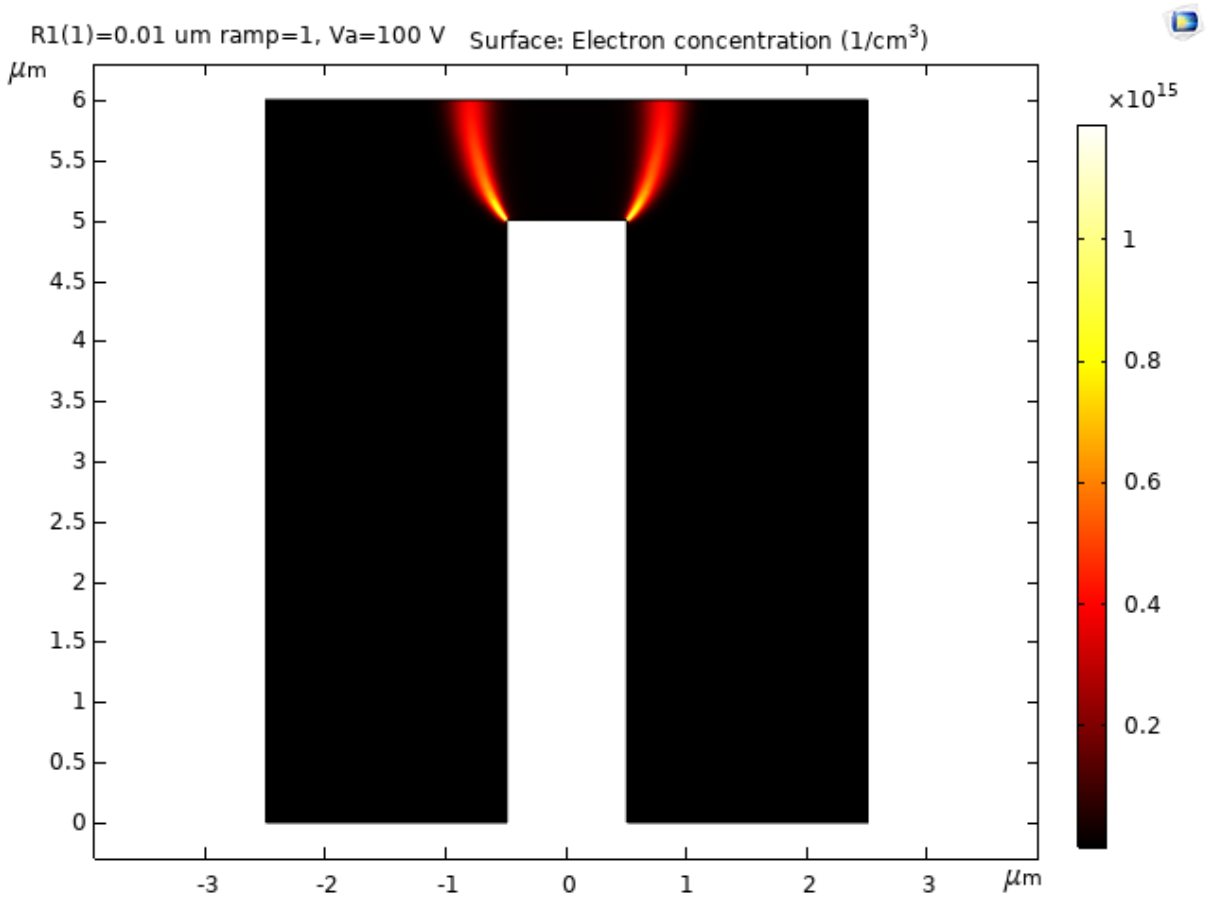

Figure 6.4 Fowler-Nordheim modelling of a surface graphitic wire with diameter 1 µm and corner radii of 0.01 µm.

In figure 6.4, a 2D simulation of a surface graphitic emitter-type structure is shown. Following a Fowler-Nordheim type field-effect emission, the resulting electron concentration can be seen to be heavily emitted from the corners, which have radii of 0.01 µm. Notable differences from the previous electrostatic modelling include the implementation of n-type doping corresponding to TLM measurements (exact concentration was what again? maybe refer to section in which I establish modelling and include the TLM models there) and a standard thermionic Schottky barrier at the cathode-diamond interface with the addition of Fowler-Nordheim tunnelling. For more details regarding the computational implementation of Fowler-Nordheim barriers, please see section (bit on meshing, Schottky barriers, some more plots of simple devices, etc. also maybe get better plots of these models, all files still saved no reason why not. normalised colour scale?). The peak electron concentration for this model was just over 1×10^{15} cm^{-3}, which is present at the corners, dropping off rapidly as the peak electric field drops following the electrostatic model of figure 6.2.

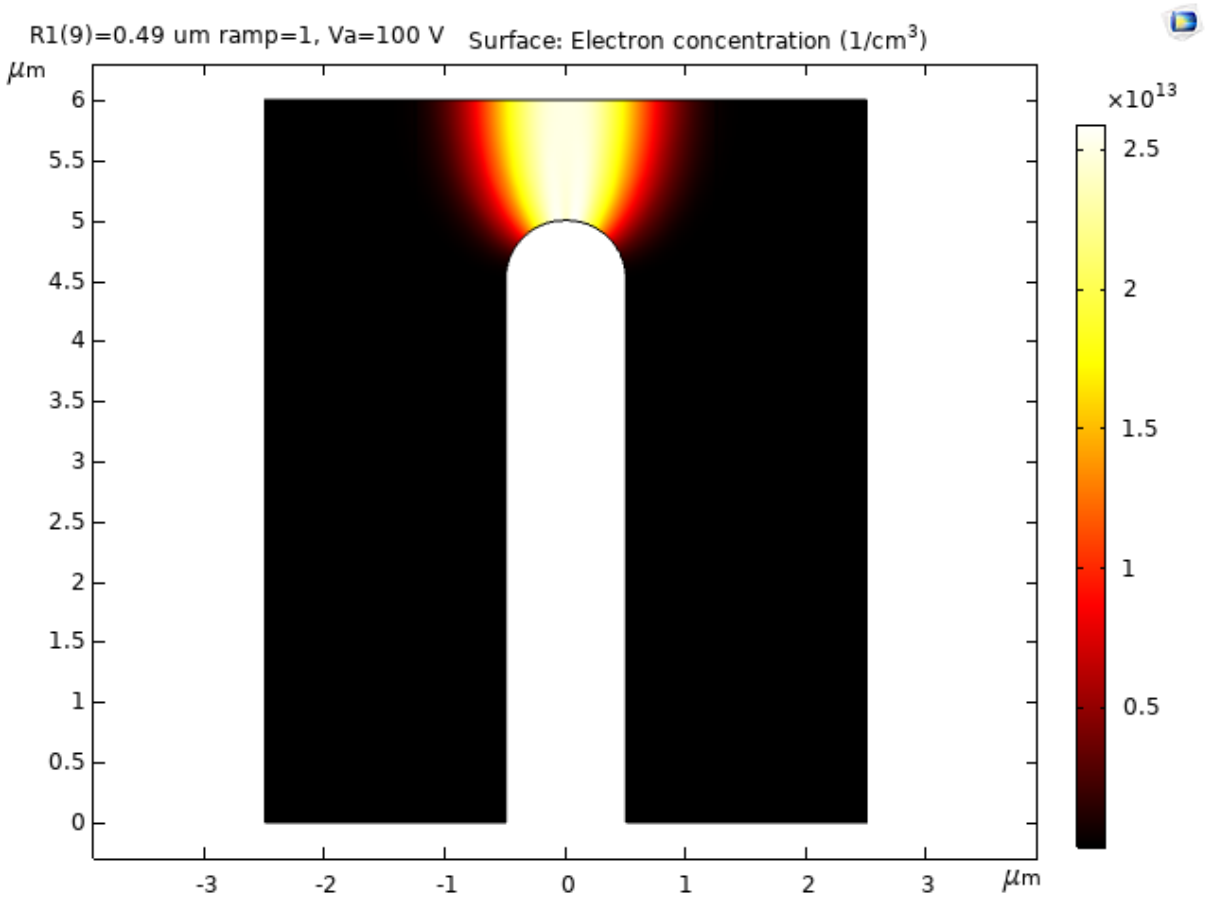

Figure 6.5 Fowler-Nordheim modelling of a surface graphitic wire with diameter 1 µm and corner radii of 0.49 µm.

In figure 6.5, a 2D simulation of a surface graphitic emitter-type structure is shown. Contrasting with figure 6.4, this model has corners of radii 0.49 µm, which are very close to the radius of the wire and hence produce a semi-circular tip. As the Fowler-Norheim emission is highly sensitive to the normal electric field, the peak electron concentration is distributed across the peak of the spherical emitter tip, where a significantly wider region is actively emitting electrons at peak concentration relative to the 0.01 µm radii. The peak concentration of electrons in this larger radii case is just over 2.5×10^{13} cm^{-3}, contrasting with the 1×10^{15} cm^{-3} of the sharper case. The order of magnitude difference of 100 with only a scale difference in the peak normal electric field of around 2 demonstrates the drastic geometric enhancement that is possible for field-effect emission.

6.2. Laser Written Emitters - Design

As discussed in section 4.1.3, laser processing with the aim of producing graphitised wires on the surface or within the bulk of diamond may be used to fabricate devices that rely upon geometric enhancement and hence field effect emission. Simulations indicated that an appreciable level of Fowler-Nordheim type tunnelling is feasible with the small dimensions of laser fabricated wires in diamond [35]. Hence, to test this prediction experimentally, arrays of sharp emitters were designed in a similar fashion to that of LTLM contacts,

to provide direct reference data to check for the presence of field effect emission current contributions.

6.2.1. Microscopy of Emitters Prior to Testing

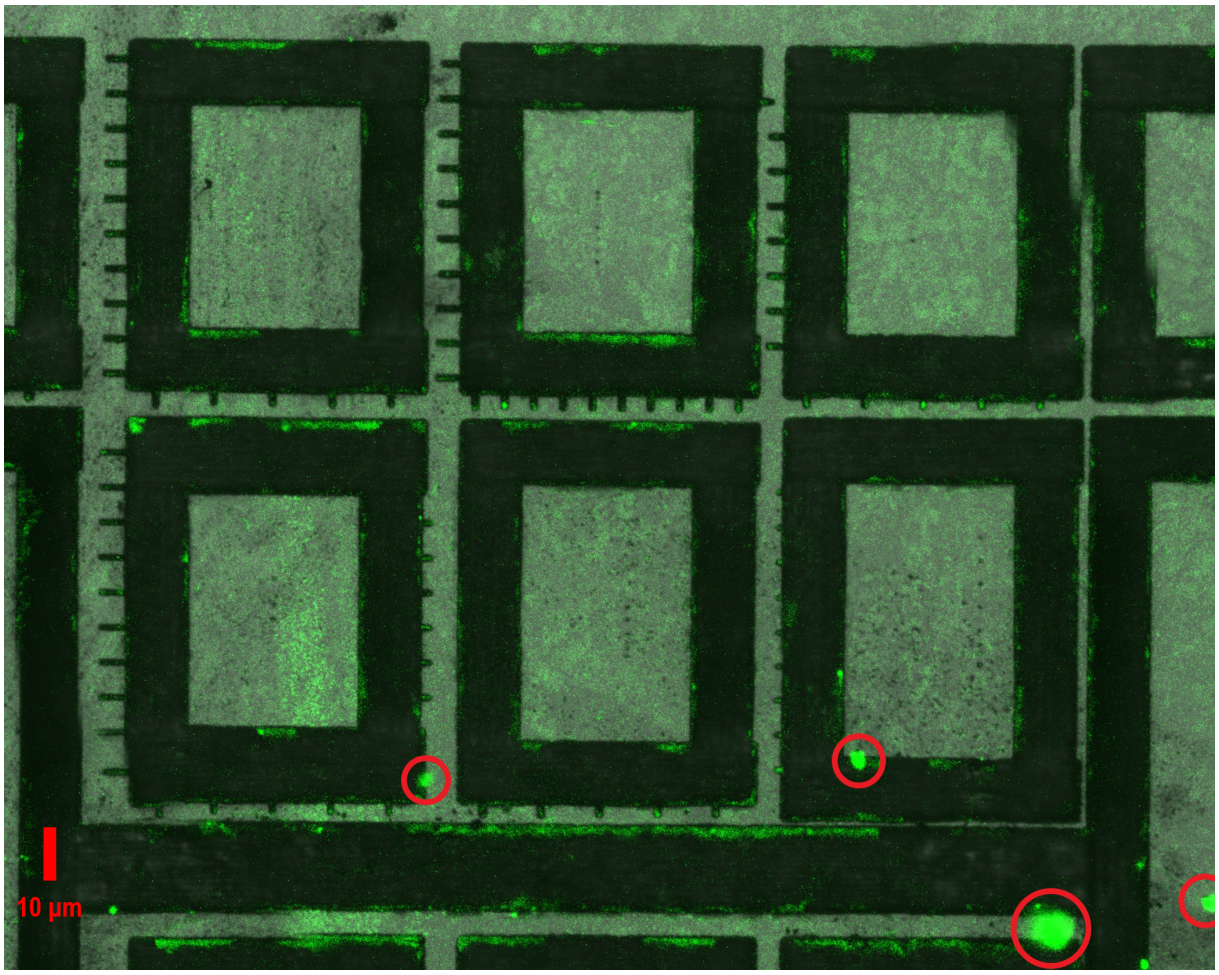

Figure 6.6 An overview of the emitter array structures via confocal microscopy with 488 nm laser illumination and 408 nm fluorescence.

In figure 6.6, the fluorescence imaging displays the observed fluorescence of these structures. Red circles are used to highlight fluorescence which has previously been speculated to be that of surface contaminants. Please see section 4.2.3 for the full analysis of fluorescence characterisation.

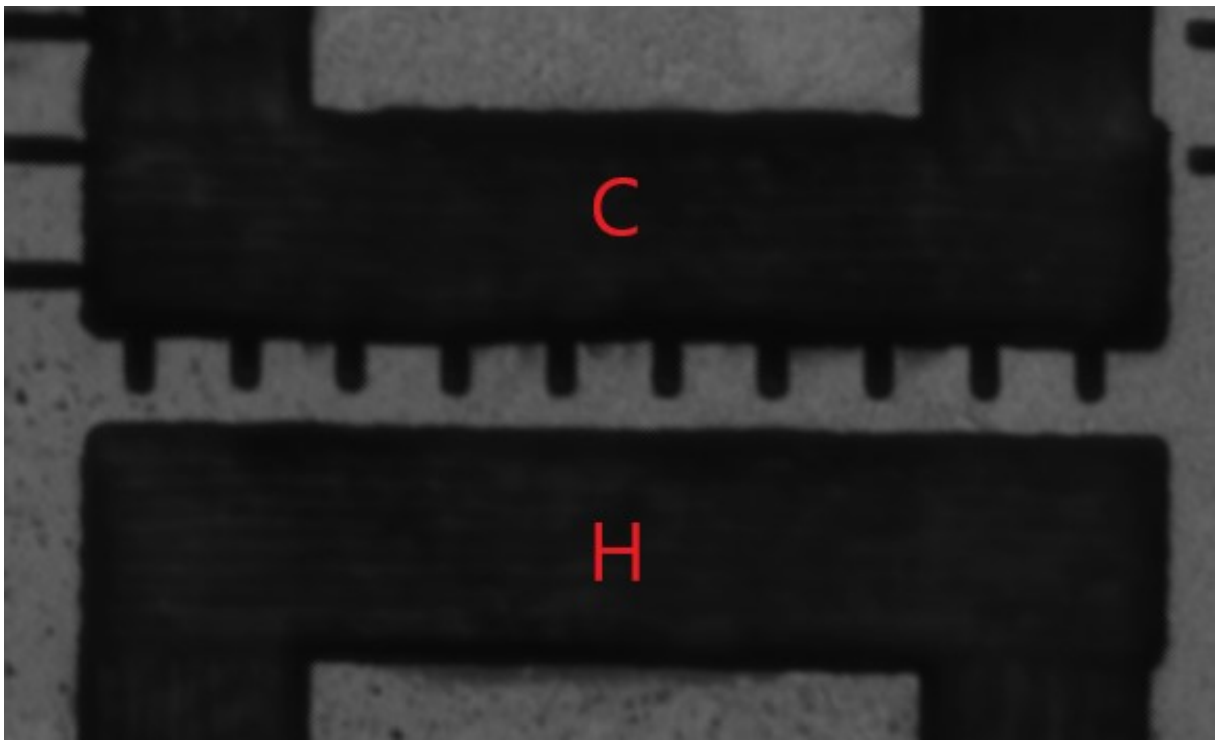

Figure 6.7 A cropped view of the CH emission channel, as seen via confocal microscopy with 488 nm laser illumination.

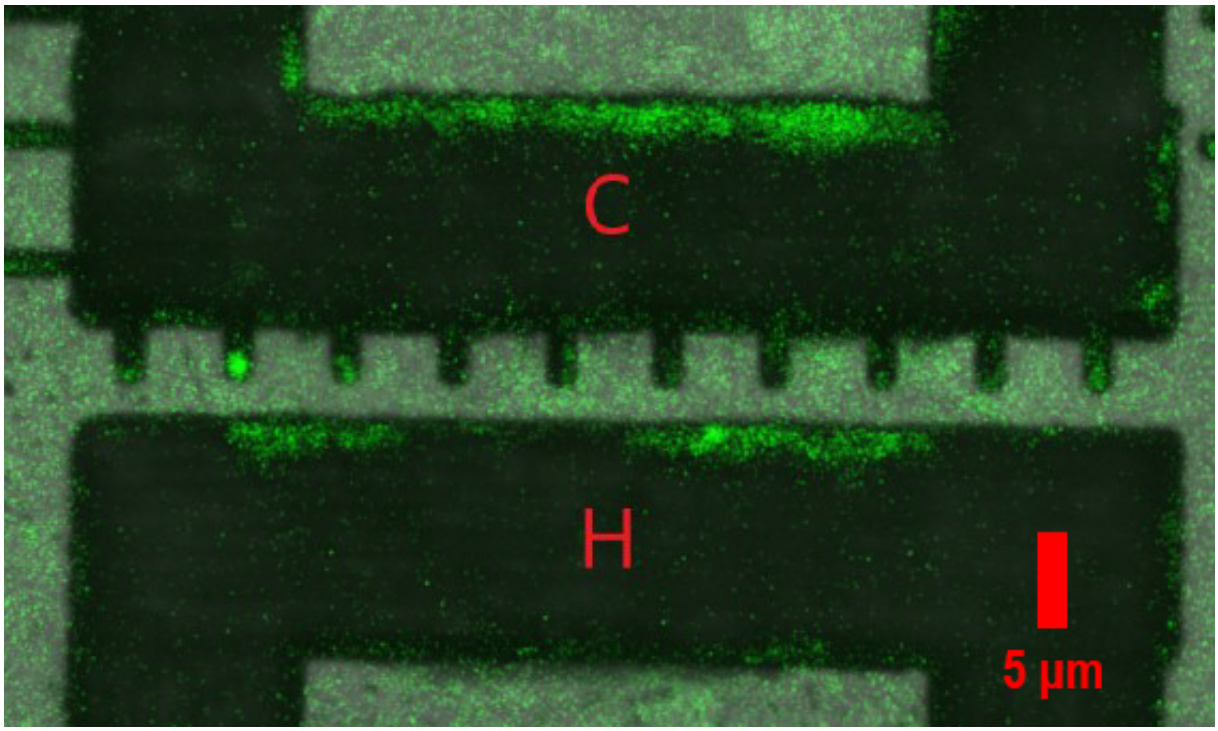

Figure 6.8 A cropped view of the CH emission channel, as seen via confocal microscopy with 488 nm laser illumination and 408 nm fluorescence.

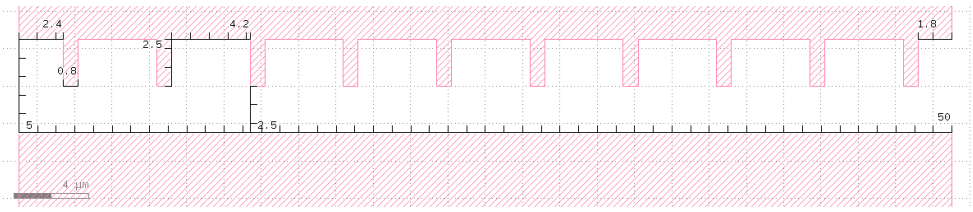

Figure 6.9 The designed channel of emitter channel CH, with measurements of all features.

Figures 6.7 and 6.8 show the confocal microscopy of the relevant channel, without and with fluorescence respectively. The emitter tip profiles are observed to follow the approximations used in modelling, with the exact radius of curvature for the effective rectangular corners appearing to match that of the expected gaussian beam profile. Due to the difficulty in interpretation of optical microscopy and the exact conductive tips, the more exact geometric profile of these emitters remains difficult to quantify. Figure 6.9 shows the designed structure of this channel, with emitter wires of thickness 0.8 µm chosen in large part due to the enhanced conductivity for slightly wider wire geometries as demonstrated in previous work by Oxford [35]. Thinner wires may have a significantly greater geometric enhancement factor. However, it has been observed that the local resistivity of the written wires is dependent upon the laser fluences used, with natural knock on effects for the cross sectional area of written wires [35]. This is linked to the process of photo and thermal graphitisation, with a summary of the theoretical models in section 2.3.2.3.

As has been discussed in the previous trial wire measurements from section 5.1, some discrepancy even within wide contact wires has been observed that may indicate a difference in sp^2 conductive carbon allotropes as generated by laser processing on this sample. The difference in observed emitter profiles hence is not unusual, as the exact profile of laser-induced change in carbon allotropes may be sensitive to local crystallinity, which is a factor for the phosphorous-doped surface layer on this sample, as will be examined in section 6.2.1.1.

Finally, the fluorescence observed in figure 6.8 for emitter array CH has some notable distinguishing features, which raised comparisons to that of AFM topographical mapping.

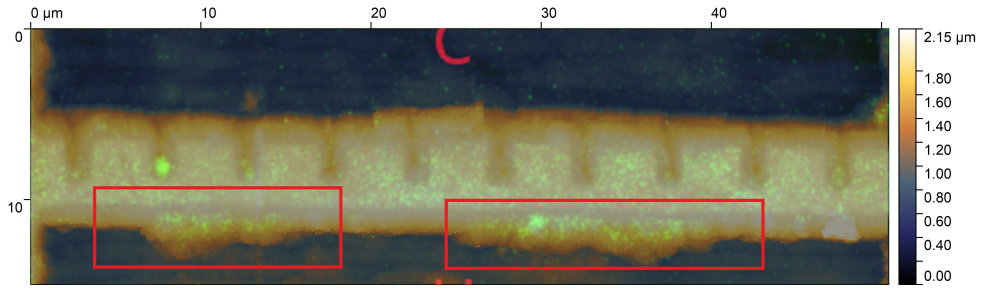

Figure 6.10 An overlay of the fluorescence observed in channel CH with the AFM topology.

Figure 6.10 is a visual overlay of the AFM topology with that of the fluorescence observed. For the AFM topology with no overlay, please see figure 4.10. Red rectangles

are used to highlight the areas where a high concentration of fluorescence is observed, while also correlating with an edge of contact H which shows a notable change in topology compared to the rest of the laser written contact. If this is material which has not fully undergone thermal graphitisation processes, then it may represent amorphous carbon, from which fluorescence is linked to surface characteristics [31, 18].

6.2.1.1. Possible Impact of Surface Topology on Emitter Profiles - HIM

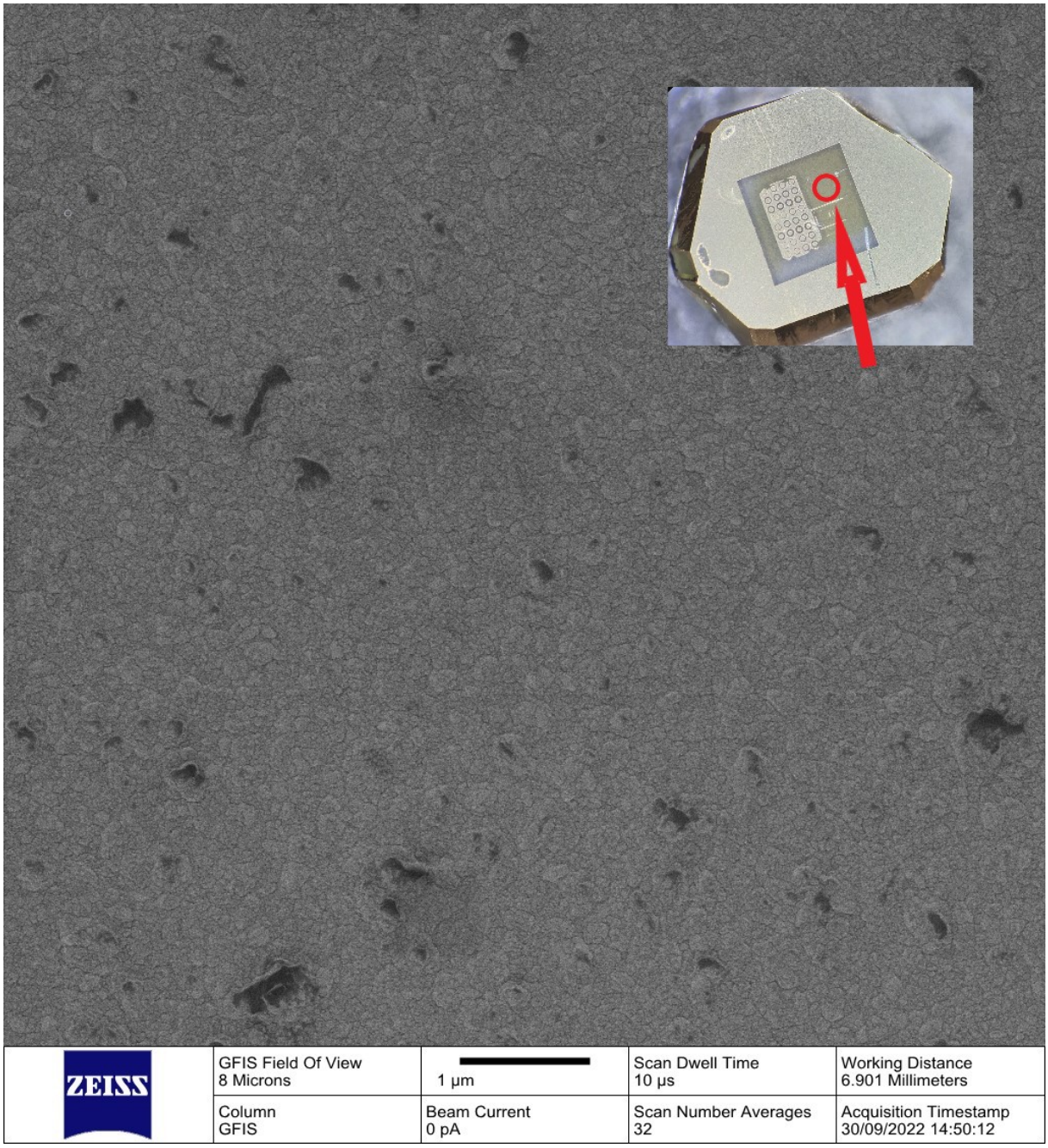

Figure 6.11 Helium ion microscopy of sample F, as was used for Ti/Au CTLM measurements. Performed in collaboration with NEXUS - Surface characterisation facility at Faculty of SAGE. Inset - picture of sample F with location of HIM marked.

To further underscore the crystallinity factor of laser processing and how it may impact the resulting profile of laser induced allotrope changes on the micro-scale, figure 6.11 shows a sample of helium ion microscopy (HIM) that was performed on sample F following CTLM characterisation. This figure is of the highly phosphorous doped diamond surface, which is grown with the same parameters as sample G - the laser processed substrate, with no metal present on this part of the sample. On the scale of ~ 200 nm, multiple "islands" of diamond growth can be seen, corresponding to highly disordered diamond growth with significant concentrations of twinning defects which are typical for (1 1 1) oriented samples [2, 27, 13, 14, 29].

One might speculate on the possible role of twinning boundaries and the modification of carbon allotropes via laser processing. Based on the size and shape of these islands, it seems likely that the exact emitter profile is dependent upon the local microstructure within the emitter channel. This would align with theoretical work into the origin of photographitisation processes being primarily defective sites in the diamond lattice [15, 16], but it is unclear on how this may relate to the more recent work on diaphitic allotropes of carbon [28, 24, 23, 25]. Field effect emission from polycrystalline films are a well studied portion of diamond electronic devices [33, 39, 40], and in particular the internal boundary of phosphorous doped polycrystalline diamond emitters has also been studied previously [34], hence the impact of a relatively polycrystalline surface layer of highly phosphorous doped diamond may be beneficial in the production of high geometric field enhancement, despite the difficulty in producing designs that rely upon planar geometries for exact device properties.

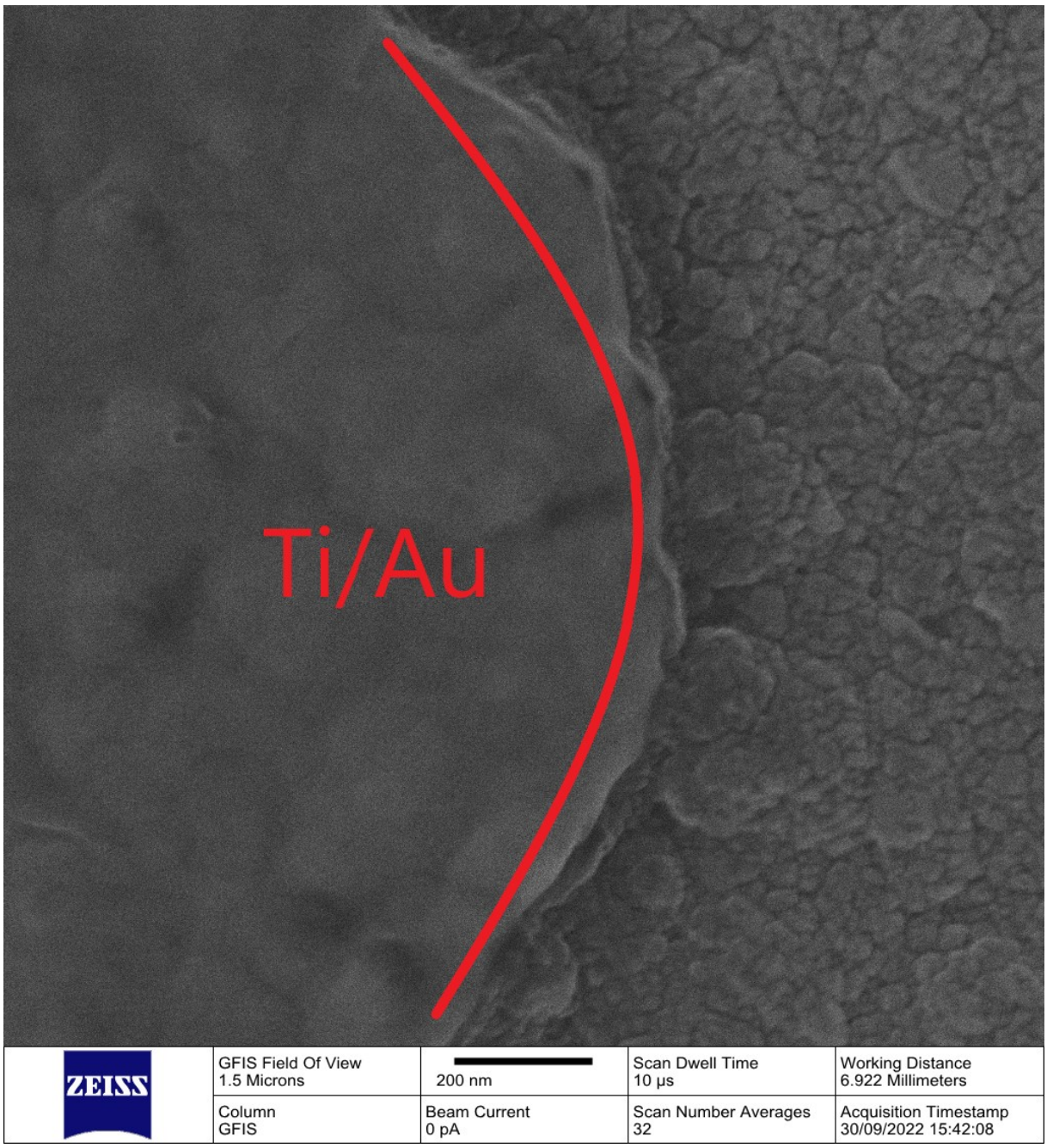

Figure 6.12 Helium ion microscopy of sample F, as was used for Ti/Au CTLM measurements. Performed in collaboration with NEXUS - Surface characterisation facility at Faculty of SAGE.

Figure 6.12 provides another HIM image of sample F, for a scan width of 1.5 µm in comparison to the previous width of 8 µm. Note the marked region on the left is a Ti/AU contact, while the right side is the uncoated phosphorous doped diamond surface, which displays a complex surface topology on the scale of tens of nanometres to hundreds of nanometres.

6.2.2. Possible Impact of Surface Topology on Emitter Profiles - D-AFM and NC-AFM

One extra set of topology characterisation data were taken via dynamic-AFM or tapping mode AFM on an untreated region of sample G, to provide some evidence that the heavily phosphorous doped surface layer grown on the two samples is similar in crystallinity. Unfortunately, the cantilevers available were the NC-AFM tips used for the earlier AFM topologies in section 4.2.2. While the depth resolution for previous scans was suitable to detect the surface ablation for emitter wires of width 0.8 µm and other such features, the diamond surface required an order of magnitude improvement. Hence, measurements were conducted with a wide sweep of the available adjustable parameters for the XE-150 AFM system, in an attempt to achieve the required resolution with cantilevers that are not suitable for contact-AFM mode characterisation.

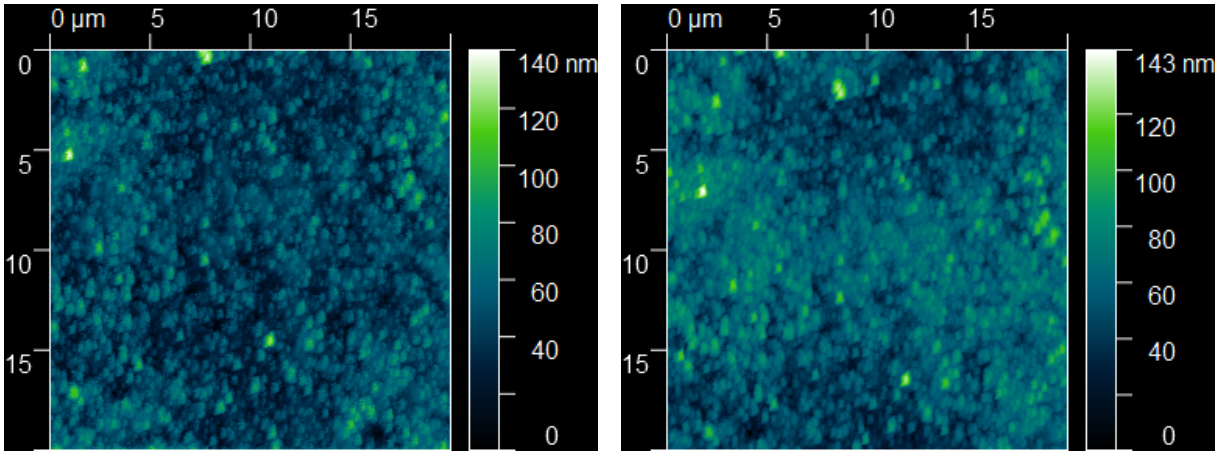

(a) D-AFM scan. **(b)** Finely calibrated NC-AFM scan.

Figure 6.13 Comparison of D-AFM and NC-AFM scans of the phosphorous doped diamond surface, in a region that was not subject to laser processing.

Figures 6.13a and 6.13b represent topological testing via D-AFM and NC-AFM respectively. Note that the images are slightly offset due to difficulties with scanning precisely the same region on the diamond sample with no visible surface features. While the HIM images demonstrate a much greater visual clarity on the nano-scale, D-AFM and NC-AFM conducted on a part of the phosphorous doped diamond surface for the laser graphitised sample confirm that there are indeed comparable features with heights of up to around 140 nm. While the resolution of these images is lower in comparison to HIM, with an effective pixel area of 78 $nm^2\,px^{-1}$, the randomly seeded nature of the as-grown diamond surface seems clear, with some quantification of the difference in height due to these different islands of diamond growth. Of the two contact methodologies employed, the tapping D-AFM mode would be expected to provide a marginally more precise topological map than the NC-AFM mode, however in figure 6.13 it is hard to distinguish the two methodologies. This may be due to the calibration steps taken to reduce noise to an absolute minimum in the NC-AFM mode. Specifically, an absolute minimum level of z-drive

was used, with a scan rate of 0.4 Hz for both D-AFM and NC-AFM over a resolution of $256x \times 56$ pixels corresponding to 78 $\mathrm{nm}^2\,\mathrm{px}^{-1}$. Additionally, several rounds of calibration were performed to reduce noise due to slight mirror misalignments or other such physical parameters. The only distinguishing detail in favour of D-AFM may be the observation of lower average troughs, which should reflect directly on the AFM tip relying on the tipping point of attractive and repulsive Van der Waals forces to identify the correct local heights.

To conclude, surface features visible via HIM and AFM characterisation on the phosphorous doped diamond surface introduce additional complexity into the formation of laser written graphitic structures. The typical diameter of such surface features is of the order of 20 to 200 nm, with observed heights of up to 140 nm. The emitter tip profiles are contingent upon a thin, sharp ending of the laser written wire. Hence, it is possible that within an emitter array of identical optical profiles, substantial grain boundaries of random orientation and sharpness may either degrade or improve the devices. While this is difficult to account for on a larger scale, this could be a crucial factor.

6.3. Emitter Electrical Characteristics

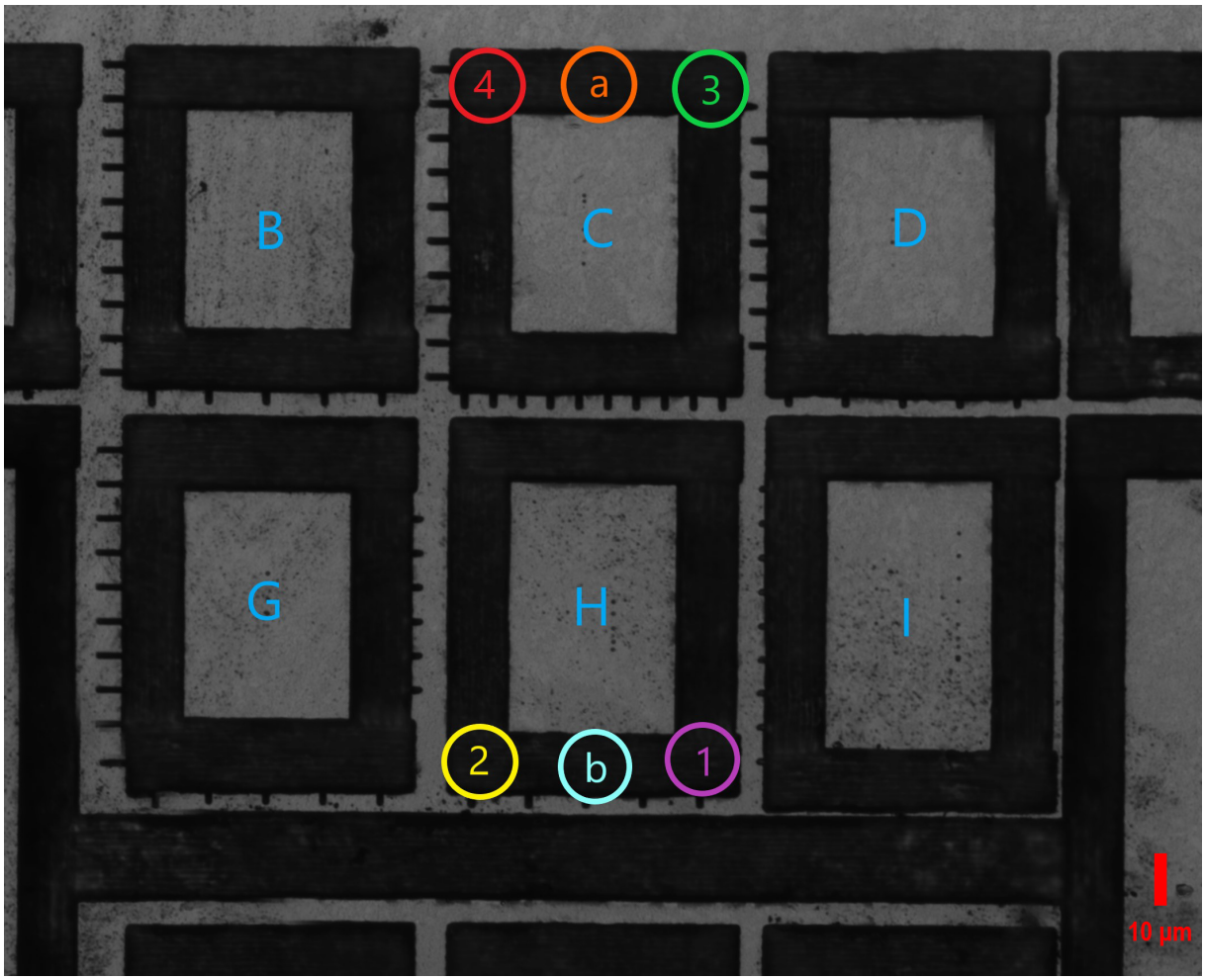

Figure 6.14 An overview of the emitter array structures via confocal microscopy with 488 nm laser illumination, and the locations of specific probes during IV characterisation of channel CH.

Figure 6.14 provides a view of the relevant emitter contact structures, and their neighbouring contacts as seen with confocal microscopy. Annotations indicate probe positions 1-4 used for the wire verification data, and positions a-b for the high voltage emitter testing.

In the following sections, the verification trials undertaken to ensure good electrical contact to the laser processed wires are summarised. In essence, the core trials involved an IV sweep of a portion of each contact, followed by low voltage sweeps across the emitter channel to verify reasonable magnitudes.

6.3.0.1. Low-Voltage Wire Testing: 4-3

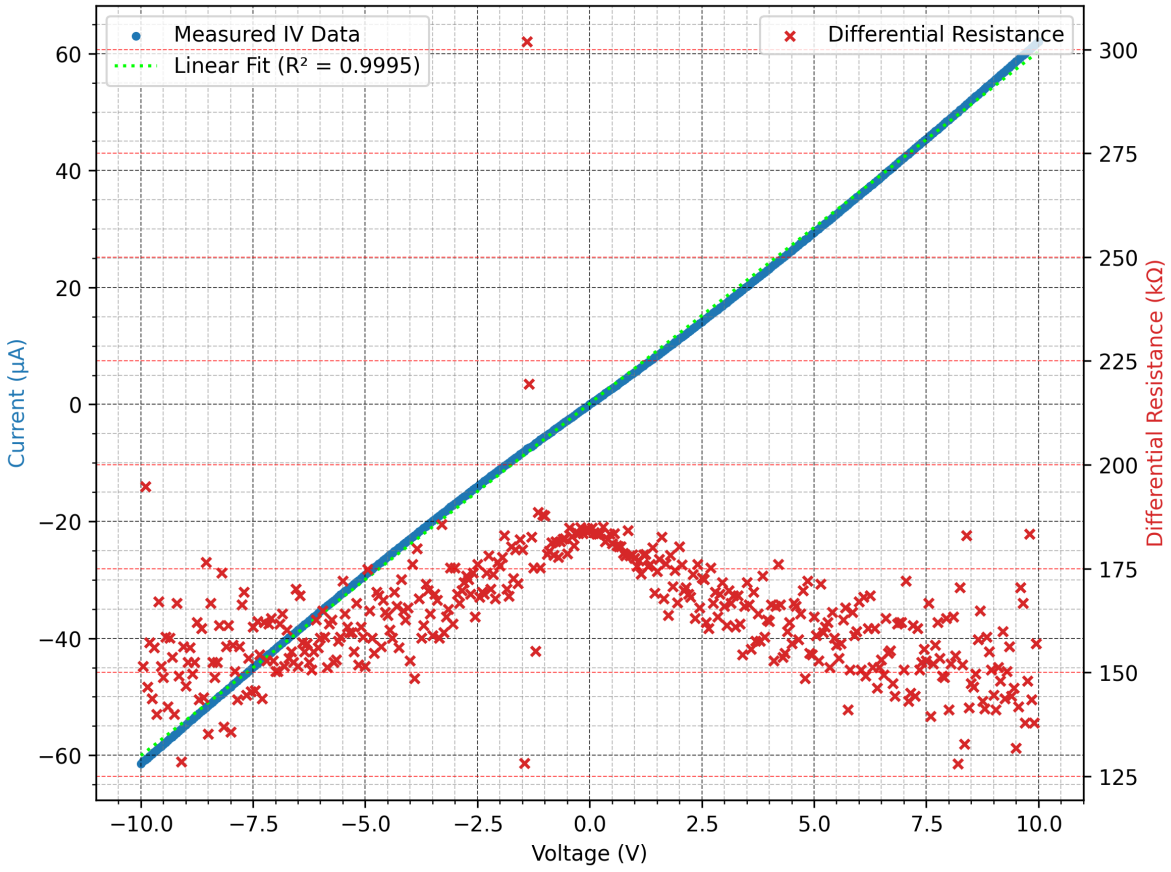

Figure 6.15 The average electrical characteristics between probe positions 4 and 3.

Voltage (V)	**Resistance (MΩ)**	**Resistivity (Ωcm)**	**Conductivity (Sm^{-1})**
10	0.166	2.08	48.2

Table 6.1 Extracted wire parameters for wire 4-3, ±10 V measurements.

Figure 6.15 shows the electrical characteristics as measured with probe positions 4-3 on the top of contact C. This essentially a measurement of the wire at the top of contact C. 401 data points across 3 separate ±10 V sweeps, with assumptions as used in the characterisation of trial wires in section 5.1 are used to provide estimated wire properties as summarised in table 6.1.

6.3.1. Low-Voltage Wire Testing: 2-1

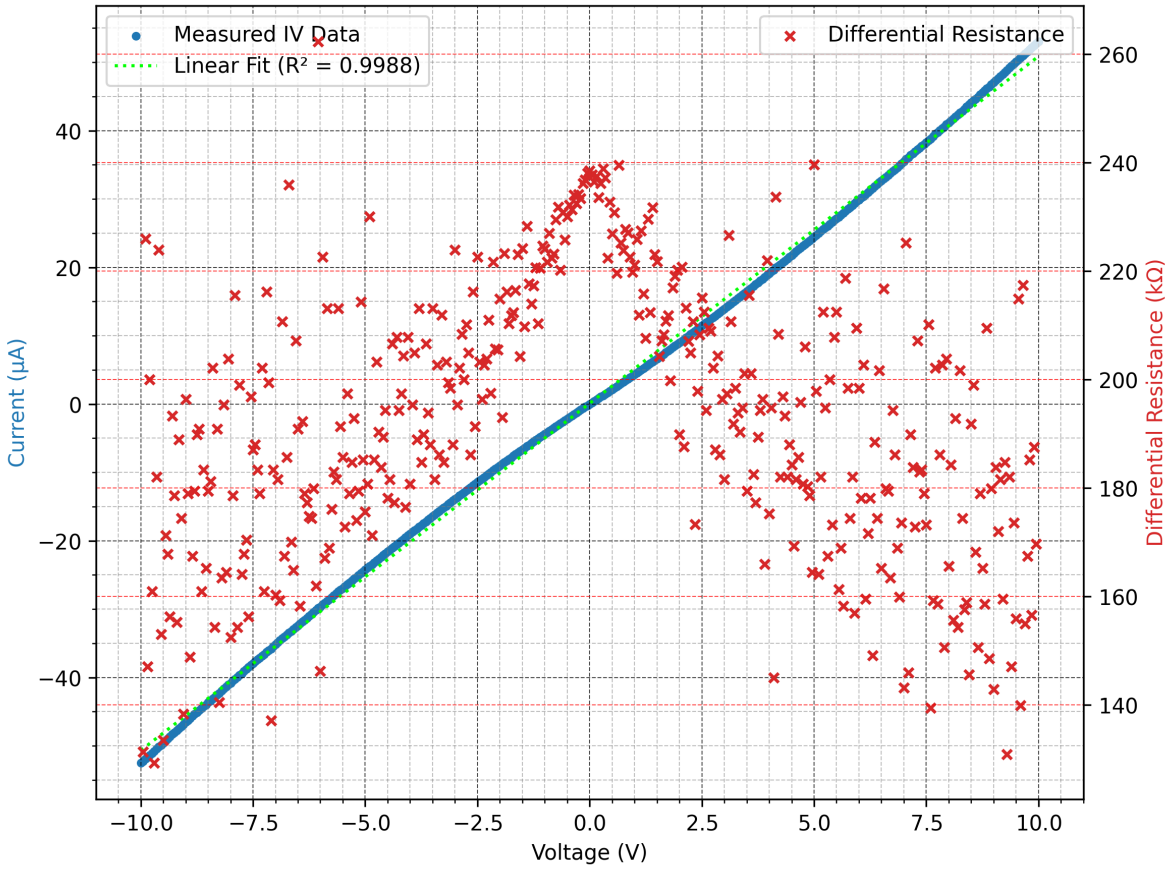

Figure 6.16 The average electrical characteristics between probe positions 2 and 1.

Voltage (V)	**Resistance** (MΩ)	**Resistivity** (Ω cm)	**Conductivity** ($\mathrm{S\,m^{-1}}$)
10	0.197	2.46	40.6

Table 6.2 Extracted wire parameters for wire 2-1, ±10 V measurements.

Figure 6.16 provides the electrical characteristics for the wire between probe positions 2-1 on contact H. The extracted parameters are summarised in table 6.2. This wire shows a slightly higher effective resistivity than the wire between 4-3, but is otherwise reasonably similar in properties. Both wires are an order of magnitude lower in conductivity than the 10 µm wires tested in section 5.1.4, which indicates some local variation in the diamond substrate or laser writing affecting the wires between these two regions. The differential resistance in figure 6.16 is notably scattered over a wider range of values than that of figure 6.15, but again the rise in resistance around a bias of 0 V is not as pronounced as in the case of data with a clear Schottky behaviour, and the scatter only shows a slight deviation from ohmic behaviour for these wires.

6.3.2. Low-Voltage Emitter Testing: 4-2

Before switching the probe positions to that of a-b, measurements were taken with the 4 probe positions as for the wire testing, which provides a first look at the IV characteristics of this emitter array.

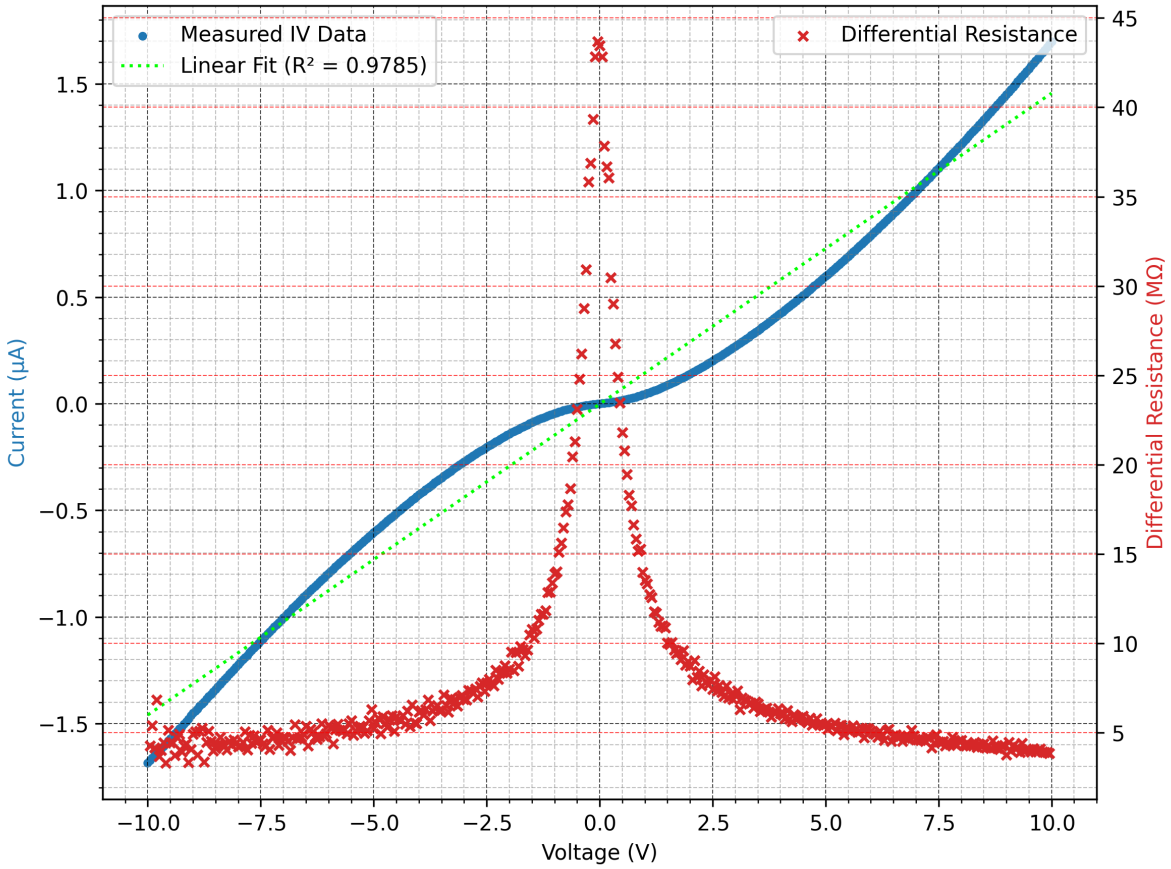

Figure 6.17 The average electrical characteristics between probe positions 4 and 2.

Voltage (V)	**Resistance** ($M\Omega$)	**Resistivity** (Ωcm)	**Conductivity** ($S m^{-1}$)
10	6.86	85.7	1.17

Table 6.3 Extracted wire parameters for "wire" approximation of 4-2, ±10 V measurements.

Figure 6.17 presents the low voltage measurements taken across probe positions 4-2, with table 6.3 providing estimated values for the resistivity using the 10 µm wire approximation for direct comparison to previous results. This approximation is useful for comparing orders of magnitude, but since the channel resistivity will be the dominant factor, the wire dimensions approximation merely shows that the electrical data reflect the emitter channel under testing. The IV characteristics here resemble those of the LTLM channels tested in section 5.3, which is a reassuring comparison, as at this potential bias the expected maximum electric field norm on emitter tips is of the order of 10^5 $V m^{-1}$. Hence, with a low applied potential difference, the expectation is for the measured current to be due to

thermionic emission. Further simulations examining the expected balance between thermal and field effect emission processes are presented in section 6.4.

6.3.3. Low-Voltage Emitter Testing: a-b Ramp-Up

With the conductivities of laser written contact wires established in the 40–48 $\mathrm{S\,m^{-1}}$ region, electrical characterisation was undertaken with the probes placed as closely as possible to the middle of the far sides of the contacts, as indicated by positions a and b in figure 6.14. This was chosen to ensure that the distances between probes and the emitter channel were close to identical on either side of the contact structures, hence presenting the best chance of all 10 emitter wires participating in the flow of current across contacts C-H. Brief electrical checks were performed with an additional probe on adjacent contact structures to ensure that the path of least resistance was indeed the emitter channel between C-H. This can be justified with the general observation via optical microscopy that no direct laser processed wires link either contact to any of the adjacent contacts, instead, there are 3 emitter channels of similar spacing as between C-H. The brief electrical checks ensured that all of these emitter channels had a similar level of current flow at low voltage, and so it is possible to focus entirely on the channel between contact C and H in these measurements.

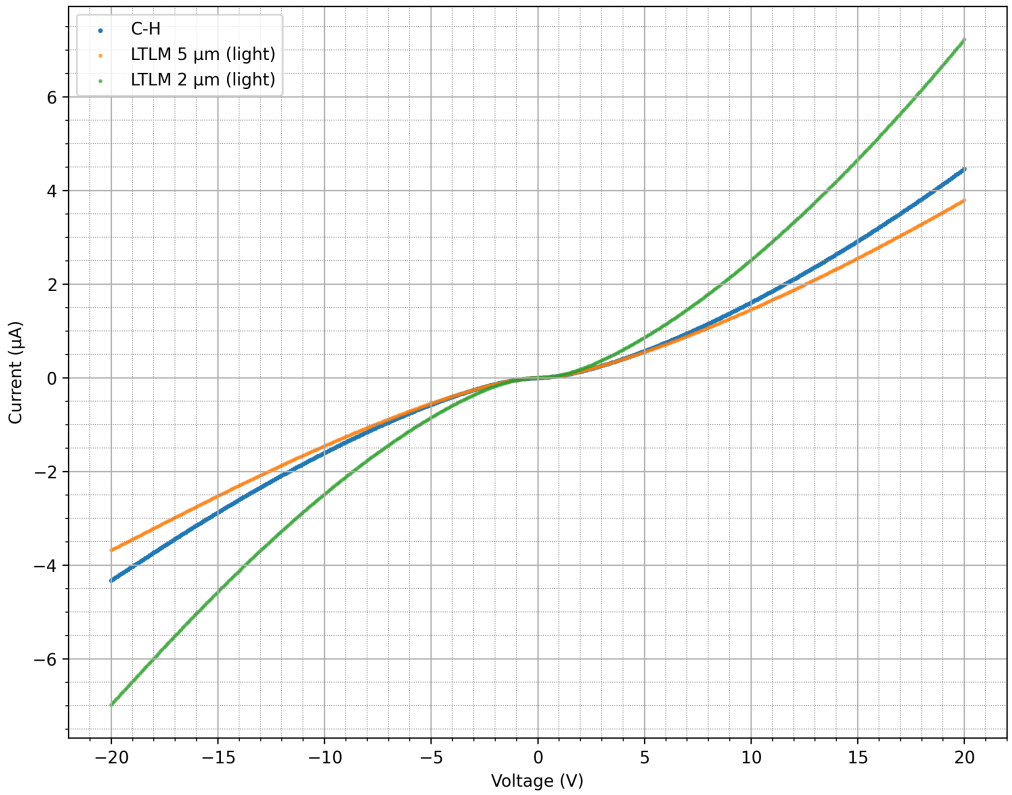

Figure 6.18 The average electrical characteristics between probes a-b representing emitter structure CH, compared to LTLM measurements across 2 and 5 µm channels.

Figure 6.18 shows and compares the 20 V IV characteristics of emitter channel CH to those of the two comparable LTLM channels. CH may be described as a 5 µm LTLM channel, with the addition of 10 small emitter wires of length 2.5 µm, reducing the actual channel length by half. Optical characterisation of the 2 µm LTLM channel revealed that the effective spacing for that structure may be slightly lower, so it is quite natural to see that in this voltage range, the CH channel presents a slightly lower resistance than the 5 µm LTLM channel, but a significantly higher resistance than the 2 µm channel. Note that in the case of emitter testing, all electrical characterisation was performed under direct illumination, hence the LTLM characteristics taken in complete darkness seen in section 5.3 are not used in this comparison.

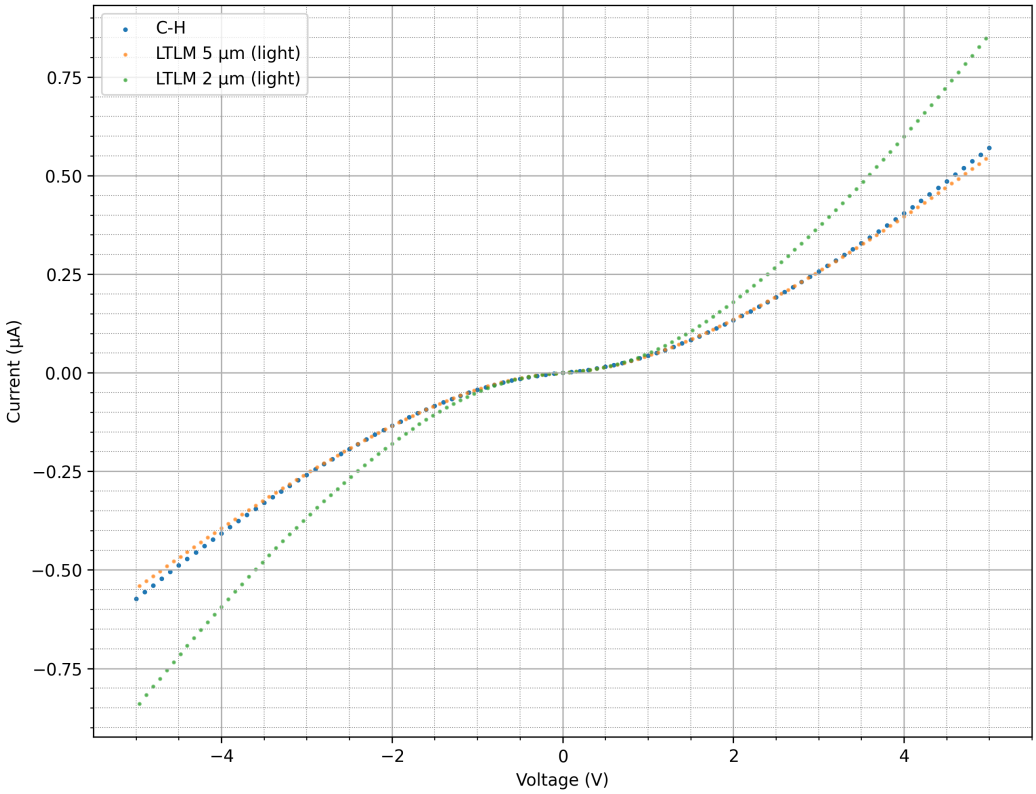

Figure 6.19 The average electrical characteristics between probes a-b representing emitter structure CH, compared to LTLM measurements across 2 and 5 µm channels.

Figure 6.19 provides a closer look at the low voltage region of emitter CH, alongside the comparable LTLM data. Again, the CH data closely resembles that of the LTLM structures in this voltage region, presenting as though this is another LTLM channel with a double Schottky structure making use of thermionic emission across a channel length between 2 and 5 µm. It is particularly similar to the 5 µm data in this comparison, perhaps indicating that the thin emitter wires have a significantly higher resistivity.

6.3.4. High-Voltage Emitter Testing: a-b Ramp-Up

Following confirmation that at low potential differences the CH emitter structure is dominated by thermionic emission, and is very similar to that of the 5 µm LTLM structure, higher voltage testing to reach normal electric fields suitable for Fowler-Nordheim type field effect emission proceeded with the bias region increasing from ±5 to 120 V, mostly in 10 V intervals. All measurements are performed with contact C (the emitter array) held at ground and a potential bias is applied to contact H (anode).

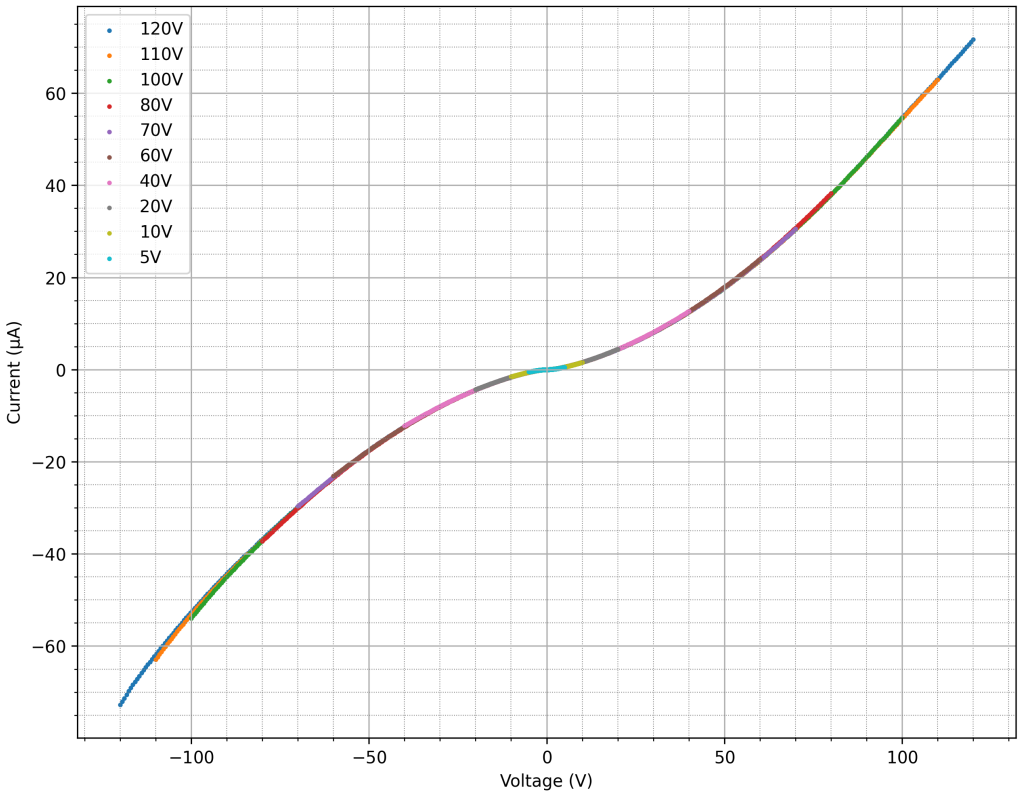

Figure 6.20 The average electrical characteristics between probes a-b representing emitter structure CH, from 5–120 V

Figure 6.20 presents a summary of the ramping up of voltage that was performed with emitter structure CH. The scatter points are overlaid from the highest bias sweep characteristics to the lowest bias sweep, to allow the closely overlapping scatter points to be distinctly visible from one another. At the higher voltages, a slight asymmetry begins to present itself, deviating from the standard double Schottky IV characteristic, however this is difficult to observe from IV characteristics.

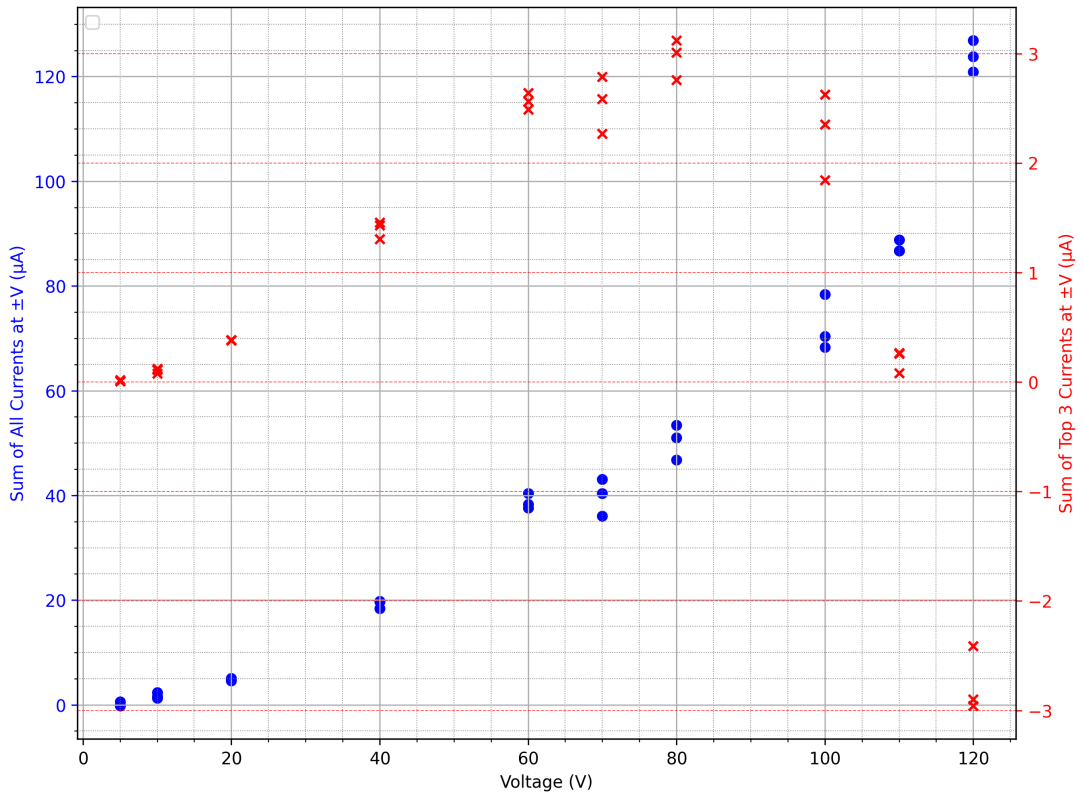

Figure 6.21 The total and peak asymmetry for emitter CH from 5–120 V

In figure 6.21, the asymmetry observed in the IV characteristics is quantified in two ways. On the left axis (blue scatter), the sum of all currents measured is plotted. In an ideal ohmic resistor, this value should be 0, as the magnitude of current drawn in forward bias is no different to that of the current in reverse bias, and the sum of positive and negative currents will be zero. Equally, with symmetric back to back Schottky contacts, it is expected that there is no preference for the direction in current. Differences are due to differing ideality factors or barrier heights between the two Schottky junctions, but in this case it is expected that at high voltage a field effect emission current will be present. Hence, asymmetry due to the total current sum may help identify field effect emission contributions to current flow.

It was noted during the experimental process that the asymmetry was particularly pronounced at the absolute maximum and minimum potential biases. The right axis (red scatter) presents the sum of the 3 highest and 3 lowest measured currents, giving an indication of asymmetrical peak current. The sum of all currents in figure 6.21 tends to increase for higher voltages, indicating an overall asymmetry in the positive bias direction. In contrast, while in agreement to begin with, the sum of the peak 3 currents rises to an asymmetry of 3 μA at 80 V, before dropping to -3 μA at 120 V. This change is visible in figure 6.20, as the lines corresponding to 100, 110 and 120 V noticeably diverge from each

other near their lowest respective negative potential biases. Finally, the asymmetry plot includes three different sets of measurements at each voltage. For the most part, the sum of total current and peak currents are very similar between differing sweeps, indicating a consistent asymmetry.

6.3.5. Emitter Testing: Significant Asymmetry

In addition to the observed asymmetry in the case of single sweeps, dual sweeps in which the bias applied to probe b ranged from negative-positive-negative were performed at 70 V to verify that the asymmetry did not depend upon the direction of voltage bias change (i.e. negative-positive, positive-negative). No significant change was observed, and the observed difference in peak asymmetry between different sweeps at the same voltage matched that of figure 6.21. However, after conducting two similar dual sweeps at 120 V, a significant peak asymmetry of -78 µA emerged during the third trial. Following this, several single sweeps of ±50 V were conducted to verify that lower voltage sweeps were symmetric, as previously observed for this device. Within this bias range, no significant asymmetry was observed.

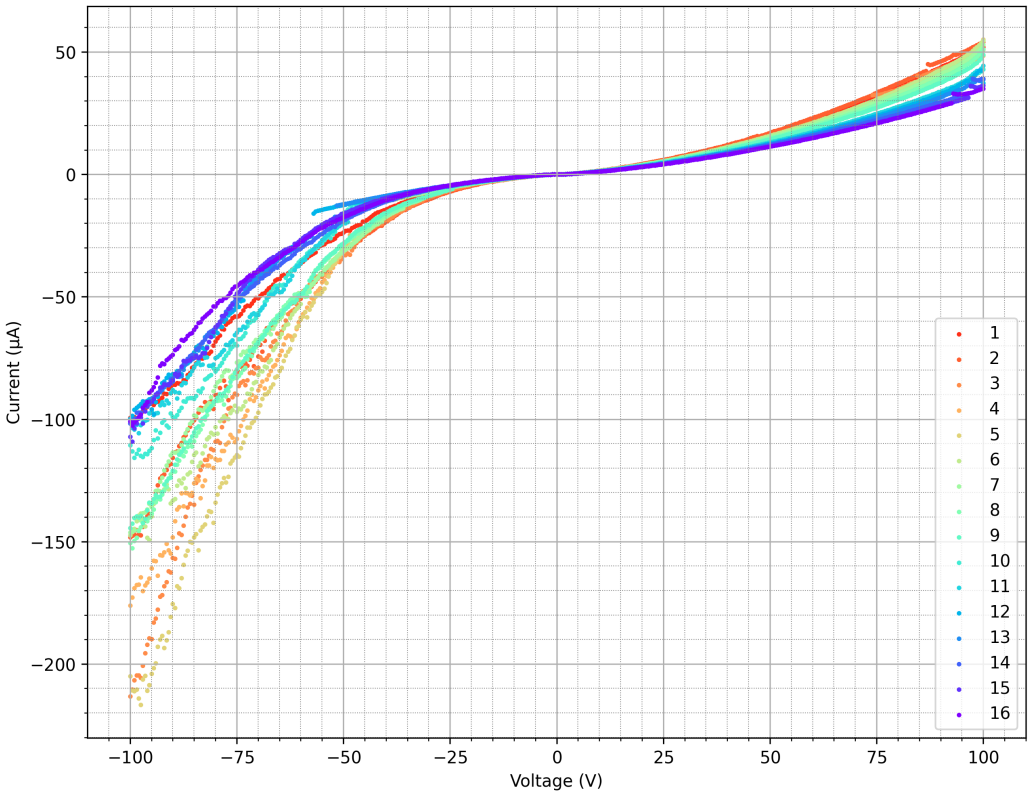

Figure 6.22 The IV characteristics across emitter CH in which significant asymmetry was measured for ±100 V.

Figure 6.22 shows the follow up ±100 V measurements to the asymmetric current observed while running dual-sweep measurements of slightly higher bias. In the positive potential bias region, the Schottky curve is visible. However, in negative bias, a significant, changing asymmetric current was measured. The data are labelled with incrementing numbers, and the legend represents a color map corresponding to the relative dataset indices. At first, the magnitude of current with negative applied voltage increased. After the data indicated by index 5, the current magnitude proceeded to decrease. This trend is also visible in the forward bias region, though the first few sets of data are closely overlapping.

Additionally, after IV sweep 3, characterisation was done with a reverse bias sweep, i.e. the potential bias began at +100 V and swept down to -100 V. This was done to verify that the observed current in the negative bias was not due to the initial starting bias. After IV sweep 5, the probe at position b was re-positioned, taking it off the contact and then placed back. This had no noticeable effect on the IV sweeps. After sweep 9, the probe on location a was similarly re-positioned, with no noticeable change. The final three sets of data were taken with a positive bias sweep, again to verify that the observed characteristics did not change with this change in sweep direction. For clarity, the potential bias was applied to the anode (contact H), and the emitter structure (contact C) was grounded. A strong current at negative bias hence implies that electrons are flowing counter to the intended direction of travel with geometrically enhanced emitter structures.

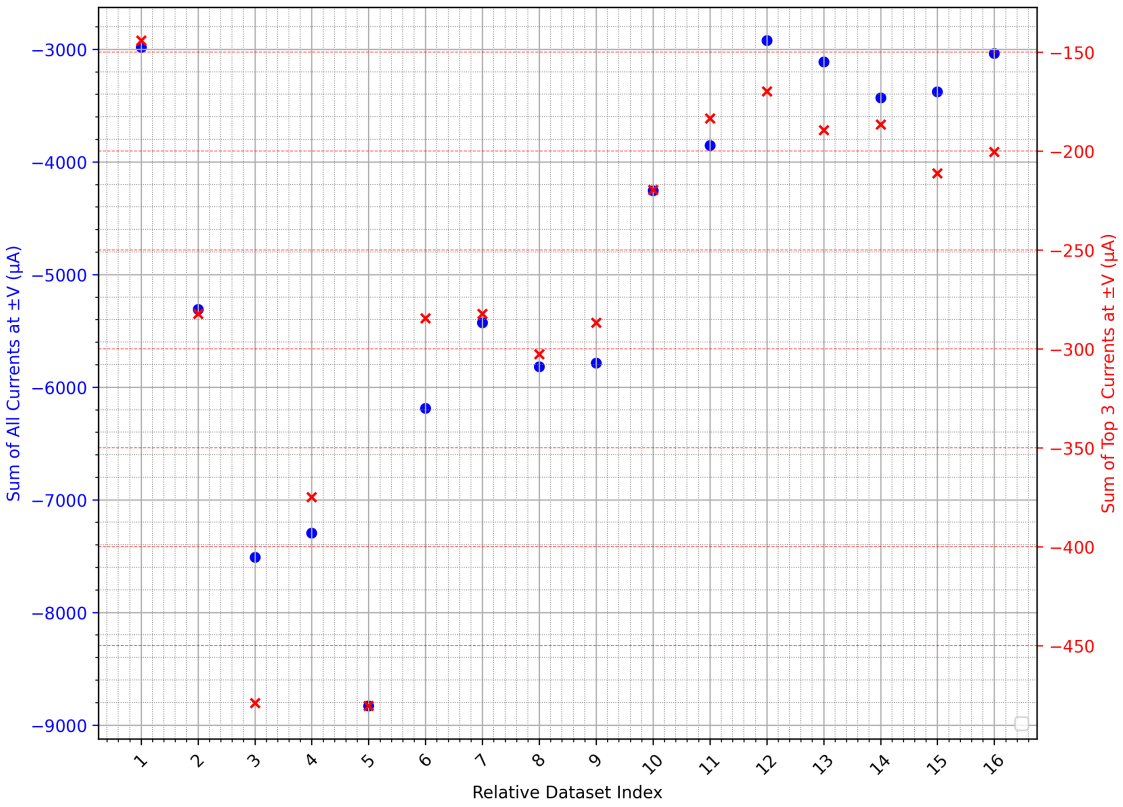

Figure 6.23 The observed asymmetry across emitter CH for ±100 V single sweeps. Blue circles are used for the left y axis, and red crosses are used for the right y axis.

In contrast to figure 6.21, which had relatively small levels of asymmetry across the full range of data that may be accounted for by a small percentage error estimation, figure 6.23 further underscores the magnitude of asymmetrical current that was observed. The sum of total positive/negative currents are consistently and significantly negative, with the sum of 3 peak positive/negative currents following the same trend. Following these measurements and the observation of changing current over multiple IV sweeps, higher voltage testing was examined to further pursue the asymmetric behaviour observed.

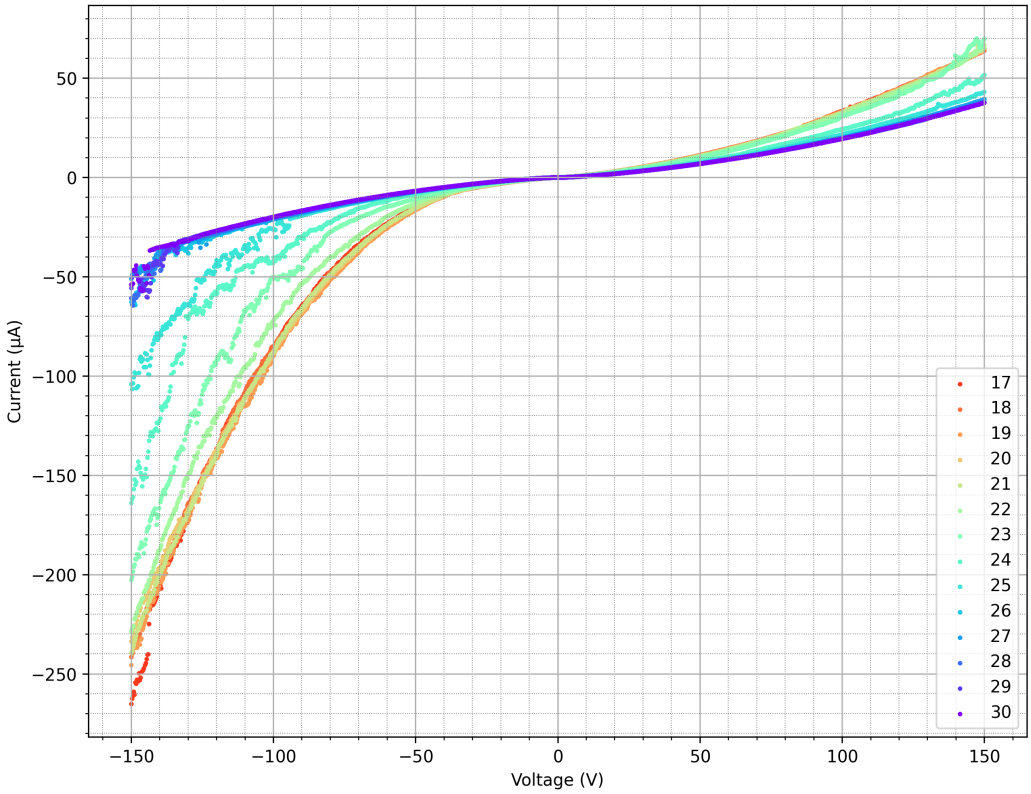

Figure 6.24 The IV characteristics across emitter CH in which significant asymmetry was measured for ±150 V.

Figure 6.24 shows the changing IV characteristics of emitter channel CH with single potential bias sweeps of ±150 V. The 100 V current matches up with relative sweeps 15 and 16 of the previous set of data. Hence, this continues the same decrease in asymmetry as previously observed, but with greater potential bias producing a more significant spread of current in the negative bias region. For this dataset, the number of data points was raised from 401 to 1001, giving a step size of 0.3 V. The IV sweep direction was negative to positive.

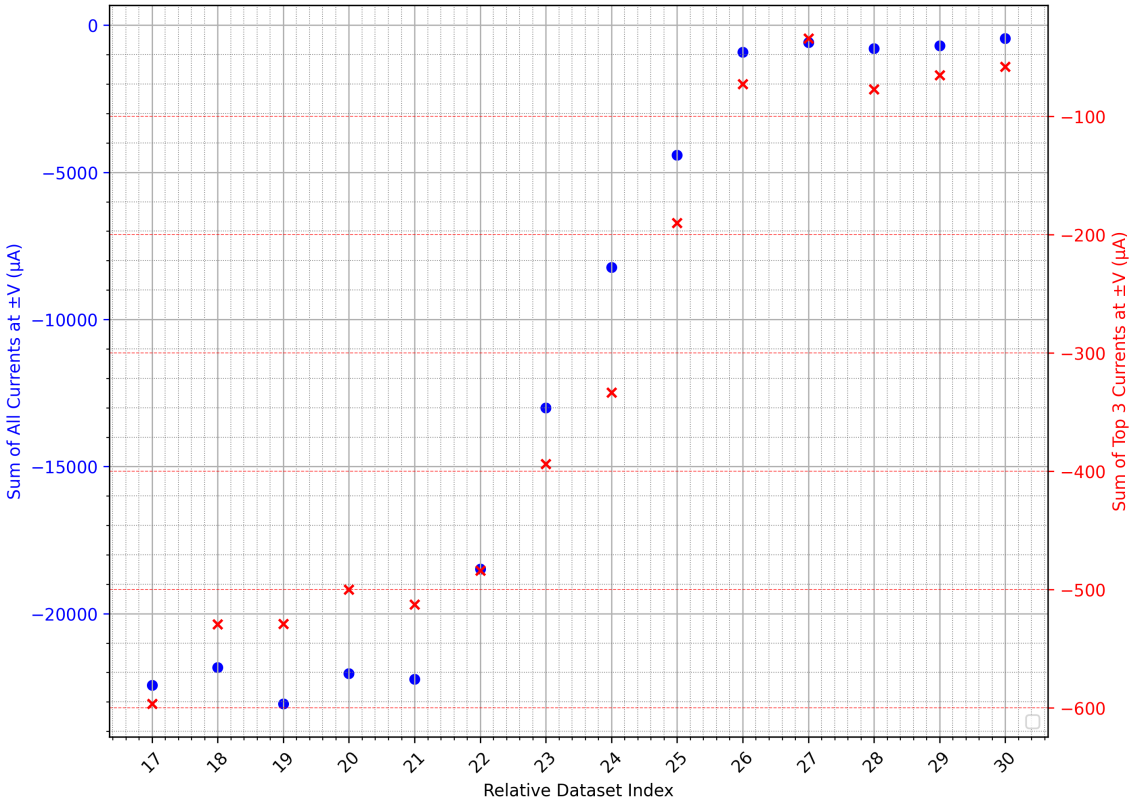

Figure 6.25 The observed asymmetry across emitter CH for ±150 V single sweeps. Blue circles are used for the left y axis, and red crosses are used for the right y axis.

In figure 6.25, the previously used method of quantifying asymmetry was used to evaluate the ±150 V IV data. As might be expected from the previous sweeps in figure 6.22, the first 4 IV sweeps show a consistent, negative asymmetry, in both the sum of all currents (left axis) and the sum of peak 3 currents (right axis). In contrast to figure 6.23, the final 5 datasets plateau much closer to the 0 mark, indicating that the IV sweeps have returned to near-symmetry.

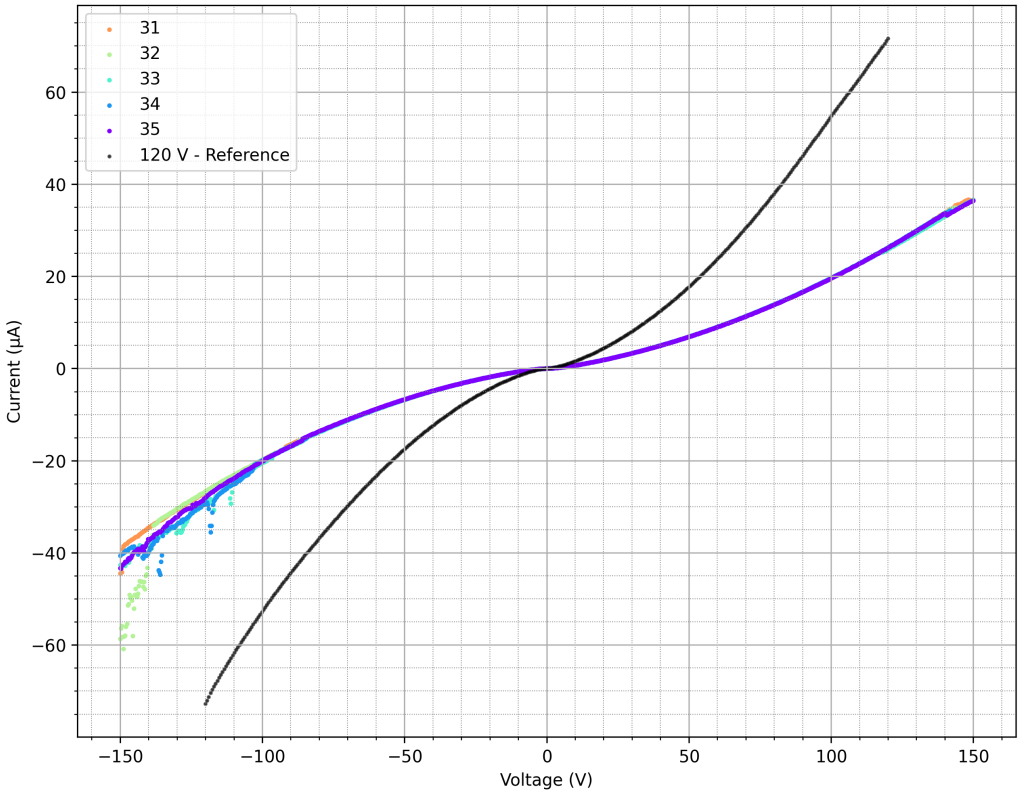

Figure 6.26 The IV characteristics across emitter CH after significant asymmetry was observed, for ±150 V (flipped IV sweep direction).

Figure 6.26 presents the continuation of previous IV sweeps, with another reversal of IV sweep direction. These data are taken with a bias direction of positive to negative, and continues to display the same symmetry as seen in the final few sweeps of figure 6.24. For reference, the first 120 V sweep of this emitter structure is also plotted, to show the disparity between these measurements. It is clear that a change in the electrical properties of this device has occurred. While there is still some noticeable spread in the measured current at peak negative voltages, the data are now generally in agreement for repeated IV sweeps.

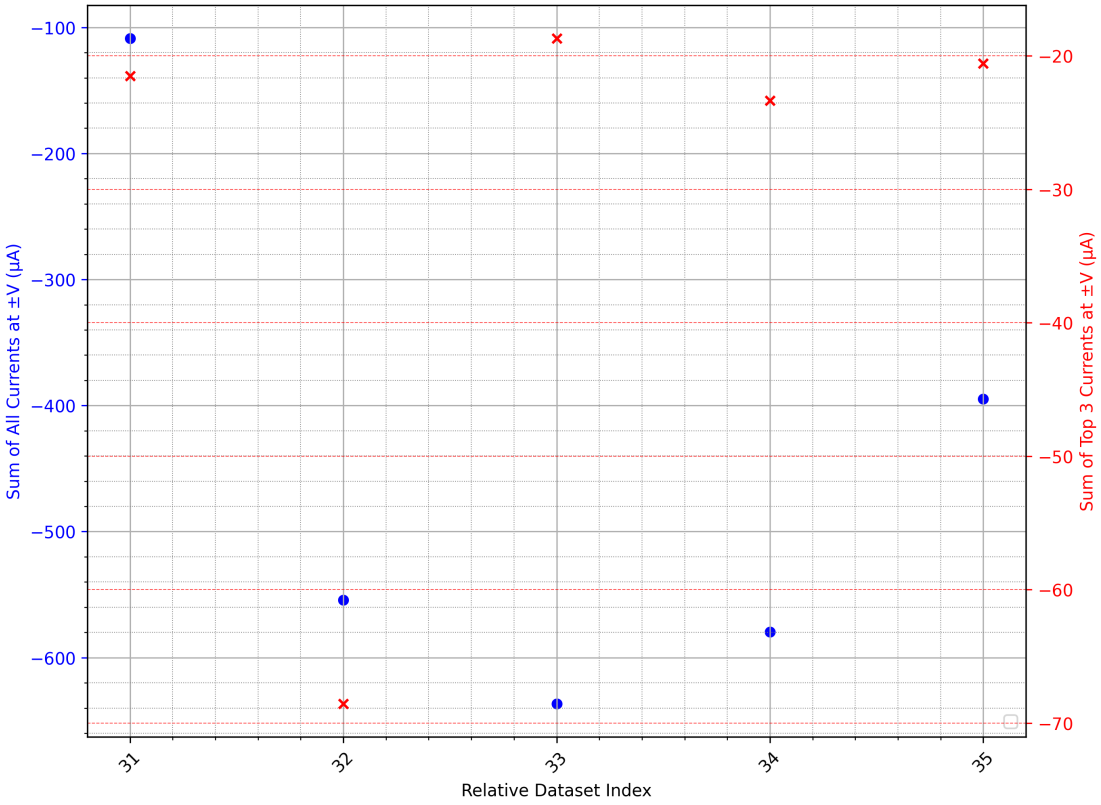

Figure 6.27 The observed asymmetry across emitter CH for ±150 V single sweeps. Blue circles are used for the left y axis, and red crosses are used for the right y axis.

In figure 6.27, these late stage IV sweeps are examined with the same asymmetry plot as previously used. Compared to the sweeps for which significant asymmetry was present, as for figures **??**, the channel now appears to be relatively consistent between positive and negative biases, at a sum much closer to 0 for both the sum of total currents and the sum of peak 3 currents. As this now resembles noise, it is reasonable to conclude that the effect causing significant asymmetry has ceased.

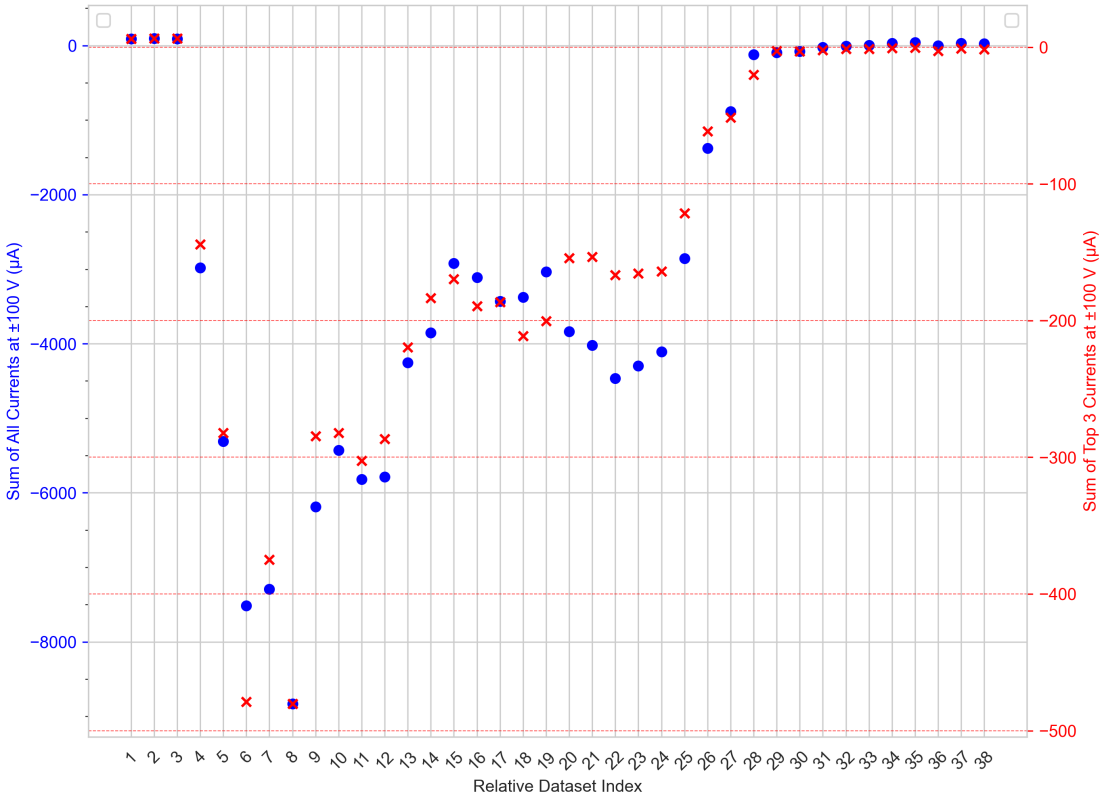

Figure 6.28 The observed asymmetry across emitter CH for all single sweeps at ±100 V. Blue circles are used for the left y axis, and red crosses are used for the right y axis.

Figure 6.28 provides a full review of the asymmetry profile presented by emitter CH during testing. In this figure, data for ±150 V sweeps are limited to ±100 V to provide direct comparison between these sweeps which were run at differing potential biases. The data included spans the full range of observed behaviour, from the symmetric Schottky profile of early sweeps, through the highly chaotic asymmetry, then back to a symmetrical behaviour for the final sweeps. Further testing with this device did not observe any change from the final sweeps shown here.

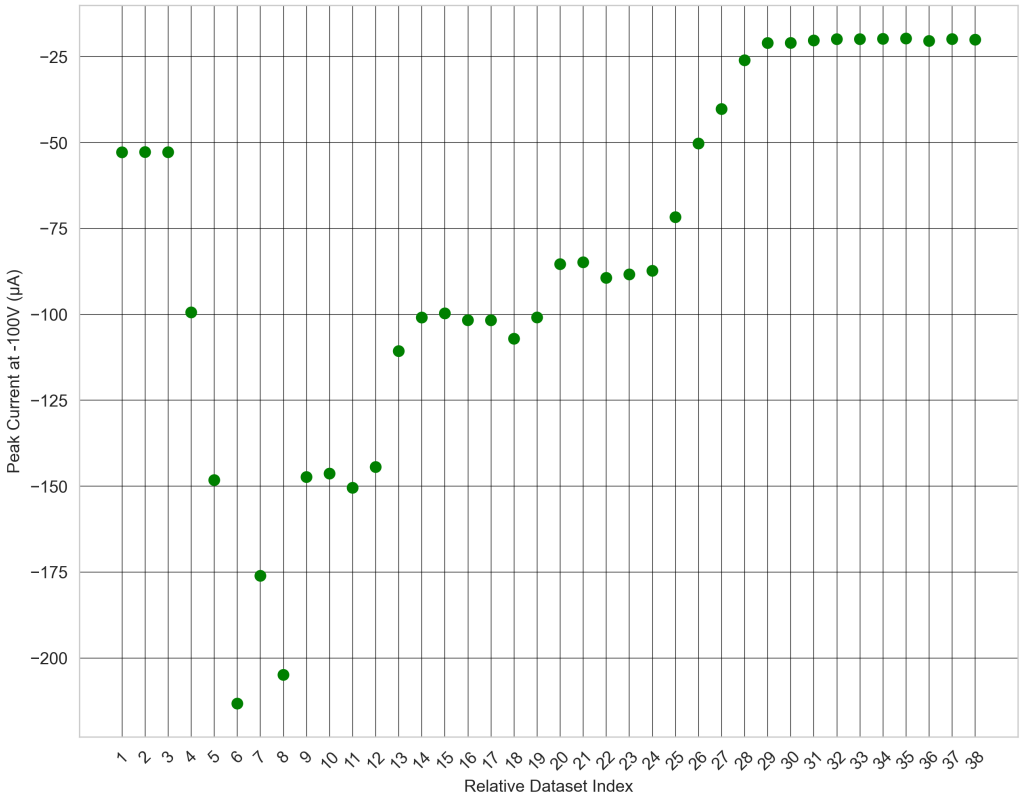

Figure 6.29 The observed peak currents at -100 V, across all single sweeps.

Finally, figure 7.7 plots the peak current measured for −100 V across all sweeps. The trend seen here correlates well with that of the two differing methodologies of quantifying asymmetry, and also provides a quick reference for the peak current values of the IV sweeps shown in Figures 6.22, 6.24, and 6.26.

6.3.5.1. Post-Electrical Characterisation Optical Microscopy

Chapter7/Figs/Raster/ch_n p

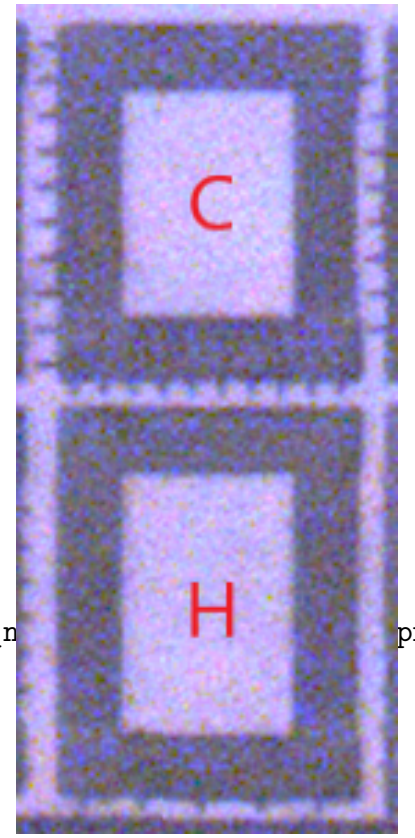

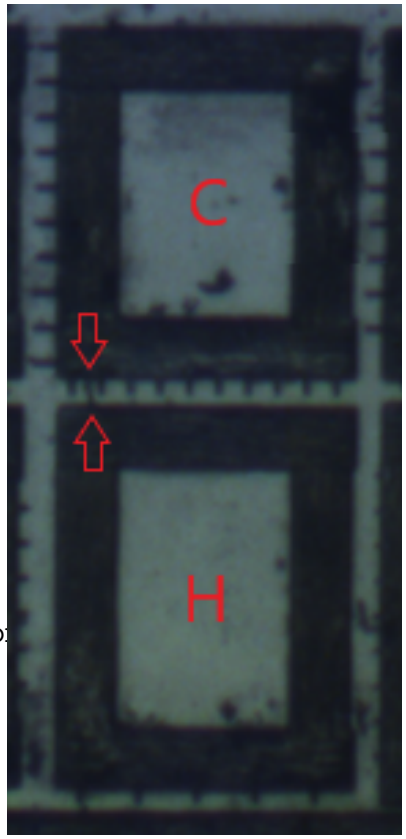

(a) Pre-emitter testing, as seen via 488 nm confocal microscopy.

(b) Pre-emitter testing, as seen via back-lit optical microscopy.

(c) Post-emitter testing, as seen via back-lit optical microscopy.

Figure 6.30 Optical microscopy of emitter structure CH before and after electrical characterisation.

Figure 6.30 provides three different optical microscopy images of emitter contacts C-H. In 6.30a, the high resolution pre-emitter testing microscopy is given. Figure 6.30b is an optical microscope image taken hours before the time of emitter testing. This image is of lower resolution, but with back lighting, it is qualitatively comparable to that of the high resolution imaging in terms of laser written material clarity. Finally, 6.30c provides imaging via the same optical microscopy setup, albeit with better imaging quality due to a longer exposure time and lower ISO setting compared to 6.30b. This reduced the visible noise substantially, but has similar issues with resolution of minimum feature sizes in comparison to the 488 nm confocal microscopy. Regardless, a clear distinguishing feature within the emitter channel is visible, highlighted with a pair of red arrows. Surface contaminants can be seen within the rectangular wire contacts of C and H, on the diamond surface itself, and are visible as small, roundish features. The feature indicated within the channel is similar to the written emitter wires, spanning the full channel width, and is narrow and wire-like. Hence, this may represent a tangible change in the emitter channel itself due to the high voltage testing.

6.4. Numerical Modelling

Following the observation of a significant negative current flow asymmetry in the testing of emitter structure CH, further numerical modelling was performed in an attempt to elucidate the possible physical origin of this transient current at high negative biases. A particular concern was the mechanism of current injection into the phosphorous doped diamond channel and the possibility of observing field effect emission due to the sharp emitters.

6.4.1. Schottky Junctions

The back to back Schottky junction is a challenging device to model accurately. Numerical methods in this area often rely upon various approximations and boundary conditions to allow for simulations which provide convergence, with models ranging from earlier works in which the two Schottky barriers are assumed to have the same heights and ideality factors [22, 12, 21], to more complete models which allow for variance between the two barriers [26, 38, 10, 5, 4, 6]. It is worth noting that single Schottky barriers can be challenging in their own right to model accurately, with significant work in the field of numerical modelling focused on single barriers, and the application of these barriers within devices [8, 41, 32]. This is especially true for wide bandgap semiconductors in which significant Fermi level pinning is observed, such as SiC [1], as well as diamond [37, 11]. For the purposes of examining predicted current flow due to thermionic and field effect emission, and identifying the dominant mechanism, simplified models of the emitter were used to attempt to resolve the origin of the observed asymmetry within the CH emitter structure.

6.4.2. Ideal Schottky Equations Used

The relevant equations which are used to solve for an ideal Schottky contact are given as outlined by Crowell [3] and Sze [36]. The semiconductor is assumed to be nondegenerate, with the contact acting as a source or sink for carriers with surface recombination mechanism:

$$\boldsymbol{J}_n \cdot n = -qv_n(n - n_0) \tag{6.1}$$

$$\boldsymbol{J}_p \cdot n = qv_p(p - p_0) \tag{6.2}$$

where $\boldsymbol{J}_{n,p}$ are the outward normal electron and hole current densities respectively, n is the outward normal electron concentration in the semiconducting region, $v_{n,p}$ are the recombination velocities for electrons and holes and n_0, p_0 are the quasi-equilibrium carrier densities of electrons and holes. These quasi-equilibrium carrier densities are determined

via:

$$n_0 = N_c \exp\left(-\frac{E_c - E_{fm}}{k_B T}\right) = N_c \exp\left(-\frac{\phi_B}{k_B T}\right), \tag{6.3}$$

$$p_0 = N_v \exp\left(-\frac{E_{fm} - E_v}{k_B T}\right) = N_v \exp\left(-\frac{E_g - \phi_B}{k_B T}\right) \tag{6.4}$$

$$\phi_B = \phi_m - \chi \tag{6.5}$$

in which ϕ_m is the metal work function, χ is the semiconductor electron affinity, E_{fm} is the metal Fermi level and crucially ϕ_b is the barrier height for electrons from the metal into the semiconductor. Also given are $E_{c,v}$ which are the conduction and valence band energy levels respectively, E_g is the bandgap energy, $N_{c,v}$ are the effective density of states in the conduction and valence band, T is the absolute temperature and k_B is the Boltzmann constant. The recombination velocities in the case of dominant thermionic emission are determined as [30]:

$$v_n = \frac{A_n^* T^2}{q N_c} \tag{6.6}$$

$$v_p = \frac{A_p^* T^2}{q N_v} \tag{6.7}$$

where $A_{n,p}^*$ are the effective Richardson's constants for electrons and holes respectively. Finally, the boundary condition on voltage is determined as:

$$V = -(\phi_B + \chi) - \frac{\Delta E}{q} + V_0 \tag{6.8}$$

where V_0 is an applied bias and ΔE is the shift in band edges.

6.4.3. Approximate Model

To computationally simulate emitter structure CH within COMSOL Multiphysics, a few assumptions are taken to simplify the model for comparison of thermionic and field effect emission. First and foremost is the usage of an ohmic anode. This is primarily due to the issues with convergence associated with a diamond double Schottky device, but is a practical way to focus on the current emission as limited by the cathode side of the emitter junction. While this approximation may not accurately model the total current that is measured, it will provide a clear description of current due to the geometrically enhanced Schottky contact.

A second assumption that resulted from attempts to model diamond based electronic devices at large is the usage of a totally ionised donor concentration at 4.2×10^{14} cm^{-3}. Incomplete ionisation models were implemented in trial models, but the slight variability in active donor concentration was negligible, especially given the experimental emitter data taken at room temperature being well within the freeze out area for phosphorous

doped diamond. The concentration used hence represents the calculated estimate for active dopant concentration within phosphorous doped diamond at this temperature.

Finally, a Murphy-Good or Good-Müller form of field effect emission is used to approximate the injected current density due to geometric enhancement of the local magnitude in electric field norm [9, 17]:

$$J_{GM} = \frac{aF_{eff}^2}{\phi_m} \exp\left\{-\frac{b\phi_m^{1.5}}{F_{eff}}\right\} \tag{6.9}$$

where $a = 1.54 \times 10^{-6}$ µA eV V^{-2} and $b = 6.83$ eV$^{-3/2}$V/nm are the standard Fowler-Nordheim constants, F_{eff} is the effective local electric field norm, defined as $F_{eff} = \sqrt{E_x \cdot E_x + E_y \cdot E_y + E_z \cdot E_z}$. This may also be referred to as the amplitude of the electric field, and is defined for each element in the finite mesh used in finite element modelling (FEM). This form of field effect emission represents one of the simplest approximations of this class of equations, with more complete derivations providing further precision in an extended Murphy-Good equation [7]. However, for the purposes of estimating field effect emission, this highly simplified form of the equation was implemented. Also note that in the following models a metal work function $\phi_m = 4.5$ eV is utilised, which is another assumption that can significantly effect the Schottky thermionic emission.

6.4.4. Full Array Electrostatics

To begin with, it is necessary to consider the larger scale situation of an emitter array, as the non planar geometry may introduce irregularities on the larger scale. In this model, the electrostatics were calculated, with the electric field norm in particular examined as this is the driving factor in all forms of field effect emission.

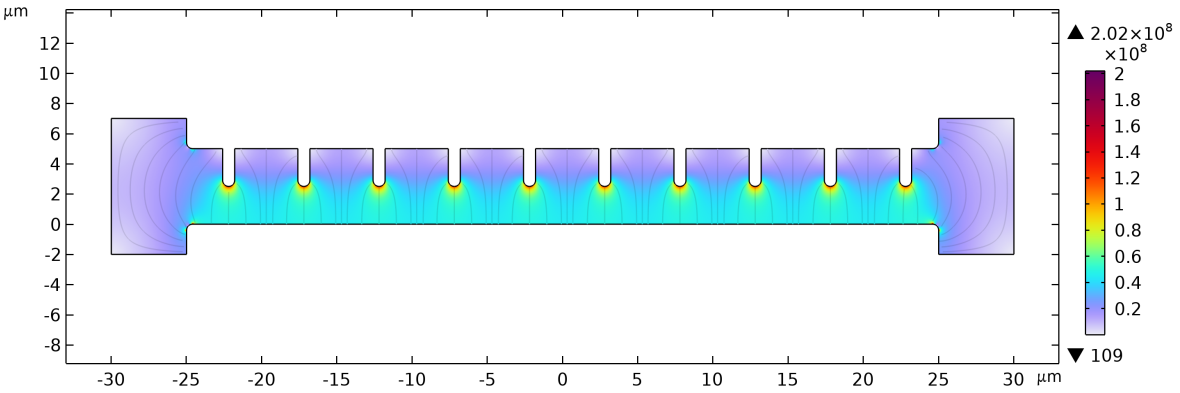

Figure 6.31 The electric field norm of an idealised geometry for emitter array CH.

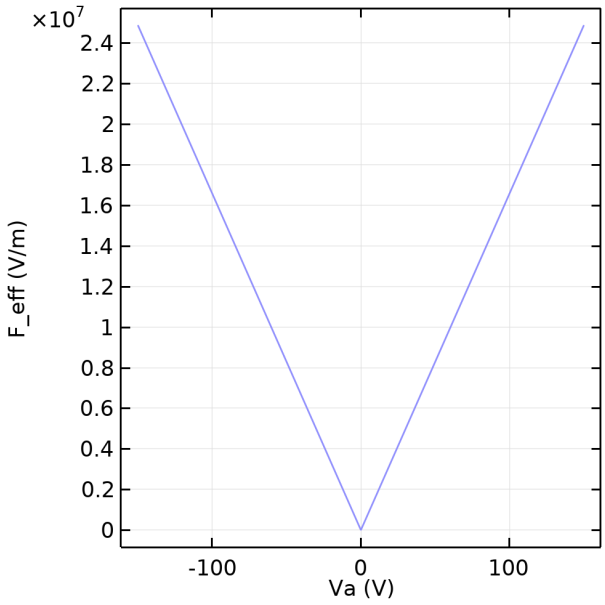

Figure 6.32 The peak electric field norm on the cathode structure for ±150 V.

In figures 7.8 and 6.33, the idealised geometry and resulting electric field norm surface plot is shown for an anode bias (V_a) of +150 V. Note that the cathode is held at 0 V. For an earlier discussion of the emitter tip profile as modelled, please see section 6.1. This electrostatic model was used for the full ±150 V range, with the resulting electric field norm maximum for the cathode plotted in figure 7.9. The slight discrepancy between peak electric field norm in this figure when compared to the full geometry of figure 7.8 can be attributed to meshing. However, the electric field norm of well over 1×10^7 $\mathrm{V\,m^{-1}}$ is substantial, and is consistent across the differing emitters in this ideal geometry setup.

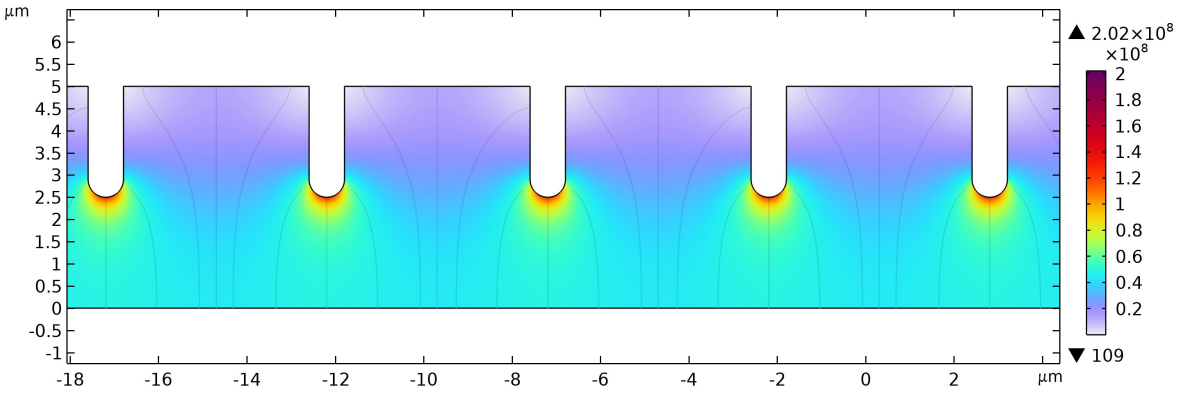

Figure 6.33 The electric field norm of an idealised geometry for emitter array CH.

Figure 6.33 shows a closer view of the electrostatic model shown in figure 7.9. At this scale, the emitters can be seen to have consistent tip electric field norms, with electric field lines only showing very minor deviations from perfect symmetry between adjacent emitters.

6.4.5. Single Emitter Electrostatics

As the emitter array displays a consistent electric field norm across all emitters in the ideal geometry case, computation of a single emitter utilising an ideal Schottky barrier with the addition of a simple Murphy-Good field effect emission contribution was implemented. Additionally, an ionised dopant concentration of 4.2×10^{14} cm^{-3} was applied to the diamond channel region.

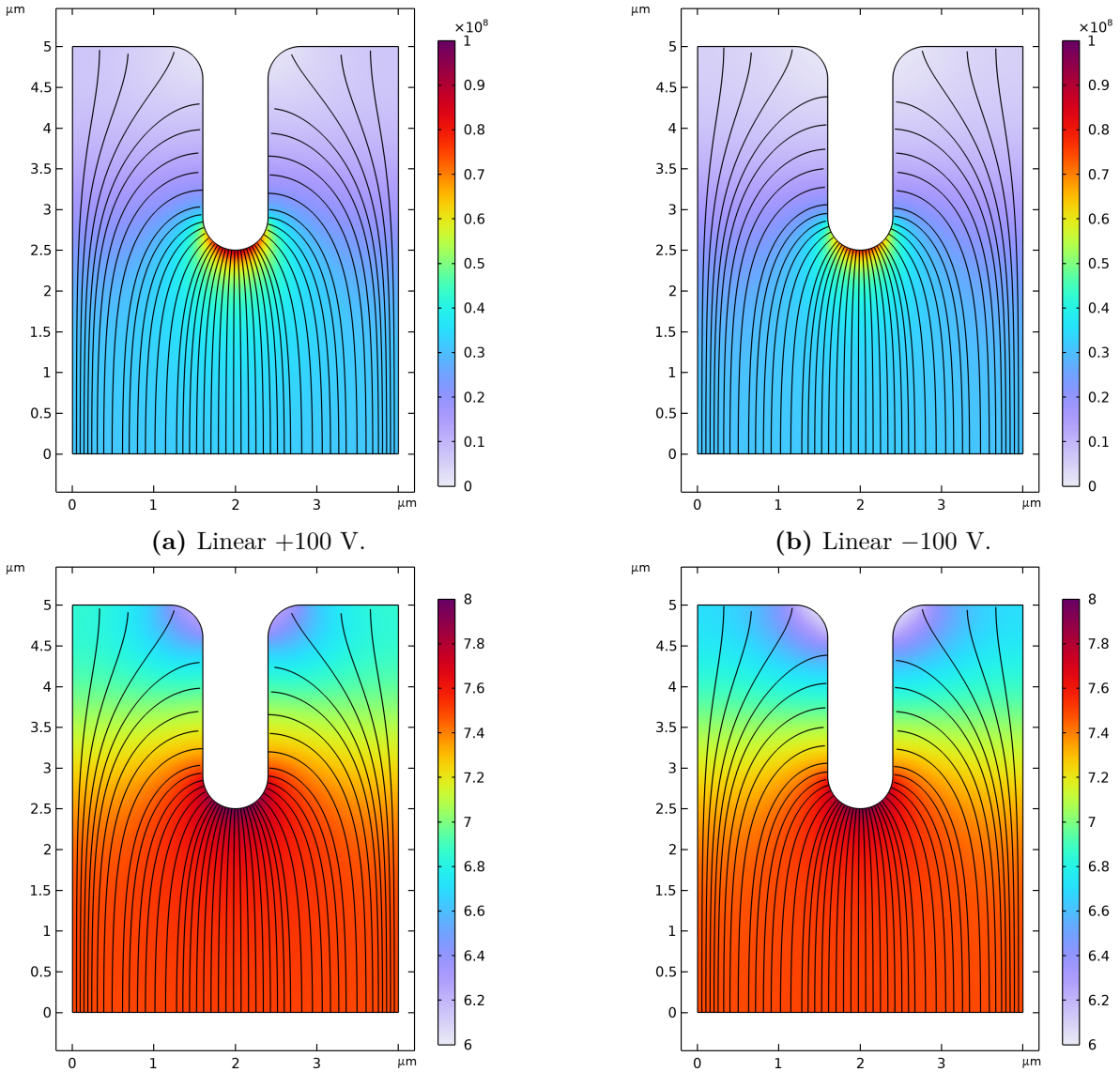

(a) Linear +100 V.

(b) Linear −100 V.

(c) Log +100 V.

(d) Log −100 V.

Figure 6.34 Electric field norm on the idealised emitter cathode.

Figure 6.34 presents both the electric field norm at maximum (left column) and minimum (right column) applied anode biases in a linear (top row) and log (bottom row) scale form for ease of visual comparison. Streamlines representing the magnitude of the electric field are included to provide further visualisation of the localisation of electric field on the emitter tips. Both extremes of potential bias in this model show a reasonably similar distribution and magnitude of electric field norm, with only a minor deviation seen as an

increase of the peak cathode electric field norm in the positive bias case, as opposed to the negatively biased anode case.

6.4.6. Single Emitter Field Emission

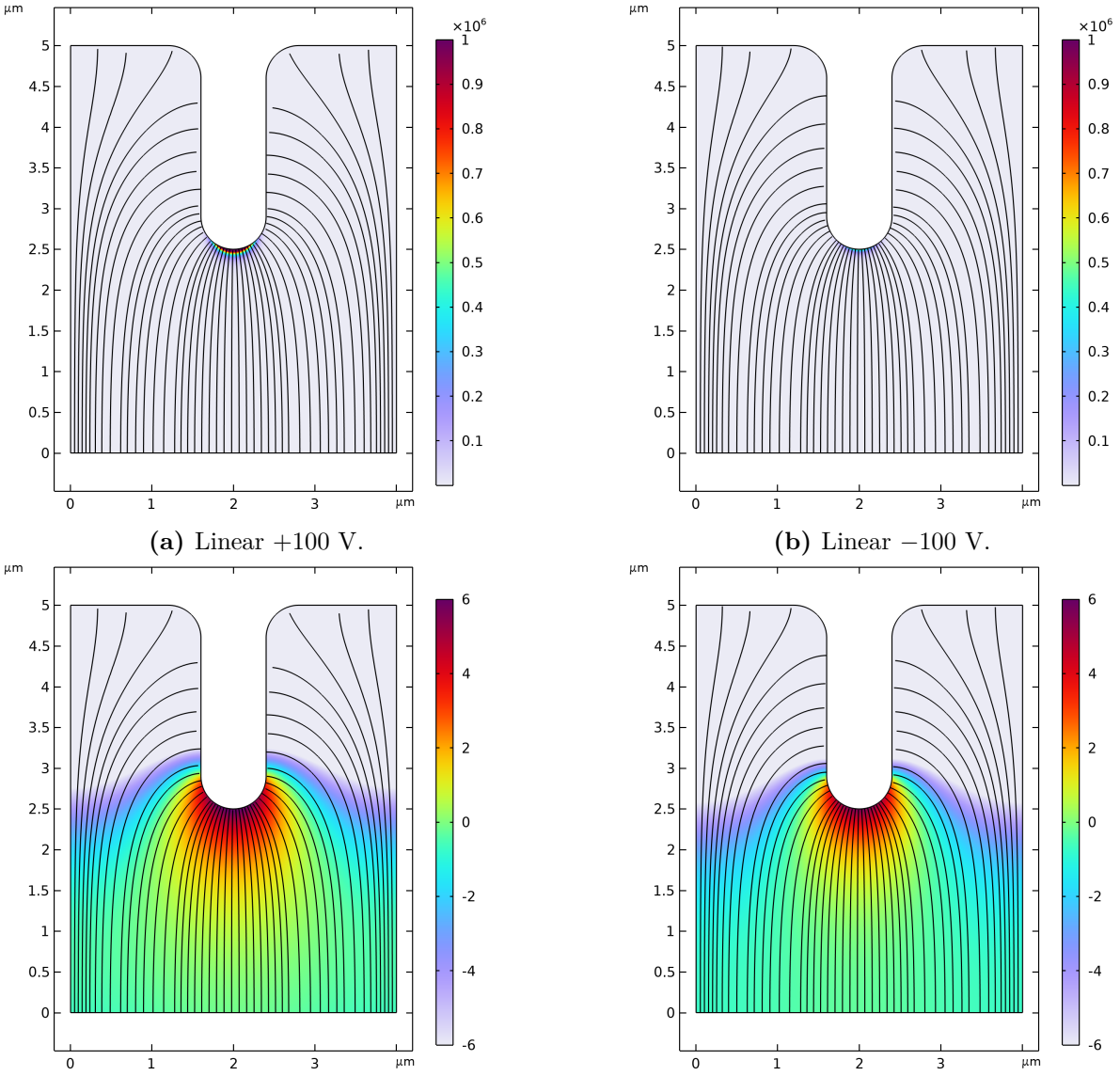

(a) Linear +100 V.

(b) Linear −100 V.

(c) Log +100 V.

(d) Log −100 V.

Figure 6.35 Simple Murphy-Good current density for idealised emitter cathode.

Figure 7.10 shows the results of applying the Murphy-Good field effect emission current density to the single emitter geometry. As for figure 6.34, the top row shows the linear scale plot, while the bottom row shows the log scale plot of current density. Overall, it can be seen that the positive and negative applied anode voltages only have a slight impact upon the observed field effect emission, with a greater emission in the positive region. The emission is concentrated quite strongly upon the very apex of the emitter in both cases too, showing that the exact geometry of these cathode structures may have a large impact upon the profile of field effect emission. While this is an idealised geometry, it is quite

evident that an irregular geometry will have a complex field emission profile, and it is entirely possible that sharper regions at a greater cathode-anode spacing may result in an appreciable field effect emission contribution.

6.4.7. Comparison of Schottky and Field Emission Current

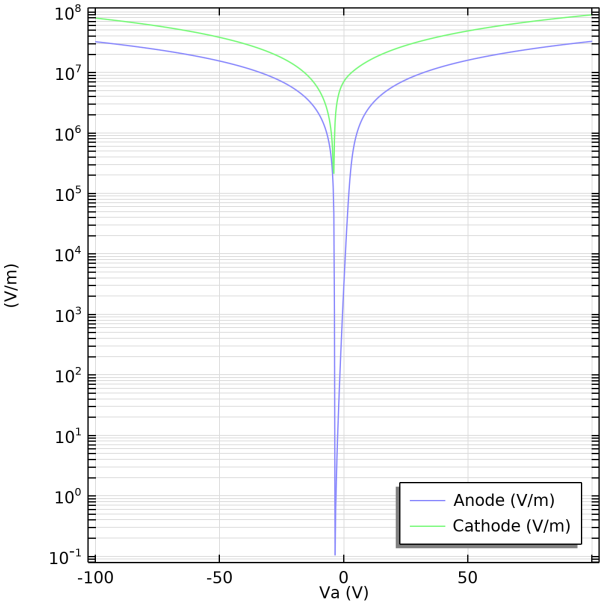

Figure 6.36 The peak electric field norm on both the anode and cathode for ±150 V.

With the ideal single emitter model as described thus far, the resulting thermionic and field effect current densities can be analysed to consider whether this ideal model represents the experimental data in any capacity. In figure 6.36, an additional electrostatic comparison of the cathode and anode is plotted for a bias range of ±100 V. The cathode has a distinctly increased electric field norm at all applied potential biases, albeit around an order of magnitude. This may indicate that at high potential biases, the possibility of field effect emission occurring on the anode itself is possible, especially with geometries that are far from ideal. Another noteworthy feature of this plot is the off-centre minima for both electrodes, which is due to charge accumulation on the cathode and anode. This is not reflected in simpler electrostatic modelling used for the array structure, and presents an ionised dopant dependency upon the electric field norm. While this model does not implement a model of band bending, it is an interesting result that surface accumulation is observed to affect the field effect emission without specifically including approximations to account for this factor.

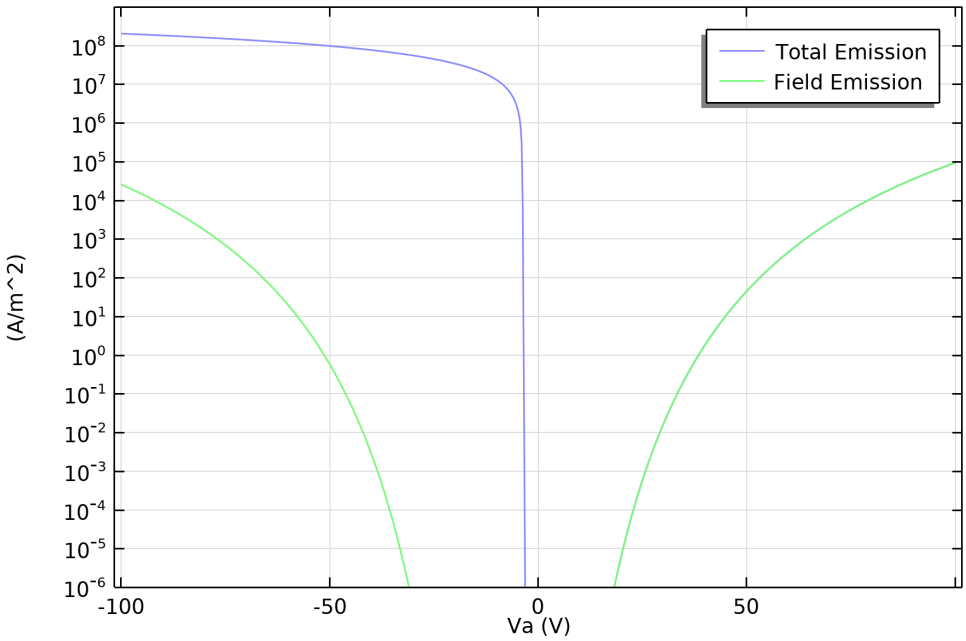

Figure 6.37 The total and field emission current densities from the cathode for anode biases of -100 to +100 V.

In figure 6.37, the total field effect emission current densities are compared over the cathode boundary. As modelled, the ideal Schottky barrier appears to present a much stronger source of current density across the negative bias region, due to the forward bias producing a strong thermionic emission current, but the field effect emission contribution is growing in significance at the highest magnitude of negatively applied potential bias. Note that in the positive region of the plot, the total current density represents the positively biased field effect emission current density, and the lines overlap exactly. This is due to the Schottky cathode being in reverse bias in this bias region, hence the effective saturation current is entirely made up of the field effect contribution.

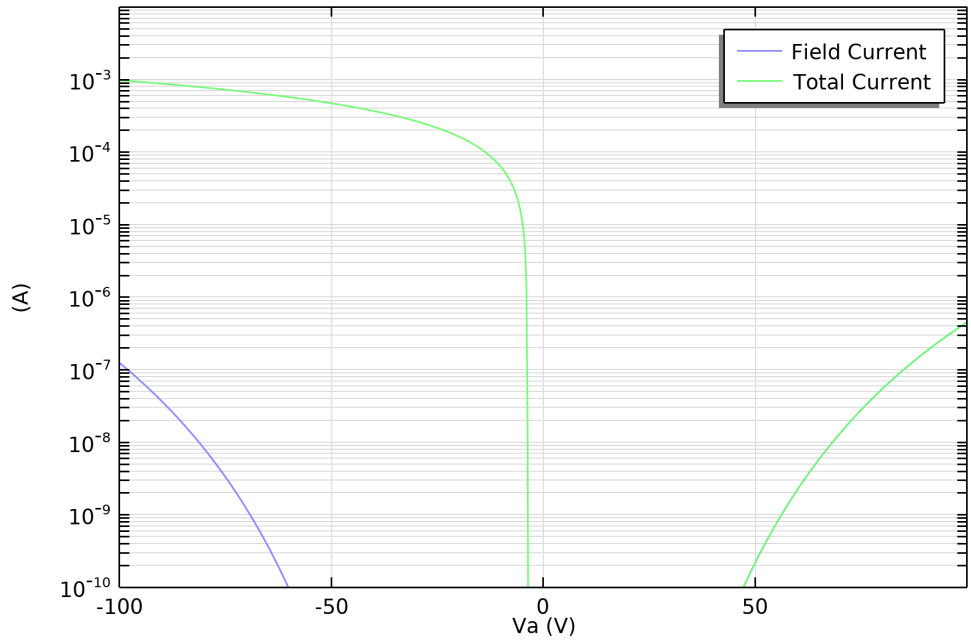

Figure 6.38 The total and field emission integrated current from the cathode for anode biases of -100 to +100 V.

Figure 6.38 presents the integrated effective current over the cathode, with the total current plotted alongside the current contribution directly from field effect emission. As this is directly dependent upon the emission current density, it is no surprise that the integrated current follows a similar trend as for figure 6.37, with a dominant forwardly biased Schottky barrier in the negative bias region and a relatively minor contribution from the field emission element in both bias directions.

References

[1] I. Baum et al. “Effects of Fermi pinning and quantum mechanisms on leakage current of 4H-SiC Schottky diodes”. In: *Journal of Applied Physics* 131.3 (Jan. 2022). ISSN: 1089-7550. DOI: 10.1063/5.0068371. URL: http://dx.doi.org/10.1063/5.0068371.

[2] James E Butler and Ivan Oleynik. “A mechanism for crystal twinning in the growth of diamond by chemical vapour deposition”. In: *Philosophical Transactions of the Royal Society A: Mathematical, Physical and Engineering Sciences* 366.1863 (Nov. 2007), pp. 295–311. ISSN: 1471-2962. DOI: 10.1098/rsta.2007.2152. URL: http://dx.doi.org/10.1098/rsta.2007.2152.

[3] C.R. Crowell and S.M. Sze. “Current transport in metal-semiconductor barriers”. In: *Solid-State Electronics* 9.11 (1966), pp. 1035–1048. ISSN: 0038-1101. DOI: https://doi.org/10.1016/0038-1101(66)90127-4. URL: https://www.sciencedirect.com/science/article/pii/0038110166901274.

[4] Antonio Di Bartolomeo et al. “A WSe2 vertical field emission transistor”. In: *Nanoscale* 11.4 (2019), pp. 1538–1548. ISSN: 2040-3372. DOI: 10.1039/c8nr09068h. URL: http://dx.doi.org/10.1039/C8NR09068H.

[5] Antonio Di Bartolomeo et al. “Asymmetric Schottky Contacts in Bilayer MoS2 Field Effect Transistors”. In: *Advanced Functional Materials* 28.28 (May 2018). ISSN: 1616-3028. DOI: 10.1002/adfm.201800657. URL: http://dx.doi.org/10.1002/adfm.201800657.

[6] Antonio Di Bartolomeo et al. “Bias Tunable Photocurrent in Metal-Insulator-Semiconductor Heterostructures with Photoresponse Enhanced by Carbon Nanotubes”. In: *Nanomaterials* 9.11 (Nov. 2019), p. 1598. ISSN: 2079-4991. DOI: 10.3390/nano9111598. URL: http://dx.doi.org/10.3390/nano9111598.

[7] Richard G. Forbes. “Comments on the continuing widespread and unnecessary use of a defective emission equation in field emission related literature”. In: *Journal of Applied Physics* 126.21 (Dec. 2019). ISSN: 1089-7550. DOI: 10.1063/1.5117289. URL: http://dx.doi.org/10.1063/1.5117289.

[8] M. Furno, F. Bonani, and G. Ghione. “Transfer matrix method modelling of inhomogeneous Schottky barrier diodes on silicon carbide”. In: *Solid-State Electronics* 51.3 (Mar. 2007), pp. 466–474. ISSN: 0038-1101. DOI: 10.1016/j.sse.2007.01.028. URL: http://dx.doi.org/10.1016/j.sse.2007.01.028.

[9] R H. Good and Erwin W. Müller. “Field Emission”. In: *Electron-Emission Gas Discharges I / Elektronen-Emission Gasentladungen I.* Springer Berlin Heidelberg, 1956, pp. 176–231. ISBN: 9783642458446. DOI: 10.1007/978-3-642-45844-6_2. URL: http://dx.doi.org/10.1007/978-3-642-45844-6_2.

[10] Alessandro Grillo and Antonio Di Bartolomeo. “A Current–Voltage Model for Double Schottky Barrier Devices”. In: *Advanced Electronic Materials* 7.2 (Dec. 2020). ISSN: 2199-160X. DOI: 10.1002/aelm.202000979. URL: http://dx.doi.org/10.1002/aelm.202000979.

[11] Zhuoran Han and Can Bayram. “Diamond p-Type Lateral Schottky Barrier Diodes With High Breakdown Voltage (4612 V at 0.01 mA/Mm)”. In: *IEEE Electron Device Letters* 44.10 (Oct. 2023), pp. 1692–1695. ISSN: 1558-0563. DOI: 10.1109/led.2023.3310910. URL: http://dx.doi.org/10.1109/LED.2023.3310910.

[12] Francisco Hernández-Ramírez et al. “Fabrication and electrical characterization of circuits based on individual tin oxide nanowires”. In: *Nanotechnology* 17.22 (Oct. 2006), pp. 5577–5583. ISSN: 1361-6528. DOI: 10.1088/0957-4484/17/22/009. URL: http://dx.doi.org/10.1088/0957-4484/17/22/009.

[13] S. Koizumi et al. “Growth and characterization of phosphorous doped {111} homoepitaxial diamond thin films”. In: *Applied Physics Letters* 71.8 (Aug. 1997), pp. 1065–1067. DOI: 10.1063/1.119729. URL: https://doi.org/10.1063/1.119729.

[14] Satoshi Koizumi, Tokuyuki Teraji, and Hisao Kanda. "Phosphorus-doped chemical vapor deposition of diamond". In: *Diamond and Related Materials* 9.3 (2000), pp. 935–940. ISSN: 0925-9635. DOI: https://doi.org/10.1016/S0925-9635(00)00217-X. URL: https://www.sciencedirect.com/science/article/pii/S092596350000217X.

[15] T.V. Kononenko et al. "Femtosecond laser microstructuring in the bulk of diamond". In: *Diamond and Related Materials* 18.2–3 (Feb. 2009), pp. 196–199. ISSN: 0925-9635. DOI: 10.1016/j.diamond.2008.07.014. URL: http://dx.doi.org/10.1016/j.diamond.2008.07.014.

[16] V V Kononenko et al. "Photoinduced graphitization of diamond". In: *Laser Physics Letters* 12.1 (2015), p. 016101. DOI: 10.1088/1612-2011/12/1/016101. URL: https://doi.org/10.1088/1612-2011/12/1/016101.

[17] A. Kyritsakis and J. P. Xanthakis. "Derivation of a generalized Fowler–Nordheim equation for nanoscopic field-emitters". In: *Proceedings of the Royal Society A: Mathematical, Physical and Engineering Sciences* 471.2174 (Feb. 2015), p. 20140811. ISSN: 1471-2946. DOI: 10.1098/rspa.2014.0811. URL: http://dx.doi.org/10.1098/rspa.2014.0811.

[18] Zhe Li et al. "Bright blue photoluminescence from the amorphous carbon via surface plasmon enhancement". In: *Optics Express* 19.19 (Aug. 2011), p. 17935. ISSN: 1094-4087. DOI: 10.1364/oe.19.017935. URL: http://dx.doi.org/10.1364/OE.19.017935.

[19] Wilhelm Melitz et al. "Kelvin probe force microscopy and its application". In: *Surface Science Reports* 66.1 (Jan. 2011), pp. 1–27. ISSN: 0167-5729. DOI: 10.1016/j.surfrep.2010.10.001. URL: http://dx.doi.org/10.1016/j.surfrep.2010.10.001.

[20] Dmitry Mikulik et al. "Conductive-probe atomic force microscopy as a characterization tool for nanowire-based solar cells". In: *Nano Energy* 41 (Nov. 2017), pp. 566–572. ISSN: 2211-2855. DOI: 10.1016/j.nanoen.2017.10.016. URL: http://dx.doi.org/10.1016/j.nanoen.2017.10.016.

[21] Takayuki Nagano et al. "Output Properties of C60 Field-Effect Transistors with Au Electrodes Modified by 1-Alkanethiols". In: *The Journal of Physical Chemistry C* 111.19 (Apr. 2007), pp. 7211–7217. ISSN: 1932-7455. DOI: 10.1021/jp0708751. URL: http://dx.doi.org/10.1021/jp0708751.

[22] C. Y. Nam, D. Tham, and J. E. Fischer. "Disorder Effects in Focused-Ion-Beam-Deposited Pt Contacts on GaN Nanowires". In: *Nano Letters* 5.10 (Sept. 2005), pp. 2029–2033. ISSN: 1530-6992. DOI: 10.1021/nl0515697. URL: http://dx.doi.org/10.1021/nl0515697.

[23] Péter Németh et al. "Complex nanostructures in diamond". In: *Nature Materials* 19.11 (Aug. 2020), pp. 1126–1131. ISSN: 1476-4660. DOI: 10.1038/s41563-020-0759-8. URL: http://dx.doi.org/10.1038/s41563-020-0759-8.

[24] Péter Németh et al. “Diamond-Graphene Composite Nanostructures”. In: *Nano Letters* 20.5 (Apr. 2020), pp. 3611–3619. ISSN: 1530-6992. DOI: 10.1021/acs.nanolett.0c00556. URL: http://dx.doi.org/10.1021/acs.nanolett.0c00556.

[25] Péter Németh et al. “Diaphite-structured nanodiamonds with six- and twelve-fold symmetries”. In: *Diamond and Related Materials* 119 (Nov. 2021), p. 108573. ISSN: 0925-9635. DOI: 10.1016/j.diamond.2021.108573. URL: http://dx.doi.org/10.1016/j.diamond.2021.108573.

[26] Ryo Nouchi. “Extraction of the Schottky parameters in metal-semiconductor-metal diodes from a single current-voltage measurement”. In: *Journal of Applied Physics* 116.18 (Nov. 2014). ISSN: 1089-7550. DOI: 10.1063/1.4901467. URL: http://dx.doi.org/10.1063/1.4901467.

[27] M. A. Prelas, G. Popovici, and L. K. Bigelow. *Handbook of Industrial Diamonds and Diamond Films*. New York: Marcel Dekker, 1998. ISBN: 0-8247-9994-1.

[28] Patrick S. Salter et al. “Laser Engineering Nanocarbon Phases within Diamond for Science and Electronics”. In: *ACS Nano* 18.4 (Jan. 2024), pp. 2861–2871. ISSN: 1936-086X. DOI: 10.1021/acsnano.3c07116. URL: http://dx.doi.org/10.1021/acsnano.3c07116.

[29] D. Shechtman, A. Feldman, and J. Hutchison. “High-order twin boundaries in CVD diamond films”. In: *Materials Letters* 17.5 (Sept. 1993), pp. 211–216. ISSN: 0167-577X. DOI: 10.1016/0167-577x(93)90001-e. URL: http://dx.doi.org/10.1016/0167-577X(93)90001-E.

[30] Michael S Shur. *Physics of semiconductor devices*. Upper Saddle River, NJ: Pearson, Jan. 1990.

[31] Abu Bakar Siddique et al. “Amorphous Carbon Dots and their Remarkable Ability to Detect 2, 4, 6-Trinitrophenol”. In: *Scientific Reports* 8.1 (June 2018). ISSN: 2045-2322. DOI: 10.1038/s41598-018-28021-9. URL: http://dx.doi.org/10.1038/s41598-018-28021-9.

[32] Daniel Splith et al. “Numerical Modeling of Schottky Barrier Diode Characteristics”. In: *physica status solidi (a)* 218.12 (May 2021). ISSN: 1862-6319. DOI: 10.1002/pssa.202100121. URL: http://dx.doi.org/10.1002/pssa.202100121.

[33] Takashi Sugino et al. “Characteristics of metal-polycrystalline diamond contact field emitters”. In: *Diamond and Related Materials* 7.2–5 (Feb. 1998), pp. 677–681. ISSN: 0925-9635. DOI: 10.1016/s0925-9635(97)00286-0. URL: http://dx.doi.org/10.1016/S0925-9635(97)00286-0.

[34] Takashi Sugino et al. “Internal Electron Emission in Phosphorus-Doped Polycrystalline Diamond Field Emitters”. In: *Japanese Journal of Applied Physics* 37.4A (Apr. 1998), p. L413. ISSN: 1347-4065. DOI: 10.1143/jjap.37.l413. URL: http://dx.doi.org/10.1143/JJAP.37.L413.

[35] Bangshan Sun, Patrick S. Salter, and Martin J. Booth. "High conductivity microwires in diamond following arbitrary paths". In: *Applied Physics Letters* 105.23 (Dec. 2014). ISSN: 1077-3118. DOI: 10.1063/1.4902998. URL: http://dx.doi.org/10.1063/1.4902998.

[36] S.M. Sze and Kwok K. Ng. *Physics of Semiconductor Devices*. Wiley, Apr. 2006. DOI: 10.1002/0470068329. URL: https://doi.org/10.1002/0470068329.

[37] Juan Wang et al. "Vertical Diamond Trench MOS Barrier Schottky Diodes With High Breakdown Voltage". In: *IEEE Transactions on Electron Devices* 69.11 (Nov. 2022), pp. 6231–6235. ISSN: 1557-9646. DOI: 10.1109/ted.2022.3206178. URL: http://dx.doi.org/10.1109/TED.2022.3206178.

[38] Zuo Wang et al. "Extraction and Analysis of the Characteristic Parameters in Back-to-Back Connected Asymmetric Schottky Diode". In: *physica status solidi (a)* 217.8 (Feb. 2020). ISSN: 1862-6319. DOI: 10.1002/pssa.201901018. URL: http://dx.doi.org/10.1002/pssa.201901018.

[39] Akihiko Watanabe, Masahiro Deguchi, and Makoto Kitabatake. "Microscopic study of field emission from diamond particles". In: *Diamond and Related Materials* 10.3–7 (Mar. 2001), pp. 818–823. ISSN: 0925-9635. DOI: 10.1016/s0925-9635(00)00588-4. URL: http://dx.doi.org/10.1016/S0925-9635(00)00588-4.

[40] Akihiko Watanabe et al. "Field emission from diamond particles studied by scanning field emission microscopy". In: *Ultramicroscopy* 95 (May 2003), pp. 145–151. ISSN: 0304-3991. DOI: 10.1016/s0304-3991(02)00311-x. URL: http://dx.doi.org/10.1016/S0304-3991(02)00311-X.

[41] Ernest Y. Wu and Baozhen Li. "The Schottky emission effect: A critical examination of a century-old model". In: *Journal of Applied Physics* 132.2 (July 2022). ISSN: 1089-7550. DOI: 10.1063/5.0087909. URL: http://dx.doi.org/10.1063/5.0087909.

Chapter 7. Conclusions and Future Work

7.1. Overview

In this thesis, a wide range of experimental techniques, combined with computational simulations, have been employed to investigate the practicality and potential improvements of diamond-based electronic devices. A particular focus has been placed on phosphorous-doped diamond, owing to its significant promise in a variety of applications. While boron-doped (p-type) diamond is relatively well-established in 2024, the continuous advancements in diamond growth techniques suggest a future where devices utilising phosphorous doping are not merely theoretical concepts. Direct laser writing of graphitic, or more recently discovered diaphitic allotropes of carbon within diamond substrates, represents a substantial improvement in the fabrication of phosphorous-doped diamond devices. The following sections provide a summary of the work presented in the preceding chapters.

Sample	Batch	Thickness (µm)	Contacts	Characterisation
A	1	0.3	None	SIMS
B	1	0.3	None	SIMS
C	2	0.3	Ti/Pt/Au - 850°C 30 mins	TLM, AFM
D	2	0.3	Ti/Pt/Au - 600°C 300 mins	TLM, AFM
E	3	1.2	None	XPS
F	3	1.2	Ti/Au - 500°C 10 mins	TLM, AFM, HIM
G	3	1.2	Laser Graphitised	TLM, AFM, FL

Table 7.1 A summary of all {111} samples, which had differing thicknesses of heavily phosphorous-doped surface layers grown via MPCVD at Evince Technology. The table indicates the various characterisation techniques used to examine the phosphorous-doped diamond and the resulting electrical contacts in each case. SIMS was performed by an external service (LSA), while XPS and HIM were conducted by Nexus at Newcastle University, with the candidate assisting in parametrisation and analysis. TLM electrical testing, FL, and AFM were performed entirely by the candidate.

7.2. Laser Writing of Phosphorous-Doped Diamond Significantly Reduces Contact Resistance

7.2.1. Summary of Linear Metal Contacts

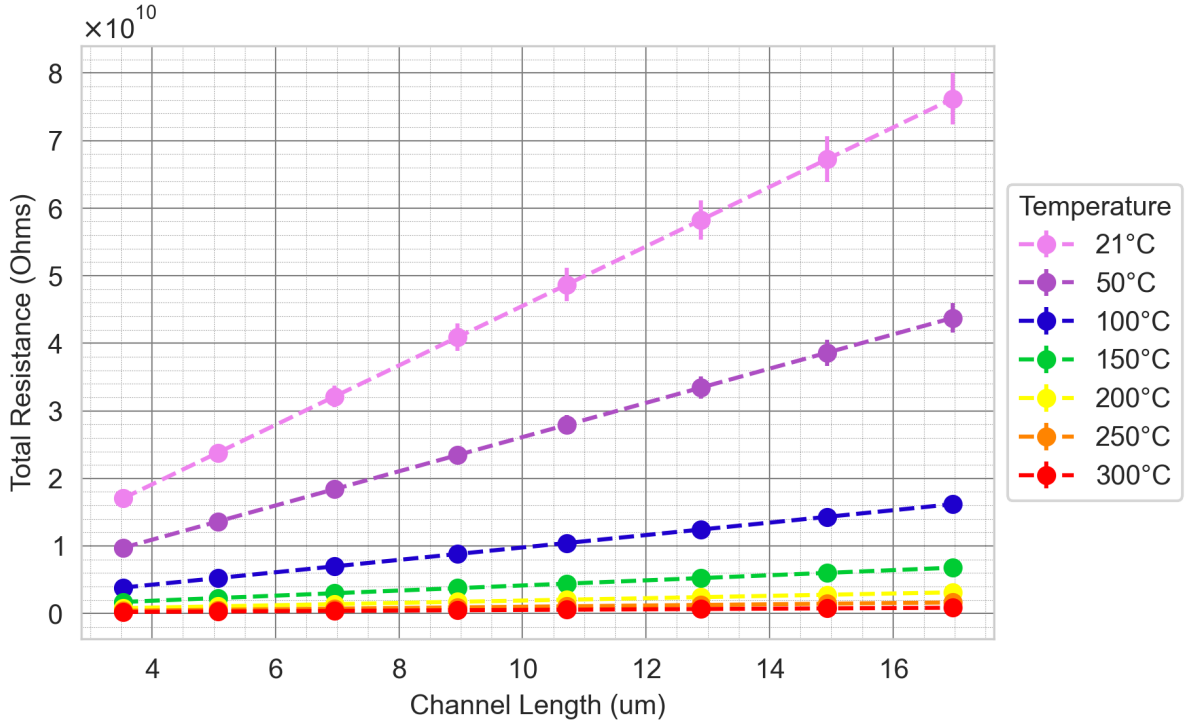

Figure 7.1 Sample C - the channel spacing vs measured total resistance for all temperatures (±10 V).

T°C	R_{sh} ($\Omega/\square$)	ρ_s ($\Omega \cdot cm$)	ρ_c ($\Omega \cdot cm^2$)	R^2
21	$1.10 \times 10^{+12}$	$1.32 \times 10^{+08}$	$4.72 \times 10^{+05}$	9.95×10^{-01}
50	$6.33 \times 10^{+11}$	$7.60 \times 10^{+07}$	$2.51 \times 10^{+05}$	9.93×10^{-01}
100	$2.30 \times 10^{+11}$	$2.76 \times 10^{+07}$	$1.88 \times 10^{+05}$	9.91×10^{-01}
150	$9.44 \times 10^{+10}$	$1.13 \times 10^{+07}$	$1.21 \times 10^{+05}$	9.49×10^{-01}
200	$4.35 \times 10^{+10}$	$5.22 \times 10^{+06}$	$5.81 \times 10^{+04}$	9.64×10^{-01}
250	$2.28 \times 10^{+10}$	$2.74 \times 10^{+06}$	$3.06 \times 10^{+04}$	9.69×10^{-01}
300	$1.16 \times 10^{+10}$	$1.39 \times 10^{+06}$	$2.43 \times 10^{+04}$	9.28×10^{-01}

Table 7.2 The summarised extracted parameters via LTLM on sample C for a 10 V range.

Table 7.2 presents the summary of LTLM analysis for sample C. At room temperature, a specific contact resistivity of 472 $k\Omega cm^2$ is observed, reducing to 24.3 $k\Omega cm^2$ at 300°C. This is paired with a phosphorous-doped diamond resistivity ranging from 132 $M\Omega cm$ to 1.39 $M\Omega cm$.

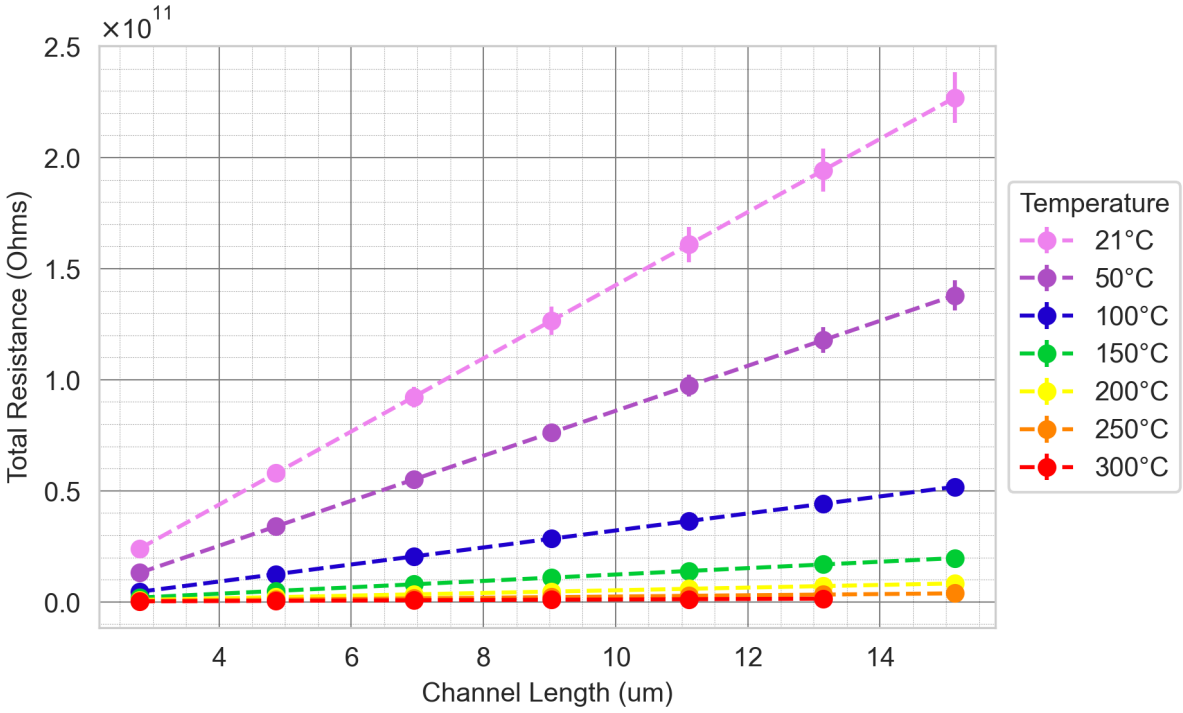

Figure 7.2 Sample D - the channel spacing vs measured total resistance for all temperatures (±10 V).

T°C	R_{sh} ($\Omega/\square$)	ρ_s ($\Omega \cdot cm$)	ρ_c ($\Omega \cdot cm^2$)	R^2
21	$4.12 \times 10^{+12}$	$4.94 \times 10^{+08}$	$6.91 \times 10^{+06}$	9.84×10^{-01}
50	$2.53 \times 10^{+12}$	$3.04 \times 10^{+08}$	$4.77 \times 10^{+06}$	9.89×10^{-01}
100	$9.58 \times 10^{+11}$	$1.15 \times 10^{+08}$	$1.93 \times 10^{+06}$	9.93×10^{-01}
150	$3.60 \times 10^{+11}$	$4.32 \times 10^{+07}$	$6.55 \times 10^{+05}$	9.92×10^{-01}
200	$1.50 \times 10^{+11}$	$1.81 \times 10^{+07}$	$2.53 \times 10^{+05}$	9.92×10^{-01}
250	$6.90 \times 10^{+10}$	$8.28 \times 10^{+06}$	$1.10 \times 10^{+05}$	9.93×10^{-01}
300	$2.94 \times 10^{+10}$	$3.53 \times 10^{+06}$	$3.42 \times 10^{+04}$	9.84×10^{-01}

Table 7.3 The summarised extracted parameters via LTLM on sample D for a 10 V range.

Table 7.3 presents the summary of LTLM analysis for sample D. At room temperature, a specific contact resistivity of 6910 $k\Omega\,cm^2$ is observed, reducing to 34.0 $k\Omega\,cm^2$ at 300°C. This is paired with a phosphorous-doped diamond resistivity ranging from 132 $M\Omega\,cm$ to 1.39 $M\Omega\,cm$.

7.2.2. Summary of Circular Metal Contacts

The literature best-case value for the specific contact resistivity with titanium contacts is 10^{-3} $\Omega\,cm^2$ [7]. With similar work exhibiting higher values[4], [9]. For the LTLM samples in this thesis, specific contact resistivity was measured to be 472 $k\Omega\,cm^2$ and 494 $k\Omega\,cm^2$, with a resistivity of the phosphorous-doped film of 132 $M\Omega\,cm$ and 464 $M\Omega\,cm$ for samples C and D, respectively, at 10 V. For sample F and the CTLM results, at a constant current condition of -100 nA, a specific contact resistivity of around 2.1 $k\Omega\,cm^2$

and resistivity of around 490 kΩcm was measured. These observations highlight the need for alternative approaches to form superior ohmic contacts on these samples, ensuring competitiveness between diamond-based power devices and current best-case values on standard materials. For example, SiC is able to achieve extremely low resistance ohmic contacts below 1×10^{-7} $\Omega\,\mathrm{cm}^2$ [8].

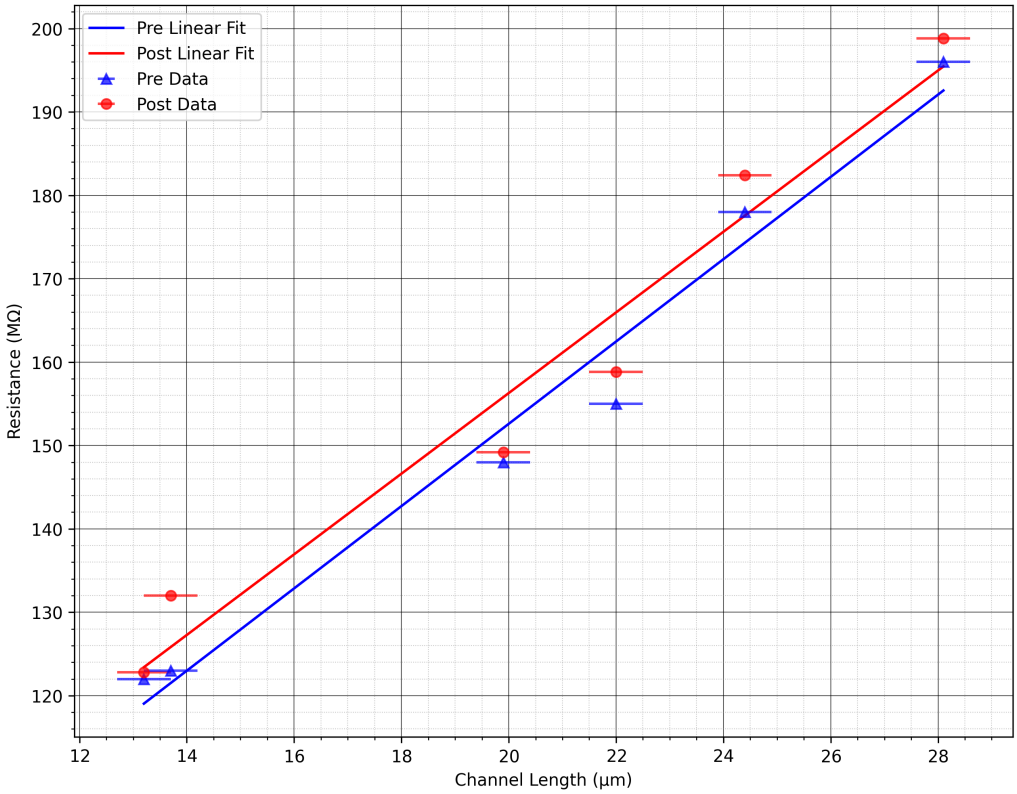

Figure 7.3 Comparison of both pre/post annealing d-R data for $I_0 = -1 \times 10^{-6}$ A, across the selected channels.

Figure 7.3 shows the CTLM plot of constant current condition -1 µA. The negative current is taken to allow for a constant current magnitude of 1 µA to be taken for all channels. As can be determined via the IV plots of section 3.5.4.1, this represents the measurements taken in the voltage region of approximately 150–200 V. At these high voltages, it is apparent that the data represent a strongly biased double Schottky structure, with only a slight asymmetry that may be attributable to the differing areas of Schottky contacts. The data for pre- and post-annealing are both plotted in figure 7.3, as indicated by the legend. A notable trend is the slight increase in total measured resistance for the post-anneal data, other than for the lowest channel lengths. It is unclear why the annealing process has not resulted in a reduction in contact resistance, reducing the total resistance of all channel lengths. This will be explored further in section 3.5.4.4, as the trivial expectation of TiC formation through annealing leading to a lower specific contact

resistivity is well established in boron-doped diamond devices. The R^2 value of the pre- and post-anneal linear fits in figure 7.3 are 0.975 and 0.960, respectively. The calculated values for the specific contact resistivity ρ_c are 462 $\Omega\,cm^2$ and 577 $\Omega\,cm^2$ for pre- and post-annealing. The corresponding sheet resistivities are 186 $k\Omega\,cm$ and 182 $k\Omega\,cm$, given sheet resistivities $\rho_s = R_{sh}t$, where t is the thickness of the phosphorous-doped surface layer, estimated at 1.2 µm. The close agreement of ρ_s between annealing conditions, compared to the notable increase in ρ_c, is intriguing, implying that the methodology is correctly identifying the change in contacts and unchanging phosphorous-doped channel. As noted in literature [3], the oxygen terminated surface may be responsible for inhibition of TiC formation, hence the lack of specific contact resistivity reduction between pre and post anneling conditions.

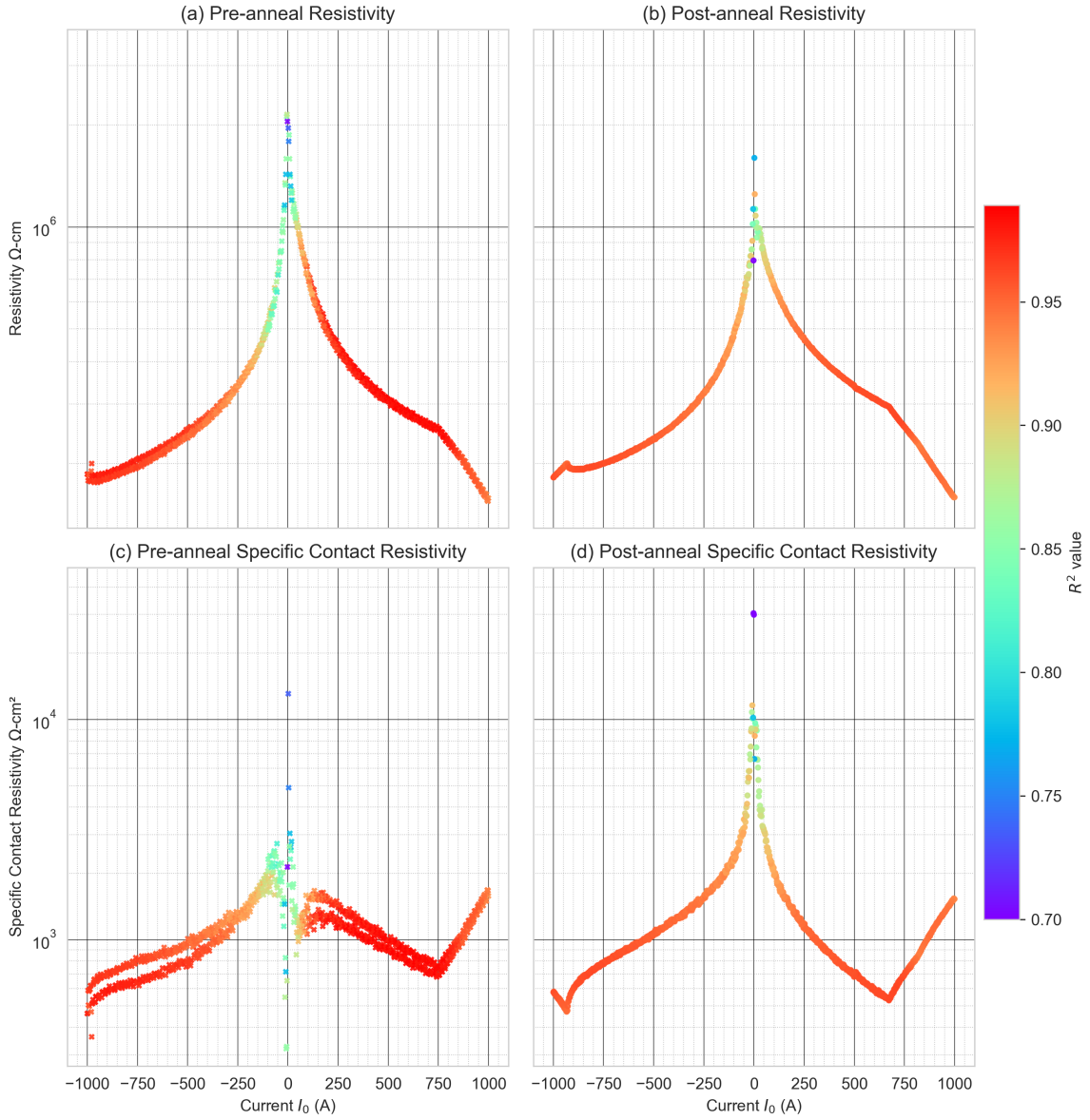

Figure 7.4 A full comparison of pre- and post-annealing on the specific contact resistivity and the observed resistivity of phosphorous-doped diamond.

Figure 7.4 provides a visual examination of the CTLM data, separating the data for ease of comparison. In addition to the resistivity and specific contact resistivity plots, a colour scale based on the corresponding R^2 value is used to help indicate the data which shows a poor linear fit when used for CTLM analysis. One important note is regarding the clear split between two separate lines of scatter points in figure c, which was initially believed to be due to oversampling of the electrical data. The potential issue lies in the usage of 500 evenly spaced data points between 0.1–1000 nA. As the measured current will most likely differ from any given constant current condition point, an absolute difference comparison was used to find the closest current values. In the case of figure c, this appears to result in two adjacent lines. However, subsequent tests of this methodology, using far fewer data points, reveal much the same double-line formation of scatter points. Hence, this is an odd pattern to observe within the pre-anneal specific contact resistivity. Further to this anomaly is the clear asymmetry between positive and negative constant currents. In particular, there is a sharp bend upwards at the $I_0 = 750$ nA mark in ρ_c for both the pre- and post-anneal cases. This trend is also reflected in figures a and b, where a shoulder is visible at the same current value. While the data is understandably noisy at very close to 0 A, this is not the case for the 750 nA feature, with consistently high R^2 values in this region. Finally, another small feature is noted in the negative constant current region, which appears to mirror that of the 750 nA feature. It is possible that this represents a real physical change in the devices as they are being tested, though it should also be noted that these features are consistent between the pre- and post-anneal testing.

7.2.3. Laser-Written LTLM Specific Contact Resistivity Reduction

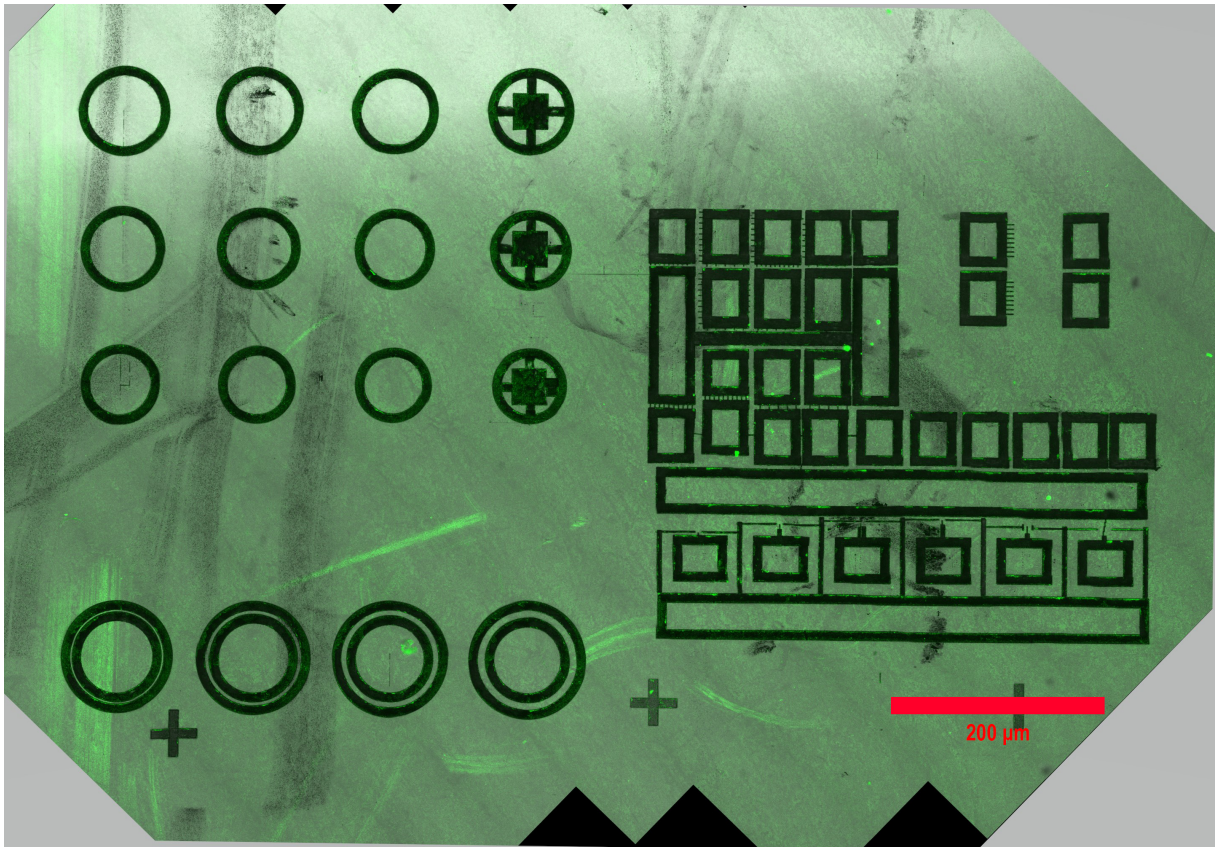

Figure 7.5 A confocal microscope mapping overview of the laser-written structures as seen using a backlit 488 nm light source. The green false colour is provided by fluorescence using an excitation laser of 408 nm.

In section 5.3, it is established that by using an LTLM setup comparable to that of the first two samples tested, a specific contact resistance of 1.62 $\Omega\,\mathrm{cm}^2$ is obtained at 5 V, with an observed phosphorous-doped resistivity of 6 $\mathrm{k}\Omega\,\mathrm{cm}$. This represents a drastic drop of five orders of magnitude in the specific contact resistance when compared to the measurements of Ti/Au contacts at around 50 V, matching the current best thermal graphitisation and coaxial arc plasma deposition nanocarbon contacts.

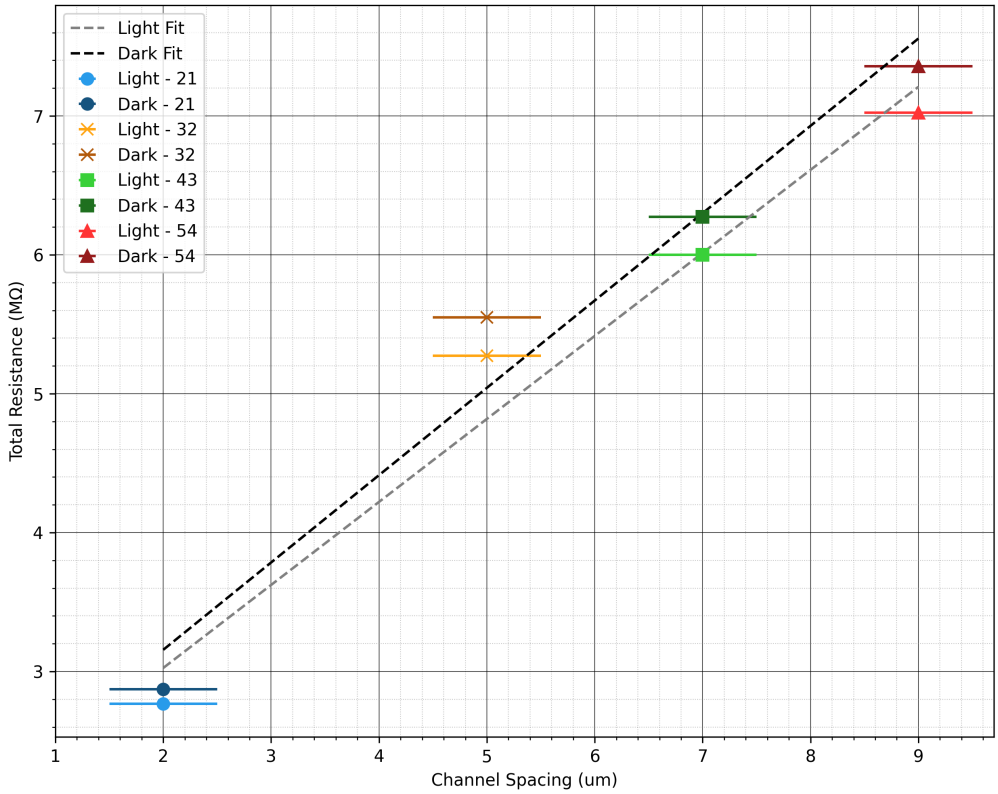

Figure 7.6 A LTLM plot of the total measured resistance against LTLM channel spacing at 20 V, with lines of best fit for both the illuminated and dark datasets. Uncertainties due to the error associated with current measurements are not possible to see at this scale; ±0.5 µm horizontal error bars are plotted.

7.3. Emitter Structures

Emitter structures, as tested, have produced a strong asymmetric current. The practicality of these device structures remains speculative, in part due to the transient nature of these emitters. The clear strengths of laser writing for the purpose of tailoring the allotropes of carbon within solid blocks of diamond are on full display. In this case, it has made phosphorous-doped diamond, which may not be suitable for conventional bulk semiconductor-type devices, into a potential emitter substrate.

7.3.1. Data

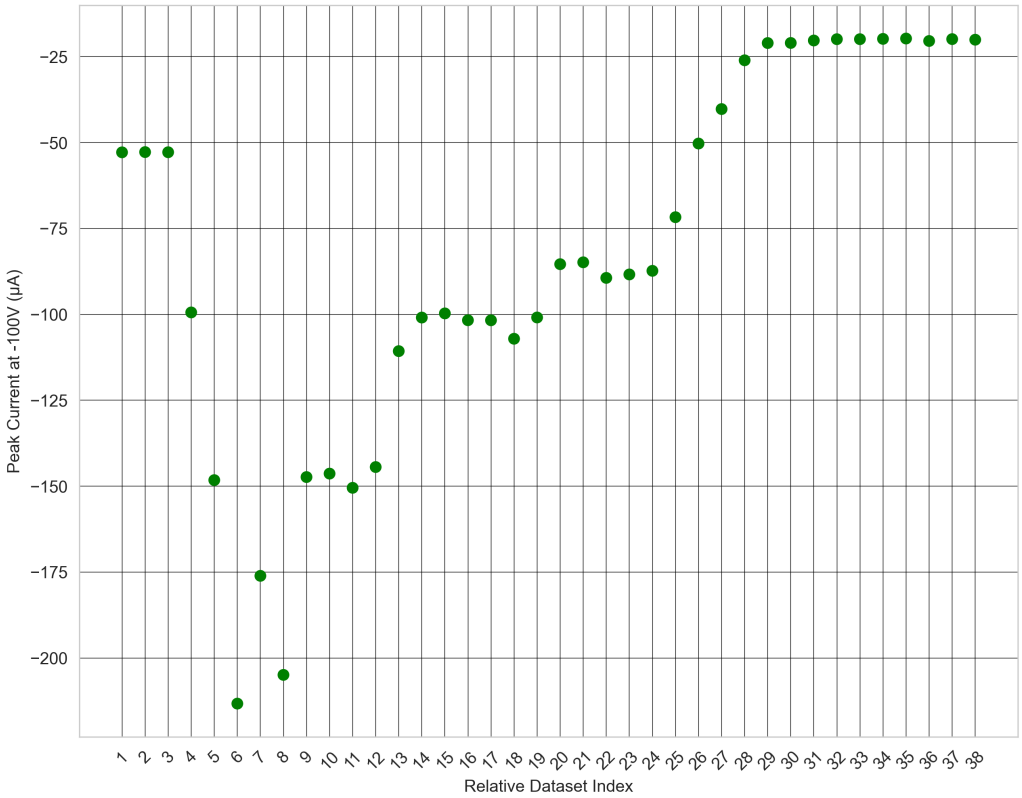

Figure 7.7 The observed peak currents at -100 V, across all single sweeps.

Finally, figure 7.7 plots the peak current measured for −100 V across all sweeps. The trend seen here correlates well with that of the two differing methodologies of quantifying asymmetry and also provides a quick reference for the peak current values of the IV sweeps shown in Figures 6.22, 6.24, and 6.26.

7.3.2. Computational Modelling

Of particular value in the computational modelling was the confirmation that field effect emission may be possible in the experimental setup achieved with laser-written structures on heavily phosphorous-doped diamond.

7.3.2.1. Array Electrostatics

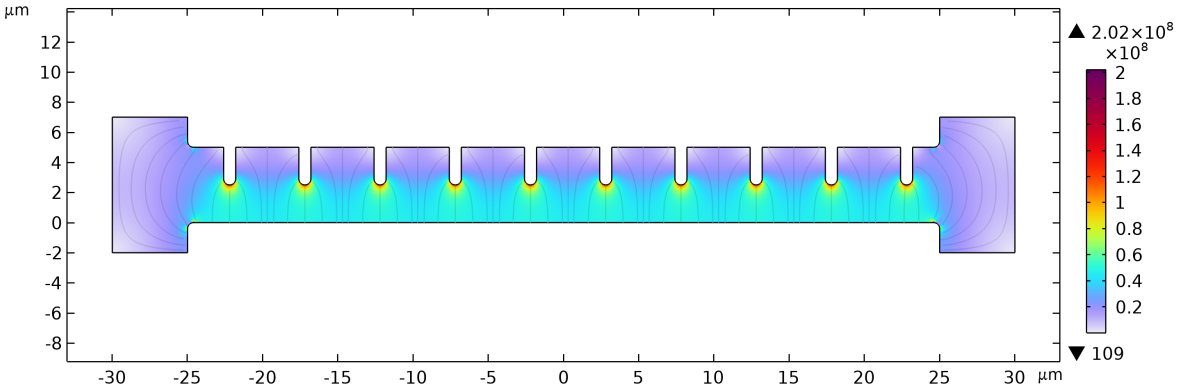

Figure 7.8 The electric field norm of an idealised geometry for emitter array CH.

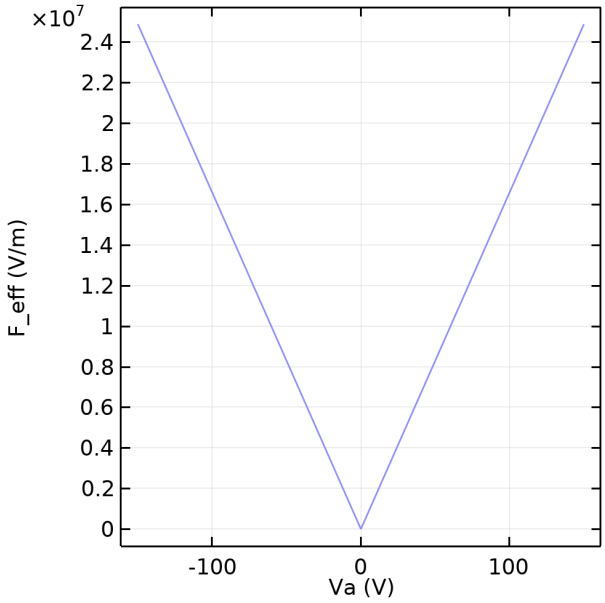

Figure 7.9 The peak electric field norm on the cathode structure for ±150 V.

In figures 7.8 and 6.33, the idealised geometry and resulting electric field norm surface plot are shown for an anode bias (V_a) of +150 V. Note that the cathode is held at 0 V. For an earlier discussion of the emitter tip profile as modelled, please see section 6.1. This electrostatic model was used for the full ±150 V range, with the resulting electric field norm maximum for the cathode plotted in figure 7.9. The slight discrepancy between the peak electric field norm in this figure when compared to the full geometry of figure 7.8 can be attributed to meshing. However, the electric field norm of well over 1×10^7 V m^{-1} is substantial and is consistent across the differing emitters in this ideal geometry setup.

7.3.2.2. Single Emitter Field Emission

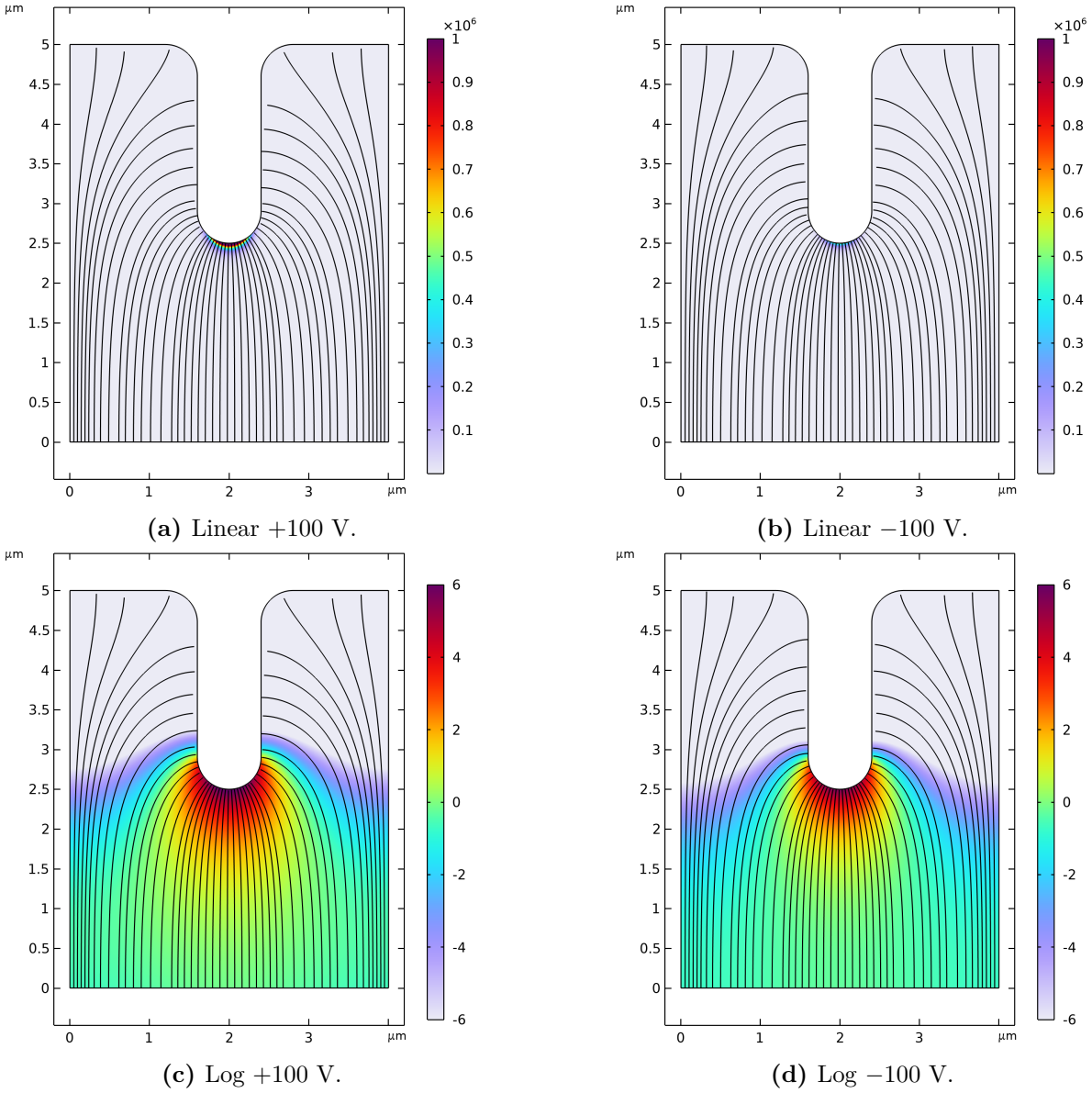

(a) Linear +100 V.

(b) Linear −100 V.

(c) Log +100 V.

(d) Log −100 V.

Figure 7.10 Simple Murphy-Good current density for idealised emitter cathode.

Figure 7.10 shows the results of applying the Murphy-Good field effect emission current density to the single emitter geometry [2]. As for figure 6.34, the top row shows the linear scale plot, while the bottom row shows the log scale plot of current density. Overall, it can be seen that the positive and negative applied anode voltages only have a slight impact upon the observed field effect emission, with greater emission in the positive region. The emission is concentrated quite strongly upon the very apex of the emitter in both cases, showing that the exact geometry of these cathode structures may have a large impact upon the profile of field effect emission. While this is an idealised geometry, it is quite evident that an irregular geometry will have a complex field emission profile, and it is entirely possible that sharper regions at a greater cathode-anode spacing may result in an

appreciable field effect emission contribution. This follows the literature models well [5, 6, 1].

7.4. Summary of Key Findings

To provide a clear overview of the results and their implications, the key findings from this thesis are summarised in Table 7.4.

Parameter	Value
Specific Contact Resistivity (Ti/Pt/Au)	472 (C), 494 (D) $k\Omega cm^2$
Phosphorous-Diamond Resistivity (Ti/Pt/Au)	132 (C), 464 (D) $M\Omega cm$
Specific Contact Resistivity (Ti/Au)	2.1 $k\Omega cm^2$
Phosphorous-Diamond Resistivity (Ti/Au)	490 $M\Omega cm$
Specific Contact Resistivity (Laser Written)	1.62 Ωcm^2
Phosphorous-Diamond Resistivity (Laser Written)	6 $k\Omega cm$

Table 7.4 Summary of Key Findings - Laser Writing

The literature best-case value for the specific contact resistivity with titanium contacts is 10^{-3} Ωcm^2 [7]. For the LTLM samples in this thesis, specific contact resistivity was measured to be 472 $k\Omega cm^2$ and 494 $k\Omega cm^2$, with a resistivity of the phosphorous doped film of 132 $M\Omega cm$ and 464 $M\Omega cm$ for samples C and D respectively at 10 V. For sample F and the CTLM results, at a constant current condition of -100 nA, a specific contact resistivity of around 2.1 $k\Omega cm^2$ and resistivity of around 490 $k\Omega cm$ was measured. Hence, sample G was used to demonstrate the potential of laser writing, with specific contact resistivity down to 1.62 Ωcm^2 and the observed sheet resistivity of 6 $k\Omega cm$ drastically reducing the contact resistance that any device would experience.

7.5. Future Work

It is the opinion of this student that laser writing for the purpose of generating a wide range of practical power electronic applications is on the near horizon. With the ability to utilise n-type diamond with a single, simple processing stage, countless studies into the etching of diamond for the sake of specific contact reduction, and the generation of mesa steps or sharp emitters can be called into question. Instead, one only needs to design a 3D structure, perhaps akin to the current generations of 3D GAAFET technology, and then they can print it within a diamond directly. Diamond power electronics that take advantage of the possibility of not only writing conductive wires between n- or p-type doped regions of diamond but also writing semiconducting phases directly within the intrinsic diamond bulk open multiple avenues of investigation. Perhaps diamond over the next century will develop from a niche, challenging material into the must-have semiconductor, especially with brand new methods of growing diamond, such as liquid metal diamond growth.

References

[1] Richard G. Forbes. “Comments on the continuing widespread and unnecessary use of a defective emission equation in field emission related literature”. In: *Journal of Applied Physics* 126.21 (Dec. 2019). ISSN: 1089-7550. DOI: 10.1063/1.5117289. URL: http://dx.doi.org/10.1063/1.5117289.

[2] R H. Good and Erwin W. Müller. “Field Emission”. In: *Electron-Emission Gas Discharges I / Elektronen-Emission Gasentladungen I.* Springer Berlin Heidelberg, 1956, pp. 176–231. ISBN: 9783642458446. DOI: 10.1007/978-3-642-45844-6_2. URL: http://dx.doi.org/10.1007/978-3-642-45844-6_2.

[3] Holly M. Johnson et al. “Cleaning diamond surfaces via oxygen plasma inhibits the formation of a TiC interface”. In: *Diamond and Related Materials* 126 (June 2022), p. 109058. ISSN: 0925-9635. DOI: 10.1016/j.diamond.2022.109058. URL: http://dx.doi.org/10.1016/j.diamond.2022.109058.

[4] Hiromitsu Kato et al. “Characterization of specific contact resistance on heavily phosphorus-doped diamond films”. In: *Diamond and Related Materials* 18.5 (2009). Proceedings of Diamond 2008, the 19th European Conference on Diamond, Diamond-Like Materials, Carbon Nanotubes, Nitrides and Silicon Carbide, pp. 782–785. ISSN: 0925-9635. DOI: https://doi.org/10.1016/j.diamond.2009.01.033. URL: https://www.sciencedirect.com/science/article/pii/S0925963509000363.

[5] A. Kyritsakis and F. Djurabekova. “A general computational method for electron emission and thermal effects in field emitting nanotips”. In: *Computational Materials Science* 128 (Feb. 2017), pp. 15–21. ISSN: 0927-0256. DOI: 10.1016/j.commatsci.2016.11.010. URL: http://dx.doi.org/10.1016/j.commatsci.2016.11.010.

[6] A. Kyritsakis and J. P. Xanthakis. “Derivation of a generalized Fowler–Nordheim equation for nanoscopic field-emitters”. In: *Proceedings of the Royal Society A: Mathematical, Physical and Engineering Sciences* 471.2174 (Feb. 2015), p. 20140811. ISSN: 1471-2946. DOI: 10.1098/rspa.2014.0811. URL: http://dx.doi.org/10.1098/rspa.2014.0811.

[7] Tsubasa Matsumoto et al. “Reduction of n-type diamond contact resistance by graphite electrode”. In: *physica status solidi (RRL) – Rapid Research Letters* 8.2 (Nov. 2013), pp. 137–140. ISSN: 1862-6270. DOI: 10.1002/pssr.201308252. URL: http://dx.doi.org/10.1002/pssr.201308252.

[8] Yue Pan et al. “Investigating extremely low resistance ohmic contacts to silicon carbide using a novel test structure”. In: *Micro/Nano Materials, Devices, and Systems*. Ed. by James Friend and H. Hoe Tan. SPIE, Dec. 2013. DOI: 10.1117/12.2033910. URL: http://dx.doi.org/10.1117/12.2033910.

[9] I. Stenger et al. “Electron mobility in (100) homoepitaxial layers of phosphorus-doped diamond”. In: *Journal of Applied Physics* 129.10 (Mar. 2021). DOI: 10.1063/5.0044326. URL: https://doi.org/10.1063/5.0044326.